

The effect of blast furnace slag chemistry on carbonation characteristics of cement-slag systems

Zhang, Y.

DOI

[10.4233/uuid:6732d452-5d85-4f06-a816-37d4e43f749b](https://doi.org/10.4233/uuid:6732d452-5d85-4f06-a816-37d4e43f749b)

Publication date

2022

Document Version

Final published version

Citation (APA)

Zhang, Y. (2022). *The effect of blast furnace slag chemistry on carbonation characteristics of cement-slag systems*. [Dissertation (TU Delft), Delft University of Technology]. <https://doi.org/10.4233/uuid:6732d452-5d85-4f06-a816-37d4e43f749b>

Important note

To cite this publication, please use the final published version (if applicable). Please check the document version above.

Copyright

Other than for strictly personal use, it is not permitted to download, forward or distribute the text or part of it, without the consent of the author(s) and/or copyright holder(s), unless the work is under an open content license such as Creative Commons.

Takedown policy

Please contact us and provide details if you believe this document breaches copyrights. We will remove access to the work immediately and investigate your claim.

**THE EFFECT OF BLAST FURNACE SLAG CHEMISTRY ON
CARBONATION CHARACTERISTICS OF CEMENT-SLAG SYSTEMS**

**THE EFFECT OF BLAST FURNACE SLAG CHEMISTRY ON
CARBONATION CHARACTERISTICS OF CEMENT-SLAG SYSTEMS**

Dissertation

for the purpose of obtaining the degree of doctor
at Delft University of Technology
by the authority of the Rector Magnificus Prof.dr.ir. T.H.J.J. van der Hagen
chair of the Board for Doctorates
to be defended publicly on
Wednesday 14 December 2022 at 12:30 o'clock

by

Yu ZHANG

Master of Engineering in Civil Engineering,
Southeast University, China,
born in Jiangsu, China.

This dissertation has been approved by the promotor.

Composition of the doctoral committee:

Rector Magnificus,	chairperson
Dr. O. Çopuroğlu	Delft University of Technology, promotor
Prof.dr.ir. E. Schlangen	Delft University of Technology, promotor

Independent Members:

Prof.dr. Q. Lyu	Southeast University, China
Prof.dr. S.R. van der Laan	Eindhoven University of Technology
Prof.dr. H.M. Jonkers	Delft University of Technology
Dr. Ö. Cizer	KU Leuven, Belgium
Dr. G. Ye	Delft University of Technology
Prof.dr.ir. M.A.N. Hendriks	Delft University of Technology, reserve member



Keywords: Slag-rich cement paste, Slag chemistry, Slag reactivity, Carbonation, Al_2O_3 and MgO, Calcium monosulfoaluminate, Hydrotalcite-like phase

Printed by: Ipskamp Printing, the Netherlands

Cover design: Yu Zhang and Yu Chen

Copyright © 2022 by Y. Zhang

All rights reserved. This copy of the thesis has been supplied on condition that anyone who consults it is understood to recognize that its copyright rests with its author and that no quotation from the thesis and no information derived from it may be published without the author's prior consent.

ISBN 978-94-6421-974-6

An electronic version of this dissertation is available at
<http://repository.tudelft.nl/>.

To my family

CONTENTS

List of Figures	xi
List of Tables	xvii
Summary	xix
Samenvatting	xxi
I General Introduction	1
1 Introduction	3
1.1 Research background	4
1.2 Research aim and objectives	6
1.3 Research scope	6
1.4 Research methodology	7
1.5 Thesis outline	8
References	9
2 Literature review	13
2.1 Introduction	14
2.2 Characteristics of anhydrous slag	14
2.2.1 Particle size distribution and density.	15
2.2.2 Amorphous content	15
2.2.3 Chemical composition.	16
2.3 The reactivity of slag	17
2.4 Hydration of cement-slag system	19
2.4.1 Main hydration products.	19
2.4.2 Ettringite and calcium monosulfoaluminate.	20
2.4.3 Hydrotalcite-like phase	21
2.5 Carbonation of cement-slag system.	23
2.5.1 Carbonation of main hydrates	24
2.5.2 Carbonation of minor hydrates	25
2.5.3 Pore structure	25
2.6 Summary and perspectives	26
References	27
II Experimental Investigation	39
3 EDS microanalysis of unhydrated blast furnace slag grains in field concretes with different service life	41
3.1 Introduction	42

3.2	Materials and methodology	42
3.2.1	Sample information	42
3.2.2	Quantitative EDS microanalysis	43
3.3	Results	46
3.3.1	Reference slag compositions in hardened cement pastes	46
3.3.2	Unhydrated slag compositions in hardened field concretes	48
3.3.3	Heterogeneity within a single slag particle	48
3.4	Discussion	52
3.4.1	Remarks on the EDS microanalysis methodologies	52
3.4.2	Sulfur and titanium in slag	53
3.4.3	Chemical composition of slag used in the Netherlands	54
3.5	Conclusions.	54
	References	55
4	Effect of slag chemistry on the reactivity of slag	59
4.1	Introduction	60
4.2	Materials and methodology	60
4.2.1	Synthesis of slag	60
4.2.2	Characterization of the structure of slag	61
4.2.3	Characterization of the reactivity of slag	62
4.3	Results	64
4.3.1	The characterization of slag	64
4.3.2	The reactivity of slag	65
4.3.3	The effect of sulfur species in commercial slag	73
4.4	Discussion	75
4.5	Conclusions.	76
	References	77
5	The role of hydrotalcite-like phase and monosulfate in slag cement paste during atmospheric and accelerated carbonation	83
5.1	Introduction	84
5.2	Materials and methodology	84
5.2.1	Sample information	84
5.2.2	Experimental methods.	85
5.3	Results	86
5.3.1	Long term natural exposure in the field	86
5.3.2	Natural exposure in the laboratory	88
5.3.3	Accelerated carbonation test.	93
5.4	Discussion	94
5.4.1	The role of hydrotalcite-like phase and monosulfate during carbonation	94
5.4.2	Degree of CO ₂ binding of different phases under different exposure environment.	97
5.5	Conclusions.	100
	References	101

6	The effect of slag chemistry on CO₂ binding capacity of C₃S-slag (-gypsum) system	105
6.1	Introduction	106
6.2	Materials and methodology	106
6.2.1	Sample information	106
6.2.2	Experimental methods	106
6.3	Results	108
6.3.1	Carbonation products	108
6.3.2	The amounts of CO ₂ bound in different phases	114
6.4	Discussion	116
6.5	Conclusions	120
	References	121
7	Effect of MgO content on the quantitative role of hydrotalcite-like phase in a cement-slag system during carbonation	127
7.1	Introduction	128
7.2	Materials and methodology	129
7.2.1	Materials	129
7.2.2	Methodology	129
7.3	Results	130
7.3.1	Phenolphthalein spray	130
7.3.2	Carbonation products	130
7.3.3	Degree of CO ₂ uptake of different carbonate phases	134
7.3.4	Microstructure	137
7.3.5	Micro-mechanical properties	140
7.4	Discussion	143
7.4.1	Distribution of Mg after carbonation	143
7.4.2	CO ₂ binding of hydrotalcite-like phase at different depths	145
7.4.3	Thermodynamic modelling	146
7.5	Conclusions	148
	References	149
8	Effect of Al₂O₃ content in slag on the relationship between slag reactivity and carbonation resistance	157
8.1	Introduction	158
8.2	Materials and methodology	159
8.2.1	Materials	159
8.2.2	Methodology	159
8.3	Results	159
8.3.1	Phenolphthalein spray	159
8.3.2	Carbonation products	160
8.3.3	Degree of CO ₂ uptake of different carbonate phases	163
8.3.4	Microstructure	166

8.4	Discussion	168
8.4.1	Slag chemistry vs. CO ₂ binding ability	168
8.4.2	Slag reactivity vs. carbonation resistance of cement-slag system	172
8.4.3	Thermodynamic modelling	173
8.5	Conclusions.	174
	References	175
III	Conclusions	179
9	Conclusions and recommendations	181
9.1	Retrospection	182
9.2	Conclusions.	183
9.3	Recommendations for further study	184
	Acknowledgments	187

LIST OF FIGURES

1.1	Map of the steel production sites in EU 27. Red dots correspond to the production sites of blast furnace slag, adapted from [1].	5
1.2	Outline of the thesis.	9
2.1	The schematic illustration of work principle of blast furnace, adapted from [2].	14
2.2	The chemistry of common SCMs, adapted from [22].	16
2.3	The range of slag chemistry over the past 100 years in Germany, adapted from [26].	17
2.4	The second aluminate peak indicated by a small shoulder following the main hydration peak in the calorimetric measurement, adapted from [67].	20
2.5	(a) Crystal structure of ettringite. Its ID in Crystallography Open Database is 1520837, and the structure was redrawn by the software Vesta. (b) Morphology of ettringite in a C ₃ S-C ₃ A-slag-gypsum system after 3 days of curing (unpublished data).	21
2.6	(a) Crystal structure of monosulfate. Its ID in Crystallography Open Database is 9013423, and the structure was redrawn by the software Vesta. (b) Morphology of monosulfate, adapted from [77].	22
2.7	Crystal structure of Mg ₄ Al ₂ (OH) ₁₂ (CO ₃)·3H ₂ O (d003 is the length of interlayer space.). Its ID in Crystallography Open Database is 9012627, and the structure was redrawn by the software Vesta.	23
2.8	MIP curves of slag cement from 1 to 28 days, adapted from [135].	25
2.9	Pore size distribution of the mortars OPC-48 and S-65 before and after carbonation, adapted from [140].	26
3.1	Monte Carlo simulation of the penetration of 200 electrons accelerated at 10 kV into a hypothetical slag particle.	45
3.2	The basic routine for quantitative EDS microanalysis. (a) A representative BSE micrograph of slag R3 cement paste; (b) several points targeted at unhydrated slag grains; (c) EDS spectra of an unreacted slag grain extracted from a single point microanalysis; (d) a typical residual spectra after standards-based quantification.	47

3.3	Box-plots of four main metal oxide contents of slag samples based on standards-based EDS microanalysis. (a) CaO (b) SiO ₂ (c) Al ₂ O ₃ (d) MgO. Small hollow box indicates the mean value, the horizontal line inside the box the median, the lower and upper ends of the box the first and third quartile, respectively, and the two whiskers connected with the box by vertical line indicate the minimum and maximum limits, and solid rhombus indicates the outliers.	49
3.4	Box-plot of four main metal oxide contents of slag in field concrete samples as quantified by EDS microanalysis. (a) CaO (b) SiO ₂ (c) Al ₂ O ₃ (d) MgO. . .	51
3.5	Two large slag particles chosen from reference slag (a) R3 and (b) R5 cement pastes, respectively.	52
4.1	Particle size distribution of slags and quartz.	62
4.2	XRD scans of nine synthetic slags and one commercial slag. The small Bragg peaks in slag M8 and CS1 can be attributed to the formation of akermanite and gehlenite, respectively.	64
4.3	SEM micrographs of (a) commercial slag S and (b) synthetic slag A18. . . .	64
4.4	FTIR spectroscopy results of slag samples in absorbance mode (Normalized, %).	65
4.5	(a) Heat flow and (b) total heat released as a function of time in calorimetric measurement for the model paste.	66
4.6	Bound water content against cumulative heat release.	67
4.7	Typical results of (a) TG, (b) and (c) DTG analysis of model pastes after curing of 7 days at 40 °C. Ht: hydrotalcite-like phase; Mc: monocarbonate; Ms: monosulfate.	68
4.8	XRD results of the selected model pastes after 7 days curing at 40 °C. E – ettringite; Ht: hydrotalcite-like phase; Hc: hemiacarbonate; Mc: monocarbonate; Ms: monosulfate.	69
4.9	(a) Ca ²⁺ (b) Si ⁴⁺ and (c) Al ³⁺ ion concentrations in the solution normalized to their molar fractions in raw slags, respectively plotted in function of time up to 3 days.	70
4.10	(a) Si ⁴⁺ and (b) Al ³⁺ concentrations in the solution normalized to their molar fraction in raw slag, respectively against cumulative heat release. . .	71
4.11	(a) Effective saturation indices of slag M8 as a function of dissolution time. A saturation index of 0.0 indicates an equilibrium state; (b) DTG result of the undissolved residual after dissolution test of seven days. Mh denotes Mg(OH) ₂ (brucite) and MC denotes MgCO ₃ , which may be originated from the carbonation of Mh during sample preparation. Ht: hydrotalcite-like phase.	72
4.12	(a) Heat flow and (b) total heat release as a function of time from calorimetric measurement of model pastes curing for 7 days at 40 °C. . . .	74
4.13	DTG analysis of model pastes curing for 7 days at 40 °C.	75

4.14 (CaO/SiO ₂)-(Al ₂ O ₃ +MgO) coordinate system in weight percentage. For the weight composition of these synthesized slags, please see data in Table 4.1. The origin of coordinate system represents slag containing CaO: 40%, SiO ₂ : 40%, Al ₂ O ₃ : 10%, MgO: 10% by mass, and this chemical composition of slag is most commonly seen in the industry.	77
5.1 (a) Illustration of the color change after spraying sample E with phenolphthalein solution; (b) and (c) Two representative BSE micrographs of the microstructure of the sample.	86
5.2 (a) Al/Ca vs. Si/Ca and (b) Mg/Si vs. Al/Si in the molar ratio of sample E.	87
5.3 DTG results, H ₂ O and CO ₂ MS curves of sample E. Ht: hydrotalcite-like phase.	88
5.4 (a) Illustration of the color change after spraying sample C with phenolphthalein solution; Microstructure of sample (b) A; (c) B; and (d) C, respectively.	89
5.5 Atomic ratios of Al/Ca against Si/Ca of sample A, B, and C.	89
5.6 DTG results, H ₂ O and CO ₂ MS curves of sample (a) A; (b) B; and (c) C, respectively. CH: portlandite; Ht: hydrotalcite-like phase; Ms: calcium monosulfoaluminate.	90
5.7 A typical sawn surface of cement-slag S2 paste after exposure in the laboratory for 2 years and the color change after spraying with phenolphthalein solution.	91
5.8 Microstructures of (a) carbonated; (c) transitional; and (e) mildly carbonated areas of cement-slag S2 paste. The DTG results, H ₂ O and CO ₂ MS curves of the corresponding areas were plotted in (b), (d), and (f) respectively. (g) XRD scans of carbonated, transitional, mildly carbonated, and fully carbonated (from accelerated carbonation, see Section 5.3.3) areas of the paste. CH: portlandite; Ht: hydrotalcite-like phase; Ms: calcium monosulfoaluminate.	92
5.9 (a) A typical BSE micrograph of the carbonated S2 paste; (b) EDS point analysis of Mg/Si vs. Al/Si in the molar ratio of carbonated and mildly carbonated areas of slag S2 paste.	93
5.10 The DTG results, H ₂ O and CO ₂ MS curves of fully carbonated area of cement-slag S2 paste exposed to accelerated carbonation. Ht: hydrotalcite-like phase.	94
5.11 (a) Illustration of the color change of a representative slag M16 sample after accelerated carbonation test with phenolphthalein solution; (b) XRD results of fully and mildly carbonated areas of the sample; The DTG results, H ₂ O and CO ₂ MS curves of (c) fully and (d) mildly carbonated areas of the sample. CH: portlandite; Ht: hydrotalcite-like phase; Ms: calcium monosulfoaluminate.	95
5.12 The CO ₂ MS curve of slag M16 cement paste after accelerated carbonation, and the integrated areas under the curve with respect to different carbonate phases.	98

5.13	The ratio of CO ₂ bound in CaCO ₃ and carbonated hydrotalcite-like plus Ca-Al AFm phases of investigated samples.	99
6.1	XRD scans of analytical reagent C ₃ S used in the research.	107
6.2	(a) TG and DTG results of C ₃ S paste after 3 months of curing; (b) DTG result, H ₂ O and CO ₂ MS curves of hydrated C ₃ S powder after full carbonation.	108
6.3	XRD analysis of C ₃ S paste after curing of 3 months and hydrated C ₃ S powder after carbonation. CH: portlandite; C: calcite; V: vaterite.	109
6.4	(a) Representative TG and DTG results of C ₃ S-slag pastes after 3 months of curing; DTG result, H ₂ O and CO ₂ MS curves of hydrated (b) slag M0 and (c) slag M16 powders after carbonation.	110
6.5	Representative XRD analysis of (a) C ₃ S-slag pastes after 3 months of curing and (b) hydrated powders after carbonation. Ht: hydrotalcite-like phase; CH: portlandite; C: calcite; V: vaterite.	111
6.6	Representative FTIR spectra of C ₃ S-slag pastes after 3 months of curing and hydrated powders after carbonation (Normalized, %).	112
6.7	(a) TG and DTG results of C ₃ S-slag-gypsum pastes after 3 months of curing; DTG result, H ₂ O and CO ₂ MS curves of hydrated (b) slag A3 and (c) slag A18 powders after carbonation. Ms: calcium monosulfoaluminate; Ht: hydrotalcite-like phase.	113
6.8	XRD analysis of (a) C ₃ S-slag-gypsum pastes after curing of 3 months and (b) hydrated powders after carbonation. AFt: ettringite; Ms: calcium monosulfoaluminate; Ht: hydrotalcite-like phase; CH: portlandite; C: calcite; V: vaterite.	114
6.9	Representative FTIR spectra of C ₃ S-slag-gypsum pastes after 3 months of curing and hydrated powders after carbonation (Normalized, %).	115
6.10	(a) The DTG result, CO ₂ MS curve of pure CaCO ₃ ; (b) The CO ₂ MS curve of carbonated slag M16 powder.	115
6.11	The areas under MS CO ₂ curve corresponding to different carbonate phases.	117
6.12	(a) and (b) Representative BSE images of slag M16 and A18 mixtures at 90 days, respectively; (c) Atomic ratio of Al/Ca against Si/Ca of slag M16 and A18 mixtures after 3 months of curing.	118
6.13	The area under MS CO ₂ curve corresponding to hydrotalcite-like phase vs. Mg/Al atomic ratio of raw slag.	119
6.14	Atomic ratio of Al/Ca against Si/Ca of slag M16 and CS1 mixtures after 3 months of curing.	120
7.1	Typical sawn surfaces of the specimens after spraying with phenolphthalein solution.	131
7.2	(a) TG and DTG results of cement-slag and quartz mixtures after 3 months of curing; (b)-(e) DTG results, H ₂ O and CO ₂ MS curves of fully carbonated cement-slag M0, M8, M16, and Qz pastes, respectively.	132

7.3	XRD analysis of cement-slag blends (a) after curing of 3 months; (b) after carbonation; and (c) 5 to 15° (2θ) of cement-slag blends before and after carbonation. CH: portlandite; E: ettringite; Ht: hydrotalcite-like phase. V: vaterite; C: calcite. The peak centered at around $2\theta = 21$ and 26° appeared to be associated with the formation of silica gel (labelled as SiO_2) [31] due to the carbonation of C-S(A)-H gel phase.	133
7.4	The FTIR spectra of cement-slag mixtures before and after carbonation, (Normalized, %).	134
7.5	The positions where powders were extracted, using slag M8 paste as an example. 1: fully carbonated area; 2: transitional area; 3: mildly carbonated area.	135
7.6	(a)-(c) The CO_2 MS curve of carbonated slag M16 paste at mildly carbonated, transitional, and fully carbonated areas, respectively.	136
7.7	Differential pore size distribution of cement-slag and quartz systems measured (a) before and (b) after accelerated carbonation test; Cumulative intrusion of cement-slag and quartz systems measured (c) before and (d) after accelerated carbonation test.	138
7.8	Typical BSE micrographs of a well-polished slag M8 sample surface exposed in the carbonation chamber for one month.	139
7.9	(a), (c), and (e): Microstructures of cement-slag M0, M8, and M16 mixtures after 3 months of curing, respectively; and (b), (d), and (f): Carbonated areas of cement-slag M0, M8, and M16 mixtures, respectively.	141
7.10	Typical plots of Al/Ca against Si/Ca in atomic ratio of slag (a) M0 and (b) M16 pastes before and after carbonation.	142
7.11	Typical plots of Mg/Si against Al/Si in atomic ratio of slag (a) M8 and (b) M16 pastes before and after carbonation.	142
7.12	Elastic modulus of (a), (c), and (e): cement-slag M0, M8, and M16 mixtures after 3 months of curing, respectively; (b), (d), and (f): cement-slag M0, M8, and M16 mixtures after carbonation, respectively.	144
7.13	Left: a typical BSE micrograph of carbonated slag M8 paste, and right top and bottom: the Mg and Al mappings correspondingly.	145
7.14	The proportion of CO_2 bound in CaCO_3 and carbonated hydrotalcite-like phase, and the ratio between these two phases from mildly to fully carbonated area.	146
7.15	Thermodynamic modelling of the phase assemblages in slag (a) M0 and (b) M16 pastes during the step-wise carbonation; (c) Phase assemblages of cement-slag system with the gradual addition of MgO at a certain amount of CO_2 uptake (10 g CO_2 /100 g binder).	147
7.16	The ratio of CO_2 bound in carbonated hydrotalcite-like phase to CaCO_3 with the gradual ingress of CO_2 through modelling.	148
8.1	Typical sawn surfaces of the specimens after spraying with phenolphthalein solution.	160

8.2	(a) TG and DTG results of representative cement-slag and quartz mixtures after 3 months of curing; (b-1)-(b-4) DTG results, H ₂ O and CO ₂ MS curves of fully carbonated cement-slag A3, CS1, A18, and Qz pastes, respectively. Ht: hydrotalcite-like phase; Ms: calcium monosulfoaluminate.	161
8.3	XRD analysis of representative cement-slag blends (a) at 90 days after curing; (b) after full carbonation. Ms: calcium monosulfoaluminate; Ht: hydrotalcite-like phase; CH: portlandite; C: calcite; V: vaterite. The peak centered at around $2\theta = 21$ and 26° appeared to be associated with the formation of silica gel (labelled as S) due to the carbonation of C-S-H gel phase [11].	162
8.4	The FTIR spectra of slag cement pastes after 3 months of curing and accelerated carbonation test, (Normalized, %).	163
8.5	The positions where powders were extracted, using slag A18 paste as an example. 1: fully carbonated area; 2: transitional area; 3: mildly carbonated area.	164
8.6	DTG results, H ₂ O and CO ₂ MS curves of (a) mildly carbonated and (b) transitional areas of slag A18 paste, respectively. Ms: calcium monosulfoaluminate; Ht: hydrotalcite-like phase; CH: portlandite.	164
8.7	(a)-(c) The CO ₂ MS curve of carbonated slag A18 paste in mildly carbonated, transitional, and fully carbonated areas, respectively.	165
8.8	Differential pore size distribution of cement-slag and quartz mixtures measured (a) before and (b) after accelerated carbonation test; (c) cumulative intrusion measured after accelerated carbonation test.	167
8.9	(a), (c), and (e): Microstructure of cement-slag A3, CS1, and A18 mixtures after curing of 3 months, respectively; and (b), (d), and (f): carbonated area of cement-slag A3, CS1, and A18 mixtures, respectively.	169
8.10	Representative plots of Al/Ca against Si/Ca in atomic ratio of slag (a) A3 and (b) A18 pastes before and after carbonation.	170
8.11	Representative plots of Mg/Si against Al/Si in atomic ratio of slag (a) A3 and (b) A18 pastes before and after carbonation.	170
8.12	The areas under MS CO ₂ curves or CO ₂ binding capacity against slag chemistry.	171
8.13	The proportions of CO ₂ bound in CaCO ₃ and carbonated Ca-Al AFm phases plus hydrotalcite-like phase from mildly to fully carbonated area of each mixture.	172
8.14	Thermodynamic modelling of the phase assemblages in A18 paste during the step-wise carbonation. Hc: calcium hemcarbonate; Mc: calcium monocarbonate; Ms: calcium monosulfoaluminate.	174

LIST OF TABLES

2.1	Typical chemical composition (wt.%) of blast furnace slag in Europe, North America, and Australia [4, 24, 25].	17
3.1	Descriptive information of the slag concrete samples studied.	43
3.2	Bulk compositions (wt.%) of reference slags as determined by XRF. Reference slag R2 and R3 with different MgO contents, and R4 and R5 with different Al ₂ O ₃ contents were chosen to be able to verify the standards-based method for different oxide levels, especially for minor constituents.	44
3.3	Compounds employed as standards for quantitative EDS microanalysis.	46
3.4	Chemical composition (wt.%) of five reference slags based on quantitative (std.-based) and semi-quantitative (standardless) EDS microanalysis.	47
3.5	The relative deviation between the values based on quantitative EDS microanalysis and semi-quantitative EDS microanalysis, as well as quantitative EDS microanalysis and XRF analysis.	48
3.6	Chemical composition (in wt.%) of slag in hardened concrete samples based on quantitative and semi-quantitative EDS microanalysis.	50
3.7	Chemical composition (wt.%) of slag determined by quantitative EDS microanalysis on single large slag grain and the corresponding coefficient of variation (CV).	52
4.1	Chemical compositions (wt.%) determined by XRF and physical properties of these ten slags.	61
4.2	Components (gram) of the blended system.	62
4.3	Dissolution rate of slag calculated based on the Si ⁴⁺ concentration from dissolution test.	73
4.4	Criteria used for different test methods to classify reactivity.	76
5.1	Chemical compositions (wt.%) and physical properties of CEM I 42,5 N and slag S2.	85
5.2	The calculated areas under MS CO ₂ curve and the corresponding proportions of different carbonate phases.	99
6.1	Compositions (wt.%) of the mixtures.	107
6.2	The areas under MS CO ₂ curve and the corresponding CO ₂ proportions of different carbonate phases.	116
7.1	The calculated areas under the MS CO ₂ curve of different carbonate phases.	135

7.2	CO ₂ concentrations of different carbonate phases calibrated with pure CaCO ₃ (/100 g).	136
8.1	The calculated areas under the MS CO ₂ curve of different carbonate phases.	165
8.2	CO ₂ concentrations of different carbonate phases calibrated with pure CaCO ₃ (/100 g).	166

SUMMARY

In order to compensate the limited availability of raw material resources and meet the growing demand for decreasing CO₂ emissions during cement and concrete productions, a practical method is to decrease the clinker content in cement. This strategy mainly consists of substituting a part of the clinker with supplementary cementitious materials (SCMs) at the cement and concrete production levels. As a mature addition in cement industry, blast furnace slag is a high-performance alternative that has been widely used in Europe and North America, as a SCM.

Cement blended with slag is known to exhibit a high resistance to many chemical deteriorations such as alkali silica reaction, sulfate attack, and chloride ingress. An exception is carbonation, which renders a poor microstructure at the skin area of slag-rich concrete.

The main aim of the thesis was to investigate the connection among slag chemistry, reactivity, and carbonation resistance of slag-rich cement paste. For this reason, the variation of slag composition was firstly identified through (1) literature review (Chapter 2) and (2) examining unhydrated slag grains existing in old slag concrete structures with different service life. Therefore, Chapter 3 studied the feasibility of using EDS microanalysis as a tool for quantitative measurement of the compositions of unhydrated slags in existing field concretes. The results revealed the variation trend of slag composition with time in the Netherlands. Then, synthetic slags covering the mentioned composition variation were produced in the laboratory, to eliminate the potential interferences and focus on slag chemistry only. The effect of slag composition on reactivity and carbonation resistance of slag-rich cement paste were investigated systematically.

In Chapter 4, synthetic slags based on CaO-SiO₂-Al₂O₃-MgO system and commercial slags were considered to estimate the correlation between slag chemistry and reactivity. It was found that higher MgO and/or Al₂O₃ contents of slag led to a higher reactivity.

Chapter 5 observed the carbonation products in the slag-rich cementitious systems (mainly CEM III/B) upon three different exposure conditions, namely, long term exposure in the field, indoor natural exposure, and accelerated carbonation testing. Emphasis was laid on the carbonation of monosulfate and hydrotalcite-like phase in particular. The author believed that there was enough evidence indicating these two phases being the key components towards formulating blast furnace slag systems resistant to carbonation. Chapter 6 revealed the correlation between slag chemistry and CO₂ binding capacity of the blended system. To simplify the composition of mixture, model paste containing only C₃S, synthetic slags and gypsum was employed. In Chapter 7 and 8, the effect of MgO and Al₂O₃ contents of slag on the carbonation characteristics of cement-slag system was explored, respectively. Accelerated carbonation testing was performed on slag cement paste. The evolution of phase

assemblage, microstructure, and micro-mechanical properties of each mixture before and after carbonation testing was evaluated.

Finally, the connection among slag chemistry, reactivity, and carbonation resistance was discussed comprehensively. It was noted that the classification employed for slag reactivity cannot be extended to characterize carbonation resistance of cement-slag system directly. The main challenge occurred for slag with high alumina content. Al_2O_3 -rich slag was reactive as a blended cement component but it did not contribute to carbonation resistance. Considering the effect of slag chemistry on reactivity and carbonation resistance together, slag, with a CaO/SiO_2 ratio ≈ 1 and presenting high MgO (> 10 wt.%) and moderate Al_2O_3 (10-15 wt.%) contents, was recommended to design slag rich concrete structure with improved hydration performance and carbonation resistance.

SAMENVATTING

Tegen de achtergrond van de beperkte beschikbaarheid van grondstofbronnen en de groeiende vraag naar het verminderen van de CO₂-uitstoot tijdens de cement- en betonproductie, is een praktische methode om het klinkergehalte in cement te verlagen. Deze strategie bestaat voornamelijk uit het vervangen van een deel van de klinker voor vulstoffen met bindmiddelfunctie (SCMs) op het productieniveau van cement en beton. Als een beproefde weloverwogen toevoeging in de cementindustrie is hoogovenslak een hoogwaardig alternatief dat op grote schaal wordt gebruikt in Europa en Noord-Amerika, als SCM.

Van cement gemengd met slak is bekend dat het een hoge weerstand vertoont tegen veel chemische aantastingen, zoals alkali-silica reactie, sulfaataantasting en binnendringen van chloride. Een uitzondering is carbonatatie, dat een slechte microstructuur veroorzaakt aan het betonoppervlak van slakrijk beton.

Het hoofddoel van dit proefschrift was om het verband tussen slakchemie, reactiviteit en carbonatatie weerstand van slakrijke cementpasta te begrijpen. Om deze reden werd de variatie in slaksamenstelling geïdentificeerd door (1) literatuuronderzoek (Hoofdstuk 2) en (2) aan de hand van oude betonconstructies op basis van slagcement met verschillende levensduur. Hoofdstuk 3 onderzocht de haalbaarheid van het gebruik van EDS-microanalyse als instrument voor een kwantitatieve meting van de chemische samenstelling van ongehydrateerde slakken die in bestaand beton is gebruikt. De resultaten onthulden een variatie van de slakkensamenstelling met de tijd in Nederland. Vervolgens werden in het laboratorium synthetische slakken met het genoemde samenstellingsbereik geproduceerd om mogelijke interferenties te elimineren en zich alleen op de slakkenchemie te concentreren. Het effect van de slaksamenstelling op de slakreactiviteit en carbonatatie weerstand van slakrijke cementpasta werd systematisch onderzocht.

In Hoofdstuk 4 werden synthetische slakken op basis van een CaO-SiO₂-Al₂O₃-MgO systeem en commerciële slakken beschouwd om de correlatie tussen slakchemie en reactiviteit te beschouwen. Het bleek dat hogere MgO- en Al₂O₃-gehalten van slakken tot een hogere reactiviteit leidden.

Hoofdstuk 5 observeerde de carbonatatieproducten in de slakrijke cementsystemen (voornamelijk CEM III/B) bij drie verschillende blootstellingsomstandigheden, namelijk langdurige blootstelling in het veld, natuurlijke blootstelling binnenshuis en versnelde carbonatatie testen. De nadruk werd vooral gelegd op de carbonatatie van monosulfaat en hydrotalciet-achtige fase. De auteur was van mening dat er voldoende bewijs was dat deze twee fasen de belangrijkste componenten zijn voor het samenstellen van hoogovenslaksystemen die bestand zijn tegen carbonatatie. Hoofdstuk 6 bestudeerde de correlatie tussen slakchemie en CO₂-bindend vermogen van een gemengde systeem. Om de samenstelling van het mengsel te vereenvoudigen, werd pasta gebruikt die alleen C₃S, synthetische slakken en gips bevat. In Hoofdstuk 7

en 8 werd respectievelijk het effect van het MgO- en Al₂O₃-gehalte van slakken op de carbonatatie-kenmerken van het cement synthetische slakstelsel onderzocht. Versnelde carbonatatieproeven werden uitgevoerd op slakcementpasta. De evolutie de van hydratatieproducten, microstructuur en micro mechanische eigenschappen van elk mengsel voor en na carbonatatieproeven werden geëvalueerd.

Ten slotte werd het verband tussen slakchemie, reactiviteit en carbonatatieweerstand uitgebreid geëvalueerd. Er werd opgemerkt dat de classificatie die wordt gebruikt voor slakreactiviteit niet kan worden uitgebreid om de carbonatatieweerstand van het cement-slakstelsel rechtstreeks te karakteriseren. De grootste uitdaging deed zich voor bij slakken met een hoog aluminiumoxidegehalte. Al₂O₃-rijke slak was reactief als een gemengde cementcomponent, maar droeg niet bij aan de carbonatatieweerstand. Gezien het effect van de slakchemie op reactiviteit en carbonatatieweerstand samen, werd slak, met een CaO/SiO₂-verhouding ≈ 1 en met een hoog MgO- en matige Al₂O₃-gehalte, aanbevolen om een slakkenrijke betonstructuur te ontwerpen met verbeterde hydratatieprestaties en carbonatatieweerstand.

I

GENERAL INTRODUCTION

1

INTRODUCTION

This chapter presented the background and motivation of the current thesis. The aim, scope and methodology of the research were introduced. Also, a summary of the thesis outline was given in the final.

1.1. RESEARCH BACKGROUND

WORLDWIDE, cementitious materials make up more than half of all the materials used. Although with low embodied energy, they account for approximately 8% of global CO₂ emissions due to large volumes [1–3]. In emerging and developing countries, it is foreseeable that the demand for cement will continue to rise to meet the demand of the growing population and urbanization. Therefore, cement and concrete industry still plays an important role in the worldwide economy as well as in reaching the goals of the Paris Agreement, which commit governments to keep global warming well below 2 °C and to pursue efforts to keep it below 1.5 °C. According to the Special Report published by the Intergovernmental Panel on Climate Change (IPCC) [4], limiting global warming to 1.5 °C required the economy to be carbon neutral globally by 2050.

Carbon neutrality is particularly challenging for the cement and concrete industry as less than 40% of CO₂ emission comes from the energy used to produce cement. More than 60% of emission is originated from the chemical breakdown of limestone – calcium carbonate (CaCO₃) – into CO₂ to produce the active component of cement, i.e., the clinker [5, 6]. Currently, there is no practical alternative to the use of limestone due to its abundance and widespread distribution in earth crust.

In order to compensate the limited availability of raw material resources and meet the growing demand of decreasing CO₂ emissions during cement and concrete productions, a practical method is to decrease the clinker content in cement. This strategy mainly consists of substituting a part of the clinker with supplementary cementitious materials (SCMs) at the cement and concrete production levels [7–10]. These SCMs can be the waste or by-products from other industries, such as fly ash from coal power plants and blast furnace slag from steel-making industry. Besides, they can also be natural materials, such as natural pozzolans or even just ground limestone.

As a mature addition in cement industry, blast furnace slag (*slag* for short) is a tried and tested, high-performance alternative that has been widely used in Europe and North America, as a SCM [11–14]. The current European standard EN 197-1 classifies 27 different cement types, 9 of which contain slag as the main component in proportions from 6 to 95 wt.%. It is a by-product from the production of pig iron, and formed from the combination of limestone fluxes, coke ashes and residues from iron ores [15]. The slag production was 24.6 Million tons in Europe in 2016, and more than 80% had already been used in cement and concrete productions [1, 16]. The availability of slag is closely related to the steel production, and Figure 1.1 shows the map of blast furnaces (steel production sites) in Europe (red dots) [1].

In the Netherlands, cement with about 65 to 70 wt.% of slag (CEM III/B) has a market share of around 60% [11], and it has been used in concrete production for nearly a century. Cement blended with slag is known to exhibit a high resistance to many chemical deteriorations such as alkali silica reaction, sulfate attack, and chloride ingress [17–20]. An exception is carbonation, which renders a poor microstructure at the skin area of slag-rich concrete [21, 22]. Moreover, there are claims from the industry that problems related to the surface durability issues partially arise due to the change of slag quality in recent years. According to a group of professionals, while slag concrete produced in the past is still performing well, some of newer structures constructed

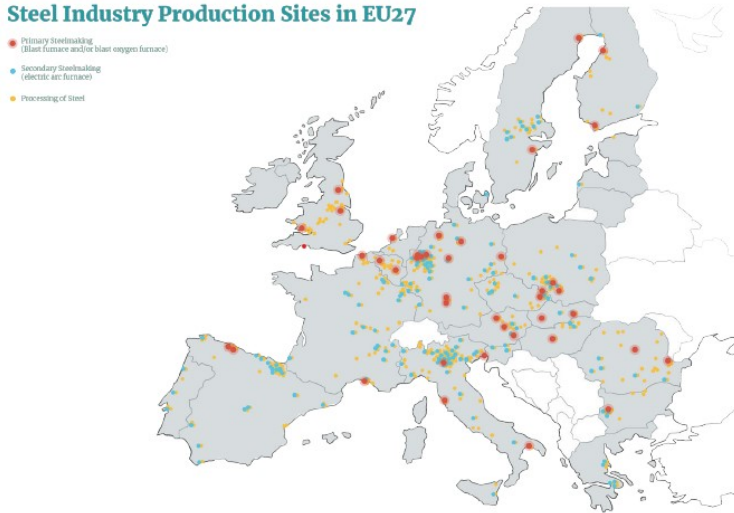


Figure 1.1: Map of the steel production sites in EU 27. Red dots correspond to the production sites of blast furnace slag, adapted from [1].

using comparable binders in the recent years have been showing performance issues only after a number of service years. These issues manifest themselves in surface deterioration in the form of carbonation, surface cracking and mass loss likely due to freezing and thawing in particular. Although there can be numerous reasons for the observed inferior performance, there is a consensus that the contemporary slag composition is likely to be the source of problems after a discussion with industry experts. For these reasons, the research background of this thesis consists of following considerations:

- Finding an effective method to identify the composition of slag used in field concretes. On the one hand, attempts to obtain slag chemistry used in older concretes are often unsuccessful possibly because the archives of QC reports are generally discarded after a number of years. On the other hand, available bulk material analysis techniques, such as X-Ray Fluorescence Spectrometer (XRF) and Inductively Coupled Plasma-Mass Spectrometer (ICP-MS) -both of which are widely used for raw material characterization- are not the most favorable techniques for characterizing unhydrated slag grains due to high interference from other phases in cement matrix.
- To eliminate potential interferences and focus on slag composition only. For most studies concerning slag chemistry, slags of different origins/countries are collected, which cannot avoid interferences e.g., thermal history, amorphous content, particle size distribution, etc. Furthermore, a single metal oxide is considered each time, and thus it cannot cover the entire range of composition

typically encountered in commercial slags and the interaction among different metal oxides.

- Assessment of the correlation between slag chemistry and carbonation resistance of cement-slag system. To the best of author's knowledge, few studies went deep into the correlation between slag chemistry and durability performance of cement-slag system, involving carbonation, freezing and thawing, etc. The lack of information on this correlation makes it a challenge to formulate improved blast furnace slag composition for better durability performance.

1.2. RESEARCH AIM AND OBJECTIVES

THE above-mentioned questions lead to the definition of research aim, which focuses on the effect of slag chemistry on carbonation characteristics of blast furnace slag cement system. To reach this end goal, the following objectives were identified:

- Determining the chemical compositions of slag used in field concretes with different service life;
- Assessing the correlation between slag chemistry and reactivity;
- Observing the carbonation behaviors of slag concretes in the field;
- Investigating the influence of slag chemistry on the carbonation resistance of cement-slag system;
- Defining the mechanism how slag chemistry drives the carbonation performance of cement-slag system, predict the performance of slag cement with a specific slag composition, and recommend slag chemistry for an improved performance in service.

1.3. RESEARCH SCOPE

IN the thesis, several slag concrete samples with different service life were collected from randomly chosen locations in the Netherlands. Synthetic slags covering the common composition range were produced in the laboratory and employed to cast slag cement paste. Additionally, commercial slags with representative compositions were also introduced when necessary. The experimental research considered chemical characterization of raw slags, as well as hydrated and carbonated slag cement pastes. Information with respect to hydration and carbonation characteristics was centered on the paste level. Although several slag concrete samples were analyzed in the study, the author mainly concentrated at the hydration and carbonation products.

It should be noted that only the following cementitious components were used in the study, i.e., CEM I 42,5 N (manufactured by ENCI Maastricht B.V.), synthetic slags (produced in the Microlab), commercial slags (provided by Ecocem Benelux B.V.). The slag to cement mass ratio was kept at 7/3 (to simulate CEM III/B) and water to binder ratio was 0.4. Cement-quartz paste with the same recipe was also cast as a reference.

The thesis proposed a standards-based quantitative EDS microanalysis to characterize unhydrated slag grains in field concretes and revealed the variation of slag

chemistry with time in the Netherlands. Moreover, emphasis was laid on minor hydration phases of slag cement paste, calcium monosulfaluminate (*monosulfate* for short) and hydrotalcite-like phase in particular, to investigate their roles during carbonation. Additionally, influence of MgO and Al₂O₃ contents of slag on the carbonation characteristics of cement-slag system was studied separately. Together with the carbonation behavior of portlandite and C-S(A)-H gel phase, the findings in the thesis provided essential insight the carbonation characteristics of slag cement paste with different slag compositions.

1.4. RESEARCH METHODOLOGY

TO understand slag chemistry so that to design cement-slag system that is more resistant to carbonation, experimental testing and characterization of the carbonation process was the main form of methodology of the thesis.

Firstly, standards-based energy dispersive X-ray spectroscopy (EDS) microanalysis, in tandem with electron imaging, was employed as a tool for quantitative measurement of chemical composition of blast furnace slag grains in hydrated cements/concretes. A favorable microanalysis protocol for acceptable elemental quantification accuracy was also proposed. In the experimental study, seven concrete samples representing various service life durations were collected from the field. The microanalysis results revealed the variation of slag composition with time in the Netherlands.

Following, both synthetic slags covering the common composition range (also covering the variation mentioned above) and commercial slags were chosen to estimate the correlation between slag chemistry and reactivity. The physical and mineralogical properties of raw slags were kept as similar as possible. The only variable can be considered as slag composition. To study reactivity, two methods were used in the thesis. The first one was hydraulicity/R3 test based on a model blended system composed of slag, calcium hydroxide, limestone and potassium-hydroxide and -sulfate solutions. The other method was the dissolution test of raw slag powder in strong NaOH solution, and the high liquid to solid ratio (l/s=1000) allowed the dissolution mechanism to be analyzed as much as possible.

As for carbonation, the thesis initially identified the carbonation products in slag-rich cementitious systems upon three different exposure conditions, namely, long term exposure in the field, indoor natural exposure, and accelerated carbonation testing. Emphasis was laid on the carbonation of minor hydrates, i.e., monosulfate and hydrotalcite-like phase in particular.

Next, to investigate the correlation between slag chemistry and CO₂ binding capacity, a model paste containing C₃S (alite, 3CaO·SiO₂), synthetic slags and gypsum was employed. The specimens were ground to powders after 3 months of sealed curing to accelerate the carbonation process. The carbonation mechanism was investigated through a complementary set of analytical methods, and the CO₂ binding capacity of each mixture was quantified by means of thermogravimetric analysis (TGA)-mass spectrometer (MS).

It is well known that the amounts of hydrotalcite-like phase and monosulfate formed in cement-slag system are directly related to the MgO and Al₂O₃ contents of slag, respectively. Therefore, the effect of MgO and Al₂O₃ contents of slag on the

carbonation behavior of cement-slag system were investigated, respectively. Accelerated carbonation testing was performed on slag cement paste. The evolution of phase assemblage, microstructure, and micro-mechanical properties of each mixture before and after carbonation testing was evaluated. Finally, the connection among slag chemistry, slag reactivity, and carbonation resistance of the system was discussed comprehensively.

1.5. THESIS OUTLINE

THE thesis outline is present in Figure 1.2. As discussed previously, the intended thesis title is "The effect of blast furnace slag chemistry on carbonation characteristics of cement-slag systems". The thesis is divided into nine chapters, and the chapter outline is summarized as follows:

The current chapter introduces the research background, objective, scope, and the corresponding methodology of the thesis.

Chapter 2 is reserved for the literature review. A systematic review of slag chemistry, slag reactivity, hydration and carbonation characteristics of cement-slag system is given. In particular, the role of monosulfate and hydrotalcite-like phase during hydration and carbonation is addressed in the context of available literature.

Chapter 3 explores the feasibility of using EDS microanalysis as a tool for quantitative measurement of chemical composition of unhydrated slags in existing field concretes. This chapter also reveals the variation trend of slag composition with time in the Netherlands.

Chapter 4 estimates the correlation between slag chemistry and reactivity. Both synthetic slags covering the common composition range and commercial slags are used in the hydraulicity and dissolution tests.

Chapter 5 observes the carbonation products in slag-rich cementitious systems upon three different exposure conditions, namely, long term exposure in the field, indoor natural exposure, and accelerated carbonation testing. Emphasis is laid on the carbonation behavior of monosulfate and hydrotalcite-like phase in particular.

Chapter 6 investigates the correlation between slag chemistry and CO₂ binding capacity. Model paste containing C₃S, synthetic slags and gypsum is employed.

Chapter 7 and 8 explore the influence of MgO and Al₂O₃ contents of slag on the carbonation performance of cement-slag system, respectively. Accelerated carbonation testing is performed on slag cement paste. The evolution of phase assemblage, microstructure, and micro-mechanical properties of each mixture before and after carbonation testing is evaluated. Moreover, the connection among slag chemistry, slag reactivity, and carbonation resistance of the system is discussed comprehensively.

Chapter 9 concludes with the main findings from **Chapter 3-8**. Based on experimental evidence, recommendations for better carbonation resistance are given with respect to slag chemistry. Besides, research perspectives for further studies are also proposed.

Chapter 1 Introduction
Chapter 2 Literature review
Chapter 3 Identify slag chemistry in old concretes
Chapter 4 Slag chemistry vs. reactivity
Chapter 5 Observations from atmospheric and accelerated carbonation
Chapter 6 Slag chemistry vs. CO ₂ binding capacity
Chapter 7 MgO vs. carbonation resistance
Chapter 8 Al ₂ O ₃ vs. carbonation resistance
Chapter 9 Conclusions, recommendations, and further research

Figure 1.2: Outline of the thesis.

REFERENCES

- [1] A. Favier, C. De Wolf, K. Scrivener, and G. Habert, *A sustainable future for the European Cement and Concrete Industry: Technology assessment for full decarbonisation of the industry by 2050*, Report (ETH Zurich, 2018).
- [2] U. Environment, K. L. Scrivener, V. M. John, and E. M. Gartner, *Eco-efficient cements: Potential economically viable solutions for a low-CO₂ cement-based materials industry*, *Cement and Concrete Research* **114**, 2 (2018).
- [3] E. Benhelal, E. Shamsaei, and M. I. Rashid, *Challenges against CO₂ abatement strategies in cement industry: A review*, *Journal of Environmental Sciences* **104**, 84 (2021).
- [4] V. Masson-Delmotte, P. Zhai, H.-O. Pörtner, D. Roberts, J. Skea, P. R. Shukla, A. Pirani, W. Moufouma-Okia, C. Péan, and R. Pidcock, *Global warming of 1.5 °C*, An IPCC Special Report on the impacts of global warming **1** (2018).
- [5] S. A. Miller, V. M. John, S. A. Pacca, and A. Horvath, *Carbon dioxide reduction potential in the global cement industry by 2050*, *Cement and Concrete Research* **114**, 115 (2018).
- [6] G. Habert, S. A. Miller, V. M. John, J. L. Provis, A. Favier, A. Horvath, and K. L. Scrivener, *Environmental impacts and decarbonization strategies in the cement and concrete industries*, *Nature Reviews Earth and Environment* **1**, 559 (2020).

- [7] M. C. Juenger and R. Siddique, *Recent advances in understanding the role of supplementary cementitious materials in concrete*, Cement and Concrete Research **78**, 71 (2015).
- [8] E. Aprianti, *A huge number of artificial waste material can be supplementary cementitious material (SCM) for concrete production—a review part II*, Journal of cleaner production **142**, 4178 (2017).
- [9] K. H. Yang, Y. B. Jung, M. S. Cho, and S. H. Tae, *Effect of supplementary cementitious materials on reduction of CO₂ emissions from concrete*, Journal of Cleaner Production **103**, 774 (2015).
- [10] M. C. Juenger, R. Snellings, and S. A. Bernal, *Supplementary cementitious materials: New sources, characterization, and performance insights*, Cement and Concrete Research **122**, 257 (2019).
- [11] J. Bijen, *Benefits of slag and fly ash*, Construction and building materials **10**, 309 (1996).
- [12] M. C. G. Juenger, F. Winnefeld, J. L. Provis, and J. H. Ideker, *Advances in alternative cementitious binders*, Cement and Concrete Research **41**, 1232 (2011).
- [13] E. Crossin, *The greenhouse gas implications of using ground granulated blast furnace slag as a cement substitute*, Journal of Cleaner Production **95**, 101 (2015).
- [14] Y. Li, Y. Liu, X. Gong, Z. Nie, S. Cui, Z. Wang, and W. Chen, *Environmental impact analysis of blast furnace slag applied to ordinary portland cement production*, Journal of Cleaner Production **120**, 221 (2016).
- [15] Y. Yang, K. Raipala, and L. Holappa, *Ironmaking*, in *Treatise on process metallurgy* (Elsevier, 2014) pp. 2–88.
- [16] J. M. De Vet, A. Pauer, E. Merkus, P. Baker, A. R. Gonzalez-Martinez, T. Kiss-Galfalvi, G. Streicher, and A. Rincon-Aznar, *Competitiveness of the European cement and lime sectors*, WIFO Studies (2018).
- [17] G. Osborne, *Durability of portland blast-furnace slag cement concrete*, Cement and Concrete Composites **21**, 11 (1999).
- [18] B. S. Divsholi, T. Y. D. Lim, and S. Teng, *Durability properties and microstructure of ground granulated blast furnace slag cement concrete*, International Journal of Concrete Structures Materials **8**, 157 (2014).
- [19] A. M. Rashad, *An overview on rheology, mechanical properties and durability of high-volume slag used as a cement replacement in paste, mortar and concrete*, Construction and Building Materials **187**.
- [20] R. B. Polder, T. Nijland, and M. de Rooij, *Blast furnace slag cement concrete with high slag content (CEM III/B)—experiences with the durability in the netherlands since the 1920's*, NPRA report SVV **270**, 72 (2014).

- [21] V. G. Papadakis, *Effect of supplementary cementing materials on concrete resistance against carbonation and chloride ingress*, Cement and Concrete Research **30**, 291 (2000).
- [22] S. von Greve-Dierfeld, B. Lothenbach, A. Vollpracht, B. Wu, B. Huet, C. Andrade, C. Medina, C. Thiel, E. Gruyaert, H. Vanoutrive, *et al.*, *Understanding the carbonation of concrete with supplementary cementitious materials: a critical review by RILEM TC 281-CCC*, Materials and structures **53**, 1 (2020).

2

LITERATURE REVIEW

This chapter was designed to systematically review the current state-of-art of cement-slag paste, and four distinct parts were organized. The first part explored the properties of raw blast furnace slag, e.g., particle size distribution, amorphous content, and chemical composition. For the second part, a comprehensive review of slag reactivity was presented. The third part summarized the hydration products of slag cement paste, and emphasis was laid on the minor hydration products, i.e., ettringite, monosulfate, and hydrotalcite-like phase. Finally, carbonation of cement-slag system was reviewed.

2.1. INTRODUCTION

BLAST furnace slag is a by-product from the production of pig iron. During production, the blast furnace (a countercurrent shaft furnace in which pig iron is extracted under reducing condition) is filled with mixtures of iron ore, ore pellet or sinter, aggregates such as limestone and dolomite, possibly other corrective substances like fluxes, and coke or other reducing agents. The liquid blast furnace slag is formed at 1450 to 1550 °C from the combination of limestone and dolomite fluxes, coke ashes and residues from iron ore. In addition, it absorbs other accompanying elements, e.g., sulfur and alkalis (Na and K). Due to the difference of density, liquid slag floats on top of the molten iron. This makes it possible to drain liquid slag together with the pig iron from the furnace during tapping and then separate them with different channels [2, 3] (see Figure 2.1). When the molten slag is rapidly cooled with water in a pond, or with powerful water jets, it turns into a fine, granular, almost fully noncrystalline, glassy form known as granulated slag. After finely ground, granulated slag has been found to exhibit excellent cementitious properties either used with Portland cement or alkali activated [4, 5].

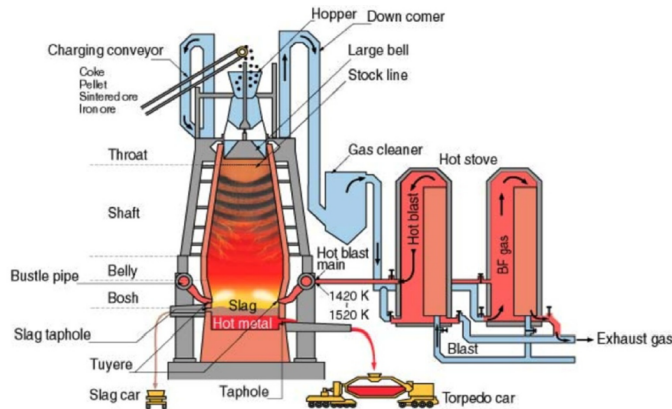


Figure 2.1: The schematic illustration of work principle of blast furnace, adapted from [2].

This chapter was designed to systematically review the current state-of-art of cement-slag paste, and four distinct parts were organized. The first part explored the properties of raw blast furnace slag, e.g., particle size distribution, amorphous content, and chemical composition. For the second part, a comprehensive review of slag reactivity was presented. The third part summarized the hydration products of slag cement paste, and emphasis was laid on the minor hydration products, i.e., ettringite, monosulfate, and hydrotalcite-like phase. Finally, carbonation of cement-slag system was reviewed.

2.2. CHARACTERISTICS OF ANHYDROUS SLAG

THE properties of anhydrous slag can be divided into physical, mineralogical, and chemical three aspects. There is a close correlation between slag properties and the

performance of cement-slag system. In this section, several important indices of anhydrous slag were chosen to give a review.

2.2.1. PARTICLE SIZE DISTRIBUTION AND DENSITY

It is well known that the grinding resistance of vitreous slag to the typical cement fineness range is often greater than that of crystalline Portland cement clinker or sulfate carrier [6, 7]. Also, slag differs significantly in terms of the grindability, and the specific grinding energy requirement (kWh/t) increases exponentially for a higher specific surface. Measurement results proved that a clear connection between the bulk density or the total porosity and the grindability of slag was noted [8]. Low bulk density or high total porosity led to a more favorable grinding behavior, i.e., to a lower specific energy requirement and easier grindability.

On the other hand, it has been reported that the particle size distribution (PSD) of slag plays a major role in influencing the fresh and hardened properties of cement-slag system, particularly at early ages [9–11]. Slag with a narrower particle size distribution shows a higher compressive strength development in the blended system. Meanwhile, it was also found that the 0–20 μm fraction of slag was generally crucial for 7 days heat release and compressive strength. As for 28 days, the fraction of 20–40 μm participated. The fraction with grain size coarser than 40 μm behaved almost as an inert material [11, 12]. Thus, to compensate the early age strength development, slag used in the blended system has been ground finer and finer with a d_{50} in the range of 10–20 μm . In ultra-fine slag-containing system, it presents a $d_{50} \approx 5 \mu\text{m}$ [13, 14].

As for slag density, it is commonly dependent on chemical composition, temperature of melting, and granulation condition. The average density of today's blast furnace slag is $\sim 2.9 \text{ g/cm}^3$ [15]. Deviations from this typical value can be an indicator for different glass or crystal contents, as well as with a constant glass content, for a change in the chemical composition.

2.2.2. AMORPHOUS CONTENT

The amorphous/glass content of slag largely depends on the quenching method. Slag with a glass content of > 95% by volume is usually produced in modern wet granulation plants. Additionally, the glass content is also associated with slag chemistry. The more acidic slag is, i.e., the lower its basicity - expressed e.g., as CaO/SiO_2 ratio - the easier it is to solidify glassy. Highly basic slag ($(\text{CaO}+\text{MgO})/\text{SiO}_2 > 1.8$), on the other hand, tends to spontaneously form crystalline phases even at higher temperature, and is very difficult to obtain completely glassy [15]. The potential crystalline phases formed in slag mainly consist of merwinite ($3\text{CaO}\cdot\text{MgO}\cdot 2\text{SiO}_2$), gehlenite ($2\text{CaO}\cdot\text{Al}_2\text{O}_3\cdot\text{SiO}_2$), calcite, etc [2].

The glass content can be determined microscopically or by means of quantitative X-ray diffraction analysis [16, 17]. The microscopic determination is carried out by counting the glassy or crystalline components of a suitable fraction, which is sieved from a slightly pre-crushed sample. This method delivers an exact and easily reproducible result. On the other hand, crystalline parts can be recognized by means of discrete reflections, whereas glassy, X-ray amorphous ones only produce a curved background ("glass hump") in the X-ray diagram [18, 19]. In the case of small crystalline components with correspondingly small reflections, as is typical for slag, an exact

quantitative determination is difficult, especially in the case of curved background, which is always provided with a certain signal noise [20].

The amorphous content of slag has been assigned great importance for its connection with latent hydraulic property. A maximum glass content is often associated with optimal hydraulic properties of slag. In general, the crystalline phases of slag have no hydraulic properties and lead to the blended system with less strength development [21].

2.2.3. CHEMICAL COMPOSITION

Chemical composition of slag varies depending on the composition of iron ore, fluxing stone and impurity of the coke fed into the furnace [2, 4]. Normally, blast furnace slag is rich in calcium oxide and silica (major constituents), with significant amount of alumina and magnesium oxide (minor constituents), and can be expressed as a CaO-SiO₂-Al₂O₃-MgO system accounting for more than 95 wt.% in the composition [2, 15]. Figure 2.2 illustrates the chemistry of common SCMs, of which slag is located between Portland cement and fly ash [22]. In other words, slag presents higher CaO and lower SiO₂ contents than fly ash, while lower CaO and higher SiO₂ contents than Portland cement.

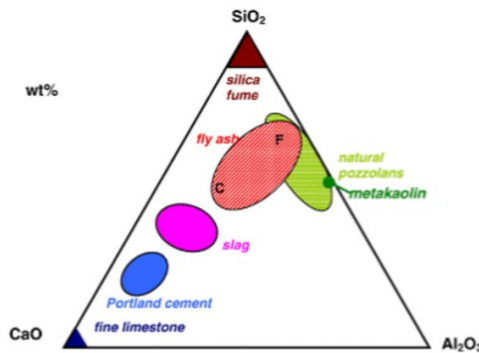


Figure 2.2: The chemistry of common SCMs, adapted from [22].

Since blast furnace used to be found in the vicinity of iron ore and/or coal deposits, and the chemical composition of slag is strongly related to the raw material compositions which can be expected to differ with geologies, thus it is no wonder that slag chemistry varies over a wide range across locations. Any change in the composition of raw materials and/or in the furnace passage affects the composition of slag. Besides, different blast furnace management and metallurgical technology change slag chemistry further [2, 4, 15, 23].

Table 2.1 demonstrates significant discrepancies with regards to slag chemistry in an international comparison. Note that these data was sourced from the self-monitoring of steelmaking factories and various associations [24]. The range of basicity, i.e., $(\text{CaO}+\text{MgO})/\text{SiO}_2$ which was an indication for the latent hydraulic property of slag, varied remarkably. Meanwhile, the minimum requirement, i.e., $\text{CaO}/\text{SiO}_2 > 1$, had been met by all slags. As for the amounts of Al₂O₃ and MgO of slag,

Table 2.1: Typical chemical composition (wt.%) of blast furnace slag in Europe, North America, and Australia [4, 24, 25].

	Europe		North America		Australia
CaO	30.9~46.1	30.7~45.6	29~50	32~45	40~43
SiO ₂	30.5~40.8	30.7~44.0	30~40	32~42	34~37
Al ₂ O ₃	5.9~17.6	5.4~16.4	7~18	7~16	12~15
MgO	1.7~17.3	3.5~17.3	0~19	5~15	4~7

they also fluctuated considerably across the world.

Next to the geographical variation, slag composition has also been observed to vary in a single location over time, as reported in [26]. Figure 2.3 shows the range of slag chemistry over the past 100 years in Germany, as an example. The changes were due, among other things, to the increasing concentration of steel industry on different locations, the use of ores or pellets exported from different countries, and a changed blast furnace management with time.

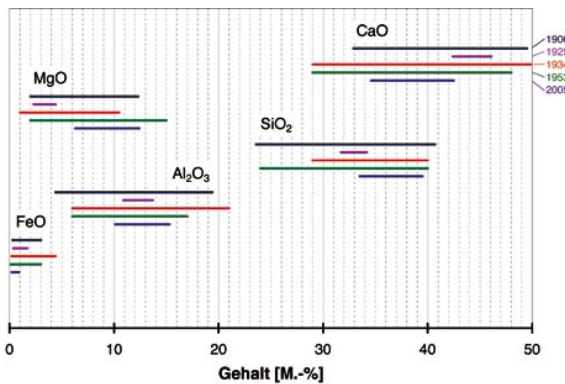


Figure 2.3: The range of slag chemistry over the past 100 years in Germany, adapted from [26].

2.3. THE REACTIVITY OF SLAG

THE reactivity (the rate of reaction with alkalis released by cement) of slag was discovered in 1862 by Emil Langen [27]. The first use of slag in cement dated back to 1865 when a slag-lime cement was commercially produced in Germany [28].

The quantitatively dominant constituents of slag, converted to oxides, are CaO, SiO₂, Al₂O₃ and MgO. Nevertheless, the trace components, such as TiO₂, MnO, CaS, Na₂O and K₂O, also have a considerable influence on the reactivity of slag. Generally, the reactivity of slag increases with the increasing CaO, Na₂O, and K₂O contents, and with the decreasing amounts of SiO₂, FeO/Fe₂O₃, TiO₂, MnO/Mn₂O₃, etc [29–36]. A high CaO/SiO₂ ratio indicates a good reactivity, and a deficiency in CaO can be compensated by MgO, as stated in EN 15167-1. Furthermore, increased Al₂O₃ content of slag was reported to enhance reaction heat release and early age strength development [35, 37]. Due to the higher molar volume of Al-containing phases, e.g., ettringite and monosulfate, they can fill up pores, thus are beneficial for the

compressive strength development [38]. In the work of [34], the authors also confirmed the positive correlation between Al_2O_3 content and slag reactivity.

On the other hand, many efforts have been made to determine a relationship that can be used to predict slag reactivity from its chemical composition. Hydraulic moduli, or *basicity*, categorized into different formulas can be found in [15]. The European Standard EN 15167-1 recommends $M_1 > 1$ (see Equation 2.1). The modulus M_2 is the most frequently used and referred to as basicity factor (see Equation 2.2). However, it was also noted that none of them gave a satisfactory result for estimating various slag used in cement [15].

$$M_1 = \frac{CaO + MgO}{SiO_2} \quad (2.1)$$

$$M_2 = \frac{CaO + MgO + Al_2O_3}{SiO_2} \quad (2.2)$$

At the same time, the reactivity of slag can also be attributed to the network structure of glass (amorphous). The more disordered and depolymerized network structure, the more easily broken up of glass, and thus the higher slag reactivity. The degree of depolymerization of network structure can be represented by NBO/T, the number of non-bridging oxygen (NBO) per tetrahedral network-forming element (T). NBO/T varying from 0 to 4 refers to fully interconnected network, sheet, chain or ring, dimer, and monomer (fully depolymerized) correspondingly [3, 17, 39–46].

Commonly, slag presents a three dimensional interconnected network structure in which, silica tetrahedral (SiO_4) is a basic building unit where each Si is bonded with four oxygen ions [3, 39, 45, 46]. Shimoda et al. [45] concluded that the polymerization structure of Si in slag was close to chain-like linkage, namely Q2(1Al) and Q2(2Al). Moreover, there is a consensus existing that in case of the presence of large amount of Al_2O_3 ($Al_2O_3 \geq 0.5 SiO_2$ in molar ratio), except for the four-fold coordinated Al considered as network former existing only in-between SiO_4 tetrahedra in the form of Si-O-Al-O-Si (Loewenstein's rule of aluminum avoidance [47]), some aluminum are also in five- and six-fold coordination states and regarded as network modifier owing to its amphoteric property [48, 49].

It is well accepted that gradual addition of network modifier will react with the bridging oxygen (BO) of silicate network (e.g., Si-O-Si bond), causing cleavage and creating non-bridging oxygen (i.e., ionic bond $O^- - Ca^{2+}$). Non-bridging oxygen is balanced by a proper distribution of cations, Ca^{2+} and K^+ in particular. The field strength, z/r^2 ratio (z and r are the charge and radius of cation, respectively), represents the strength of bond between a non-bridging oxygen and a cation and plays a key role in modification of the glass structure [50]. It is concluded that a cation with larger z/r^2 (i.e., Mg^{2+}) tends to generate a lower degree of polymerization. The order of field strength among cations commonly seen in slag follows: $K^+ \leq Na^+ \leq Ca^{2+} \leq Mg^{2+}$ [42]. In the network structure of slag, Mg^{2+} ion with smaller radius tends to act as network modifier while Ca^{2+} ion performs charge compensation. Results from [46, 51] confirmed that MgO in slag had relatively small ion radii, presenting stronger capacity to break the linkage of network structure. However, when the amount of CaO was

sufficient, the role of MgO was insignificant as the network structure had already been depolymerized [52].

Dutt et al. [53] studied the structure model of calcium aluminosilicate glass and suggested that NBO/T can be estimated by the chemical composition using Equation 2.3 as following. Novatski, A et al. [54] put forward a modified formula based on Eq. 2.3 as they believed that the total amount of Al_2O_3 as network former should be subtracted from the sum of network modifier, as Equation 2.4 shows. Considering that slag contained some trace components, the equation was revised into Equation 2.5 further in [55].

$$NBO/T = \frac{2(CaO) - (Al_2O_3)}{(SiO_2) + (Al_2O_3)} \quad (2.3)$$

$$NBO/T = \frac{2(CaO) + a(Al_2O_3) - (1 - a)(Al_2O_3)}{(SiO_2) + (1 - a)(Al_2O_3)} \quad (2.4)$$

$$NBO/T = \frac{2(CaO + MgO + Na_2O + K_2O + a(Al_2O_3) + b(Fe_2O_3) - (1 - a)(Al_2O_3) - (1 - b)(Fe_2O_3))}{(SiO_2) + TiO_2 + (1 - a)(Al_2O_3) + (1 - b)(Fe_2O_3)} \quad (2.5)$$

The quantity in the bracket represents the constituent in mol%, and the parameters a and b involved are percentages of Al_2O_3 and Fe_2O_3 acting as network modifier correspondingly.

2.4. HYDRATION OF CEMENT-SLAG SYSTEM

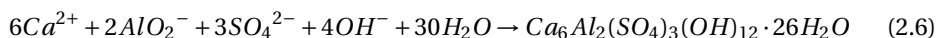
THE ground granulated blast furnace slag can be blended with (Ordinary) Portland cement to produce cement-slag system. These two ingredients hydrate at different rates. Upon contacting with water, Portland cement in the blended mixture starts to hydrate immediately. Meanwhile, a very small volume of slag (the fine fraction) reacts. During the first day, slag can be assumed as an inert filler. Subsequently, the hydration of slag is activated by alkalis (Na and K released from cement) and later by portlandite originated from the hydration of cement clinker. In general, the hydration rate of slag is much slower than that of cement clinker [30, 56–59].

2.4.1. MAIN HYDRATION PRODUCTS

During the curing of slag cement paste, the main components of cement clinker, i.e., C_3S , C_2S , C_3A , and C_4AF react at different rates to produce calcium silicate hydrate (C-S-H), portlandite, ettringite, monosulfate, and other trace hydration products [60]. On the other hand, the hydration of slag grains mainly depends on the breakdown of slag network structure by OH^- ions, in the form of alkali (Na and K) hydroxide and $Ca(OH)_2$. Compared with pure cement paste, blending cement with slag increases the amount of C-S(A)-H gel phase and lowers its Ca/Si atomic ratio as slag contains more SiO_2 and less CaO [61–63]. Additionally, a higher Al/Si atomic ratio is ultimately obtained in the gel due to the incorporation of Al dissolved from slag. Low Ca/Si gel phases fill up capillary pores, reduce the total porosity and thus contribute to an enhanced durability [62, 63].

2.4.2. ETTRINGITE AND CALCIUM MONOSULFOALUMINATE

Ettringite, the mineral name for calcium sulfoaluminate ($3\text{CaO}\cdot\text{Al}_2\text{O}_3\cdot 3\text{CaSO}_4\cdot 26\text{H}_2\text{O}$), is a minor constituent of hydrated Portland cement. Calcium sulfate sources, such as gypsum, is intentionally added to Portland cement to regulate early age hydration and prevent flash setting, improve strength development, and reduce drying shrinkage through the formation of ettringite, as the following Equation 2.6 shows [64–66].



During the accelerating stage, a fast precipitation of C-S-H gel phase results in an earlier consumption of gypsum because of sulfate absorption into the gel. After depletion, sulfate is desorbed from C-S-H gel phase and available to react with aluminate phases to form ettringite, leading to the second/renewed aluminate reaction (as Eq. 2.6 shows) [67–71]. This reaction is indicated by a small shoulder following the main hydration peak in the calorimetric measurement (see Figure 2.4).

In a properly sulfated cement system, gypsum and other sulfate compounds react with calcium aluminate (C_3A) to form ettringite within one day after mixing with water, and most sulfate in the system is consumed to its formation [65, 67, 71].

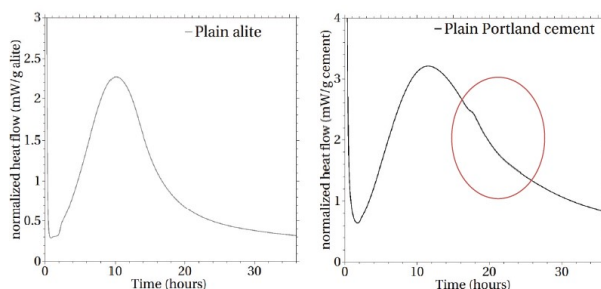


Figure 2.4: The second aluminate peak indicated by a small shoulder following the main hydration peak in the calorimetric measurement, adapted from [67].

At atomic level, ettringite has a structure that runs parallel to the c axis, i.e., the needle axis. Sulfate ions and H_2O molecules lie in the middle (see Figure 2.5(a)) [72, 73]. Therefore, ettringite crystal presents a needle-like shape, as shown in Figure 2.5(b). At approximately one day after mixing, ettringite is uniformly and discretely dispersed throughout the cement matrix at a submicroscopic level (less than one micrometer in the cross-section).

After the consumption of sulfate ions, the transformation from ettringite to monosulfate becomes increasingly prominent with the continuous supply of Al^{3+} ions, as the following Equation 2.7 displays. In general, ettringite will disappear after 7 days of curing [60]. It is worthwhile to mention here that besides that released from cement clinker, sulfate and aluminate phases can also be present in SCMs and admixtures [61–63].

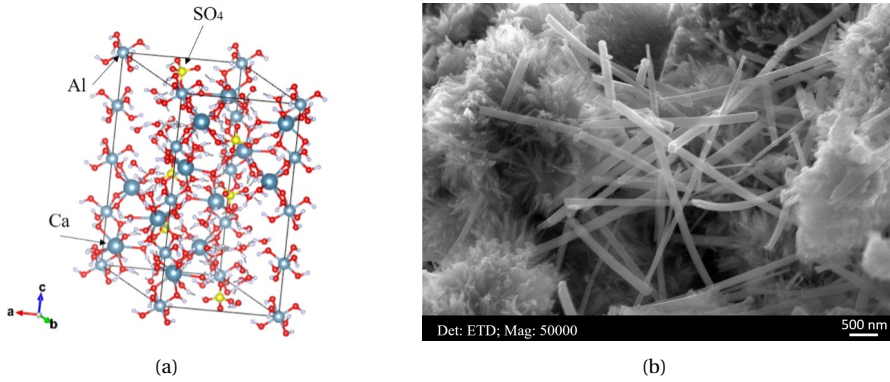
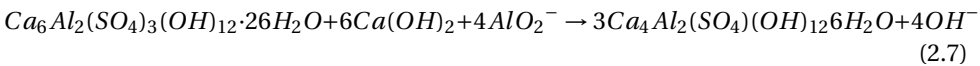


Figure 2.5: (a) Crystal structure of ettringite. Its ID in Crystallography Open Database is 1520837, and the structure was redrawn by the software Vesta. (b) Morphology of ettringite in a C_3S - C_3A -slag-gypsum system after 3 days of curing (unpublished data).



In fact, monosulfate belongs to a family of hydrated calcium aluminate phases, i.e., AFm phases, which mainly occur in the hydrated cement paste. A representative formula of this family is $[Ca_2Al(OH)_6] \cdot X \cdot nH_2O$, where X stands for an exchangeable singly charged (e.g., chloride, hydroxide) or half of a doubly charged anion (e.g., sulfate, carbonate) [74, 75].

A typical structure of monosulfate at atomic level is shown in Figure 2.6(a). It consists of sheets of $Ca(OH)_6$ octahedral ions, similar to brucite or portlandite while with one third of the Ca^{2+} ion replaced by Al^{3+} ion. The resulting charge imbalance gives the layers a net positive charge and the interlayer spacing is much greater than that in brucite or portlandite owing to the need to intercalate charge-balancing anions. The interlayer anion contents are sensitive to both cement composition and service environment. In (Ordinary) Portland cement, it can be hydroxide, sulfate and carbonate. Under service, chloride often displaces other anions [76, 77]. Figure 2.6(b) presents the morphology of monosulfate, which is a relatively coarse hexagonal plate.

2.4.3. HYDROTALCITE-LIKE PHASE

Secondary formations, e.g., C-S(A)-H and hydrotalcite-like phases originated from the dissolution of slag have been identified [60]. Hydrotalcite-like phase, considered as a functional compound with a Layered Double Hydroxides (LDHs) structure, is closely mixed with C-S(A)-H gel phase forming the so-called 'inner' hydration products of slag [58, 60, 78].

Pure hydrotalcite is well recognized as anionic clays because of its strong anion-exchange property [79–81]. It can be expressed as a general formula $[M_{1-x}^{2+}M_x^{3+}(OH)_2]_{A_x/n}^{n-} \cdot yH_2O$, where M^{2+} and M^{3+} are cations of divalent and trivalent, A^{n-} is the anion fixed in the interlayer with a valence of n, and x equals to

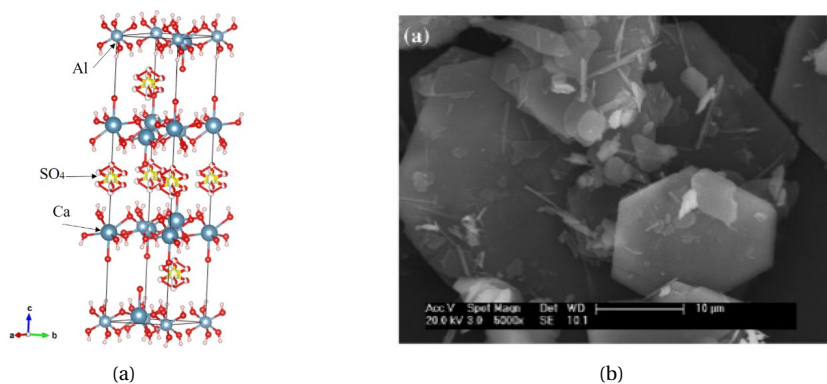


Figure 2.6: (a) Crystal structure of monosulfate. Its ID in Crystallography Open Database is 9013423, and the structure was redrawn by the software Vesta. (b) Morphology of monosulfate, adapted from [77].

$M^{3+}/(M^{2+}+M^{3+})$ in molar fraction, ranging from 0.17 to 0.33 [81]. The brucite-like trioctahedral layers present positive charge due to the isomorphous substitution of M^{3+} for M^{2+} , and anions are thus necessitated to be intercalated into the interlayer to maintain the charge balance. Water molecules occupy the free space of the interlayer via hydrogen bonding. In naturally occurring hydrotalcite, the most common anion detected is carbonate (CO_3^{2-}). Nonetheless, hydrotalcite can actually accommodate various anionic species in the interlayer without restriction [81–84]. A typical structure of Mg-Al hydrotalcite at atomic level is illustrated in Figure 2.7.

However, the Mg/Al atomic ratio of this phase formed in slag cement or alkali-activated slag paste is not fixed and differs over a wide range [58, 60, 85]. It was observed to be close to hydrotalcite ($Mg_6Al_2(OH)_{16}(CO_3) \cdot 4H_2O$) compositionally and structurally. However, the latest findings from evolved gas studies showed that the hydrotalcite-like phase in slag cement paste was closer to meixnerite ($Mg_6Al_2(OH)_{16}(OH)_2 \cdot 4H_2O$) [86].

In cement chemistry, hydrotalcite-like phase actually represents a group of phases formed during hydration, e.g., Mg-Al LDHs formed in slag containing systems and AFm Ca-Al LDHs (e.g., monosulfate), the hydration products of tricalcium silicate (C_3A) [60]. Mg-Al hydrotalcite-like phase plays an important role in the durability-related performance of slag containing paste and concrete, as it presents a strong capacity to fix chloride (Cl^-) [83, 87, 88], sulfate (SO_4^{2-}) [89, 90], carbonate (CO_3^{2-}) [91–93], and other potentially harmful species as interlayer ions. When referring to Mg-Al hydrotalcite-like phase, two important parameters should be noted. One is Mg/Al atomic ratio and the other one is interlayer anion, the amount of which is strongly dependent on Mg/Al ratio for electro-neutrality. It is well demonstrated that this ratio can be obtained from the slope of regression line when fitting the scatter plot of Mg/Si vs. Al/Si through scanning electron microscopy (SEM) [37, 52, 94–96] and transmission electron microscopy (TEM) [58, 86, 97].

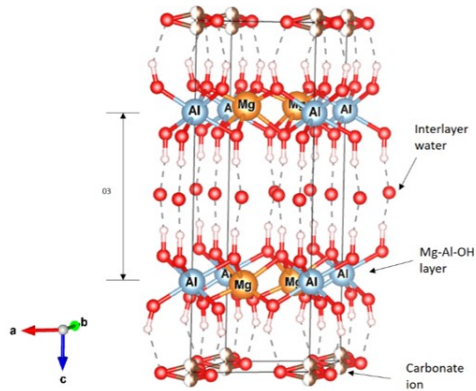
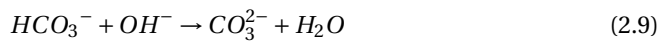
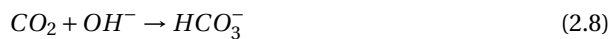


Figure 2.7: Crystal structure of $Mg_4Al_2(OH)_{12}(CO_3) \cdot 3H_2O$ (d_{003} is the length of interlayer space.). Its ID in Crystallography Open Database is 9012627, and the structure was redrawn by the software Vesta.

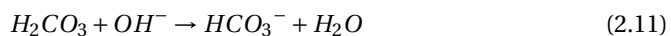
2.5. CARBONATION OF CEMENT-SLAG SYSTEM

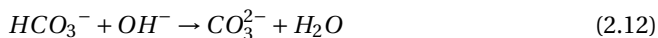
THE carbonation of cementitious materials refers to the neutralization process, in which the acid gas CO_2 in the atmosphere penetrates the matrix and reacts with the alkaline species (mainly OH^- ion) in the pore solution, leading to the reduction of alkalinity (pH) and the change of phase assemblages [98–100]. It is one of the main degradation mechanisms that can affect the durability of reinforced cement-based structure by inducing uniform corrosion [101]. When the neutralization depth is close to the thickness of protective layer, the passive film on the surface of steel bar will be destroyed. The volume expansion caused by steel corrosion can result in cracks in the structure surface along the length of steel bar and peel off the protective layer, damage or fail the structural component eventually [102, 103].

It is well known that the first step of neutralization process in cementitious materials is the pore solution carbonation. Once CO_2 enters into the material, gaseous CO_2 rapidly dissolves into the alkaline pore solution (pH > 10) and hydrolyses to bicarbonate (HCO_3^-) at first and carbonate (CO_3^{2-}) subsequently via a multi-step reaction sequence [104]:



When pH < 8, direct hydration of CO_2 occurs and leads to the formation of carbonic acid H_2CO_3 , which can then dissociate into HCO_3^- and CO_3^{2-} ions [104]:





When $8 < \text{pH} < 10$, both mechanisms exist. Following, the carbonate ions interact with calcium ions that are extracted from hydrated phases, and precipitate as calcium carbonate. Collectively, carbonation can be regarded as a diffusion-dissolution-reaction-precipitation process. For Portland cement-based materials, the carbonation rate at 20 °C reaches maximum value when relative humidity (RH) is between 40-80% [105–107]. Note that the presence of water (internal relative humidity) lowers the diffusion of gaseous CO_2 . However, water provides the medium for the dissolution and reaction between calcium-containing phases and carbon dioxide.

Generally, the carbonation rate of slag cement paste is higher than that of Ordinary Portland cement paste with the same water/binder ratio, partially due to its lower calcium hydroxide content [108–113]. Portlandite, as the main CO_2 binding phase, can delay the decalcification of the most essential hydration product, C-S(A)-H gel phase [100, 109, 114]. During the hydration process of cement-slag system, C-S(A)-H gel phase with a lower Ca/Si ratio is produced [60, 61], which is more easily carbonated, reaching a critical Ca/Si ratio of 0.67 [115–117]. This resulting silica gel is poorly organized and presents a low molar volume, which certainly leads to an increase in porosity and a high risk of carbonation shrinkage. Therefore, although a lower permeability can be obtained by a proper curing of slag cement paste, the reduction in portlandite content and carbonation of C-S(A)-H gel phase with a lower Ca/Si ratio dominates over the pore refinement [100, 109, 114].

2.5.1. CARBONATION OF MAIN HYDRATES

Portlandite is the first major hydrate that decomposes to calcium carbonate (calcite in principle) during carbonation, resulting in a moderate volume increase as the molar volume of calcite ($36.9 \text{ cm}^3/\text{mol}$) is greater than that of portlandite ($33.0 \text{ cm}^3/\text{mol}$). During this process, the pH remains stable at around 12.5 [118]. According to [119], it occurs as a consequence of a dissolution-precipitation reaction, the reaction kinetic of which is initially more rapid than the carbonation of C-S-H gel phase. Calcium carbonate grows on the surface of portlandite, and the further carbonation is slowed down by the limiting transport of water and CO_2 [120, 121].

After all accessible portlandite is consumed, C-S-H gel phase starts to decalcify. A two-step decalcification process of C-S-H gel phase is predicted [117, 122]. The first step is a gradual decalcification of C-S-H gel phase where calcium is removed from the interlayer and defect sites in the silicate chains until $\text{Ca/Si} = 0.67$ is reached, ideally corresponding to infinite silicate chains. In the second step, calcium from the principal layers is consumed, resulting in the final decomposition of C-S-H gel phase and formation of amorphous silica gel phase. The main carbonation product of C-S-H gel phase is calcium carbonate, which can precipitate in different crystalline polymorphs: calcite, aragonite, and vaterite, depending on the internal conditions [123], and the presence of impurities and/or additives [124, 125]. The work in [126–128] also stated that in the real environment, considering that metastable phases including amorphous calcium carbonate, vaterite, and aragonite were in contact with water, they would

transform into calcite eventually through dissolution-precipitation process with the fluctuation of temperature and pressure. During accelerated carbonation test, amorphous calcium carbonate and vaterite formed in the early stage [129]. Calcite and vaterite were the most common forms of CaCO_3 found in carbonated cement-based paste [109, 130, 131].

2.5.2. CARBONATION OF MINOR HYDRATES

In the past decades, much attention has been paid to the carbonation of portlandite and C-S-H gel phase; however, few investigations went deep into the carbonation of minor hydration phases, e.g., monosulfate and hydrotalcite-like phase. Justnes et al. [132] found that the carbonation of ettringite and monosulfate led to a substantial volume decrease since crystal water went back into liquid form. It was thought to be the dominating reason for the formation of coarser pores in the carbonated zone of CEM II/B-V. The findings in [133, 134] confirmed that the formation of hydrotalcite-like phase reduced the susceptibility to carbonation of alkali-activated slag paste produced with higher MgO content, which appeared to act as an internal CO_2 sorbent. Besides, Mg-Al LDHs had already been proven to be effective as an anti-carbonation additive [92, 93].

As stated in [100], understanding of the roles of minor hydrates in the carbonation process is imperative if next-generation binders are to be designed to favor formation of specific microstructural features to maximize their carbonation resistance.

2.5.3. PORE STRUCTURE

Porosity of cementitious mixtures plays an important role in relation to the carbonation resistance, as it is directly linked to the diffusion of CO_2 . In general, slag blended cement paste has a higher total porosity at early age compared to Ordinary Portland cement paste due to the lower cement clinker content and the slow hydration rate of slag. At later age, the positive effect of pozzolanic reaction starts to dominate (Figure 2.8). Overall, investigations report similar or smaller pore entry sizes for slag blended cements. It can be ascribed to the increasing production of C-S(A)-H gel phase with low Ca/Si atomic ratio, which is able to fill space [62, 63].

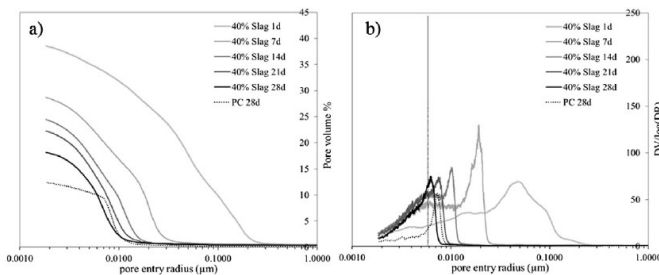


Figure 2.8: MIP curves of slag cement from 1 to 28 days, adapted from [135].

However, with the increasing carbonation of C-S(A)-H gel phase, the percentage of CaCO_3 that is present as calcite is found to be reduced, while amorphous calcium

carbonate, metastable aragonite and vaterite tend to increase [109, 136, 137]. Compared with pure Portland cement paste with the same w/b ratio, a higher porosity after carbonation is confirmed in slag cement paste (Figure 2.9) [138–140].

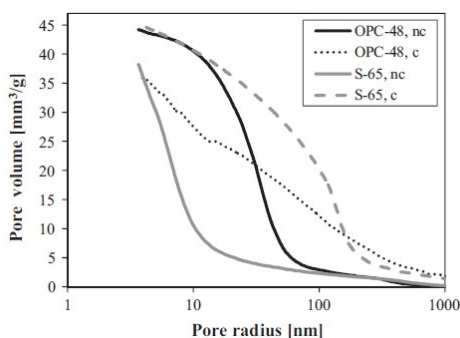


Figure 2.9: Pore size distribution of the mortars OPC-48 and S-65 before and after carbonation, adapted from [140].

Castellote et al. [141] reported that pore clogging and formation of dense, carbonated areas as the main cause for the limited carbonation rate in pure Portland cement pastes. A decreasing total porosity and a refinement in pore size distributions using mercury intrusion porosimetry was concluded in [142, 143]. On the other hand, several studies [112, 144, 145] also identified a decrease in the total porosity in combination with a coarsening of the capillary pores during the carbonation of pure Portland cement pastes. As for slag-containing cement paste, an increase in porosity (coarsening of the pore structure) has been reported [109, 114, 145, 146]. This coarsening is usually associated with the carbonation of C-S(A)-H gel phase. Porous silica gel phase is formed during CO₂ attack, and micro-cracks are induced by carbonation shrinkage.

2.6. SUMMARY AND PERSPECTIVES

BASED on the information discussed in this chapter, the following conclusions can be drawn:

- The slag chemistry varies with time and geographical location. Available bulk material analysis techniques, such as XRF and ICP-MS are not the most favorable techniques for characterizing unhydrated slag grains due to high interference from other phases in the matrix.
- To understand the influence of slag composition, four main metal oxides were commonly investigated separately in the existing literature, and thus the interaction among each other was missing. In other words, a systematic research covering the common slag composition is needed.
- Most of the existing studies were concentrated at the carbonation of main hydration products, e.g., portlandite and C-S-H gel phase, and the review showed

a lack of information on the carbonation of minor hydrates in slag cement paste, e.g., monosulfate and hydrotalcite-like phase.

- It appears that much attention from both industry and academia has been paid to estimating the correlation between slag chemistry and reactivity; however, the correlation between slag chemistry and carbonation resistance of slag cement paste is scarce, also for other durability-related performances.

Therefore, more work is needed to identify the role of minor hydrates in slag cement paste during carbonation, and build the correlation among slag chemistry, slag reactivity, and carbonation resistance of slag-rich cement paste. Under this circumstance, it is foreseeable to predict the performance of slag cement with a specific slag composition, and recommend slag chemistry for an improved carbonation performance in service life.

REFERENCES

- [1] Y. Zhang, Z. Wan, L. M. de Lima Junior, and O. Çopuroğlu, *Early age hydration of model slag cement: Interaction among C_3S , gypsum and slag with different Al_2O_3 contents*, *Cement and Concrete Research* **161**, 106954 (2022).
- [2] Y. Yang, K. Raipala, and L. Holappa, *Ironmaking*, in *Treatise on process metallurgy* (Elsevier, 2014) pp. 2–88.
- [3] I. Sohn and D. J. Min, *A review of the relationship between viscosity and the structure of calcium-silicate-based slags in ironmaking*, *steel research international* **83**, 611 (2012).
- [4] E. Özbay, M. Erdemir, and H. İ. Durmuş, *Utilization and efficiency of ground granulated blast furnace slag on concrete properties—A review*, *Construction and Building Materials* **105**, 423 (2016).
- [5] A. M. Rashad, *An overview on rheology, mechanical properties and durability of high-volume slag used as a cement replacement in paste, mortar and concrete*, *Construction and Building Materials* **187**.
- [6] H. Li, X. Yang, Z. Jiang, Z. Suo, G. Zhang, J. Wu, and L. Yu, *Effect of different grinding aids on property of granulated blast furnace slag powder*, *Materials and Structures* **48**, 3885 (2015).
- [7] N. Tsuyuki and K. Koizumi, *Granularity and surface structure of ground granulated blast-furnace slags*, *Journal of the American Ceramic Society* **82**, 2188 (1999).
- [8] Y. Wang, X. He, Y. Su, H. Tan, J. Yang, M. Lan, M. Ma, and B. Strnadel, *Self-hydration characteristics of ground granulated blast-furnace slag (GGBFS) by wet-grinding treatment*, *Construction and Building Materials* **167**, 96 (2018).
- [9] F. Olorunsogo, *Particle size distribution of GGBS and bleeding characteristics of slag cement mortars*, *Cement and Concrete Research* **28**, 907 (1998).

- [10] J. Zhu, Q. Zhong, G. Chen, and D. Li, *Effect of particlesize of blast furnace slag on properties of portland cement*, *Procedia Engineering* **27**, 231 (2012).
- [11] P. Wang, R. Trettin, and V. Rudert, *Effect of fineness and particle size distribution of granulated blast-furnace slag on the hydraulic reactivity in cement systems*, *Advances in cement research* **17**, 161 (2005).
- [12] Y. Zhang and X. Zhang, *Grey correlation analysis between strength of slag cement and particle fractions of slag powder*, *Cement and Concrete Composites* **29**, 498 (2007).
- [13] S. Teng, T. Y. D. Lim, and B. S. Divsholi, *Durability and mechanical properties of high strength concrete incorporating ultra fine ground granulated blast-furnace slag*, *Construction and Building Materials* **40**, 875 (2013).
- [14] P. Sharmila and G. Dhinakaran, *Compressive strength, porosity and sorptivity of ultra fine slag based high strength concrete*, *Construction and Building Materials* **120**, 48 (2016).
- [15] N. De Belie, M. Soutsos, and E. Gruyaert, *Properties of fresh and hardened concrete containing supplementary cementitious materials*, Vol. 25 (Springer, 2018).
- [16] Y. Kashiwaya, Y. In-Nami, and T. Akiyama, *Development of a rotary cylinder atomizing method of slag for the production of amorphous slag particles*, *ISIJ international* **50**, 1245 (2010).
- [17] C. Li, H. H. Sun, and L. T. Li, *Glass phase structure of blast furnace slag*, in *Advanced Materials Research*, Vol. 168 (Trans Tech Publ) pp. 3–7.
- [18] R. Snellings, A. Salze, and K. Scrivener, *Use of X-ray diffraction to quantify amorphous supplementary cementitious materials in anhydrous and hydrated blended cements*, *Cement and Concrete Research* **64**, 89 (2014).
- [19] M. Tossavainen, F. Engstrom, Q. Yang, N. Menad, M. L. Larsson, and B. Bjorkman, *Characteristics of steel slag under different cooling conditions*, *Waste management* **27**, 1335 (2007).
- [20] Y. P. Stetsko, N. Shanahan, H. Deford, and A. Zayed, *Quantification of supplementary cementitious content in blended portland cement using an iterative Rietveld–PONKCS technique*, *Journal of Applied Crystallography* **50**, 498 (2017).
- [21] K. Schuldyakov, L. Y. Kramar, and B. Y. Trofimov, *The properties of slag cement and its influence on the structure of the hardened cement paste*, *Procedia Engineering* **150**, 1433 (2016).
- [22] B. Lothenbach, K. Scrivener, and R. Hooton, *Supplementary cementitious materials*, *Cement and Concrete Research* **41**, 1244 (2011).
- [23] N. M. Piatak, M. B. Parsons, and R. R. Seal II, *Characteristics and environmental aspects of slag: A review*, *Applied Geochemistry* **57**, 236 (2015).

- [24] ACI, *Slag cement in concrete and mortar*, Report (American Concrete Institute, 2003).
- [25] A. Ehrenberg and D. Algermissen, *Alternative Nutzungsmöglichkeiten von Elektroofenschlacke zur Klinker- und Hüttensandsubstitution*, in *Berliner Konferenz Mineralische Nebenprodukte und Abfälle 4* (2017).
- [26] A. Ehgrenberg, *Huettensand: ein leistungsfähiger Baustoff mit Tradition und Zukunft: Teile 1 und 2*, *BETON-INFORMATIONEN* **46** (2006).
- [27] P. Hewlett and M. Liska, *Lea's chemistry of cement and concrete* (Butterworth-Heinemann, 2019).
- [28] H. Smolczyk, *ZUM EINFLUSS DER CHEMIE DES HUETTENSANDS AUF DIE FESTIGKEITEN VON HOCHAFENZEMENTEN*, (1978).
- [29] H. S. Pietersen, *Reactivity of fly ash and slag in cement*, (1993).
- [30] J. Escalante, L. Gomez, K. Johal, G. Mendoza, H. Mancha, and J. Mendez, *Reactivity of blast-furnace slag in portland cement blends hydrated under different conditions*, *Cement and Concrete Research* **31**, 1403 (2001).
- [31] A. Bougara, C. Lynsdale, and N. Milestone, *Reactivity and performance of blastfurnace slags of differing origin*, *Cement and Concrete Composites* **32**, 319 (2010).
- [32] S. Kucharczyk, J. Deja, and M. Zajac, *Effect of slag reactivity influenced by alumina content on hydration of composite cements*, *Journal of Advanced Concrete Technology* **14**, 535 (2016).
- [33] A. Schöler, F. Winnefeld, M. B. Haha, and B. Lothenbach, *The effect of glass composition on the reactivity of synthetic glasses*, *Journal of the American Ceramic Society* **100**, 2553 (2017).
- [34] S. Kucharczyk, M. Zajac, C. Stabler, R. M. Thomsen, M. Ben Haha, J. Skibsted, and J. Deja, *Structure and reactivity of synthetic CaO-Al₂O₃-SiO₂ glasses*, *Cement and Concrete Research* **120**, 77 (2019).
- [35] S. Blotevogel, A. Ehrenberg, L. Steger, L. Doussang, J. Kaknics, C. Patapy, and M. Cyr, *Ability of the R3 test to evaluate differences in early age reactivity of 16 industrial ground granulated blast furnace slags (GGBS)*, *Cement and Concrete Research* **130**, 105998 (2020).
- [36] S. Blotevogel, L. Steger, D. Hart, L. Doussang, J. Kaknics, M. Poirier, H. Bornhöft, J. Deubener, C. Patapy, and M. Cyr, *Effect of TiO₂ and 11 minor elements on the reactivity of ground-granulated blast-furnace slag in blended cements*, *Journal of the American Ceramic Society* **104**, 128 (2021).

- [37] M. Whittaker, M. Zajac, M. Ben Haha, F. Bullerjahn, and L. Black, *The role of the alumina content of slag, plus the presence of additional sulfate on the hydration and microstructure of Portland cement-slag blends*, Cement and Concrete Research **66**, 91 (2014).
- [38] R. Snellings, X. Li, F. Avet, and K. Scrivener, *Rapid, Robust, and Relevant (R3) Reactivity Test for Supplementary Cementitious Materials*, ACI MATERIALS JOURNAL **116** (2019).
- [39] M. Sajid, C. Bai, M. Aamir, Z. You, Z. Yan, and X. Lv, *Understanding the structure and structural effects on the properties of blast furnace slag (BFS)*, ISIJ International **59**, 1153 (2019).
- [40] E. Gao, W. Wang, and L. Zhang, *Effect of alkaline earth metal oxides on the viscosity and structure of the CaO-Al₂O₃ based mold flux for casting high-Al steels*, Journal of Non-Crystalline Solids **473**, 79 (2017).
- [41] G. H. Kim and I. Sohn, *Effect of Al₂O₃ on the viscosity and structure of calcium silicate-based melts containing Na₂O and CaF₂*, Journal of Non-Crystalline Solids **358**, 1530 (2012).
- [42] K. C. Mills, *The influence of structure on the physico-chemical properties of slags*, ISIJ international **33**, 148 (1993).
- [43] B. O. Mysen, F. J. Ryerson, and D. Virgo, *The influence of TiO₂ on the structure and derivative properties of silicate melts*, American Mineralogist **65**, 1150 (1980).
- [44] J. H. Park, D. J. Min, and H. S. Song, *Amphoteric behavior of alumina in viscous flow and structure of CaO-SiO₂(-MgO)-Al₂O₃ slags*, Metallurgical and Materials Transactions B **35**, 269 (2004).
- [45] K. Shimoda, Y. Tobu, K. Kanehashi, T. Nemoto, and K. Saito, *Total understanding of the local structures of an amorphous slag: perspective from multi-nuclear (²⁹Si, ²⁷Al, ¹⁷O, ²⁵Mg, and ⁴³Ca) solid-state NMR*, Journal of non-crystalline solids **354**, 1036 (2008).
- [46] S. Zhang, X. Zhang, W. Liu, X. Lv, C. Bai, and L. Wang, *Relationship between structure and viscosity of CaO-SiO₂-Al₂O₃-MgO-TiO₂ slag*, Journal of non-crystalline solids **402**, 214 (2014).
- [47] W. Loewenstein, *The distribution of aluminum in the tetrahedra of silicates and aluminates*, American Mineralogist **39**, 92 (1954).
- [48] C. I. Merzbacher, B. L. Sherriff, J. S. Hartman, and W. B. White, *A high-resolution ²⁹Si and ²⁷Al NMR study of alkaline earth aluminosilicate glasses*, Journal of Non-Crystalline Solids **124**, 194 (1990).
- [49] D. R. Neuville, L. Cormier, and D. Massiot, *Al coordination and speciation in calcium aluminosilicate glasses: Effects of composition determined by ²⁷Al MQ-MAS NMR and Raman spectroscopy*, Chemical geology **229**, 173 (2006).

- [50] K. Mills, L. Yuan, Z. Li, G. Zhang, and K. Chou, *A review of the factors affecting the thermophysical properties of silicate slags*, High Temperature Materials Processes **31**, 301 (2012).
- [51] W. Xuan, J. Zhang, and D. Xia, *The influence of MgO on the crystallization characteristics of synthetic coal slags*, Fuel **222**, 523 (2018).
- [52] B. Walkley, R. San Nicolas, M.-A. Sani, S. A. Bernal, J. S. van Deventer, and J. L. Provis, *Structural evolution of synthetic alkali-activated CaO-MgO-Na₂O-Al₂O₃-SiO₂ materials is influenced by Mg content*, Cement and Concrete Research **99**, 155 (2017).
- [53] D. Dutt, P. Higby, and D. Griscom, *A structural model for low silica content calcium aluminosilicate glasses*, Physics and chemistry of glasses **33**, 51 (1992).
- [54] A. Novatski, A. Steimacher, A. Medina, A. Bento, M. Baesso, L. Andrade, S. Lima, Y. Guyot, and G. Boulon, *Relations among nonbridging oxygen, optical properties, optical basicity, and color center formation in CaO-MgO aluminosilicate glasses*, Journal of Applied Physics **104**, 094910 (2008).
- [55] K. Mills, L. Yuan, and R. Jones, *Estimating the physical properties of slags*, Journal of the Southern African Institute of Mining and Metallurgy **111**, 649 (2011).
- [56] J. I. Escalante-Garcia and J. H. Sharp, *The chemical composition and microstructure of hydration products in blended cements*, Cement and Concrete Composites **26**, 967 (2004).
- [57] K. Luke and E. Lachowski, *Internal composition of 20-year-old fly ash and slag-blended ordinary Portland cement pastes*, Journal of the American Ceramic Society **91**, 4084 (2008).
- [58] R. Taylor, I. Richardson, and R. Brydson, *Composition and microstructure of 20-year-old ordinary Portland cement-ground granulated blast-furnace slag blends containing 0 to 100% slag*, Cement and Concrete Research **40**, 971 (2010).
- [59] V. Kocaba, *Development and evaluation of methods to follow microstructural development of cementitious systems including slags*, Report (EPFL, 2009).
- [60] H. F. Taylor, *Cement chemistry*, Vol. 2 (Thomas Telford London, 1997).
- [61] W. Chen and H. Brouwers, *The hydration of slag, part 2: reaction models for blended cement*, Journal of Materials Science **42**, 444 (2007).
- [62] I. Richardson and G. Groves, *The structure of the calcium silicate hydrate phases present in hardened pastes of white Portland cement/blast-furnace slag blends*, Journal of Materials Science **32**, 4793 (1997).
- [63] I. G. Richardson, *The nature of CSH in hardened cements*, Cement and Concrete Research **29**, 1131 (1999).

- [64] A. Quennoz and K. L. Scrivener, *Hydration of C₃A–gypsum systems*, Cement and Concrete Research **42**, 1032 (2012).
- [65] A. Quennoz and K. L. Scrivener, *Interactions between alite and C₃A-gypsum hydrations in model cements*, Cement and Concrete Research **44**, 46 (2013).
- [66] S. Bergold, F. Goetz-Neunhoffer, and J. Neubauer, *Interaction of silicate and aluminate reaction in a synthetic cement system: Implications for the process of alite hydration*, Cement and Concrete Research **93**, 32 (2017).
- [67] E. M. J. Berodier, *Impact of the supplementary cementitious materials on the kinetics and microstructural development of cement hydration*, Report (EPFL, 2015).
- [68] J. Cheung, A. Jeknavorian, L. Roberts, and D. Silva, *Impact of admixtures on the hydration kinetics of Portland cement*, Cement and Concrete Research **41**, 1289 (2011).
- [69] M. Antoni, J. Rossen, F. Martirena, and K. Scrivener, *Cement substitution by a combination of metakaolin and limestone*, Cement and Concrete Research **42**, 1579 (2012).
- [70] P. T. Durdziński, R. Snellings, C. F. Dunant, M. B. Haha, and K. L. Scrivener, *Fly ash as an assemblage of model Ca–Mg–Na-aluminosilicate glasses*, Cement and Concrete Research **78**, 263 (2015).
- [71] F. A. Zunino Sommariva, *Limestone calcined clay cements (LC3): raw material processing, sulfate balance and hydration kinetics*, Report (EPFL, 2020).
- [72] A. Moore and H. Taylor, *Crystal structure of ettringite*, Acta Crystallographica Section B: Structural Crystallography and Crystal Chemistry **26**, 386 (1970).
- [73] D. Min and T. Mingshu, *Formation and expansion of ettringite crystals*, Cement and Concrete Research **24**, 119 (1994).
- [74] A. N. Christensen, T. R. Jensen, and J. C. Hanson, *Formation of ettringite, Ca₆Al₂(SO₄)₃(OH)₁₂·26H₂O, AFt, and monosulfate, Ca₄Al₂O₆(SO₄)·14H₂O, AFm-14, in hydrothermal hydration of Portland cement and of calcium aluminum oxide–calcium sulfate dihydrate mixtures studied by in situ synchrotron X-ray powder diffraction*, Journal of solid state chemistry **177**, 1944 (2004).
- [75] I. Baur, P. Keller, D. Mavrocordatos, B. Wehrli, and C. A. Johnson, *Dissolution-precipitation behaviour of ettringite, monosulfate, and calcium silicate hydrate*, Cement and Concrete Research **34**, 341 (2004).
- [76] B. Lothenbach and F. Winnefeld, *Thermodynamic modelling of the hydration of Portland cement*, Cement and Concrete Research **36**, 209 (2006).
- [77] T. Matschei, B. Lothenbach, and F. P. Glasser, *Thermodynamic properties of Portland cement hydrates in the system CaO–Al₂O₃–SiO₂–CaSO₄–CaCO₃–H₂O*, Cement and Concrete Research **37**, 1379 (2007).

- [78] H. Ye, *Nanoscale attraction between calcium-aluminosilicate-hydrate and Mg-Al layered double hydroxides in alkali-activated slag*, *Materials Characterization* **140**, 95 (2018).
- [79] S. Miyata, *Physico-chemical properties of synthetic hydrotalcites in relation to composition*, *Clays and Clay minerals* **28**, 50 (1980).
- [80] S. Miyata, *Anion-exchange properties of hydrotalcite-like compounds*, *Clays and Clay minerals* **31**, 305 (1983).
- [81] W. T. Reichle, *Synthesis of anionic clay minerals (mixed metal hydroxides, hydrotalcite)*, *Solid State Ionics* **22**, 135 (1986).
- [82] J. T. Klopoggea, J. Kristófb, and R. L. Frosta, *Thermogravimetric analysis-mass spectrometry (TGA-MS) of hydrotalcites containing CO_3^{2-} , NO_3^- , Cl , SO_4^{2-} or ClO_4^-* , *Clay Odyssey* **1**, 451 (2001).
- [83] Z. Yang, H. Fischer, and R. Polder, *Synthesis and characterization of modified hydrotalcites and their ion exchange characteristics in chloride-rich simulated concrete pore solution*, *Cement and Concrete Composites* **47**, 87 (2014).
- [84] E. Bernard, W. J. Zucha, B. Lothenbach, and U. Mäder, *Stability of hydrotalcite (Mg-Al layered double hydroxide) in presence of different anions*, *Cement and Concrete Research* **152**, 106674 (2022).
- [85] X. Ke, S. A. Bernal, and J. L. Provis, *Uptake of chloride and carbonate by Mg-Al and Ca-Al layered double hydroxides in simulated pore solutions of alkali-activated slag cement*, *Cement and Concrete Research* **100**, 1 (2017).
- [86] I. Richardson and S. Li, *Composition and structure of an 18-year-old 5M KOH-activated ground granulated blast-furnace slag paste*, *Construction and Building Materials* **168**, 404 (2018).
- [87] J. Csizmadia, G. Balázs, and F. D. Tamás, *Chloride ion binding capacity of aluminoferrites*, *Cement and Concrete Research* **31**, 577 (2001).
- [88] M. Balonis, B. Lothenbach, G. Le Saout, and F. P. Glasser, *Impact of chloride on the mineralogy of hydrated Portland cement systems*, *Cement and Concrete Research* **40**, 1009 (2010).
- [89] L. Guo, Y. Wu, P. Duan, and Z. Zhang, *Improving sulfate attack resistance of concrete by using calcined Mg-Al- CO_3 LDHs: Adsorption behavior and mechanism*, *Construction and Building Materials* **232**, 117256 (2020).
- [90] J. Xu, Q. Tan, and Y. Mei, *Corrosion protection of steel by Mg-Al layered double hydroxides in simulated concrete pore solution: Effect of SO_4^{2-}* , *Corrosion Science* **163**, 108223 (2020).

- [91] S. Walspurger, P. D. Cobden, O. V. Safonova, Y. Wu, and E. J. Anthony, *High CO₂ storage capacity in alkali-promoted hydrotalcite-based material: In situ detection of reversible formation of magnesium carbonate*, Chemistry—A European Journal **16**, 12694 (2010).
- [92] P. Duan, W. Chen, J. Ma, and Z. Shui, *Influence of layered double hydroxides on microstructure and carbonation resistance of sulphoaluminate cement concrete*, Construction and Building Materials **48**, 601 (2013).
- [93] Z. Shui, R. Yu, Y. Chen, P. Duan, J. Ma, and X. Wang, *Improvement of concrete carbonation resistance based on a structure modified Layered Double Hydroxides (LDHs): Experiments and mechanism analysis*, Construction and Building Materials **176**, 228 (2018).
- [94] S. D. Wang, K. L. J. C. Scrivener, and C. Research, *Hydration products of alkali activated slag cement*, **25**, 561 (1995).
- [95] M. B. Haha, B. Lothenbach, G. Le Saout, and F. Winnefeld, *Influence of slag chemistry on the hydration of alkali-activated blast-furnace slag — Part I: Effect of MgO*, Cement and Concrete Research **41**, 955 (2011).
- [96] M. B. Haha, B. Lothenbach, G. Le Saout, and F. Winnefeld, *Influence of slag chemistry on the hydration of alkali-activated blast-furnace slag — Part II: Effect of Al₂O₃*, Cement and Concrete Research **42**, 74 (2012).
- [97] I. Richardson and G. Groves, *Microstructure and microanalysis of hardened cement pastes involving ground granulated blast-furnace slag*, Journal of materials science **27**, 6204 (1992).
- [98] V. G. Papadakis, C. G. Vayenas, and M. Fardis, *A reaction engineering approach to the problem of concrete carbonation*, AIChE Journal **35**, 1639 (1989).
- [99] V. G. Papadakis, *Effect of supplementary cementing materials on concrete resistance against carbonation and chloride ingress*, Cement and Concrete Research **30**, 291 (2000).
- [100] S. von Greve-Dierfeld, B. Lothenbach, A. Vollpracht, B. Wu, B. Huet, C. Andrade, C. Medina, C. Thiel, E. Gruyaert, H. Vanoutrive, *et al.*, *Understanding the carbonation of concrete with supplementary cementitious materials: a critical review by RILEM TC 281-CCC*, Materials and structures **53**, 1 (2020).
- [101] M. T. Liang, W. L. Jin, R. J. Yang, and N.-M. Huang, *Predeterminate model of corrosion rate of steel in concrete*, Cement and Concrete Research **35**, 1827 (2005).
- [102] L. Parrott, *Some effects of cement and curing upon carbonation and reinforcement corrosion in concrete*, Materials and Structures **29**, 164 (1996).
- [103] M. Moreno, W. Morris, M. Alvarez, and G. Duffó, *Corrosion of reinforcing steel in simulated concrete pore solutions: Effect of carbonation and chloride content*, Corrosion Science **46**, 2681 (2004).

- [104] P. V. Danckwerts, *Gas-liquid reactions*, (1970).
- [105] V. G. Papadakis, C. G. Vayenas, and M. N. Fardis, *Fundamental modeling and experimental investigation of concrete carbonation*, *Materials Journal* **88**, 363 (1991).
- [106] V. Papadakis, C. Vayenas, and M. Fardis, *Physical and chemical characteristics affecting the durability of concrete*, *ACI materials journal* **88**, 186 (1991).
- [107] I. Galan, C. Andrade, and M. Castellote, *Natural and accelerated CO₂ binding kinetics in cement paste at different relative humidities*, *Cement and Concrete Research* **49**, 21 (2013).
- [108] P. Sulapha, S. Wong, T. Wee, and S. Swaddiwudhipong, *Carbonation of concrete containing mineral admixtures*, *Journal of materials in civil engineering* **15**, 134 (2003).
- [109] P. H. Borges, J. O. Costa, N. B. Milestone, C. J. Lynsdale, and R. E. Streatfield, *Carbonation of CH and C-S-H in composite cement pastes containing high amounts of BFS*, *Cement and Concrete Research* **40**, 284 (2010).
- [110] Y. Gao, L. Cheng, Z. Gao, and S. Guo, *Effects of different mineral admixtures on carbonation resistance of lightweight aggregate concrete*, *Construction and Building Materials* **43**, 506 (2013).
- [111] R. Bucher, P. Diederich, G. Escadeillas, and M. Cyr, *Service life of metakaolin-based concrete exposed to carbonation: Comparison with blended cement containing fly ash, blast furnace slag and limestone filler*, *Cement and Concrete Research* **99**, 18 (2017).
- [112] V. Shah and S. Bishnoi, *Carbonation resistance of cements containing supplementary cementitious materials and its relation to various parameters of concrete*, *Construction and Building Materials* **178**, 219 (2018).
- [113] S. Rathnarajan, B. Dhanya, R. G. Pillai, R. Gettu, and M. Santhanam, *Carbonation model for concretes with fly ash, slag, and limestone calcined clay-using accelerated and five-year natural exposure data*, *Cement and Concrete Composites* **126**, 104329 (2022).
- [114] B. Wu and G. Ye, *Development of porosity of cement paste blended with supplementary cementitious materials after carbonation*, *Construction and Building Materials* **145**, 52 (2017).
- [115] X. Liu, P. Feng, Y. Cai, X. Yu, and Q. Liu, *Carbonation behaviors of calcium silicate hydrate (CSH): Effects of aluminum*, *Construction and Building Materials* **325**, 126825 (2022).
- [116] B. Wu and G. Ye, *Carbonation mechanism of different kind of CSH: rate and products*, in *Int. RILEM Conference on Materials, Systems and Structures in Civil Engineering 2016-Segment on Concrete with Supplementary Cementitious Materials* (Rilem) pp. 163–272.

- [117] T. F. Sevelsted and J. Skibsted, *Carbonation of C–S–H and C–A–S–H samples studied by ^{13}C , ^{27}Al and ^{29}Si MAS NMR spectroscopy*, *Cement and Concrete Research* **71**, 56 (2015).
- [118] B. Lagerblad, *Carbon dioxide uptake during concrete life cycle: State of the art* (Swedish Cement and Concrete Research Institute Stockholm, 2005).
- [119] G. W. Groves, A. Brough, I. G. Richardson, and C. M. Dobson, *Progressive changes in the structure of hardened C_3S cement pastes due to carbonation*, *Journal of the American Ceramic Society* **74**, 2891 (1991).
- [120] I. Galan, F. P. Glasser, D. Baza, and C. Andrade, *Assessment of the protective effect of carbonation on portlandite crystals*, *Cement and Concrete Research* **74**, 68 (2015).
- [121] Cizer, K. Van Balen, J. Elsen, and D. Van Gemert, *Real-time investigation of reaction rate and mineral phase modifications of lime carbonation*, *Construction and Building Materials* **35**, 741 (2012).
- [122] B. Wu and G. Ye, *Study of carbonation rate of synthetic CSH by XRD, NMR and FTIR*, *Heron* **64**, 21 (2019).
- [123] E. Dubina, L. Korat, L. Black, J. Strupi-Šuput, and J. Plank, *Influence of water vapour and carbon dioxide on free lime during storage at 80 °C, studied by Raman spectroscopy*, *Spectrochimica Acta Part A: Molecular and Biomolecular Spectroscopy* **111**, 299 (2013).
- [124] C. Y. Tai and F. Chen, *Polymorphism of CaCO_3 , precipitated in a constant-composition environment*, *AIChE Journal* **44**, 1790 (1998).
- [125] L. Fernández-Díaz, Fernández-González, and M. Prieto, *The role of sulfate groups in controlling CaCO_3 polymorphism*, *Geochimica et Cosmochimica Acta* **74**, 6064 (2010).
- [126] G. Villain, M. Thiery, and G. Platret, *Measurement methods of carbonation profiles in concrete: Thermogravimetry, chemical analysis and gammadensimetry*, *Cement and Concrete Research* **37**, 1182 (2007).
- [127] M. Thiery, G. Villain, P. Dangla, and G. Platret, *Investigation of the carbonation front shape on cementitious materials: Effects of the chemical kinetics*, *Cement and Concrete Research* **37**, 1047 (2007).
- [128] A. Morandau, M. Thiery, and P. Dangla, *Investigation of the carbonation mechanism of CH and CSH in terms of kinetics, microstructure changes and moisture properties*, *Cement and Concrete Research* **56**, 153 (2014).
- [129] Cizer, C. Rodriguez-Navarro, E. Ruiz-Agudo, J. Elsen, D. Van Gemert, and K. Van Balen, *Phase and morphology evolution of calcium carbonate precipitated by carbonation of hydrated lime*, *Journal of Materials Science* **47**, 6151 (2012).

- [130] L. Black, C. Breen, J. Yarwood, K. Garbev, P. Stemmermann, and B. Gasharova, *Structural features of C–S–H (I) and its carbonation in air—a raman spectroscopic study. Part II: carbonated phases*, *Journal of the American Ceramic Society* **90**, 908 (2007).
- [131] E. T. Stepkowska, J. Pérez-Rodríguez, M. Sayagues, and J. Martinez-Blanes, *Calcite, vaterite and aragonite forming on cement hydration from liquid and gaseous phase*, *Journal of thermal analysis calorimetry* **73**, 247 (2003).
- [132] H. Justnes, J. Skocek, T. A. Østnor, C. J. Engelsen, and O. Skjølsvold, *Microstructural changes of hydrated cement blended with fly ash upon carbonation*, *Cement and Concrete Research* **137**, 106192 (2020).
- [133] S. A. Bernal, R. San Nicolas, R. J. Myers, R. M. de Gutiérrez, F. Puertas, J. S. van Deventer, and J. L. Provis, *MgO content of slag controls phase evolution and structural changes induced by accelerated carbonation in alkali-activated binders*, *Cement and Concrete Research* **57**, 33 (2014).
- [134] S. M. Park, J. Jang, and H. K. Lee, *Unlocking the role of MgO in the carbonation of alkali-activated slag cement*, *Inorganic Chemistry Frontiers* **5**, 1661 (2018).
- [135] E. Berodier and K. Scrivener, *Evolution of pore structure in blended systems*, *Cement and Concrete Research* **73**, 25 (2015).
- [136] A. Leemann, H. Pahlke, R. Loser, and F. Winnefeld, *Carbonation resistance of mortar produced with alternative cements*, *Materials and Structures* **51**, 1 (2018).
- [137] P. Van den Heede, M. De Schepper, and N. De Belie, *Accelerated and natural carbonation of concrete with high volumes of fly ash: chemical, mineralogical and microstructural effects*, *Royal Society open science* **6**, 181665 (2019).
- [138] J. Branch, R. Epps, and D. Kosson, *The impact of carbonation on bulk and ITZ porosity in microconcrete materials with fly ash replacement*, *Cement and Concrete Research* **103**, 170 (2018).
- [139] A. Leemann, R. Loser, B. Münch, and P. Lura, *Steady-state O₂ and CO₂ diffusion in carbonated mortars produced with blended cements*, *Materials and Structures* **50**, 1 (2017).
- [140] A. Leemann, P. Nygaard, J. Kaufmann, and R. Loser, *Relation between carbonation resistance, mix design and exposure of mortar and concrete*, *Cement and Concrete Composites* **62**, 33 (2015).
- [141] M. Castellote, L. Fernandez, C. Andrade, and C. Alonso, *Chemical changes and phase analysis of OPC pastes carbonated at different CO₂ concentrations*, *Materials and Structures* **42**, 515 (2009).
- [142] N. Hyvert, A. Sellier, F. Duprat, P. Rougeau, and P. Francisco, *Dependency of C–S–H carbonation rate on CO₂ pressure to explain transition from accelerated tests to natural carbonation*, *Cement and Concrete Research* **40**, 1582 (2010).

- [143] D. Anstice, C. Page, and M. Page, *The pore solution phase of carbonated cement pastes*, *Cement and Concrete Research* **35**, 377 (2005).
- [144] V. Shah, K. Scrivener, B. Bhattacharjee, and S. Bishnoi, *Changes in microstructure characteristics of cement paste on carbonation*, *Cement and Concrete Research* **109**, 184 (2018).
- [145] V. Ngala and C. Page, *Effects of carbonation on pore structure and diffusional properties of hydrated cement pastes*, *Cement and Concrete Research* **27**, 995 (1997).
- [146] M. Frías and S. Goñi, *Accelerated carbonation effect on behaviour of ternary Portland cements*, *Composites Part B: Engineering* **48**, 122 (2013).

II

EXPERIMENTAL INVESTIGATION

3

EDS MICROANALYSIS OF UNHYDRATED BLAST FURNACE SLAG GRAINS IN FIELD CONCRETES WITH DIFFERENT SERVICE LIFE

In this chapter, the author explored the feasibility of using EDS microanalysis as a tool for quantitative measurement of the chemical composition of unhydrated slag in existing field concretes representing different time periods, so that a snapshot of the compositional variation of slag during the past years in the Netherlands can be depicted.

3.1. INTRODUCTION

As mentioned in Chapter 2, slag composition varies depending on the composition of iron ore, fluxing stone, and impurity of the coke fed into the furnace [2]. A better understanding of slag chemistry in a well performing aged concrete can be useful in designing and predicting the service life of modern slag-rich concrete. Moreover, the claims from the industry (see Chapter 1) are based purely on observations and experience, and it needs scientific evidence to be considered valid which is the main motivation of this research.

Attempts to obtain the chemical composition of slag used in hydrated cement and concrete are often unsuccessful possibly because the archives of QC reports are generally discarded after a number of years. Also, available bulk material analysis techniques, such as XRF and ICP-MS -both of which are widely used for raw material characterization- are not the most favorable techniques for characterizing unhydrated slag grains due to high interference from other phases in the matrix. On the other hand, Energy Dispersive X-ray Spectroscopy (EDS) stands out as a favorable technique as EDS allows semi-quantitative and quantitative elemental analysis at a high spatial resolution. With this technique, characteristic X-rays released upon electron-solid interaction in a small volume were captured, analyzed and identified [3, 4]. Moreover, standards-based quantitative EDS microanalysis is preferred over standardless analysis when higher absolute accuracy of the individual element percentage is desired [5–7]. It should be noted that accuracy of the microanalysis depends on several experimental parameters including chemical composition and homogeneity of the compounds used as microanalysis standards, beam current, accelerating voltage, working distance and take off angle [5, 8]. Quantitative EDS microanalysis together with Scanning Electron Microscope-Back Scattered Electron (BSE) imaging has been used successfully in many cementitious materials researches [9–12], especially for durability-related characterization; most of which attempted to quantify the chloride content in cement paste matrices [13–18].

In this chapter, the author explored the feasibility of using EDS microanalysis as a tool for quantitative measurement of the chemical composition of unhydrated slag in existing field concretes representing different time periods, so that a snapshot of the compositional variation of slag during the past years in the Netherlands can be depicted.

3.2. MATERIALS AND METHODOLOGY

3.2.1. SAMPLE INFORMATION

SEVEN slag concrete samples were collected from randomly chosen locations in the Netherlands. A brief description of the samples is given in Table 3.1. Samples of different service life were investigated as the author aimed to take a snapshot of the compositional variation of slags used in the past years in the Netherlands. It should be noted that it was plausible to assume that the Portland cement clinkers that were blended with slag did also show variations with respect to chemical composition and fineness.

Table 3.1: Descriptive information of the slag concrete samples studied.

Sample	
A	The sample was taken from a stairwell dating back to around 1940. Exact location was unknown.
B	The sample was collected from a wind deflection screen near Calandbrug, Europoort Rotterdam (Port of Rotterdam), which was built in 1985. The cement type was reported as CEM III/B.
C	The sample sourced from a parking garage built around 1980. It was located in Jupiterstraat, Hoofddorp.
D	The sample came from 2nd Benelux tunnel in Vlaardingen, Rotterdam. It was built in 2000, and made of CEM III/B.
E	The sample was drilled from the beams above a tunnel in Delft, which was built in 2002. The binder used was mainly CEM III/B.
F	The sample was casted in Microlab, Delft University of Technology, Delft, in 2006. CEM III/B was employed as the binder.
G	The sample was from the underpass "Neherkade" in Hague built in 2015. In the concrete mixture, CEM III/C was used.

3.2.2. QUANTITATIVE EDS MICROANALYSIS

To verify the accuracy of the standards-based method (a.k.a. quantitative EDS microanalysis), five reference slags (R1 to R5) with known chemical compositions were blended with CEM I 42,5 N. Slag R1 was provided by Ecocem Benelux B.V., Netherlands and the rest four slags were synthesized in the lab with slag R1 and AR (analytical reagent, provided by Honeywell Research Chemicals, Germany) CaO, SiO₂, Al₂O₃, MgO (In fact, nine slags were synthesized in the current research (see Chapter 4), four of which were used in this chapter.). The mixtures were mixed into a homogeneous blend by combining the materials with pure ethyl alcohol, grinding the mixture in a ball milling machine at a low speed for 2 hours and drying them at 100 °C for 24 hours. The dried material was then ground to finer than 200 μm using a mortar and pestle for improved homogeneity. The raw materials were melted in an Al₂O₃ crucible at 1550 °C in the oven (High temperature furnace, Carbolite) for around 6 hours (Heated from room temperature to 1550 °C at 10 °C/min and maintained at 1550 °C for 3 hours). The molten liquid was water quenched quickly to obtain the glassy slag when moved out, rinsed with isopropanol and dried at 100 °C for 24 hours, subsequently. Finally, it was crushed and ground down to the required particle size distribution in a ball mill (Retsch PM 100).

Using the produced binders, the slag cement pastes were cast, sealed and cured in the laboratory at 20±3 °C for 3 months. The slag to cement ratio was 7:3 by mass and the water to binder ratio was 0.40. Bulk compositions of reference slags as determined by standards-based XRF are presented in Table 3.2. At the end of curing, chemical compositions of these five reference slags were determined using quantitative (standards-based) and semi-quantitative (standardless) EDS microanalysis on randomly selected unhydrated slag particles, and the results were compared with the original bulk slag compositions that were detected by XRF correspondingly. For standardless EDS microanalysis, the results were generated using the internal standards of the X-ray microanalysis software.

Table 3.2: Bulk compositions (wt.%) of reference slags as determined by XRF. Reference slag R2 and R3 with different MgO contents, and R4 and R5 with different Al₂O₃ contents were chosen to be able to verify the standards-based method for different oxide levels, especially for minor constituents.

	R1		R2		R3		R4		R5	
	Std.-based	Normalized								
CaO	41.00	41.67	41.60	41.90	32.32	34.09	43.42	42.07	35.23	35.23
SiO ₂	37.07	37.68	40.79	41.08	31.27	32.99	44.68	43.30	33.74	33.74
Al ₂ O ₃	10.48	10.65	16.32	16.44	14.27	15.05	3.81	3.69	19.17	19.17
MgO	6.91	7.02	0.41	0.41	15.23	16.07	11.18	10.83	8.97	8.97
TiO ₂	0.62	0.63	-	-	0.69	0.73	-	-	0.99	0.99
MnO/Mn ₂ O ₃	0.12	0.12	-	-	0.15	0.16	-	-	0.25	0.25
Na ₂ O	0.23	0.23	-	-	0.21	0.22	-	-	0.61	0.61
K ₂ O	0.32	0.33	-	-	0.20	0.21	-	-	0.40	0.40
SO ₃	1.21	1.23	0.01	0.01	0.01	0.01	0.01	0.01	0.02	0.02
Others	0.44	0.44	0.17	0.17	0.45	0.47	0.10	0.10	0.62	0.62
Total	98.4	100.0	99.3	100.0	94.8	100.0	103.2	100.0	100.1	100.0

SAMPLE PREPARATION FOR MICROANALYSIS

Samples of approximately 6 mm in height were cut and immersed in isopropanol solution for one week to stop hydration. Afterwards the samples were dried at 40 °C oven for 1 hour, and then impregnated with low-viscosity epoxy resin. Once cured, the excess epoxy was removed from the sample surfaces by grinding and polishing operations, i.e., with #180, #220, #320, #800, and #1200 SiC grinding paper cooled with pure ethanol sequentially (For paste sample, it was recommended to start from #320.), and polished by 9, 3, 1, and 0.25 μm diamond paste in turn. After each step, the samples were immersed briefly in an ultrasonic bath filled with 99.9% ethanol for cleaning. Finally, the well-polished samples were carbon coated in a Leica EM CED 030 carbon evaporator at a thickness of about 10 nm.

INSTRUMENTAL PARAMETERS

For the microanalysis, a FEI QUANTA FEG 650 ESEM (Thermo Fisher Scientific) equipped with a solid-state EDS detector was used in high vacuum chamber condition. The detector used was silicon drift detector (SDD) under NORVAR window with a resolution of 126.7 eV for the Mn K line at 10 kV accelerating voltage. All microanalysis was carried out at a working distance of 10 mm and an accelerating voltage of 10 kV, respectively. The take-off angle of the detector was 35.3°.

During the analysis, an electron beam current of approximately 1.2 nA was measured by means of a picoammeter and a Faraday cup, regularly. The X-ray collection time was set to 60 live-seconds per analysis in order to obtain acceptable statistics without introducing excessive thermal damage on the sample. X-ray spectra of the microanalysis standards were collected under stable beam condition, defined as less than 5% variation in beam current over 60 live-seconds per analysis. Around 50 randomly chosen points from ~5 cross sections per sample were investigated in order to increase the representability and reliability. Each point analysis was performed exclusively on an unhydrated slag particle.

ELECTRON-SLAG INTERACTION VOLUME

The electron-slag interaction volume (Figure 3.1) was estimated by Monte Carlo simulation using CASINO software version 2.48 (<https://www.gel.usherbrooke.ca/casino/>), assuming a density of 2.95 g/cm³ for slag as an input parameter at 10 kV accelerating voltage, similar to the work in [17, 18].

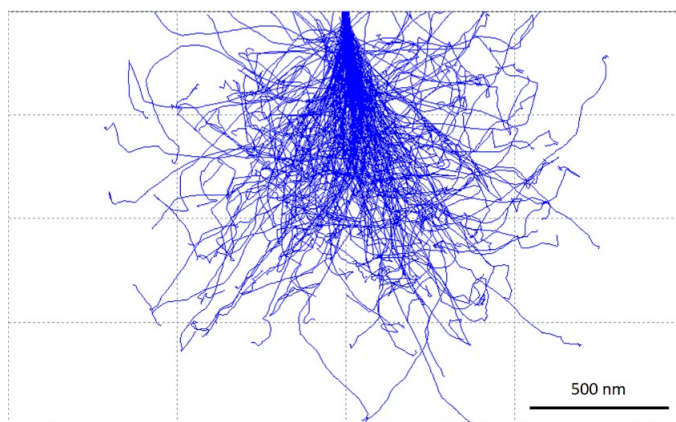


Figure 3.1: Monte Carlo simulation of the penetration of 200 electrons accelerated at 10 kV into a hypothetical slag particle.

Figure 3.1 illustrates the maximum penetration depth of electron trajectories, i.e., $\sim 1.2 \mu\text{m}$ into a hypothetical slag particle. The lateral dimension was close to the depth of interaction volume when assuming a 10 nm diameter beam [3], and thus, an interaction volume of $\sim 1.5 \mu\text{m}^3$ was determined by the simulation. Considering the typical diameter of the analyzed slag grains were around $10\text{--}20 \mu\text{m}$, choosing analysis spots sufficiently far from the grain perimeter ensured collection of X-rays that were representative and free from interference from the surrounding matrix. The microanalysis results were reported in wt.% of the slag particles, representing the interaction volume, i.e., the portion of material from which X-rays were generated and analyzed by the detector.

MICROANALYSIS STANDARDS

The compounds selected as quantitative microanalysis standards were obtained from a commercial mineral standard mount (see Table 3.3, MINM25-53 Serial BW from Astimex scientific ltd.).

Because the current study focuses on four major elements, i.e., Ca, Si, Al and Mg, and a number of trace elements, i.e., Ti, Mn, K, Na and S of slag, only the eight minerals shown in Table 3.3 were employed. Besides, it was noticed that the signal/noise ratio was too weak to identify the amount of aluminum when using albite as standard in some cases during the quantification. Therefore, the EDS spectra of pure aluminum was also employed here as reference to increase the signal/noise ratio.

Figure 3.2 presents the essential steps in the quantitative EDS microanalysis routine from 3.2(a) to 3.2(d). As an example, a representative BSE micrograph of slag R3 cement paste was acquired in Figure 3.2(a). Subsequently, several points targeted at the unhydrated slag particles were chosen for electron bombardment as displayed in Figure 3.2(b). Note that the points were chosen close to the grain center on the relatively large particles, in order to avoid interference from the surrounding matrix. Figure 3.2(c) displays a typical EDS microanalysis spectrum of an unhydrated slag grain in 3.2(b). It contained seven main X-ray peaks as labelled; the carbon (C) signal was mainly due to

Table 3.3: Compounds employed as standards for quantitative EDS microanalysis.

Target element	Mineral	Composition
Ca	Calcite	CaCO ₃
Si	Quartz	SiO ₂
Al	Albite/Pure Aluminum	NaAlSi ₃ O ₈ /Al
Mg	Dolomite	MgCa(CO ₃) ₂
Ti	Rutile	TiO ₂
Mn	Rhodonite	MnSiO ₃
Na	Albite	NaAlSi ₃ O ₈
K	Sanidine	KAlSi ₃ O ₈
S	Anhydrite	CaSO ₄

the carbon coating. Here, the user-defined threshold (minimum energy cutoff) was set to 200 eV in order to include oxygen (O) which was present in all EDS spectra (In this chapter, the author quantified oxygen stoichiometrically). The calibration to the reference standard mount was modelled with NIST DTSA-II Microscopium software [6, 7]. The peaks from unknown spectra were quantified using k-ratio fitting routine with the known compositions of standards spectra. A typical residual spectrum is rendered in Figure 3.2(d). As can be seen, the analysis was completed with acceptable accuracy, as no unassigned minor peak was left, and the residual count was sufficiently low.

3.3. RESULTS

3.3.1. REFERENCE SLAG COMPOSITIONS IN HARDENED CEMENT PASTES

A statistical summary of the EDS microanalysis of the reference slags (R1 to R5) were computed and exported in Table 3.4. The results included the mean value of each metal oxide and the standard deviation of the corresponding data set. The relative deviation (RD) between the values determined by quantitative and semi-quantitative EDS microanalysis (RD1), as well as quantitative EDS microanalysis and XRF analysis (RD2) were reported in Table 3.5. Overall, the microanalysis provided acceptable quantification accuracy regarding the four main metal oxides contents (CaO, SiO₂, Al₂O₃, and MgO) of slag considering that the RD was generally less than 5%. The relatively large deviation and uncertainty regarding the trace elements, among different methods (see Table 3.5), Ti, Mn and S in particular, can be attributed to the following reasons: (1) EDS microanalysis was based on individual point or interaction volume, and it was different from XRF measurement which measured the bulk composition. (2) The amounts of trace elements of slag were quite low, some of which were even close to the detection limit. Therefore, a minor fluctuation in noise can lead to a high relative deviation. Wavelength Dispersive X-ray Spectrometry (WDS) is recommended due to its relatively high spectral resolution by a factor of ten or more if trace element is the main target for research. (3) In addition, it was very likely that trace elements were distributed unevenly within the slag grains [19].

Figure 3.3 shows a box-plot based on the quantitative microanalysis results of the four main metal oxide contents in the reference slag cement samples. Each plot

Table 3.5: The relative deviation between the values based on quantitative EDS microanalysis and semi-quantitative EDS microanalysis, as well as quantitative EDS microanalysis and XRF analysis.

	R1		R2		R3		R4		R5	
	RD1	RD2	RD1	RD2	RD1	RD2	RD1	RD2	RD1	RD2
CaO	1.77	3.00	1.37	3.14	3.43	5.14	1.39	1.95	5.10	2.12
SiO ₂	1.66	0.99	5.00	6.10	1.16	9.49	2.05	0.60	2.45	1.58
Al ₂ O ₃	6.31	2.69	2.28	32.68	1.70	5.39	34.27	33.22	4.43	5.04
MgO	3.84	2.07	473.08	57.69	2.31	2.25	5.34	4.68	2.20	23.58
TiO ₂	26.72	46.55	120.0	-	16.28	19.77	-	-	13.68	15.38
MnO/Mn ₂ O ₃	78.57	14.29	-	-	-	114.29	-	-	-	316.67
Na ₂ O	62.96	14.81	25.0	-	-	16.0	-	-	2.70	64.86
K ₂ O	19.05	23.81	700.0	-	26.92	23.08	-	-	8.51	14.89
SO ₃	88.51	39.08	-	-	-	-	-	-	-	-

corresponds to a single metal oxide mass percentage. Results showed that a few points fell outside the box and the whisker ends, which indicated sporadic compositional imperfections. Additionally, the slender boxes did imply a relatively homogeneous composition.

3.3.2. UNHYDRATED SLAG COMPOSITIONS IN HARDENED FIELD CONCRETES

UPON verifying the suitability of the microanalysis standards on the reference samples, the same methodology was applied on the field concrete specimens. The oxide compositions of the unhydrated slag grains are determined and listed in Table 3.6 and the statistical variation of the main oxides are summarized in Figure 3.4. The analytical total was a slightly higher compared to the ideal 98-102% range, although it can be considered acceptable considering the heterogeneity of the slag grains compared to pure compounds. Furthermore, the microanalysis results led to the following observations: (1) The results of sample A, which was dated back to 1940s, displayed comparably large scatter reflected by the size of box plot; (2) As for samples B to F, the change in slag chemistry was insignificant; however, elevated in CaO and SiO₂ contents were found in slag used for sample G, opposite to that of Al₂O₃ and MgO; Especially for MgO, it showed a gradual decreasing tendency over the years; (3) Besides the main metal oxides of slag grain (expressed as CaO-SiO₂-Al₂O₃-MgO system), sulfur tended to be the next important element when mass percentage was considered.

3.3.3. HETEROGENEITY WITHIN A SINGLE SLAG PARTICLE

WITHIN a single slag particle, some elements showed an affinity for the small droplets of metallic iron. These elements were partitioned between the metallic and the glassy phases of slag, leading to the formation of heterogeneous slag grains with uneven element distribution [20]. Moreover, higher amounts of metallic phases resulted in lower glass content due to the partitioning. In slag grain with heavy metallic oxides such as TiO₂ and MnO, heterogeneity was more apparent [19]. This phenomenon might increase the standard deviation of microanalysis results, therefore more analysis was needed to get a good estimation.

Five reference slags R1 to R5 were almost entirely amorphous based on X-ray

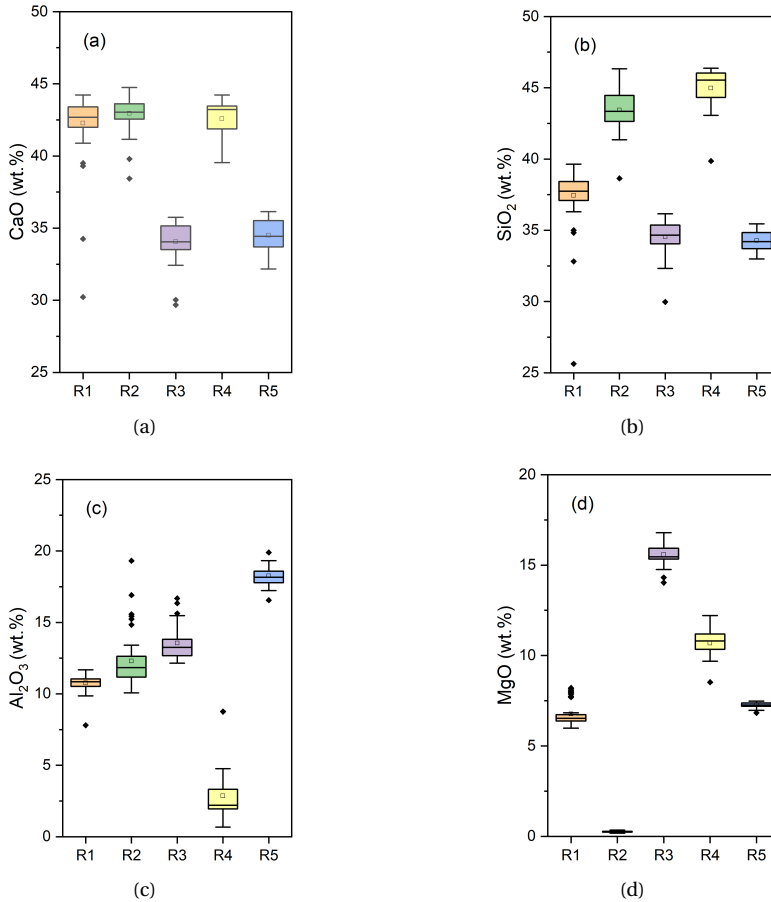


Figure 3.3: Box-plots of four main metal oxide contents of slag samples based on standards-based EDS microanalysis. (a) CaO (b) SiO₂ (c) Al₂O₃ (d) MgO. Small hollow box indicates the mean value, the horizontal line inside the box the median, the lower and upper ends of the box the first and third quartile, respectively, and the two whiskers connected with the box by vertical line indicate the minimum and maximum limits, and solid rhombus indicates the outliers.

Table 3.6: Chemical composition (in wt.%) of slag in hardened concrete samples based on quantitative and semi-quantitative EDS microanalysis.

	A		B		C		D		E		F		G	
	Std.-based	Standardless	Std.-based	Standardless	Std.-based	Standardless	Std.-based	Standardless	Std.-based	Standardless	Std.-based	Standardless	Std.-based	Standardless
CaO	38.36±3.78	36.33±5.68	36.69±1.48	35.32±3.53	35.14±0.77	35.01±5.99	36.51±1.36	35.47±1.07	34.83±1.33	31.17±8.63	34.86±0.78	35.77±1.07	42.49±2.32	40.15±7.99
SiO ₂	35.49±2.41	38.44±7.70	31.93±1.09	31.50±0.73	32.37±0.75	31.70±5.31	33.02±1.17	32.04±0.74	32.94±1.01	35.05±5.29	32.42±1.00	32.08±0.80	36.63±0.84	36.30±3.41
Al ₂ O ₃	10.97±0.73	9.47±3.29	16.98±0.78	16.14±1.78	16.51±0.40	15.19±1.88	16.63±0.62	16.07±0.38	16.17±0.54	16.52±5.41	16.11±0.42	16.26±0.39	10.85±2.22	11.28±7.35
MgO	11.75±3.63	11.00±5.00	12.33±0.81	12.21±1.51	12.55±0.47	12.86±3.92	11.71±0.65	11.88±0.66	11.20±0.85	10.49±4.98	11.27±0.73	11.16±0.63	9.99±1.15	9.42±2.28
TiO ₂	0.73±0.23	0.75±0.35	1.12±0.27	1.09±0.23	0.98±0.16	1.24±0.53	1.17±0.34	1.73±0.49	1.65±0.65	1.74±1.01	1.70±0.39	1.20±0.51	0.81±0.31	0.63±0.42
MnO/Mn ₂ O ₃	0.32±0.35	0.25±0.49	0.39±0.21	0.29±0.50	0.53±0.33	0.10±0.38	0.30±0.26	0.08±0.26	0.40±0.22	0.08±0.30	0.18±0.24	0.05±0.20	0.21±0.24	-
Na ₂ O	0.34±0.10	0.26±0.22	0.47±0.12	0.53±0.08	0.53±0.07	0.52±0.19	0.41±0.06	0.44±0.10	0.42±0.06	0.43±0.18	0.40±0.04	0.46±0.09	0.37±0.09	0.35±0.16
K ₂ O	0.41±0.15	0.38±0.22	0.54±0.20	0.55±0.15	0.68±0.20	0.73±0.21	0.38±0.06	0.37±0.10	0.44±0.08	0.37±0.19	0.42±0.10	0.34±0.09	0.48±0.14	0.37±0.14
SO ₃	0.84±0.31	3.12±0.64	1.12±0.41	2.37±0.33	1.42±0.42	2.65±0.74	0.78±0.12	2.62±0.44	0.90±0.17	4.15±3.12	0.87±0.20	2.68±0.50	0.98±0.30	1.50±0.67
Total	99.21±0.87	100.0	101.58±2.23	100.0	100.72±0.75	100.0	101.10±3.26	100.0	98.95±1.83	100.0	98.23±0.57	100.0	102.82±1.44	100.0

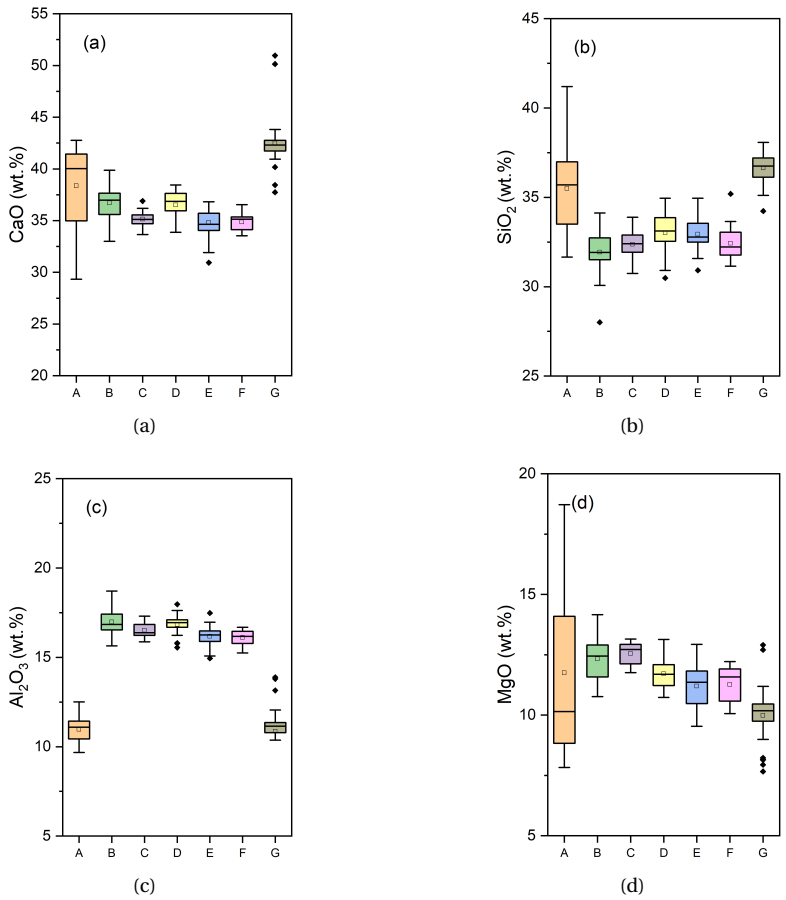


Figure 3.4: Box-plot of four main metal oxide contents of slag in field concrete samples as quantified by EDS microanalysis. (a) CaO (b) SiO₂ (c) Al₂O₃ (d) MgO.

Table 3.7: Chemical composition (wt.%) of slag determined by quantitative EDS microanalysis on single large slag grain and the corresponding coefficient of variation (CV).

	R3	CV(%)	R5	CV(%)
CaO	34.12±0.25	0.73	36.39±0.28	0.77
SiO ₂	34.79±0.24	0.69	33.23±0.20	0.60
Al ₂ O ₃	13.82±0.45	3.26	17.4±0.25	1.44
MgO	15.88±0.17	1.07	8.01±0.08	1.00

diffraction characterization with low heavy metal oxides contents, e.g., TiO₂ and MnO. Therefore, significant heterogeneity was not expected in these slag grains. The homogeneity of slag grains was then evaluated with EDS point analysis for confirmation. Two relatively large slag particles were selected from reference R3 and R5 slag cement pastes respectively, on which around ten spot analysis points were chosen as displayed in Figure 3.5. A statistical summary of the chemical compositions regarding the four main metal oxide contents is shown in Table 3.7. Compared with the results in Table 3.4, the standard deviation of points within a single slag grain decreased remarkably, and the extremely low coefficient of variation (Table 3.7) further proved that these two slags were highly homogeneous, and there was negligible heterogeneity.

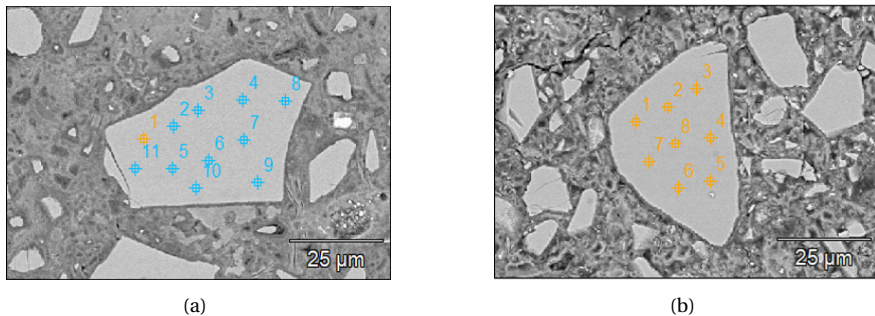


Figure 3.5: Two large slag particles chosen from reference slag (a) R3 and (b) R5 cement pastes, respectively.

3.4. DISCUSSION

3.4.1. REMARKS ON THE EDS MICROANALYSIS METHODOLOGIES

As mentioned in [5], a considerably large number of EDS microanalysis results are generated using commercial “standardless” routines instead of employing the k-ratio/matrix corrections protocols using microanalytical standards. Relying on the internal standards only leads to normalization of the detected composition, which can be highly erroneous for hydrated compounds. Because the standardless routine normalizes the mass percentage total of all constituents to exactly 100%, critical information will be lost, and analyst cannot estimate whether or not the points selected on slag grains are accurately characterized. It is reflected by the results shown in Table 3.6, as a evident difference was observed regarding the mass percentages of four main

metal oxides between standards-based and standardless microanalysis. Meanwhile, a much lower standard deviation is obtained for most metal oxides calculated from standards-based microanalysis. Outliers with extremely lower or higher analytical total can be removed from the data set, which decreases the standard deviation considerably. Also, the analyst would be wise to further investigate the source of error e.g., instrumental parameters or the presence of an omitted component in slag [21].

As for the relatively large analytical total range in the present chapter compared to the convention (98-102%), it could be explained by the following reasons: (1) The porosity of slag grain. It was found that the average density of wet granulated blast furnace slag was $\sim 2.9 \text{ g/cm}^3$ and its total porosity was around 5-10% by volume [22]. These pores in slag grain may result in errors on both excitation (Z) and absorption (A) corrections during quantitative microanalysis. Electron interaction in a porous matrix even contributed to different backscattering coefficients compared to crystalline materials [23], and analytical totals decreased with increasing local porosity [24]. (2) Differences in matrix correction factors between slag grain and standard minerals. Commonly, available rock-forming minerals do not resemble slag grain in terms of structure and composition. Thus, the selection of standards for each element of slag leads to variation in analytical total due to the matrix effect between the standard minerals and slag grain. Therefore, it is suggested that calibration studies should be carried out with available microanalysis standards in the future.

3.4.2. SULFUR AND TITANIUM IN SLAG

THE sulfur (S) in slag comes from iron pyrite (used as raw material) and coke for fuel. During quenching, sulfur will be released in the form of H_2S with water vapor and the residual sulfur can be found as sulfide in slag. As revealed in Table 3.6, besides the four main metal oxides of slag grains, sulfur tends to be the most important minor constituent when mass percentage is considered. It varies around 2~4 wt.% in slags in field concretes. European Standard EN 15167-1 requires that the sulfide and sulfate contents in slag should be below 2.0 wt.% and 2.5 wt.%, respectively. However, the standard did not specify how to measure sulfide and sulfate contents in slag.

During the quantitative EDS microanalysis, anhydrite was used as a microanalytical standard, and sulfate (SO_3) was assumed to be the oxide form existing in slag, therefore in order to generate the oxide table, three oxygen atoms were assigned to one sulfur atom, stoichiometrically. Conversely, part or even most of sulfur exists in the form of sulfide (S^{2-}) in slag, which could not be distinguished by the analysis. It is the same for XRF analysis, both of which are based on X-ray characterization. Therefore, the sulfur content based on XRF or EDS analysis should not be considered accurate.

European Standard EN 196-2 recommends to ignite slag in an oxidizing atmosphere at $950 \pm 50 \text{ }^\circ\text{C}$ to ensure the oxidation of sulfide, and then to determine its amount. However, the oxidation of any iron or manganese may influence the result. ICP-Ion chromatography (IC) appears to be an alternative method, which has been used to determine the amounts of different forms of sulfur (S^{2-} , $\text{S}_2\text{O}_3^{2-}$, and SO_4^{2-}) [25–27]. Based on the affinity to ion exchanger, this method can separate almost all charged ions [28]. Therefore, if sulfur content is the main concern of research, the author recommends to combine these methods together and find the one or ones of best

availability.

As for trace element Ti, TiO_2 content in slag is commonly found less than 1 wt.% and regarded as uncritical [22]. There is no specific requirement regarding the amount of TiO_2 in slag in EN 15167-1. Some studies found that if the TiO_2 content exceeded a critical limit, which was about 1 wt.%, it resulted in a more or less pronounced reduction in the strength of cements produced with this slag [19, 29, 30]. In this chapter, the amount of Ti varies around 1~2 wt.% when quantifying it in reference slag cement pastes and field slag concrete samples. However, a large relative deviation is found among different characterization methods. It is partially arising from the accelerating voltage of 10 kV employed here, and thus a lower overvoltage ratio is obtained for Ti compared to other elements. In addition, it is challenging for concentration characterization as a trace element in slag. Therefore, WDS at higher accelerating voltage is recommended to determine the amount of TiO_2 in slag due to its relatively higher spectral resolution by a factor of ten or more unless its heterogeneously distributed in the particles as trace constituent.

3.4.3. CHEMICAL COMPOSITION OF SLAG USED IN THE NETHERLANDS

As reviewed in Chapter 2, slag compositions have been observed to vary in a single location over time [22]. The findings in this chapter reveal that an evident increase in CaO and SiO_2 contents is found in slag used for sample G (2015). Also, MgO shows a gradual decreasing tendency over the years. Moreover, a survey on the recent publications (2019-2021) highlighted a trend for consistent production of lime-rich and magnesium-poor slag in cement manufacturing, which appeared to be especially distinct across Europe [20, 31–34], North America [35–37] and Australia [38]. The lime and magnesia in slag originates from the flux added into the blast furnace. The trend indicates an increasing amount of limestone use over dolomite as the flux. It appears that the trend of producing Ca-rich/Mg-poor slag arises partly owing to the need for compensating decreased viscosity of molten slag at melting point. According to [39–41], for example, for a blast furnace slag with a CaO/ SiO_2 mass ratio a little higher than 1, a MgO content between 6.2~6.6 wt.% and a Al_2O_3 content at around 14 wt.% is optimal to produce slag that melts easily. No doubt this trend deserves more attention both from industry and academia. Thus in the following chapters, the author attempts to build the correlation among slag chemistry, slag reactivity, and carbonation resistance of cement-slag paste.

3.5. CONCLUSIONS

THIS chapter explored the potential to use EDS microanalysis as a tool for quantitative measurement of the chemical composition of unhydrated slag grains in existing concretes. The results showed that EDS microanalysis provided reliable quantification regarding the four main metal oxides contents (CaO, SiO_2 , Al_2O_3 , and MgO) of slag. Other main conclusions drawn were as follows:

- For samples B to F, the change in slag chemistry was insignificant; however, an evident increasing in CaO and SiO_2 contents was found in slag used for sample G, opposite to that of Al_2O_3 and MgO. Especially for MgO, it showed a gradual

decreasing tendency over the years.

- For sulfur and titanium, a large relative deviation was found among different characterization methods when determining their concentrations, which was related to the heterogeneity of slag particle and oxidation state of sulfur. Therefore, a higher resolution technique such as WDS should be considered when these elements are of concern.

REFERENCES

- [1] Y. Zhang, K. Saravanakumar, and O. Çopuroğlu, *EDS Microanalysis of Unhydrated Blast Furnace Slag Grains in Field Concrete with Different Service Life*, *Microscopy and Microanalysis*, 1 (2022).
- [2] Y. Yang, K. Raipala, and L. Holappa, *Ironmaking*, in *Treatise on process metallurgy* (Elsevier, 2014) pp. 2–88.
- [3] J. Goldstein, *Practical scanning electron microscopy: electron and ion microprobe analysis* (Springer Science Business Media, 2012).
- [4] S. J. B. Reed, *Electron microprobe analysis and scanning electron microscopy in geology* (Cambridge university press, 2005).
- [5] D. E. Newbury and N. W. Ritchie, *Is scanning electron microscopy/energy dispersive X-ray spectrometry (SEM/EDS) quantitative?* *Scanning* **35**, 141 (2013).
- [6] D. E. Newbury and N. W. Ritchie, *Quantitative electron-excited X-ray microanalysis of borides, carbides, nitrides, oxides, and fluorides with scanning electron microscopy/silicon drift detector energy-dispersive spectrometry (SEM/SDD-EDS) and NIST DTSA-II*, *Microscopy Microanalysis* **21**, 1327 (2015).
- [7] D. E. Newbury and N. W. Ritchie, *Performing elemental microanalysis with high accuracy and high precision by scanning electron microscopy/silicon drift detector energy-dispersive X-ray spectrometry (SEM/SDD-EDS)*, *Journal of materials science* **50**, 493 (2015).
- [8] J. I. Goldstein, D. E. Newbury, J. R. Michael, N. W. Ritchie, J. H. J. Scott, and D. C. Joy, *Quantitative analysis: From k-ratio to composition*, in *Scanning Electron Microscopy and X-Ray Microanalysis* (Springer, 2018) pp. 289–307.
- [9] A. Harrisson, H. F. Taylor, and N. Winter, *Electron-optical analyses of the phases in a Portland cement clinker, with some observations on the calculation of quantitative phase composition*, *Cement and Concrete Research* **15**, 775 (1985).
- [10] M. Mouret, A. Bascoul, and G. Escadeillas, *Microstructural features of concrete in relation to initial temperature-SEM and ESEM characterization*, *Cement and Concrete Research* **29**, 369 (1999).

- [11] C. Famy, A. Brough, and H. Taylor, *The CSH gel of Portland cement mortars: Part I. The interpretation of energy-dispersive X-ray microanalyses from scanning electron microscopy, with some observations on CSH, AFm and AFt phase compositions*, Cement and Concrete Research **33**, 1389 (2003).
- [12] L. Sorbier, E. Rosenberg, and C. Merlet, *Microanalysis of porous materials*, Microscopy Microanalysis **10**, 745 (2004).
- [13] D. Koleva, J. Hu, A. Fraaij, P. Stroeven, N. Boshkov, and J. De Wit, *Quantitative characterisation of steel/cement paste interface microstructure and corrosion phenomena in mortars suffering from chloride attack*, Corrosion Science **48**, 4001 (2006).
- [14] S. J. Jaffer and C. M. Hansson, *Chloride-induced corrosion products of steel in cracked-concrete subjected to different loading conditions*, Cement and Concrete Research **39**, 116 (2009).
- [15] U. H. Jakobsen, *Microstructural surface deterioration of concrete exposed to seawater: results after 2 years exposure*, in *14th Euroseminar on Microscopy Applied to Building Materials* (2013) pp. 10–14.
- [16] O. Copuroglu, *Microanalysis of crystalline ASR products from a 50 year-old concrete structure*, 14th Euroseminar on Microscopy Applied to Building Materials , 10 (2013).
- [17] J. Pacheco, O. Çopuroğlu, and R. Polder, *Optimisation of chloride quantification in cementitious mortars using energy-dispersive X-ray analysis*, (2013).
- [18] J. Pacheco and O. Çopuroğlu, *Quantitative energy-dispersive X-ray microanalysis of chlorine in cement paste*, Journal of Materials in Civil Engineering **28**, 04015065 (2016).
- [19] S. Blotevogel, L. Steger, D. Hart, L. Doussang, J. Kaknics, M. Poirier, H. Bornhöft, J. Deubener, C. Patapy, and M. Cyr, *Effect of TiO₂ and 11 minor elements on the reactivity of ground-granulated blast-furnace slag in blended cements*, Journal of the American Ceramic Society **104**, 128 (2021).
- [20] S. Blotevogel, A. Ehrenberg, L. Steger, L. Doussang, J. Kaknics, C. Patapy, and M. Cyr, *Ability of the R3 test to evaluate differences in early age reactivity of 16 industrial ground granulated blast furnace slags (GGBS)*, Cement and Concrete Research **130**, 105998 (2020).
- [21] D. E. Newbury, C. R. Swyt, and R. L. Myklebust, *"standardless" quantitative electron probe microanalysis with energy-dispersive X-ray spectrometry: is it worth the risk?* Analytical chemistry **67**, 1866 (1995).
- [22] A. Ehgrenberg, *Huettensand: ein leistungsfahiger Baustoff mit Tradition und Zukunft: Teile 1 und 2*, BETON-INFORMATIONEN **46** (2006).

- [23] D. Poirier and R. Gauvin, *X-ray microanalysis of porous materials using Monte Carlo simulations*, Scanning **33**, 126 (2011).
- [24] K. Kjellsen, O. Wallevik, and L. Fjällberg, *Microstructure and microchemistry of the paste—aggregate interfacial transition zone of high-performance concrete*, Advances in Cement Research **10**, 33 (1998).
- [25] F. P. Glasser, K. Luke, and M. Angus, *Modification of cement pore fluid compositions by pozzolanic additives*, Cement and Concrete Research **18**, 165 (1988).
- [26] A. Gruskovnjak, B. Lothenbach, L. Holzer, R. Figi, and F. Winnefeld, *Hydration of alkali-activated slag: comparison with ordinary Portland cement*, Advances in cement research **18**, 119 (2006).
- [27] B. Lothenbach, G. Le Saout, M. B. Haha, R. Figi, and E. Wieland, *Hydration of a low-alkali CEM III/B–SiO₂ cement (LAC)*, Cement and Concrete Research **42**, 410 (2012).
- [28] A. J. Ninfa, D. P. Ballou, and M. Benore, *Fundamental laboratory approaches for biochemistry and biotechnology* (John Wiley Sons, 2009).
- [29] E. Demoulian, P. Gourdin, F. Hawthorn, and C. Vernet, *Influence de la composition chimique et de la texture des laitiers sur leur hydraulicité*, Vil Intem. Congr. Chem. Cem., 89 (1980).
- [30] D. Le Cornec, L. Galois, L. Izoret, L. Cormier, N. Trcera, and G. Calas, *Structural role of titanium on slag properties*, Journal of the American Ceramic Society **104**, 105 (2021).
- [31] A. Kiiashko, M. Chaouche, and L. Frouin, *Effect of phosphonate addition on sodium carbonate activated slag properties*, Cement and Concrete Composites **119**, 103986 (2021).
- [32] M. Alonso, C. Gascó, M. M. Morales, J. Suárez-Navarro, M. Zamorano, and F. Puertas, *Olive biomass ash as an alternative activator in geopolymer formation: A study of strength, radiology and leaching behaviour*, Cement and Concrete Composites **104**, 103384 (2019).
- [33] X. Dai, S. Aydin, M. Y. Yardimci, R. Qiang, K. Lesage, and G. De Schutter, *Rheology, early-age hydration and microstructure of alkali-activated GGBFS-Fly ash-limestone mixtures*, Cement and Concrete Composites **124**, 104244 (2021).
- [34] J. O. Ukpata, P. M. Basheer, and L. Black, *Expansion of CEM I and slag-blended cement mortars exposed to combined chloride-sulphate environments*, Cement and Concrete Research **123**, 105794 (2019).
- [35] S. Y. Wang, E. McCaslin, and C. E. White, *Effects of magnesium content and carbonation on the multiscale pore structure of alkali-activated slags*, Cement and Concrete Research **130**, 105979 (2020).

- [36] M. Sakr and M. Bassuoni, *Performance of concrete under accelerated physical salt attack and carbonation*, Cement and Concrete Research **141**, 106324 (2021).
- [37] O. Burciaga-Díaz, *Parameters affecting the properties and microstructure of quicklime (CaO)-activated slag cement pastes*, Cement and Concrete Composites **103**, 104 (2019).
- [38] M. Samarakoon, P. Ranjith, W. H. Duan, and V. De Silva, *Properties of one-part fly ash/slag-based binders activated by thermally-treated waste glass/NaOH blends: A comparative study*, Cement and Concrete Composites **112**, 103679 (2020).
- [39] G. Mußnug, *Beitrag zur Frage der Mahlbarkeit von Hochofenschlacken (Zementschlacken) und klinkern*, Zement **31**, 183 (1942).
- [40] T. Jiang, S. Wang, Y. Guo, F. Chen, and F. Zheng, *Effects of basicity and MgO in slag on the behaviors of smelting vanadium titanomagnetite in the direct reduction-electric furnace process*, Metals **6**, 107 (2016).
- [41] F. Shen, X. Hu, H. Zheng, X. Jiang, Q. Gao, H. Han, and F. Long, *Proper MgO/Al₂O₃ ratio in blast-furnace slag: Analysis of proper MgO/Al₂O₃ ratio based on observed data*, Metals **10**, 784 (2020).

4

EFFECT OF SLAG CHEMISTRY ON THE REACTIVITY OF SLAG

In this chapter, both synthetic slags based on CaO-SiO₂-Al₂O₃-MgO system and commercial slags were considered to estimate the correlation between slag chemistry and reactivity. The idea behind the design of synthetic slags was to cover the range of composition typically encountered in commercial slags as much as possible (reviewed in Chapter 2) and the variation of slag composition in the Netherlands, as revealed in Chapter 3. Meanwhile, attention was paid to the contents of Al₂O₃ and MgO in particular. In order to study reactivity, two methods were used in the study. The first one was hydraulicity/R3 test on a model blended system composed of slag, calcium hydroxide, limestone and potassium-hydroxide and -sulfate solutions. The other test was the dissolution test of slag powder in a strong NaOH solution. Additionally, the author attempted to estimate the reactivity of slag using a novel graphical method based on a cartesian coordinate system of (CaO/SiO₂)-(Al₂O₃+MgO) in weight percentage, which provided a new insight on the influence of chemical composition on the reactivity of slag.

Parts of this chapter were published in Construction and Building Materials **335**, 127493 (2022) [1] and Construction and Building Materials **316**, 125266 (2022) [2].

4.1. INTRODUCTION

IN order to assess the quality/reactivity of blast furnace slag, many efforts have been made to determine a relationship that can be used to predict slag reactivity from its chemical composition [3, 4]. Several different hydraulic moduli (or basicity) were reviewed in the literature, e.g., [4]. However, none of them gave a satisfactory result for estimating various slag used in cement [5].

In the recent years, several researchers examined synthetic CaO-SiO₂-Al₂O₃ based glasses with controlled chemical composition in the laboratory condition [6–9] to simulate the performance of SCMs in the blended cements. This approach was particularly preferred in order to eliminate potential interferences from other internal or external sources. These studies showed that chemical composition played a key role on the network structure of glass, which affected the surface free energy, hence its reactivity. It is generally accepted that the reactivity increases with the increasing depolymerization of the silicate structure.

In this chapter, the author extended the CaO-SiO₂-Al₂O₃ based system to CaO-SiO₂-Al₂O₃-MgO for simulating slag. Both synthetic and commercial slags were considered to estimate the correlation between slag chemistry and reactivity. The idea behind the design of synthetic slags was to cover the range of composition typically encountered in commercial slags as much as possible (reviewed in Chapter 2) and the variation of slag chemistry in the Netherlands, as revealed in Chapter 3. Meanwhile, attention was paid to the contents of Al₂O₃ and MgO in particular. In order to study reactivity, two methods were used in the study. The first one was hydraulicity/R3 test on a model blended system composed of slag, calcium hydroxide, limestone and potassium-hydroxide and -sulfate solutions. The aim of this blended system is to simulate the environment occurring in a hydrating slag cement paste [10–15]. The other test was the dissolution test of slag powder in a strong NaOH solution. In principle, the hydration process can be recognized as a couple of reactions involving dissolution of raw material and precipitation of hydrates. Therefore, a more underlying insight into the dissolution process of slag in alkaline solution is essential to understand the reaction between slag and calcium hydroxide [16–18]. Additionally, the author attempted to estimate the reactivity of slag using a novel graphical method based on a cartesian coordinate system of (CaO/SiO₂)(Al₂O₃+MgO) in weight percentage, which provided a new insight on the influence of chemical composition on the reactivity of slag.

4.2. MATERIALS AND METHODOLOGY

4.2.1. SYNTHESIS OF SLAG

NINE synthetic slags (M0, M8, M16; A3, A3-1, A12, A18; CS1, CS2), one commercially available slag (S), and quartz powder (Qz) were used in the study. The detailed production process was introduced in Chapter 3. In M series, CaO/SiO₂ ratio was kept at around 1 and the amount of Al₂O₃ fluctuated at around 14 wt.%, while MgO content was determined from 0.33 to 16.07 wt.%. Similarly, for A3, A12 and A18 in A series, CaO/SiO₂ ratio was also maintained at around 1.0 and the amount of MgO was stabilized at about 10 wt.%, while Al₂O₃ content varied from 3.69 to 18.19 wt.%. As for

Table 4.1: Chemical compositions (wt.%) determined by XRF and physical properties of these ten slags.

	M0	M8	M16	A3	A3-1	A12	A18	CS1	CS2	S
CaO	43.16	37.04	34.09	42.07	38.39	37.32	36.87	32.98	28.05	37.40
SiO ₂	42.99	37.79	32.99	43.30	48.41	39.11	34.43	38.67	42.84	37.82
Al ₂ O ₃	13.30	14.51	15.05	3.69	2.39	12.32	18.19	14.51	17.12	13.58
MgO	0.33	8.83	16.07	10.83	10.58	9.43	7.98	11.22	9.67	8.11
FeO/Fe ₂ O ₃	0.07	0.28	0.34	0.07	0.09	0.30	0.40	0.36	0.35	0.36
TiO ₂	-	0.70	0.73	-	-	0.70	0.84	1.02	0.89	1.22
MnO/Mn ₂ O ₃	-	0.17	0.16	-	-	0.15	0.27	0.22	0.19	0.3
Na ₂ O	-	0.24	0.22	-	0.07	0.24	0.37	0.36	0.31	-
K ₂ O	-	0.25	0.21	-	-	0.21	0.41	0.36	0.32	0.28
SO ₃	0.01	0.01	0.01	0.01	0.01	0.03	0.03	0.05	0.08	0.93
Residual	0.14	0.18	0.13	0.03	0.06	0.19	0.21	0.25	0.08	-
CaO/SiO ₂	1.00	0.98	1.03	0.97	0.79	0.95	1.07	0.85	0.65	0.99
(CaO+MgO)/SiO ₂	1.01	1.21	1.52	1.22	1.01	1.20	1.30	1.14	0.88	1.20
NBO/T	1.33	1.67	2.10	2.48	2.17	1.80	1.53	1.64	1.15	1.73
Physical properties										
d ₅₀ (μm)	24.35	22.73	22.29	19.67	20.69	20.35	20.85	20.40	20.11	20.94
SSA (m ² /g)	0.77	0.90	0.96	1.09	0.91	0.92	0.90	0.93	1.08	0.94

synthetic slag A3-1 in A series, it contained almost the same amount of MgO and Al₂O₃ compared to slag A3 while the CaO content was ~10 wt.% less than that of SiO₂. The purpose of CS series was to investigate the effect of CaO/SiO₂ ratio on the reactivity of slag, and the MgO and Al₂O₃ contents levelled-off at approximately 10 and 15 wt.%, respectively. Especially for CS2, the (CaO+MgO)/SiO₂ ratio of which was less than 1, which did not conform the European Standard EN 15167-1. Commercial slag S was used as a reference and had a similar chemical composition with the synthetic slag M8.

The chemical composition of raw materials are presented in Table 4.1. Their particle size distributions were measured by laser diffraction (EyeTech, Ankersmid) and are shown in Figure 4.1. It was obvious that they had a similar d₅₀. The specific surface area (SSA) of these slags was measured by nitrogen adsorption with 11-point BET method (Micromeritics, Gemini VII 2390p). The slag powders were dried at 105 °C and degassed before the experiments. The analytical error was in limit of ±2%. Comparatively, a low specific surface area was obtained for slag M0, which was partially due to its relatively coarser particle size distribution as reflected by the d₅₀. As for the degree of depolymerization of slag network structure (represented by NBO/T), it was determined by the equation proposed in [19].

4.2.2. CHARACTERIZATION OF THE STRUCTURE OF SLAG

X-ray diffraction (XRD) measurement was employed to determine possible crystal phase formations. It was performed on a Philips PW 1830/40 Powder diffractometer employing the Cu K-alpha radiation (employing Bragg-Brentano reflection geometry). The machine was operated with an acceleration voltage of 40 kV and an X-ray beam current of 40 mA. Analysis was performed with a step size of 0.03°, for a 2θ range from 5 to 60°.

Another part of slag powders were further coated with carbon to examine their morphology using FEI QUANTA FEG 650 ESEM with an accelerating voltage of 15 kV and at a working distance of 10 mm in secondary electron (SE) detection mode.

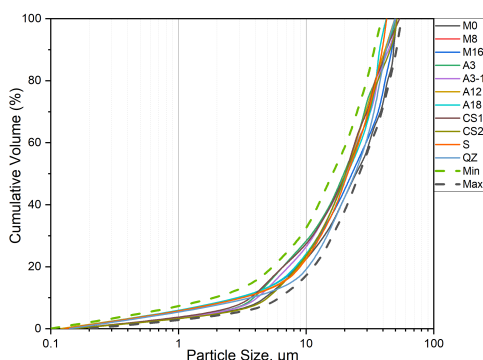


Figure 4.1: Particle size distribution of slags and quartz.

Table 4.2: Components (gram) of the blended system.

	Syn. Slag	Portlandite	Limestone	Potassium solution
Blended system	10.0	30.0	5.0	54

Morphology between the synthetic slags and the commercial slag was compared based on SE micrographs.

Fourier transform infrared spectroscopy (FTIR) was performed using Spectrum TM 100 Optical ATR-FTIR spectrometer over the wavelength range from 600 to 1600 cm^{-1} to identify the chemical bonding environment of Si structural units. A single-beam configuration was used, and each sample was scanned 20 times with a fixed instrument resolution of 4 cm^{-1} .

4.2.3. CHARACTERIZATION OF THE REACTIVITY OF SLAG

HYDRAULICITY TEST

The composition of the model system employed here is shown in Table 4.2. Details of the method can be found elsewhere [10–15]. Calcium hydroxide was used to trigger pozzolanic activity. A very small quantity of limestone (CaCO_3) was added to facilitate reactions with the dissolved aluminum from slag. Potassium hydroxide and potassium sulfate were combined in certain proportion and dissolved in reagent water to obtain dissolved ions such as SO_4^{2-} and OH^- to mimic the pore solution of slag cement. Potassium solution was prepared by dissolving 4.0 g of potassium hydroxide and 20.0 g of potassium sulfate in 1.0 L of reagent water (pH \approx 12.85) conditioned at 20 ± 3 °C.

40 °C calorimetry was performed over 7 days. Within 5 min after mixing, paste was casted into an air-tight specimen container and transferred into the equipment. In addition, paste samples were also casted in 20 mL plastic bottle and cured under 40 °C for 7 days for further investigation. Elevated temperature (40 °C) was employed to accelerate the rate of reaction between slag and calcium hydroxide. Also, 7 days was considered to be sufficient enough to determine the level of reactivity and the variability of test results was low [10, 14, 15].

Thermogravimetric analysis (TGA) and XRD scans were also introduced to observe

the hydration products of this model system. Slices cut from the specimens were immersed into isopropanol bath for one week to stop hydration (refreshed every day). Then, they were crushed and ground to below 63 μm for measurement immediately. TGA was performed with a Netzsch STA 449 F3 Jupiter under argon atmosphere. Approximately 50 mg of the material was heated from 40 to 900 $^{\circ}\text{C}$ with a heating rate of 10 $^{\circ}\text{C}/\text{min}$ in an Al_2O_3 crucible and an identical crucible as reference. Two methods were employed here to calculate the bound water content, one is to measure the mass loss of crushed sample paste heated at 350 $^{\circ}\text{C}$ for 2 hours in a furnace (BW1) [10] and the other one is to obtain it from thermogravimetric measurement corrected for the water bound in portlandite (BW2) according to the following equation:

$$BW = \frac{W_{50} - W_{550} - W_{\text{H}_2\text{O,CH}}}{W_{550}} \quad (4.1)$$

with W_{50} = sample weight at 50 $^{\circ}\text{C}$, W_{550} = sample weight at 550 $^{\circ}\text{C}$, and $W_{\text{H}_2\text{O,CH}}$ = mass loss from the decomposition of portlandite by tangent method. For XRD measurements, identical procedure was used as described in Section 4.2.2.

DISSOLUTION TEST

To gain a more instrumental insight between reactivity and chemical composition, batch dissolution test was carried out. Slag powders with the particle size distribution shown in Figure 4.1 were also employed for dissolution test. All slag samples were isolated and reacted in a closed dilute system, and high liquid to solid ratio (1000) allowed the dissolution mechanism to be analyzed as much as possible. The concentration of ion release measured provides evidence of the dissolution kinetics of slag under alkaline condition, indicating the reactivity to a certain extent. Although the setup cannot guarantee pure dissolution, it still offers a good approximation to the slag dissolution characteristics in a realistic blended cement system.

Concentrations of the four main ions (Ca^{2+} , Si^{4+} , Al^{3+} , and Mg^{2+}) were measured in NaOH solution with a pH of 13.2 (5.6 g NaOH particle was dissolved in 1000 g deionized water, and the concentration of NaOH was 0.14 M.), corresponding to that of pore solution in a hydrated blended cement paste [16–18]. The experiment was carried out in 1000 mL PE bottle at 20 ± 2 $^{\circ}\text{C}$. To avoid abrasion, the solution was not stirred while these bottles were put on the rotary table with a small rotor in each of them at a low speed. Solution was sampled at 1, 2, 4, 6, 8, 24, 48 and 72 hours (3 days) during test. About 10 mL solution was taken each time, filtered (2.5 μm filter paper) and stored at 4 $^{\circ}\text{C}$. After each sampling, the same amount of NaOH solution (0.14 M) was added to keep the volume in the bottle constant (1000 mL). The pH of solution was measured with a pH meter 827 Metrohm during the dissolution, and after 7 days, it decreased only a little to around 13.0. The concentrations of Ca, Si, Al, and Mg were measured by ICP-OES (Optima 5300 DV) with matrix-matched standard. Concentration below 0.1 mg/L cannot be detected by the equipment. In the preliminary test, replicates were prepared and subjected to the analysis. The variation was within $\pm 3\%$ for the measurement of Ca, Si, Al and Mg concentrations.

After 7 days, dissolution test was stopped, solution was filtered and undissolved particle residue was collected, rinsed with isopropanol, and dried at 40 $^{\circ}\text{C}$ oven for ~ 10 min. These residues were collected and subsequently ground for TGA measurement.

4.3. RESULTS

4.3.1. THE CHARACTERIZATION OF SLAG

As presented in Figure 4.2, it was found that the nine synthetic slags and one commercial slag were almost entirely amorphous with no observed crystal peak, which indicated the lack of long-range structural order. For M series, the position of amorphous hump shifted a little bit toward higher diffraction angle with increasing MgO content while it moved to lower angle with decreasing CaO+MgO content (i.e., increasing Al_2O_3 content) in A series conversely. Similarly, the position shifted left a small quantity with decreasing CaO/SiO₂ ratio. In fact, the change of the position of amorphous hump was minor, and it fluctuated at about 30° (2 θ).

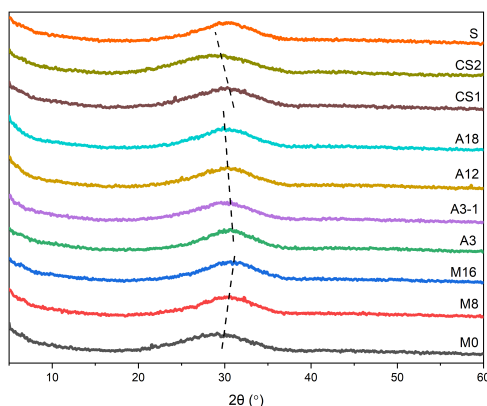
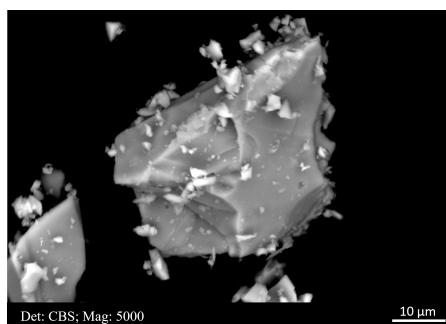


Figure 4.2: XRD scans of nine synthetic slags and one commercial slag. The small Bragg peaks in slag M8 and CS1 can be attributed to the formation of akermanite and gehlenite, respectively.

Figure 4.3 shows the morphology of commercial slag S and synthetic slag A18 as observed by SEM, all of which were predominantly irregular with clear fracture edges and angles, indicating the existing of glassy phase in the structure of slag.



(a)



(b)

Figure 4.3: SEM micrographs of (a) commercial slag S and (b) synthetic slag A18.

Figure 4.4 shows the FTIR spectroscopy results of slag samples within the wavenumber region between 1200 and 600 cm^{-1} . This region represents the symmetric stretching vibration band of the $[\text{SiO}_4]^{4-}$ tetrahedra between 1200 and 760 cm^{-1} and the asymmetric stretching vibration band of the $[\text{AlO}_4]^{5-}$ tetrahedra between 760 and 610 cm^{-1} . Moreover, the $[\text{SiO}_4]^{4-}$ tetrahedral vibration band can be divided into four characteristic bands further, in terms of $[\text{Si}_4\text{O}_{10}]^{4-}$ (sheet, 1100-1050 cm^{-1}), $[\text{Si}_3\text{O}_{10}]^{8-}$ (chain, 980-950 cm^{-1}), $[\text{Si}_2\text{O}_7]^{6-}$ (dimer, 920-900 cm^{-1}), and $[\text{SiO}_4]^{4-}$ (monomer, 880-850 cm^{-1}), respectively [20–23].

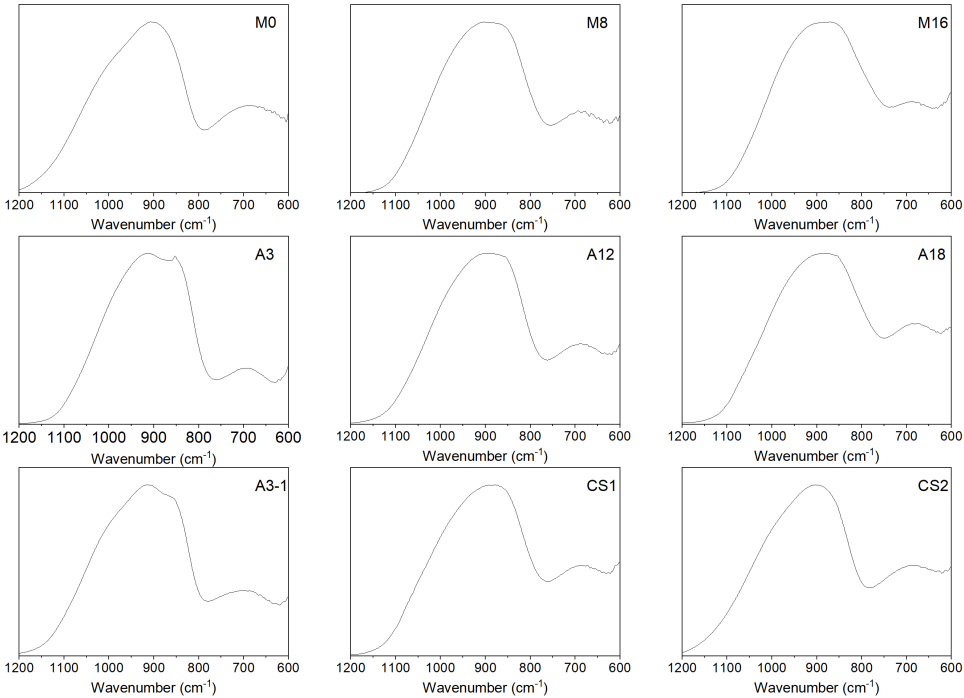


Figure 4.4: FTIR spectroscopy results of slag samples in absorbance mode (Normalized, %).

From the graph, no clear difference was found between slag samples with different compositions. The broad absorption band from 800 to 1000 cm^{-1} indicated the existence of different $[\text{SiO}_4]^{4-}$ tetrahedral vibration bands. Additionally, note that the relative intensity of AlO_4 tetrahedra at about 690 cm^{-1} decreased with MgO addition in M series. Probably it was related to the reduction of relative abundance of AlO_4 tetrahedral incorporated into the silicate network. On the contrary, it was foreseeable that the relative intensity of AlO_4 tetrahedra increased with Al_2O_3 addition in A series.

4.3.2. THE REACTIVITY OF SLAG

HYDRAULICITY TEST

The hydraulicity/R3 test involves isothermal calorimetry for determining the heat flow and cumulative heat evolution of the model system, and thermogravimetric

measurement to calculate the amount of chemically bound water in hydrated phases.

CALORIMETRY

The recorded heat flow and cumulative heat release of the model paste during 7 days of curing is presented in Figure 4.5(a) and 4.5(b), respectively. The reference sample paste with quartz was also measured under the identical condition. The initial peak, which occurred immediately after mixing with water, was associated with the wetting and dissolution of components. A main peak, indicating the reaction between slag and $\text{Ca}(\text{OH})_2$, arose at about 12 hours after mixing in all paste samples except the reference. In M series, the heat flow rose significantly with the increasing MgO content, in which the reaction between slag M16 and $\text{Ca}(\text{OH})_2$ seemed to be the fastest among all. It resulted in a 52.8% higher total heat release at 7 days in comparison to M0 blend. Similarly, the heat flow went up considerably from slag A3 to A18 in A series. Among all these slags, A3 and A3-1 which had the least Al_2O_3 content showed the lowest chemical reactivity. In CS series, the difference between heat flow and total heat release was very small although the CaO/SiO_2 ratio decreased from 0.85 for CS1 to 0.65 for CS2 (As for $(\text{CaO}+\text{MgO})/\text{SiO}_2$ ratio, it decreased from 1.14 to 0.88 correspondingly).

4

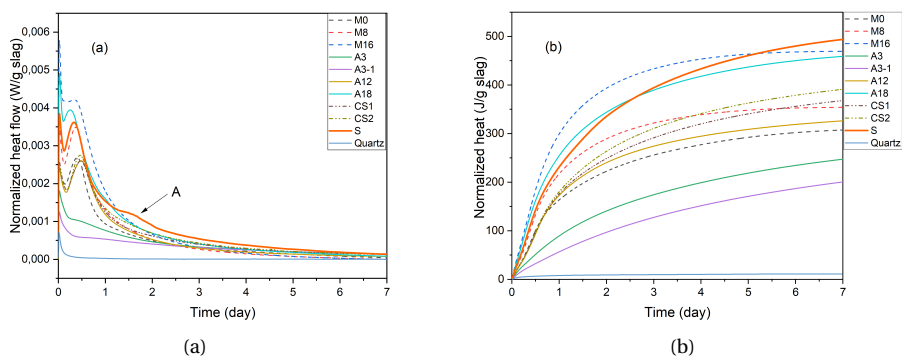


Figure 4.5: (a) Heat flow and (b) total heat released as a function of time in calorimetric measurement for the model paste.

Although the chemical composition of commercial slag S was similar to that of M8, and the heat of hydration characteristics were identical during the first 24 hours, an additional peak was observed in the model paste with the commercial slag S after the main peak. This peak (labelled A) was analogous to the hump seen in commercial cement system due to the transformation of ettringite into AFm phases [24], which was actually because of the incorporation of sulfur species in commercial slag S (see Section 4.3.3). The total heat released by the model paste S overtook M8 after one day and reached the highest total heat release eventually.

BOUND WATER CONTENT

The chemically bound water content based on the aforementioned two methods against cumulative heat release is plotted in Figure 4.6. Considering the relative uncertainty of the whole process, bound water due to the formation of hydrates was clearly visible after 7 days of curing.

Generally, the trend of chemically bound water content among these slags was

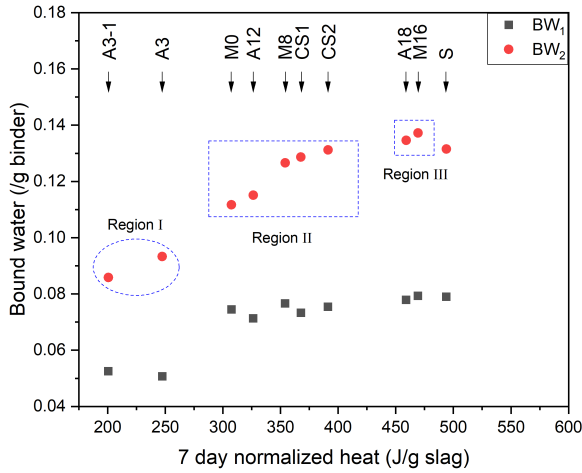


Figure 4.6: Bound water content against cumulative heat release.

positively associated with that of 7 days heat release from the calorimetric measurements. Results showed that higher MgO and Al₂O₃ contents led to higher bound water content, and the highest bound water content was detected for the model pastes with synthetic slag M16 and A18, and commercial slag S. Conversely, slag A3 and A3-1 containing model pastes showed the least amount of chemically bound water. It should be noted that the results based on BW₁ represented only a small range of binder mass (~0.05 to ~0.08), which reduced the the reliability of using chemically bound water as an index to distinguish the reactivity of slags.

Further analysis of the results based on BW₂ showed that these nine synthetic slags could be classified into three clusters: Cluster I contains slag A3 and A3-1, which shows the least heat release (≤ 250 J/g) and bound water content (≤ 0.10); Cluster III involves slag M16 and A18, which presents the most heat release (≥ 450 J/g) and bound water content (≥ 0.13); For other slags, they are located in cluster II with medium heat release (300-400 J/g) and bound water content (0.10-0.13).

HYDRATION PRODUCTS

For a clear view, TG and DTG results from five model pastes are shown in Figure 4.7. The main hydrates formed in all these blends were similar. The mass loss at 400-500 °C and 700-800 °C were attributed to the dehydration of portlandite and decarbonation of limestone, respectively. Ettringite was observed, and the formation of monocarbonate or hemicarbonate with the presence of limestone prevented the precipitation of monosulfate and stabilized ettringite indirectly [25–27]. Hydrotalcite-like phase could also be detected with the provision of MgO and Al₂O₃ from slag. In the M16 mixture, very little precipitation of monocarbonate or hemicarbonate was observed whereas a distinct amount of hydrotalcite-like phase was indicated. This may imply that Al³⁺ ion was more preferable to be incorporated into hydrotalcite-like phase when compared with monocarbonate and hemicarbonate. Moreover, the authors in [28, 29] investigated the potential effect of MgO content of slag in alkali-activated system, and they also

found that the amount of Al incorporation into C-S-H gel phase decreased with increasing MgO content in slag, indicated by the lower Al/Si atomic ratio. As for the model paste A18, ettringite became unstable and more monocarbonate was detected. When the amount of MgO in slag was fixed as in series A, a distinct dependence on the alumina content of slag and the amount of AFm phases was noticed. Also, the literature showed that the higher the alumina in slag, the more monocarbonate formation was observed [28, 29]. For samples A3 and A3-1 (Figure 4.7(c)), peaks seen in other pastes at ~ 100 and ~ 200 °C merged into the peak at ~ 150 °C, and the broadened peak at ~ 350 °C remained.

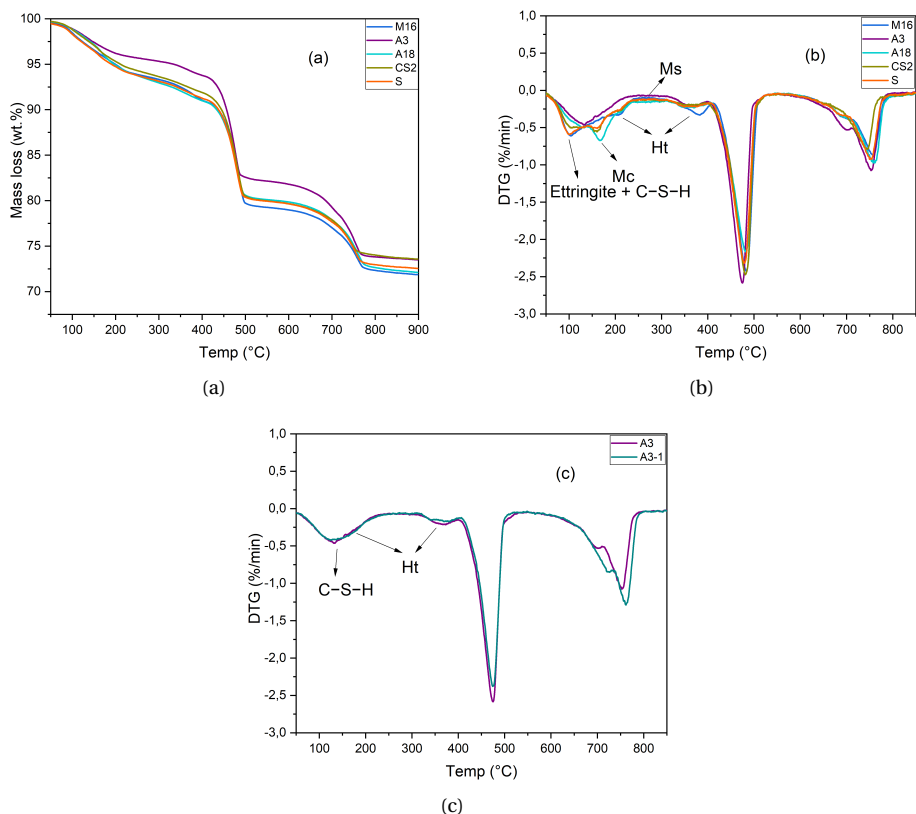


Figure 4.7: Typical results of (a) TG, (b) and (c) DTG analysis of model pastes after curing of 7 days at 40 °C. Ht: hydrotoalcite-like phase; Mc: monocarbonate; Ms: monosulfate.

Similarly, typical XRD results from five model pastes are presented in Figure 4.8. No trace of monosulfate was detected, and ettringite was observed in all investigated samples except for the pastes of A3 and A18, peaks of which at 2-theta ~ 9.1 and $\sim 15.8^\circ$ were undistinguishable. It was also confirmed by the TGA results (Figure 4.7) that ettringite became unstable, and much more monocarbonate was formed in A18 paste. Despite the reported low crystallinity of carbonate-containing AFm phases such as

monocarbonate and hemicarbonate, XRD allows a distinction between them. Monocarbonate was detected without hemicarbonate, independently of the chemical composition of slag. It was also found that hemicarbonate was the main carbonate bearing phase during the first few days while monocarbonate precipitated at a later stage with the presence of limestone in [24, 25, 27]. For M16 paste, the peak indicating hydrotalcite-like phase seemed to dominate over monocarbonate, which was consistent with the TG and DTG results shown in Figure 4.7(b), meaning that more hydrotalcite-like phase would be observed at the expense of AFm phases with the increasing amount of MgO present in slag. As for A3 paste, lack of peaks indicated a poor crystallinity.

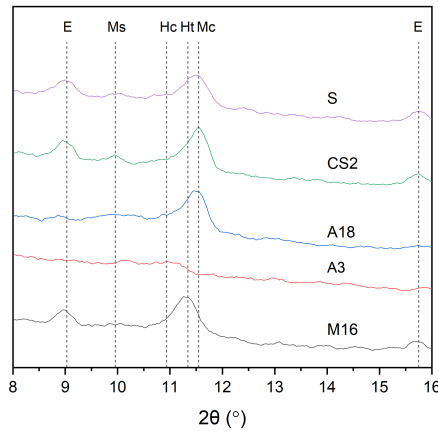


Figure 4.8: XRD results of the selected model pastes after 7 days curing at 40 °C. E – ettringite; Ht: hydrotalcite-like phase; Hc: hemicarbonate; Mc: monocarbonate; Ms: monosulfate.

DISSOLUTION TEST

In slag cement paste where slag is exposed to highly alkaline environment, OH^- ion attacks the surface of slag, leading to the release of calcium, silicon and aluminum species into pore solution. Once supersaturation has been reached, hydrates such as calcium-silicate (alumino) hydrates (C-S(A)-H), ettringite, AFm phases and a hydrotalcite-like phase start to nucleate and grow [30–32]. Thus, there is a consensus that the hydration process of slag can be regarded as a series of coupled reactions involving the dissolution of slag and precipitation of hydrates, and the dissolution process is strongly associated with its chemical composition.

ELEMENTAL CONCENTRATIONS

Elemental concentrations (Ca, Si, and Al) of five representative slags in the solution is shown in Figure 4.9. It was found that an initially nonlinear concentration increase was followed by a linear development for Ca, Si, and Al concentrations with time. The observed deceleration of dissolution rate after 1 day was likely to be caused by ion accumulation in the solution, which lowered undersaturation [17], i.e., the driving force for dissolution. The concentration of Mg^{2+} ion in the solution was very low, even under the detection limit in some sampling points.

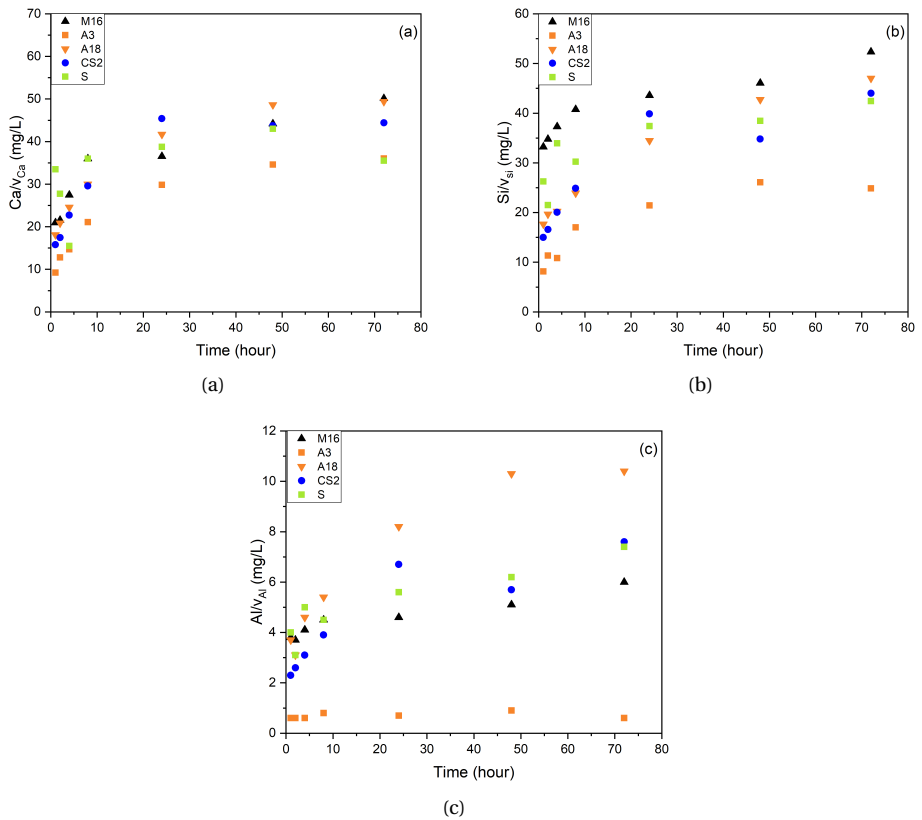


Figure 4.9: (a) Ca^{2+} (b) Si^{4+} and (c) Al^{3+} ion concentrations in the solution normalized to their molar fractions in raw slags, respectively plotted in function of time up to 3 days.

The concentrations of Si^{4+} and Al^{3+} at 3 days against cumulative heat release is shown in Figure 4.10. The Si^{4+} concentration in the diluted system showed a significant correlation with 7 days heat release from calorimetric measurement (Figure 4.10(a)). Generally, higher MgO and Al_2O_3 contents led to higher Si^{4+} concentration in the solution. Similarly, these nine synthetic slags can be divided into three regions based on Si^{4+} concentration and cumulative heat release: Region I contained slag A3 and A3-1, which showed the least amount of heat release (≤ 250 J/g) and Si^{4+} concentration normalized to its molar fraction (≤ 30 mg/L); Region III represented slag M16 and A18, corresponding to the highest heat release (≥ 450 J/g) and Si^{4+} concentration (≥ 45 mg/L); For other slags, they were located in Region II with medium heat release (300-400 J/g) and Si^{4+} concentration (30-45 mg/L). However, the correlation between Al^{3+} concentration and 7 days heat release was not as good as that of Si^{4+} (Figure 4.10(b)). The concentration of Al^{3+} showed a decreasing trend with increasing MgO mass percentage of raw slag with the order: M0 < A12 < CS1 < CS2 < M16 as the arrow indicated in Figure 4.10(b). Among all, M16 presented an Al^{3+} concentration of ~ 35 mg/L, only over that of slag A3 and A3-1 although it released the most heat. It was also noted that in contrast to high heat release and bound water content determined from hydraulicity test, commercial slag S only presented a medium Si^{4+} concentration at 3 days.

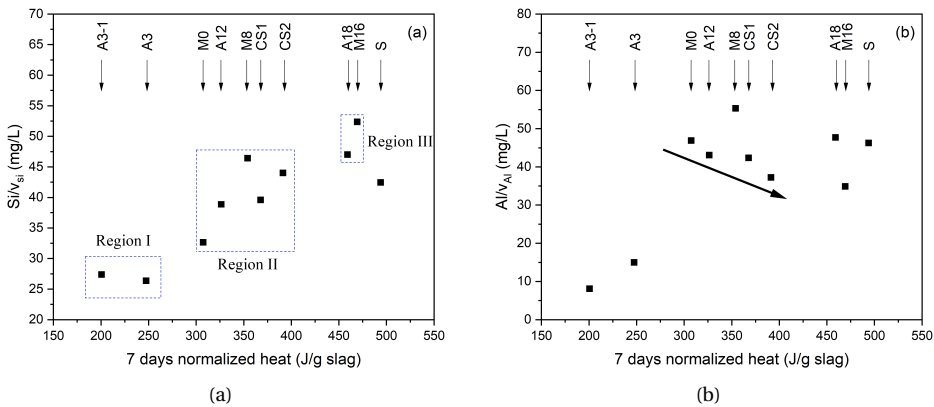


Figure 4.10: (a) Si^{4+} and (b) Al^{3+} concentrations in the solution normalized to their molar fraction in raw slag, respectively against cumulative heat release.

EFFECTIVE SATURATION INDICES

Saturation index (SI) is an indicator to assess which solid phase can form or will dissolve from a thermodynamic point of view. It is given by Equation 4.2, where ion activity product IAP is activities derived from the measured concentrations, and K_{so} corresponds to the solubility product of the regarding solid phase. Effective saturation indices (ESI) is determined by dividing the saturation indices by the number of ions participating in the reaction (see Equation 4.3) [33, 34]. A positive value implies oversaturation when the respective solid phase can form or precipitate while a negative effective saturation index suggests undersaturation with regard to this solid phase,

meaning that it cannot form or will dissolve. For the K_{so} values of phases involved in the study, please refer to [35].

$$SI = \log \frac{IAP}{K_{so}} \quad (4.2)$$

$$ESI = \frac{1}{N} \log \frac{IAP}{K_{so}} \quad (4.3)$$

Figure 4.11(a) presents the ESI of slag M8 with respect to hydrotalcite-like phase, brucite and C-S(A)-H gel phase as a function of dissolution time, as an example. It showed clearly that hydrotalcite-like phase and brucite were saturated from the first hour after dissolution. C-S(A)-H gel phase was below saturation at that time, and it was saturated at around 8 hours. These precipitations were also confirmed by the DTG results shown in Figure 4.11(b). The mass loss at ~ 150 and ~ 350 °C were attributed to the dehydration of C-S(A)-H gel phase and hydrotalcite-like phase, respectively. Small shoulders after 500 °C was associated with the decomposition of low crystallinity $Mg(OH)_2$ and its carbonation form $MgCO_3$ [36]. The results suggested the fact that aluminum was consumed during the formation of hydrotalcite-like phase. The higher the MgO content of slag, the more aluminum was fixed into hydrotalcite-like phase, which led to a lower amount of Al^{3+} ion available in the solution, as confirmed by Figure 4.10(b).

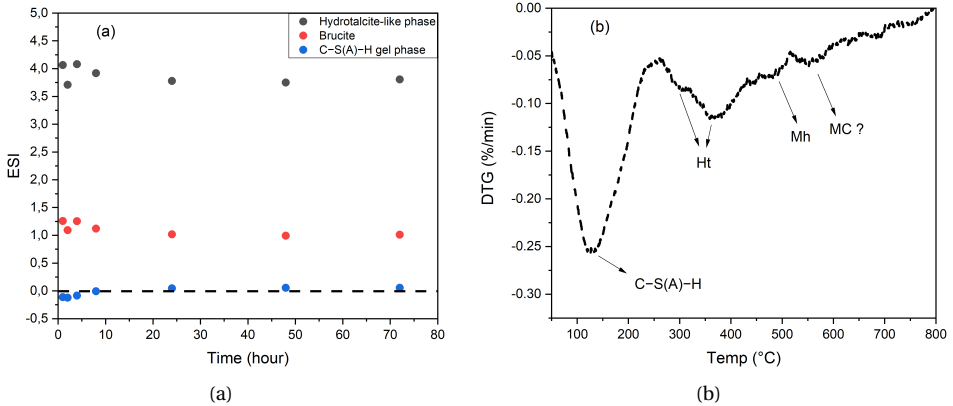


Figure 4.11: (a) Effective saturation indices of slag M8 as a function of dissolution time. A saturation index of 0.0 indicates an equilibrium state; (b) DTG result of the undissolved residual after dissolution test of seven days. Mh denotes $Mg(OH)_2$ (brucite) and MC denotes $MgCO_3$, which may be originated from the carbonation of Mh during sample preparation. Ht: hydrotalcite-like phase.

DISSOLUTION RATE

The dissolution rate (r_+) using Si^{4+} concentration as indicator was calculated based on the initial increase of Si^{4+} concentration (before 6 hours) as the following Equation 4.4 shows [16]:

$$r_+ = \frac{d(Si)}{\Delta t} \frac{v_{Si} V_{solution}}{mS} \quad (4.4)$$

Table 4.3: Dissolution rate of slag calculated based on the Si^{4+} concentration from dissolution test.

Slag	M0	M8	M16	A3	A3-1	A12	A18	CS1	CS2	S
Si^{4+} Dissolution rate $\times 10^{-8}$ (mol/m ² /s)	0.63	0.53	0.69	0.39	0.44	0.60	0.69	0.57	0.62	0.76

where v_{Si} represents the molar fraction of Si in raw slag, m designates the mass of slag sample (1.0 g), S corresponds to the initial specific surface area of slag measured by BET method (Table 4.1), and V_{solution} is the solution volume (1.0 L). Table 4.3 summarizes the dissolution rate calculated for all the slag samples. Based on effective saturation indices determined above, C-S(A)-H gel phase became supersaturated at different time. For comparison, data at 6 hours of dissolution was used for calculation. At this stage, the main driving force for dissolution was undersaturation degree and Si-bearing phase was still undersaturated for most slag samples.

Basically, the dissolution rates (Table 4.3) showed similar trend with regard to the Si^{4+} concentration at 3 days, namely higher MgO (slag M16) and Al_2O_3 (slag A18) contents led to a higher dissolution rate. In addition, the relatively high dissolution rate of slag M0 could be explained by its small specific surface area (Table 4.1). On the other hand, note that the solution started to be saturated from the beginning regarding Mg-bearing phases (brucite and hydrotalcite-like phase) as confirmed by effective saturation indices. Thus, more research is needed to figure out whether these precipitations have any impact on the release of Si from slag.

4.3.3. THE EFFECT OF SULFUR SPECIES IN COMMERCIAL SLAG

Sulfur content in slag is generally determined in the form of SO_3 by XRF. The presence of several forms of sulfur anions, such as S^{2-} , $\text{S}_2\text{O}_3^{2-}$ and SO_4^{2-} , has been reported in the leachates of hydrated cements containing slag [37–39]. Oxidation to the most stable product, i.e., SO_4^{2-} can take place by molecular oxygen at $\text{pH} > 8.5$, considering the alkaline and mildly reductive environment occurring in the pore solution of slag cement pastes [40]. In this chapter for the production of synthetic slag, the remelting process of commercial slag was under oxidizing condition (non-inert atmosphere), whereas the real commercial slag was produced under reducing condition. The oxidizing condition might modify the oxidation state of sulphur species in slag, most likely shifting it towards more oxidized species or straight-out volatilizing it. It explained the low SO_3 content detected in synthetic slags (Table 4.1).

As presented earlier in Figure 4.5(a), an additional peak or hump was observed in the model paste of commercial slag S after the main peak. To investigate this phenomenon, another commercial slag, S1 was introduced. Its chemical composition was determined in wt.% by XRF as; CaO: 37.97, SiO_2 : 35.6, Al_2O_3 : 13.12, MgO: 7.24, FeO/Fe₂O₃: 0.37, MnO/Mn₂O₃: 0.35, Na₂O: 0.31, SO_3 : 0.99, Residual: 4.05. The loss-on-ignition (LOI) determined by TGA under air environment at 950 ± 50 °C for commercial slag S and S1 was -0.87% and -1.27%, respectively. This value was -0.02% for synthetic slag M8. The negative LOI is related to the oxidation of sulfur rich species in slag when exposed to air. Slag M8, S and S1 had a similar chemical composition except the sulfur content. Note that the exact thermal history of commercial slag was unknown. The author received the

coarse-granulated slag S and S1 from Ecocem Benelux B.V. and milled them to a similar PSD to other synthetic slags subsequently.

Figure 4.12 illustrates the heat flow and cumulative heat release of model pastes of M8, S and S1 during 7 days' curing at 40 °C. As labelled (A), the additional peak was only observed right after the main peak for commercial slag S and S1 although the time of occurrence was slightly different. It was also evident that the curves of cumulative heat release overlapped with each other up to about 24 hours and deviated from then on as depicted in Figure 4.12(b). About 150 J/g slag more heat was released by commercial slag S and S1 compared with synthetic slag M8 after 7 days owing to the hump. Besides, when checked in TGA measurement as displayed in Figure 4.13, the peak at about 100 °C was more distinct in the model paste S and S1, and the amounts of portlandite remained in S and S1 pastes decreased compared with that of M8. Therefore, it is plausible to assume that the additional peak A originates from the precipitation of ettringite following the Equation 2.6

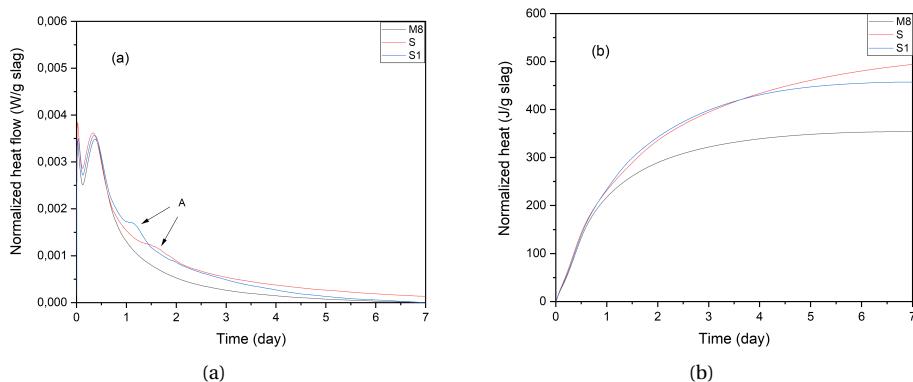


Figure 4.12: (a) Heat flow and (b) total heat release as a function of time from calorimetric measurement of model pastes curing for 7 days at 40 °C.

Considering the enthalpy of formation $\Delta_f H^0$ (-17535 kJ/mol [41]) of ettringite, it was calculated that $\sim 2.5 \times 10^{-3}$ g SO_4^{2-} /g slag participated in the reaction. It was reasonable as the oxidation of reduced sulfur species occurred when water was consumed and sufficient air entered the paste sample.

On the other hand, one needs to keep in mind that the above observation is based on a TGA peak that can be assigned to both C-S-H gel phase and ettringite. For a clearer attribution, evidence showing that the amount of ettringite (significantly) increases is preferred. Also, questions, e.g., why the sulfur species in slag is released only at a specific point after the main hydration peak, and the model paste already contains sulfate contributed by the potassium solution still remain unsolved. Therefore, more properties should be explored in the following studies such as the influence of minor elements, quenching rate, etc.

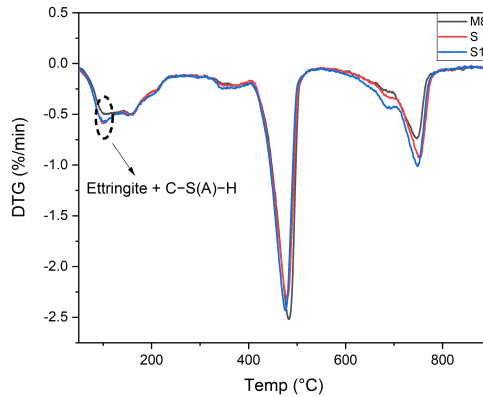


Figure 4.13: DTG analysis of model pastes curing for 7 days at 40 °C.

4.4. DISCUSSION

As mentioned, the reactivity of slag can be attributed to the network structure of glass. The more disordered and depolymerized a structure is, the more easily it can be broken up, and thus shows higher reactivity. The degree of depolymerization of a network structure can be represented by NBO/T, the number of non-bridging oxygen per tetrahedral network-forming element [42, 43]. In all slags investigated in this chapter, considering $\text{Al}_2\text{O}_3 < 0.5 \text{SiO}_2$ in molar ratio, Al should be regarded as network former existing only in-between SiO_4 tetrahedra in the form of Si-O-Al-O-Si (Loewenstein's rule of aluminum avoidance [44]), and the charge difference between AlO_4^{5-} and SiO_4^{4-} tetrahedra was balanced by Ca^{2+} and K^+ , in principle [45–47]. However, it can be seen that more heat was released from calorimetric measurement, more bound water was fixed in the hydrates, and higher concentration of Si was observed in the dissolution test with increasing Al_2O_3 content, in contrast to the values determined by NBO/T (Table 4.1).

Then, the author attempted to estimate the reactivity of slag through assessing its chemical composition from a new perspective, using a graphical method. The method classified the reactivity of slag into different regions based on their main oxide compositions. The slags located at each region presented *a similar performance* based on above tests. Additionally, the graph can explain the interaction among oxides of slag. It was based on a coordinate system of $(\text{CaO}/\text{SiO}_2)$ - $(\text{Al}_2\text{O}_3+\text{MgO})$ in weight percentage. The accuracy of this method was verified by the results of the current study.

In $(\text{CaO}/\text{SiO}_2)$ - $(\text{Al}_2\text{O}_3+\text{MgO})$ coordinate system of weight percentage as employed in Figure 4.14, the effect of Al_2O_3 and MgO was highlighted. The coordinate system could be divided into three regions following: $\text{Al}_2\text{O}_3+\text{MgO} < 15 \text{ wt.}\%$ as well as $15 < \text{Al}_2\text{O}_3+\text{MgO} < 25 \text{ wt.}\%$ & $\text{CaO}/\text{SiO}_2 < 0.9$ (Region I), $15 < \text{Al}_2\text{O}_3+\text{MgO} < 25 \text{ wt.}\%$ & $0.9 < \text{CaO}/\text{SiO}_2 < 1.1$ (Region II), and $\text{Al}_2\text{O}_3+\text{MgO} > 25 \text{ wt.}\%$ & $\text{CaO}/\text{SiO}_2 > 0.9$ (Region III). The position of a slag in each region corresponded to the reactivity determined based on cumulative heat release (Figure 4.5), chemically bound water (BW2, Figure 4.6), and Si^{4+} concentration (Figure 4.10(a)). For the detailed criteria used for these test methods to classify reactivity,

Table 4.4: Criteria used for different test methods to classify reactivity.

	Low	Medium	How
Cumulative heat release (J/g)	< 250 (A3-1, A3)	250-450 (M0, A12, M8, CS1, CS2)	> 450 (A18, M16)
Chemically bound water	< 0.10 (A3-1, A3)	0.10-0.13 (M0, A12, M8, CS1, CS2)	> 0.13 (A18, M16)
Si ⁴⁺ concentration (mg/L)	< 30.0 (A3-1, A3)	30.0-45.0 (M0, A12, M8, CS1, CS2)	> 45.0 (A18, M16)

please refer to Table 4.4. Region I involves slag with low Al₂O₃ and/or MgO contents showing low reactivity (A3-1, A3, and M0), while Region III represents slag with high Al₂O₃ and/or MgO contents presenting high reactivity (A18 and M16). For other slags, they are included in Region II with medium Al₂O₃ and/or MgO contents and medium reactivity (A12, M8, CS1, and CS2). In the present research, slag M0 was identified as low reactivity, as it was always located at the boundary of low and medium reactivity in different characterization methods.

Note that synthetic slag CS1 and CS2, the CaO/SiO₂ ratio of which is less than 1, are not frequently used in the industry. However, the negative effect of decreasing CaO/SiO₂ ratio on reactivity was compensated by high Al₂O₃ and MgO contents. The graphical method proposed is able to recognize reactive slags accurately while standard moduli can misinterpret their performance. For example, slag CS2 shows a relatively medium reactivity due to its high Al₂O₃ and MgO contents; however hydraulicity modulus of EN 15167-1 classifies this slag as insufficiently reactive through (CaO+MgO)/SiO₂ = 0.88 < 1.0. As for commercial slag S and S1, they can be classified as medium reactivity according to the graphic method proposed.

For the area covered with solid diagonal (Figure 4.14), it was undefined in the present research as there was no slag located at this region. Therefore, further research is deserved in the future to examine whether the continuous increasing in CaO content in slag can enhance the reactivity of slag to the level of slag M16 and A18 or not.

4.5. CONCLUSIONS

THIS chapter proposed a new insight on the influence of chemical composition on slag reactivity. The results obtained in this chapter can lead to formulating improved blast furnace slag compositions for better reactivity. The main conclusions were:

- The reactivity determined from calorimetric measurement and bound water content quantification of the model pastes containing synthetic slag, portlandite, limestone and alkaline solution followed similar tendency.
- According to the results of dissolution test with high liquid to solid ratio, Si⁴⁺ concentration and its dissolution rate supported the findings from the calorimetric measurements. Higher Al₂O₃ and MgO contents of slag led to a higher dissolution rate.
- The sulfur species in slag caused the additional peak in the model paste of commercial slag S and S1 in calorimetric measurements. It originated from the precipitation of ettringite. Therefore, when calorimetric measurement was used to assess the reactivity of slag, the effect of sulfur species must be taken into

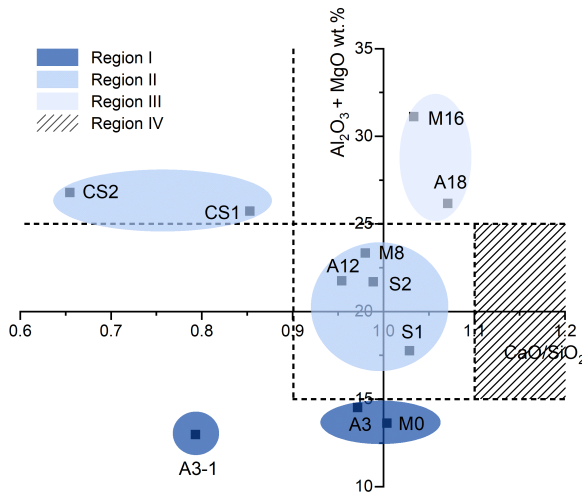


Figure 4.14: $(\text{CaO}/\text{SiO}_2)$ - $(\text{Al}_2\text{O}_3+\text{MgO})$ coordinate system in weight percentage. For the weight composition of these synthesized slags, please see data in Table 4.1. The origin of coordinate system represents slag containing CaO: 40%, SiO_2 : 40%, Al_2O_3 : 10%, MgO: 10% by mass, and this chemical composition of slag is most commonly seen in the industry.

consideration as even a small quantity of it can contribute to a large difference of cumulative heat release.

- A graphical method based on $(\text{CaO}/\text{SiO}_2)$ - $(\text{Al}_2\text{O}_3+\text{MgO})$ coordinate system in weight percentage, was proposed to estimate the reactivity of slag. It was also found that the adverse effect of decreasing CaO/SiO_2 ratio on reactivity can be compensated by higher Al_2O_3 and/or MgO contents, which can be recognized with the proposed graphical method.

REFERENCES

- [1] Y. Zhang, S. Zhang, Y. Chen, and O. Çopuroğlu, *The effect of slag chemistry on the reactivity of synthetic and commercial slags*, *Construction and Building Materials* **335**, 127493 (2022).
- [2] Y. Zhang, E. Schlangen, and O. Çopuroğlu, *Effect of slags of different origins and the role of sulfur in slag on the hydration characteristics of cement-slag systems*, *Construction and Building Materials* **316**, 125266 (2022).
- [3] J. Escalante, L. Gomez, K. Johal, G. Mendoza, H. Mancha, and J. Mendez, *Reactivity of blast-furnace slag in portland cement blends hydrated under different conditions*, *Cement and Concrete Research* **31**, 1403 (2001).
- [4] N. De Belie, M. Soutsos, and E. Gruyaert, *Properties of fresh and hardened concrete containing supplementary cementitious materials*, Vol. 25 (Springer, 2018).
- [5] S. Blotevogel, A. Ehrenberg, L. Steger, L. Doussang, J. Kaknics, C. Patapy, and M. Cyr, *Ability of the R3 test to evaluate differences in early age reactivity of 16 industrial*

- ground granulated blast furnace slags (GGBS)*, Cement and Concrete Research **130**, 105998 (2020).
- [6] P. T. Durdziński, R. Snellings, C. F. Dunant, M. B. Haha, and K. L. Scrivener, *Fly ash as an assemblage of model Ca–Mg–Na–aluminosilicate glasses*, Cement and Concrete Research **78**, 263 (2015).
- [7] A. Schöler, F. Winnefeld, M. B. Haha, and B. Lothenbach, *The effect of glass composition on the reactivity of synthetic glasses*, Journal of the American Ceramic Society **100**, 2553 (2017).
- [8] S. Kucharczyk, J. Deja, and M. Zajac, *Effect of slag reactivity influenced by alumina content on hydration of composite cements*, Journal of Advanced Concrete Technology **14**, 535 (2016).
- [9] S. Kucharczyk, M. Zajac, C. Stabler, R. M. Thomsen, M. Ben Haha, J. Skibsted, and J. Deja, *Structure and reactivity of synthetic CaO–Al₂O₃–SiO₂ glasses*, Cement and Concrete Research **120**, 77 (2019).
- [10] X. Li, R. Snellings, M. Antoni, N. M. Alderete, M. Ben Haha, S. Bishnoi, Ö. Cizer, M. Cyr, K. De Weerd, Y. Dhandapani, *et al.*, *Reactivity tests for supplementary cementitious materials: RILEM TC 267-TRM phase 1*, Materials and Structures **51**, 1 (2018).
- [11] F. Avet, X. Li, M. Ben Haha, S. A. Bernal, S. Bishnoi, Ö. Cizer, M. Cyr, S. Dolenc, P. Durdzinski, J. Haufe, *et al.*, *Report of RILEM TC 267-TRM phase 2: optimization and testing of the robustness of the R3 reactivity tests for supplementary cementitious materials*, Materials and Structures **55**, 1 (2022).
- [12] D. Londono-Zuluaga, A. Gholizadeh-Vayghan, F. Winnefeld, F. Avet, M. Ben Haha, S. A. Bernal, Ö. Cizer, M. Cyr, S. Dolenc, P. Durdzinski, *et al.*, *Report of RILEM TC 267-TRM phase 3: validation of the R3 reactivity test across a wide range of materials*, Materials and Structures **55**, 1 (2022).
- [13] R. D. Kalina, S. Al-Shmaisani, R. D. Ferron, and M. C. Juenger, *False Positives in ASTM C618 Specifications for Natural Pozzolans*, ACI MATERIALS JOURNAL **116** (2019).
- [14] J. Skibsted and R. Snellings, *Reactivity of supplementary cementitious materials (SCMs) in cement blends*, Cement and Concrete Research **124**, 105799 (2019).
- [15] R. Snellings, X. Li, F. Avet, and K. Scrivener, *Rapid, Robust, and Relevant (R3) Reactivity Test for Supplementary Cementitious Materials*, ACI MATERIALS JOURNAL **116** (2019).
- [16] R. Snellings and C. Jantzen, *Solution-Controlled Dissolution of Supplementary Cementitious Material Glasses at pH 13: The Effect of Solution Composition on Glass Dissolution Rates*, Journal of the American Ceramic Society **96**, 2467 (2013).

- [17] R. Snellings and G. Scherer, *Surface Chemistry of Calcium Aluminosilicate Glasses*, Journal of the American Ceramic Society **98**, 303 (2015).
- [18] K. C. Newlands, M. Foss, T. Matchei, J. Skibsted, and D. E. Macphee, *Early stage dissolution characteristics of aluminosilicate glasses with blast furnace slag- and fly-ash-like compositions*, Journal of the American Ceramic Society **100**, 1941 (2017).
- [19] K. Mills, L. Yuan, and R. Jones, *Estimating the physical properties of slags*, Journal of the Southern African Institute of Mining and Metallurgy **111**, 649 (2011).
- [20] B. O. Mysen, F. J. Ryerson, and D. Virgo, *The influence of TiO₂ on the structure and derivative properties of silicate melts*, American Mineralogist **65**, 1150 (1980).
- [21] Y. Sun, Z. Zhang, L. Liu, and X. Wang, *FTIR, Raman and NMR investigation of CaO–SiO₂–P₂O₅ and CaO–SiO₂–TiO₂–P₂O₅ glasses*, Journal of Non-Crystalline Solids **420**, 26 (2015).
- [22] G. H. Kim and I. Sohn, *Effect of Al₂O₃ on the viscosity and structure of calcium silicate-based melts containing Na₂O and CaF₂*, Journal of Non-Crystalline Solids **358**, 1530 (2012).
- [23] S. M. Han, J. G. Park, and I. Sohn, *Surface kinetics of nitrogen dissolution and its correlation to the slag structure in the CaO–SiO₂, CaO–Al₂O₃, and CaO–SiO₂–Al₂O₃ slag system*, Journal of non-crystalline solids **357**, 2868 (2011).
- [24] M. Whittaker, M. Zajac, M. Ben Haha, F. Bullerjahn, and L. Black, *The role of the alumina content of slag, plus the presence of additional sulfate on the hydration and microstructure of Portland cement-slag blends*, Cement and Concrete Research **66**, 91 (2014).
- [25] A. Schöler, B. Lothenbach, F. Winnefeld, and M. Zajac, *Hydration of quaternary portland cement blends containing blast-furnace slag, siliceous fly ash and limestone powder*, Cement and Concrete Composites **55**, 374 (2015).
- [26] S. Adu Amankwah, M. Zajac, C. Stabler, B. Lothenbach, and L. Black, *Influence of limestone on the hydration of ternary slag cements*, Cement and Concrete Research **100**, 96 (2017).
- [27] T. Matschei, B. Lothenbach, and F. P. Glasser, *The role of calcium carbonate in cement hydration*, Cement and concrete research **37**, 551 (2007).
- [28] S. Kucharczyk, M. Zajac, and J. Deja, *The influence of limestone and Al₂O₃ content in the slag on the performance of the composite cements*, Procedia Engineering **108**, 402 (2015).
- [29] M. B. Haha, B. Lothenbach, G. Le Saout, and F. Winnefeld, *Influence of slag chemistry on the hydration of alkali-activated blast-furnace slag — Part I: Effect of MgO*, Cement and Concrete Research **41**, 955 (2011).

- [30] W. Chen and H. Brouwers, *The hydration of slag, part 2: reaction models for blended cement*, Journal of Materials Science **42**, 444 (2007).
- [31] B. Kolani, L. Buffo-Lacarrière, A. Sellier, G. Escadeillas, L. Boutillon, and L. Linger, *Hydration of slag-blended cements*, Cement and Concrete Composites **34**, 1009 (2012).
- [32] E. Özbay, M. Erdemir, and H. İ. Durmuş, *Utilization and efficiency of ground granulated blast furnace slag on concrete properties—A review*, Construction and Building Materials **105**, 423 (2016).
- [33] B. Lothenbach, G. Le Saout, E. Gallucci, and K. Scrivener, *Influence of limestone on the hydration of Portland cements*, Cement and Concrete Research **38**, 848 (2008).
- [34] B. Lothenbach, *Thermodynamic equilibrium calculations in cementitious systems*, Materials and Structures **43**, 1413 (2010).
- [35] T. Matschei, B. Lothenbach, and F. P. Glasser, *Thermodynamic properties of Portland cement hydrates in the system $\text{CaO}-\text{Al}_2\text{O}_3-\text{SiO}_2-\text{CaSO}_4-\text{CaCO}_3-\text{H}_2\text{O}$* , Cement and Concrete Research **37**, 1379 (2007).
- [36] R. S. Karen Scrivener and B. Lothenbach, *A Practical Guide to Microstructural Analysis of Cementitious Materials* (CRC Press, New York, 2016).
- [37] F. P. Glasser, K. Luke, and M. Angus, *Modification of cement pore fluid compositions by pozzolanic additives*, Cement and Concrete Research **18**, 165 (1988).
- [38] A. Gruskovnjak, B. Lothenbach, L. Holzer, R. Figi, and F. Winnefeld, *Hydration of alkali-activated slag: comparison with ordinary Portland cement*, Advances in cement research **18**, 119 (2006).
- [39] B. Lothenbach, G. Le Saout, M. B. Haha, R. Figi, and E. Wieland, *Hydration of a low-alkali CEM III/B-SiO₂ cement (LAC)*, Cement and Concrete Research **42**, 410 (2012).
- [40] W. E. Kleinjan, A. de Keizer, and A. J. Janssen, *Kinetics of the chemical oxidation of polysulfide anions in aqueous solution*, Water Research **39**, 4093 (2005).
- [41] B. Lothenbach, T. Matschei, G. Möschner, and F. P. Glasser, *Thermodynamic modelling of the effect of temperature on the hydration and porosity of Portland cement*, Cement and Concrete Research **38**, 1 (2008).
- [42] D. Dutt, P. Higby, and D. Griscom, *A structural model for low silica content calcium aluminosilicate glasses*, Physics and chemistry of glasses **33**, 51 (1992).
- [43] A. Novatski, A. Steimacher, A. Medina, A. Bento, M. Baesso, L. Andrade, S. Lima, Y. Guyot, and G. Boulon, *Relations among nonbridging oxygen, optical properties, optical basicity, and color center formation in CaO-MgO aluminosilicate glasses*, Journal of Applied Physics **104**, 094910 (2008).
- [44] W. Loewenstein, *The distribution of aluminum in the tetrahedra of silicates and aluminates*, American Mineralogist **39**, 92 (1954).

- [45] C. I. Merzbacher, B. L. Sherriff, J. S. Hartman, and W. B. White, *A high-resolution ^{29}Si and ^{27}Al NMR study of alkaline earth aluminosilicate glasses*, *Journal of Non-Crystalline Solids* **124**, 194 (1990).
- [46] D. R. Neuville, L. Cormier, and D. Massiot, *Al coordination and speciation in calcium aluminosilicate glasses: Effects of composition determined by ^{27}Al MQ-MAS NMR and Raman spectroscopy*, *Chemical geology* **229**, 173 (2006).
- [47] D. Neuville, L. Cormier, V. Montouillout, and D. Massiot, *Local Al site distribution in aluminosilicate glasses by ^{27}Al MQMAS NMR*, *Journal of Non-Crystalline Solids* **353**, 180 (2007).

5

THE ROLE OF HYDROTALCITE-LIKE PHASE AND MONOSULFATE IN SLAG CEMENT PASTE DURING ATMOSPHERIC AND ACCELERATED CARBONATION

The aim of this chapter was to identify the carbonation products in the slag-rich cementitious systems (mainly CEM III/B) upon three different exposure conditions, namely, long term exposure in the field, indoor natural exposure, and accelerated carbonation testing. Emphasis was laid on the carbonation behaviors of hydrotalcite-like phase and monosulfate in particular. Additionally, the agreements and disagreements between experimental and thermodynamic modelling results were discussed. Overall, the results obtained in this chapter served as a basis for the studies conducted in following chapters, as they provided insight about the carbonation characteristics of slag-rich cement systems, especially with the involvement of hydrotalcite-like phase and monosulfate. The author believed that there was enough evidence indicating these two phases being the key components towards formulating blast furnace slag systems resistant to carbonation.

Parts of this chapter were published in *Cement and Concrete Composites* **132**, 104642 (2022) [1].

5.1. INTRODUCTION

BLAST furnace slag cement concrete is known to exhibit a high resistance to many chemical deterioration mechanisms such as alkali silica reaction, sulfate attack, and chloride ingress [2]. An exception is carbonation, which renders a poor microstructure at the skin area of slag-rich concrete [3].

As discussed in Chapter 2, much attention has been paid to the carbonation of portlandite and C-S-H gel phase in the past decades [4–7]. However, few investigations went deep into the carbonation of minor hydration phases, e.g., hydrotalcite-like phase (specific to slag-containing systems) and monosulfate. Yet, there were a number of questions that need to be addressed, e.g., moment of their reactions with CO₂, the corresponding carbonation products, etc. Additionally, there were continuous concerns about whether accelerated carbonation performed in the laboratory was capable of being representative of natural carbonation [8–11].

Hence, the aim of this chapter was to identify the carbonation products in the slag-rich cementitious systems (mainly CEM III/B) upon three different exposure conditions, namely, long term exposure in the field, indoor natural exposure, and accelerated carbonation testing. Emphasis was laid on the carbonation behavior of hydrotalcite-like phase and monosulfate in particular. Additionally, the agreements and disagreements between experimental and thermodynamic modelling results were discussed. Overall, the results obtained in this chapter served as a basis for the studies conducted in following chapters, as they provided insight about the carbonation characteristics of slag-rich cement systems, especially with the involvement of hydrotalcite-like phase and monosulfate. The author believed that there was enough evidence indicating these two phases being the key components towards formulating blast furnace slag systems resistant to carbonation.

5.2. MATERIALS AND METHODOLOGY

5.2.1. SAMPLE INFORMATION

IN Chapter 3, some slag concrete samples were collected from randomly chosen locations in the Netherlands. Four of them were employed in this chapter for analysis, i.e., sample A, B, C, and E. It was worthwhile to mention that sample E was drilled from beams above a tunnel, the surface of which suffered severe deterioration in the form of carbonation shrinkage and surface cracking. For other structures where sample A, B, and C were taken from, there was no visible damage on the surface.

For indoor natural exposure and accelerated carbonation testing performed in the laboratory, CEM I 42,5 N and two slag products (denoted as S2 provided by Ecocem Benelux B.V. and M16 synthesized in the lab) were employed to produce custom blended slag cement systems. Chemical compositions of the parent cement and slag S2 as determined by XRF are given in Table 5.1. For the composition of slag M16, please refer to Table 4.1. The Na₂O_{eq} employed for cement and slag (see Table 4.1) was identical, namely Na₂O+0.658*K₂O.

Table 5.1: Chemical compositions (wt.%) and physical properties of CEM I 42,5 N and slag S2.

	Cement	S2
CaO	64	39.91
SiO ₂	20	38.79
Al ₂ O ₃	5	10.94
MgO	-	6.82
FeO/Fe ₂ O ₃	3	0.31
TiO ₂	-	0.77
MnO/Mn ₂ O ₃	-	0.21
Na ₂ O _{eq}	0.58	0.60
SO ₃	2.93	1.40
Residual	4.49	0.16

5.2.2. EXPERIMENTAL METHODS

In the blended paste that was cast to be exposed to indoor natural carbonation and accelerated carbonation testing, the cement was partially replaced by slag at a constant substitution level of 70 wt.% to simulate CEM III/B. The water to binder (cement+slag) ratio was kept at 0.40. Paste specimens were prepared and cast in plastic containers of 20 mL, which were sealed with thin para film on the seal to prevent further ingress of CO₂ and evaporation of mixing water.

After 3 months of sealed curing, specimens were taken out of the plastic bottles, and the top surfaces (~5 mm thickness) were sawn off to obtain a microstructure that was relatively free of bleeding effect. Half of the slag S2 paste was exposed to the laboratory environment directly for 2 years before any measurement. For the slag M16 paste and the other half of slag S2 paste were exposed to elevated CO₂ level in an accelerated carbonation test chamber. Before moving into the carbonation chamber, pastes were kept one month in a RH-controlled climate chamber at 65% and 20 °C for preconditioning. Accelerated carbonation testing was performed in the carbonation chamber with a regulated CO₂ concentration of 3%±0.2, at 20±3 °C and 65±5% of RH (using saturated NaNO₂ solution). The carbonation exposure lasted up to 6 months.

To identify the phase assemblage evolution during carbonation, TGA and XRD were performed. Slices cut from the specimens were immersed in isopropanol solution, dried at 40 °C oven, ground and sieved below 63 μm grain size. XRD analysis was performed as explained in Section 4.2.2. TGA was carried out on a Netzsch STA 449 F3 Jupiter coupled with mass spectrometer (MS) Netzsch QMS 430 C under Argon atmosphere. For the detailed information, please refer to Section 4.2.3. Thanks to mass spectrometer, the emissions of H₂O and CO₂ from the samples after heating were thus confirmed. The area under the MS CO₂ curve was determined through a commercial software Origin Pro 2019 (peak integral). This value was served as an index to characterize the CO₂ binding degree of different phases in the investigated samples.

In addition, polished sections were prepared for the microanalysis. The sample preparation process was described in Section 3.2.2. All microanalysis was carried out at a working distance of 10 mm and an accelerating voltage of 10 kV, respectively. Phases in cement matrix and slag rims around unhydrated slag particles were characterized by EDS microanalysis with internal standard (standardless microanalysis).

5.3. RESULTS

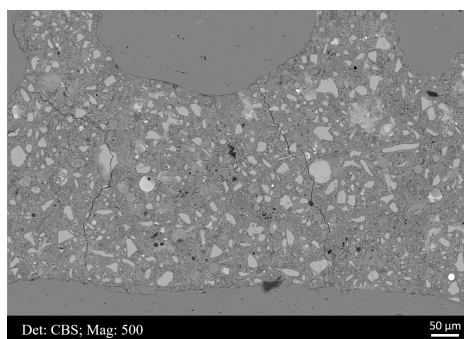
5.3.1. LONG TERM NATURAL EXPOSURE IN THE FIELD

SAMPLE WITH CARBONATION INDUCED DAMAGE

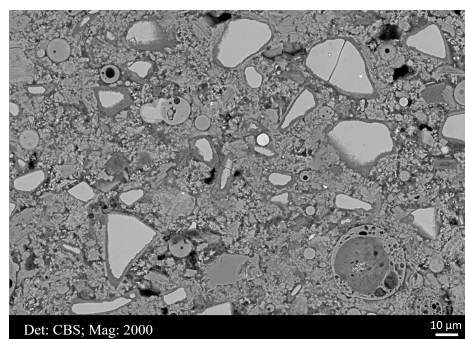
As described in Section 5.2.1, sample E was drilled from the beams above a tunnel, the surface of which suffered severe deterioration in the form of carbonation shrinkage and surface cracking. After phenolphthalein spraying, no color change was observed (Figure 5.1(a)), which implied that sample E had been carbonated fully. The typical BSE micrographs of the microstructure can be seen in Figure 5.1(b) and 5.1(c).



(a)



(b)



(c)

Figure 5.1: (a) Illustration of the color change after spraying sample E with phenolphthalein solution; (b) and (c) Two representative BSE micrographs of the microstructure of the sample.

As can be seen, two different types of C-S(A)-H gel phase were formed in the matrix of sample E, as revealed in Figure 5.2(a). After carbonation, C-S(A)-H gel phase started to decalcify and decompose up to a Si/Ca atomic ratio of around 1.50 eventually [6]. Besides, it was also noted that the Al/Si ratio of decalcified gel was significantly higher than that of uncarbonated C-S(A)-H gel phase, further confirming the occurrence of amorphous alumina gel along with carbonation [6].

As for hydrotalcite-like phase, its Mg/Al atomic ratio obtained from the slope of

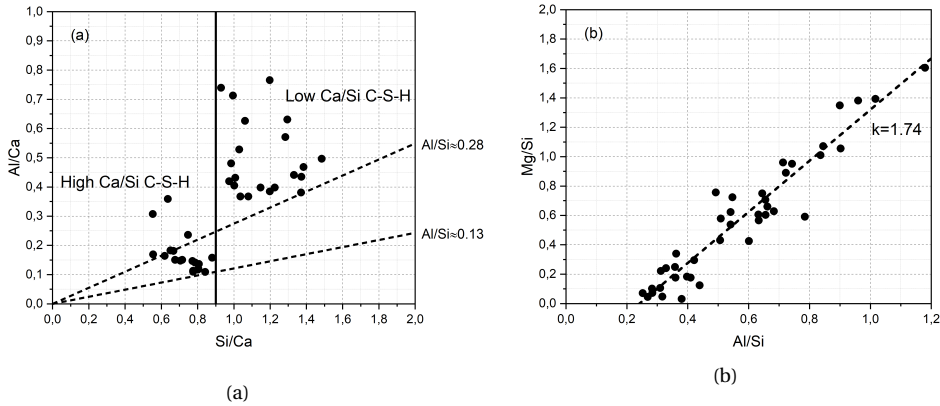


Figure 5.2: (a) Al/Ca vs. Si/Ca and (b) Mg/Si vs. Al/Si in the molar ratio of sample E.

regression line (Figure 5.2(b)) was still in the range commonly found in cement paste with high slag replacement [12], e.g., CEM III/B used in this case.

DTG results of sample E are shown in Figure 5.3. No doubt that the sample had been carbonated completely, and no trace of portlandite and monosulfate was observed. Three phases were left related to carbonation. The broad peaks after 500 °C indicated the presence of different forms of calcium carbonate [13–15]. It was consistent with the MS CO₂ curve, which confirmed that the mass loss after 500 °C was mainly originated from the CO₂ emission. The peak for C-S(A)-H gel phase (containing amorphous silica and alumina gel) at 100-150 °C was still pronounced. Most of the mass loss at this temperature range was sourced from dehydration, in the form of free water, physically bound, and/or chemically bound water. A small amount of CO₂ release was also noted here. It can be assigned to the formation of carbonated Ca-Al AFm phases partially accommodating carbonate species (amorphous or nano-crystalline), e.g., the carbonation of AFm-OH phase, AFm-SO₄ phase (or monosulfate), etc [16]. After heating, incorporated carbonate would be decomposed and release CO₂.

The broad peak located at approximately 350-450 °C implied the persistence of hydrotalcite-like phase after carbonation. Slag rims, where hydrotalcite-like phase was mainly concentrated, were still visible around unreacted slag particles as illustrated in Figure 5.1(c). It was in agreement with the EDS point analysis results shown in Figure 5.2(b). Additionally, it was found that both H₂O and CO₂ were released at this temperature range after heating.

SAMPLES WITHOUT CARBONATION INDUCED DAMAGE

As mentioned, there was no carbonation-related damage occurring on the surface of structures where sample A, B, and C were taken. Figure 5.4(a) illustrates the color change of sample C after spraying with phenolphthalein as an example (The top side was the surface exposed to the environment.). Although not clear, the pink color was still visible across the matrix. On the other hand, Figure 5.4(b)-5.4(d) show the microstructures of sample A, B, and C, respectively. Homogeneous and dense cement matrix, embedding

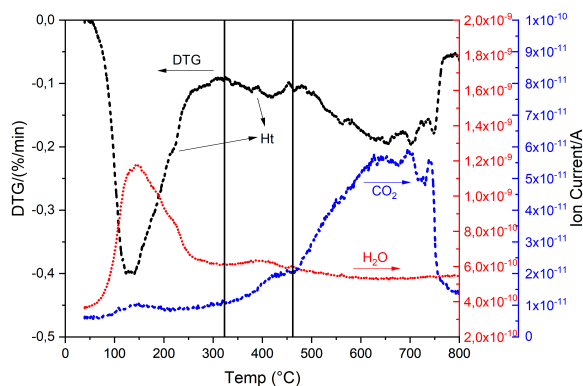


Figure 5.3: DTG results, H₂O and CO₂ MS curves of sample E. Ht: hydrotalcite-like phase.

anhydrous slag particles and few unhydrated cement grains were observed in these three slag concrete samples.

The elemental compositions of cement matrix of sample A, B, and C as characterized by EDS point analysis presented similar average Ca/Si atomic ratios fluctuating at around 1.0, although the Al/Si atomic ratios varied considerably (Figure 5.5). These measured Ca/Si atomic ratios agreed well with values reported in [12, 17, 18], further confirming that there was no decalcification of C-S(A)-H gel phase occurring in these samples.

On the other hand, a small amount of CO₂ was actually found to be diffused into these samples after a long service life (20~40 years). This process was slow and mild, far less severe compared with that happened in sample E. Figure 5.6(a)-5.6(c) present the DTG results, H₂O and CO₂ MS curves of samples A, B, and C, respectively. Compared with the results of sample E shown in Figure 5.3, both monosulfate and calcium hydroxide were detected in these samples, the H₂O releasing peaks of which were located at 150-200 °C and 400-500 °C, respectively. Calcium carbonate and carbonated hydrotalcite-like phase were the main CO₂-bearing phases. The formation of calcium carbonate was attributed to the reaction between CO₂ and calcium hydroxide, and/or C-S(A)-H gel phase. Meanwhile, CO₂ was also absorbed by hydrotalcite-like phase in the interlayer space originally occupied by water molecules. As shown in the MS curves, both H₂O and CO₂ were liberated from hydrotalcite-like phase after heating up to 350-450 °C. It was also noted that the small peak at 100-150 °C in the CO₂ MS curve, indicating the presence of carbonated Ca-Al AFm phases, was negligible. Thus, it can be concluded reasonably that these three samples were mildly carbonated (In the thesis, term “mildly carbonated area” was employed to represent the area exhibiting pink color after spraying with phenolphthalein. In fact, it presented a similar implication to term “non-carbonated area” commonly found in the literature.).

5.3.2. NATURAL EXPOSURE IN THE LABORATORY

Cement-slag S2 specimen was exposed in the laboratory (indoor) environment directly for 2 years before any measurement. Temperature and relative humidity were kept at

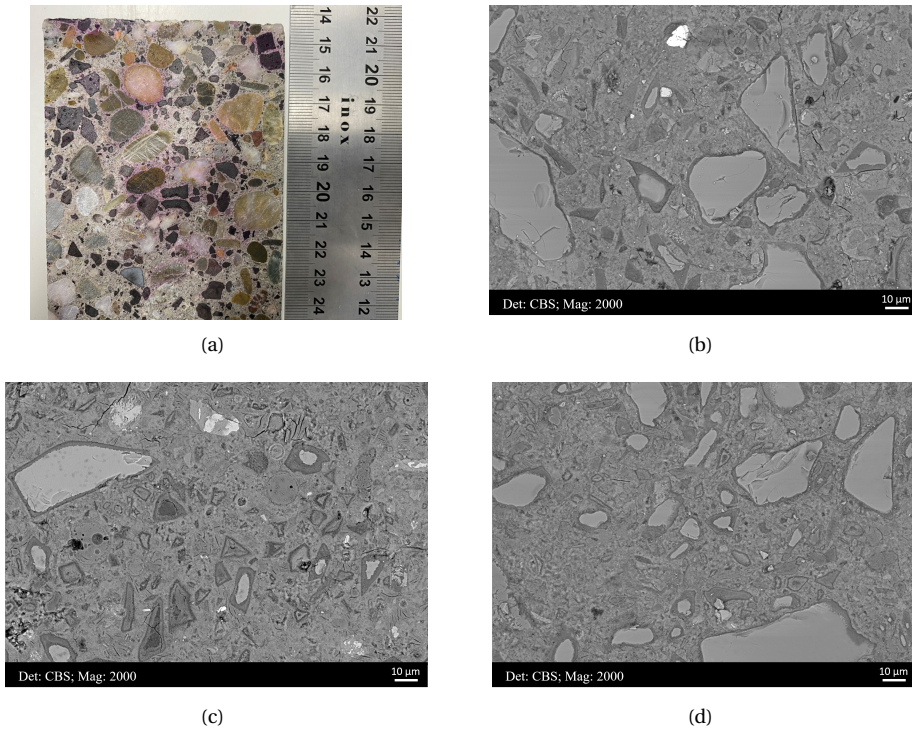


Figure 5.4: (a) Illustration of the color change after spraying sample C with phenolphthalein solution; Microstructure of sample (b) A; (c) B; and (d) C, respectively.

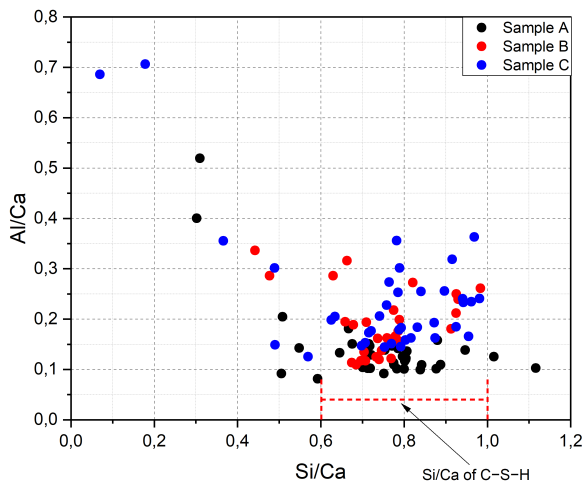
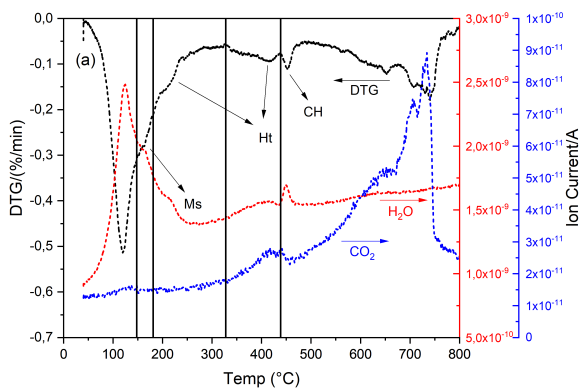
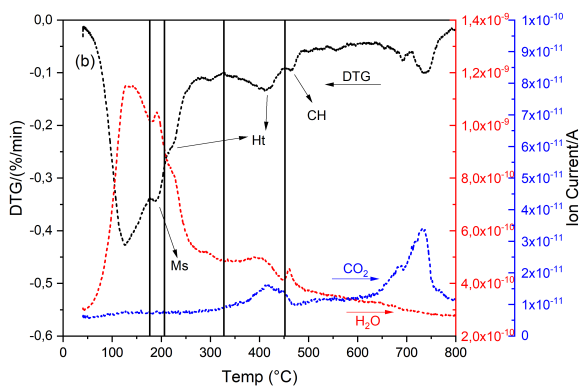


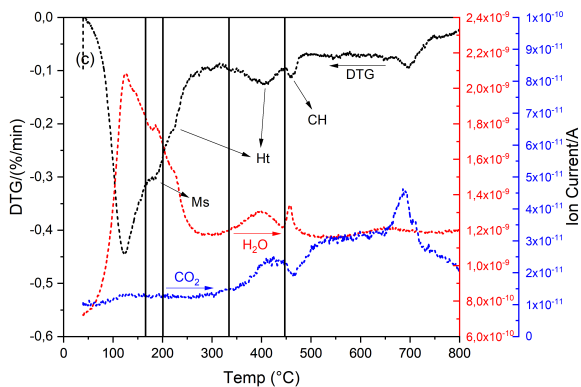
Figure 5.5: Atomic ratios of Al/Ca against Si/Ca of sample A, B, and C.



(a)



(b)



(c)

Figure 5.6: DTG results, H₂O and CO₂ MS curves of sample (a) A; (b) B; and (c) C, respectively. CH: portlandite; Ht: hydrotalcite-like phase; Ms: calcium monosulfoaluminate.

20 ± 5 °C and $50\pm 5\%$, respectively. A typical cross-sectional surface of the specimen before and after spraying with phenolphthalein is shown in Figure 5.7. Three different coloration zones corresponded roughly to carbonated (labelled as 1), transition (2), and mildly carbonated (3) zones due to the accompanied diffusion of CO_2 and O_2 . The green coloration of zone 3 was known to be originated from the formation of blue-green metal sulfides such as CaS, FeS, MnS etc. during hydration under anoxic conditions with the incorporation of sulfide in slag [19–21]. Therefore, little CO_2 and O_2 reached this region.

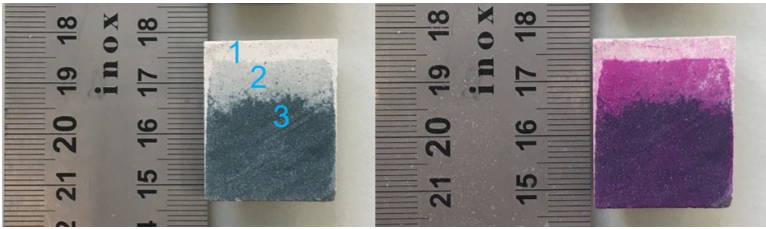


Figure 5.7: A typical sawn surface of cement-slag S2 paste after exposure in the laboratory for 2 years and the color change after spraying with phenolphthalein solution.

Cement matrix of the S2 paste experienced heavy degradation in the carbonated zone (Figure 5.8(a)). Micro-cracks and pores were widespread, especially for the micro-cracks, which were interconnected and even propagated into the transitional area (Figure 5.8(c)). In the mildly carbonated area (Figure 5.8(e)), there was no trace of micro-cracks, and the cement matrix was homogeneous and dense intermixed with unhydrated cement clinkers and slag particles.

The DTG results, H_2O and CO_2 MS curves of carbonated, transitional, and mildly carbonated areas are plotted in Figure 5.8(b), 5.8(d), and 5.8(f) respectively. In the carbonated area, no monosulfate was detected, while calcium hydroxide still persisted, although far less compared to mildly carbonated area. C-S(A)-H gel phase suffered heavy decalcification as revealed by the BSE image (Figure 5.8(a)). The main CO_2 -bearing phases in this area were calcium carbonate, sourcing from the reaction between CO_2 and calcium hydroxide as well as C-S(A)-H gel phase. Hydrotalcite-like phase was also carbonated as confirmed by the increase in the ion current intensity of CO_2 at ~ 250 °C and 350–450 °C.

In the transitional area, monosulfate became visible. The amount of calcium hydroxide here was also reduced compared with that in the mildly carbonated area. Overall, the situation here was nearly the same as that in the mildly carbonated area where much less CO_2 penetrated. Note that the scale of y-axis indicating the ion current of CO_2 release was different in Figure 5.8(b), 5.8(d), and 5.8(f).

Figure 5.8(g) illustrates the XRD scans of carbonated, transitional, mildly carbonated, and fully carbonated (accelerated carbonation, see Section 5.3.3) areas of the paste. In agreement with the results measured by TGA, hydrotalcite-like phase was detected in each area. The peak intensity of portlandite reduced from mildly carbonated to carbonated area, and it disappeared in the fully carbonated area. Monosulfate was not visible in carbonated and fully carbonated areas, also consistent

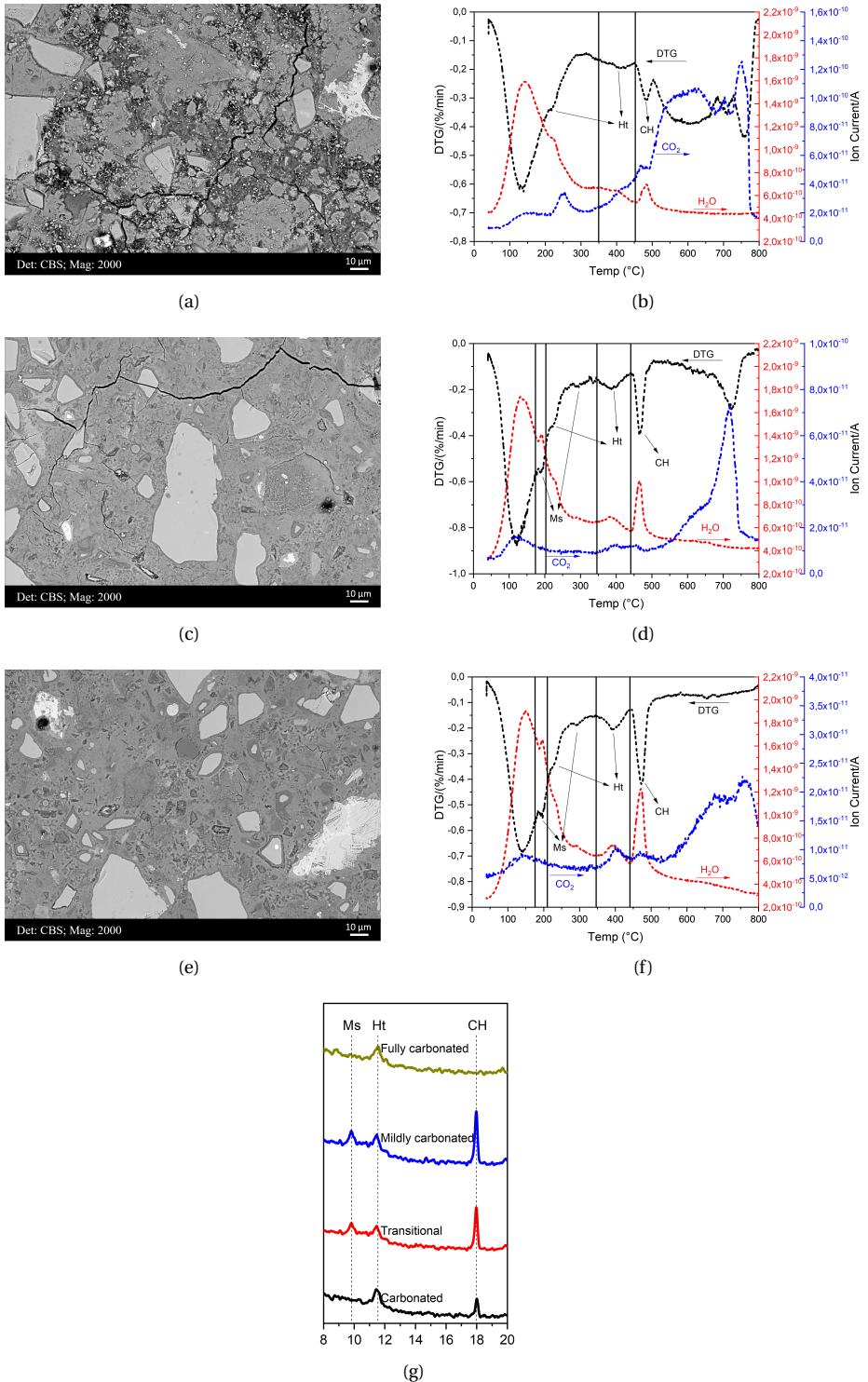


Figure 5.8: Microstructures of (a) carbonated; (c) transitional; and (e) mildly carbonated areas of cement-slag S2 paste. The DTG results, H₂O and CO₂ MS curves of the corresponding areas were plotted in (b), (d), and (f) respectively. (g) XRD scans of carbonated, transitional, mildly carbonated, and fully carbonated (from accelerated carbonation, see Section 5.3.3) areas of the paste. CH: portlandite; Ht: hydrotalcite-like phase; Ms: calcium monosulfaluminate.

with the TGA results.

The main decomposition peak of hydrotalcite-like phase (350-450 °C) gradually became broader from mildly carbonated to carbonated zone. On the one hand, it had been verified that hydrotalcite-like phase had been carbonated, and part or all of hydroxide was replaced by CO_3^{2-} ion, which would change the interlayer distance of hydrotalcite-like phase (d-spacing $d(003)$) [22–24], thus modifying its decomposition peak present in the DTG curve. On the other hand, slag rims, where hydrotalcite-like phase was concentrated, were surrounded by different external environments due to the carbonation of cement matrix (Figure 5.9(a)). For example, the cement matrix surrounding the slag particle displayed in circle #2 remained intact, and slag rim was thus not affected by the CO_2 attack. However, C-S(A)-H gel phase close to the slag particles shown in circles #1 was degraded remarkably, and became very porous. It can be ascribed to the formation of poorly organized silica gel of a low molar volume and the resulted shrinkage. The pore solution filling in these pores might partially dissolve hydrates precipitated at the rims of slag grains and alter the decomposition peak of hydrotalcite-like phase as a result. However, according to the scatter plot of Mg/Si vs. Al/Si, the Mg/Al atomic ratio of hydrotalcite-like phase in the carbonated and mildly carbonated areas did not vary significantly (Figure 5.9(b)).

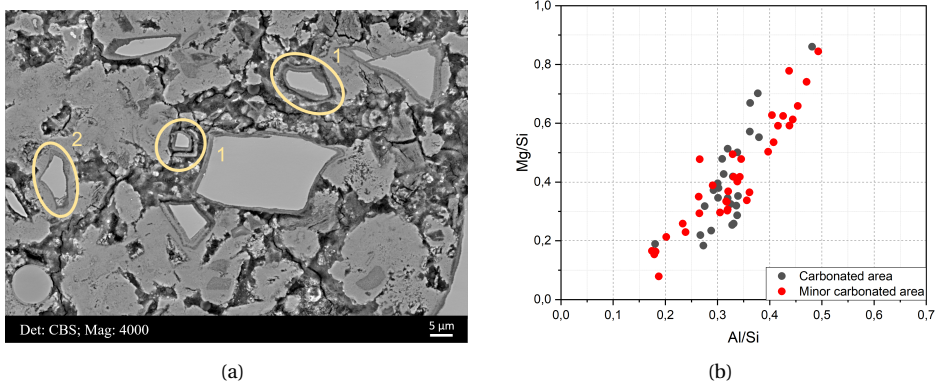


Figure 5.9: (a) A typical BSE micrograph of the carbonated S2 paste; (b) EDS point analysis of Mg/Si vs. Al/Si in the molar ratio of carbonated and mildly carbonated areas of slag S2 paste.

5.3.3. ACCELERATED CARBONATION TEST

At the same time, accelerated carbonation test was performed on cement-slag S2 and M16 paste specimens in the carbonation chamber regulated by a CO_2 concentration of $3\% \pm 0.2$, at 20 ± 3 °C and $65 \pm 5\%$ of RH.

The phase assemblages in the (nearly) fully carbonated zone of cement-slag S2 paste under accelerated carbonation (Figure 5.10) was similar to that formed under natural exposure in the laboratory (Figure 5.8(b)), except that there was no calcium hydroxide left due to a higher degree of carbonation in the former. Thus, more CO_2 , indicated by the higher ion current, was released from the decomposition of calcium carbonate

under accelerated carbonation test. As for mildly carbonated area, negligible difference was found between these two carbonation regimes.

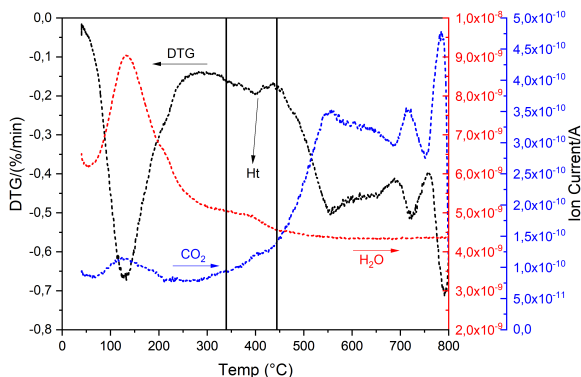


Figure 5.10: The DTG results, H₂O and CO₂ MS curves of fully carbonated area of cement-slag S2 paste exposed to accelerated carbonation. Ht: hydrotalcite-like phase.

5

Figure 5.11(a) displays the color change of a representative slag M16 sample after accelerated carbonation test with phenolphthalein solution. Apparently, the top part (approximately 8 mm) had been carbonated completely, thus presenting a colorless appearance with phenolphthalein solution. On the contrary, the bottom part exhibited a pink color and corresponded to mildly carbonated area roughly. Figure 5.11(b) exhibits the XRD results of fully and mildly carbonated areas of the sample. The peak for monosulfate and portlandite disappeared in the fully carbonated area, while hydrotalcite-like phase still persisted after such a heavy CO₂ attack, the peak of which was located at ~11°. On the other hand, the DTG results of these two areas are plotted in Figure 5.11(c) and 5.11(d), respectively. In the fully carbonated area, neither monosulfate nor calcium hydroxide was observed. The main CO₂-bearing phases in this area were calcium carbonate, carbonated hydrotalcite-like phase and Ca-Al AFm phases. In the mildly carbonated area, monosulfate and calcium hydroxide became visible.

5.4. DISCUSSION

5.4.1. THE ROLE OF HYDROTALCITE-LIKE PHASE AND MONOSULFATE DURING CARBONATION

THE results showed that different exposure environments did not change the type of carbonation products of slag cement paste, fundamentally. However, the overall carbonation sequence of hydration products identified in the slag cement paste was hard to distinguish. Considering the mildly carbonated area as the representative for the initial carbonation stage, irrespective of the exposure conditions, the carbonation of portlandite, C-S(A)-H gel phase, hydrotalcite-like phase and monosulfate appeared to progress simultaneously (Figure 5.6(a)-5.6(c), 5.8(f), 5.11(d)). Initially, the reaction rate between CO₂ and portlandite is more rapid than the carbonation of C-S-H gel phase [25]. Because C-S(A)-H gel phase was the most abundant Ca-bearing phase in the

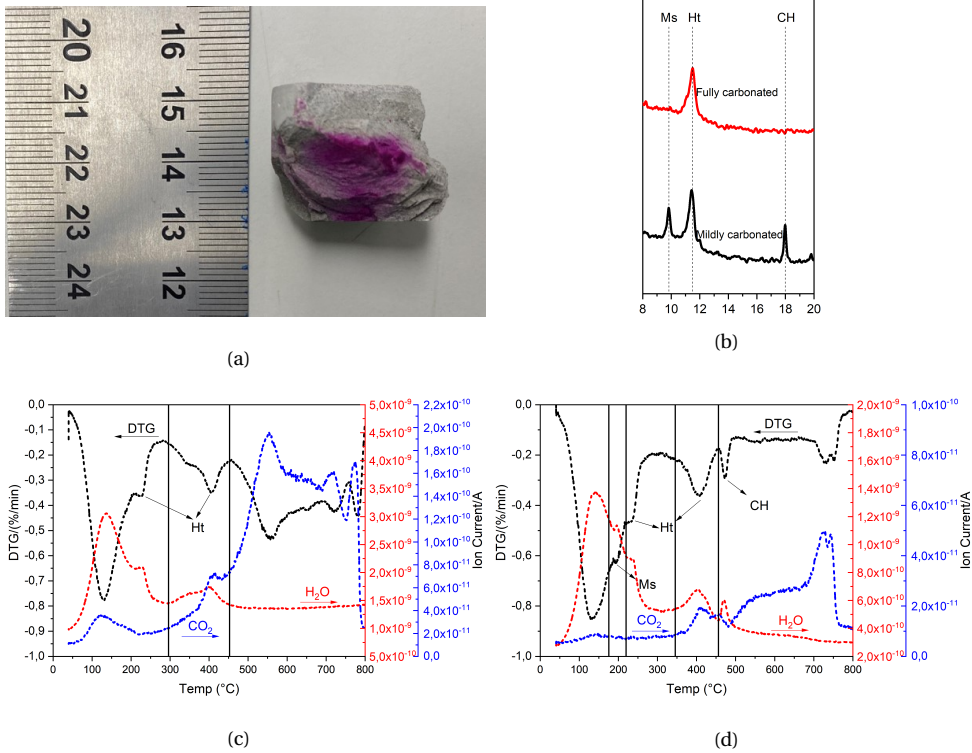


Figure 5.11: (a) Illustration of the color change of a representative slag M16 sample after accelerated carbonation test with phenolphthalein solution; (b) XRD results of fully and mildly carbonated areas of the sample; The DTG results, H₂O and CO₂ MS curves of (c) fully and (d) mildly carbonated areas of the sample. CH: portlandite; Ht: hydrocalcite-like phase; Ms: calcium monosulfoaluminate.

hydrated matrix, it was reasonable to postulate that the reaction between CO₂ and calcium hydroxide as well as C-S(A)-H gel began synchronously. Meanwhile, a small amount of CO₂ was absorbed into carbonated hydrotalcite-like phase and Ca-Al AFm phases in the mildly carbonated area. Especially for sample A, B, and C, hydrotalcite-like phase was the secondary CO₂-bearing phase while monosulfate seemed to be unaffected at this stage or in the corresponding area.

In the (fully) carbonated areas, or the areas that suffered heavy CO₂ attack of all exposure regimes studied, no monosulfate clusters were observed (Figure 5.3, 5.8(b), 5.10, and 5.11(c)). However, this cannot be evidence for monosulfate to be the first to react with CO₂, as concluded in [26]. It was more plausible to suggest that the nonexistence of monosulfate was due to its small amount produced after hydration. Therefore, it would be consumed at first under continuous CO₂ attack. From this aspect, calcium monosulfoaluminate can be seen as an indicator to evaluate the degree of carbonation (damage). In other words, detecting monosulfate phase should mean that the system may still have sufficient Ca budget to carbonate; however, lack of monosulfate indicates that the carbonation degree has reached a certain value, accompanied by a coarser pore structure and degradation of micromechanical properties.

The works in [27] concluded that monosulfate carbonation led to the formation of calcium carbonate, gibbsite and gypsum, which caused a net volume reduction. The migration of element sulfur from carbonated to uncarbonated area was also verified by pore solution analysis [28] and EDS mapping [29]. Meanwhile, the results in [26] showed that monosulfate- and hemicarbonates-AFm phases, if present, would be destabilized to monocarbonate-AFm, initially. However, no calcium hemi- or mono-carboaluminate was observed as a monosulfate-based carbonation product in this study. On the other hand, a small amount of CO₂ release was noted at 100-150 °C in all investigated samples. The authors assigned it to the formation of carbonated Ca-Al AFm phases, originated from the carbonation of AFm-OH and/or AFm-SO₄. Similar to hydrotalcite-like phase, AFm-OH and AFm-SO₄ phases formed in cement-based materials do also present a double-layer structure [30], which provides a site for CO₂ absorption. The work in [16] also confirmed that monosulfate can absorb CO₂, forming sulfate and carbonate monosulfate solid solution. Nonetheless, we cannot exclude the possibility that some CO₂ can also be adsorbed by C-S(A)-H gel phase and released after heating to this temperature range. However, note that sample powders employed for thermogravimetric analysis was immersed in isopropanol solution for one week before any measurements. Carbonate ions which were weakly absorbed by the gel would be exchanged out. Additionally, if carbonated Ca-Al AFm phases were the carbonation products of monosulfate, partial replacement of SO₄²⁻ by CO₃²⁻ ion would not change the volume of AFm phases significantly [31].

The existence of portlandite in the carbonated area was dependent on the carbonation degree or the extent of CO₂ attack. At the end of the accelerated carbonation testing, hardly any calcium hydroxide was left (Figure 5.10 and 5.11(c)), whereas under natural exposure (Figure 5.8(b)), a small amount of portlandite was detected although C-S(A)-H gel phase did suffer severe degradation, as well. This situation has been commonly reported in naturally carbonated samples [32, 33].

Specific to slag-rich pastes, hydrotalcite-like phase is the main precipitation within the rim of slag. At atomic level, hydrotalcite-like phase is also referred to as LDHs, and the interlayer space between the stacked layers enables it strong ion exchange ability, including CO₂ [34–36]. In the well-functioned field sample A, B, and C, carbonated hydrotalcite-like phase was the main CO₂-bearing phase only next to calcium carbonate. Similar observations were made in the mildly carbonated area of slag S2 and M16 pastes. Furthermore, it was found that the CO₂ content fixed within the hydrotalcite-like phase was associated with the amount of hydrotalcite-like phase produced during slag hydration. This argumentation was plausible as the greater the amount of hydrotalcite-like phase, the more interlayer space to accommodate CO₂. During the accelerated carbonation testing of slag M16 paste specimen, due to its high MgO content, more hydrotalcite-like phase was produced after hydration than that of slag S2 paste. As a result, a significant peak occurred in the CO₂ MS curve (Figure 5.11(c)) at 350-450 °C, implying an intense release of CO₂ from carbonated hydrotalcite-like phase.

C-S-H gel phase decomposes into Ca-modified silica gel, liberates a large amount of free water, and thus leads to a coarser of pore structure. Our observations suggested that unlike C-S(A)-H gel phase, hydrotalcite-like phase can remain intact during carbonation, which was in line with the results of Zajac et al. [37]. The scatter plot of at. Mg/Si vs. at. Al/Si of carbonated and mildly carbonated areas (Figure 5.9(b)) indicated that the Mg/Al atomic ratio of hydrotalcite-like phase in these two areas did not vary significantly. Thus, it can be theorized that hydrotalcite-like phase can delay the continuous carbonation of C-S(A)-H gel phase; and the larger it is produced, the greater carbonation resistance of slag cement paste.

5.4.2. DEGREE OF CO₂ BINDING OF DIFFERENT PHASES UNDER DIFFERENT EXPOSURE ENVIRONMENT

In the thesis, the author defined the degree of CO₂ binding of a phase as the area under the CO₂ MS curve between a corresponding temperature range. In Figure 5.12, slag M16 specimen was used as an example to quantify the degree of CO₂ binding after the accelerated carbonation testing. The areas A1, A2, and A3 corresponded to certain amounts of CO₂ liberated from the carbonated Ca-Al AFm phases, carbonated hydrotalcite-like phase, and calcium carbonate, respectively.

It is well accepted that calcium carbonate exist in several polymorphs after carbonation. They start to decompose from ~500 °C and the decomposition peaks overlap with each other noticeably [13–15]. However, the exact polymorphs of calcium carbonate were not the concern here, and the simultaneous presence of these polymorphs did not affect the determination of total CO₂ bound in calcium carbonate. As for carbonated hydrotalcite-like phase, it releases CO₂ at 250-450 °C, and an apparent decomposition peak is noted in this temperature range [38, 39]. Fortunately, no other phases released CO₂ within this range in the carbonated slag cement sample.

As observed from the CO₂ MS curve of all investigated samples, there was no fundamental change of the CO₂-bearing phases in slag cement paste after carbonation. The calculated area under MS CO₂ curve and the corresponding proportion of different carbonate phases in all investigated samples is given in Table 5.2. Portlandite and

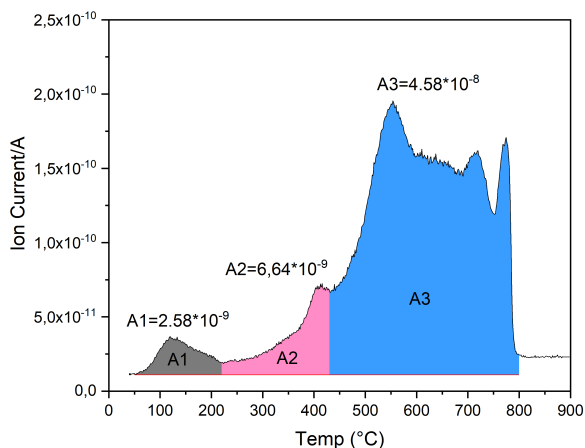


Figure 5.12: The CO₂ MS curve of slag M16 cement paste after accelerated carbonation, and the integrated areas under the curve with respect to different carbonate phases.

5

C-S(A)-H gel phases were the main CO₂-bearing phases, and their carbonation products were calcium carbonate of different forms. Hydrotalcite-like phase and monosulfate also fixed a certain amount of CO₂, forming carbonated hydrotalcite-like phase and carbonated Ca-Al AFm phases, respectively.

When shifting from mildly carbonated area to fully carbonated area, the absolute amount of CO₂ absorbed by each phase increased, correspondingly. However, the proportion of CO₂ absorbed into carbonated Ca-Al AFm phases appeared to level off, fluctuating at less than 5% except that in the mildly carbonated area of slag S2 paste. The MS measurements showed that the ratio varied between the carbonated hydrotalcite-like phase and calcium carbonate considerably (Figure 5.13). Regardless the exposure conditions and chemistry of raw materials, more than 20% CO₂ entered into carbonated hydrotalcite-like phase as well as Ca-Al AFm phases in the mildly carbonated area, and the involved reactions were harmless without any detrimental effect on cement matrix, as discussed above. However, more than 80% CO₂ reacted with portlandite and C-S(A)-H gel phase in the fully carbonated area, leading to a coarser pore structure with connected micro-cracks throughout the matrix.

The ratio of CO₂ bound in different carbonate phases from mildly carbonated area to fully carbonated area depicted a different image about the carbonation sequence in slag cement paste. Initially, all hydration products of slag cement, including monosulfate, hydrotalcite-like phase, portlandite, and C-S(A)-H gel phase acted as CO₂ sink. The role of hydrotalcite-like phase should be addressed here. Due to its crystal structure, the interlayer space, presenting a large specific surface area comparable to that of C-S-H gel phase [40], was the natural site to fix free CO₂ molecules [22, 24]. It absorbed more than 15% CO₂ at the beginning. With the continuous supply of CO₂ externally, monosulfate was consumed at first due to its small amount, transforming into carbonated Ca-Al AFm phases. In all exposure conditions, carbonated Ca-Al AFm phases bound around 5% of the entire CO₂ fixed within the matrix.

Table 5.2: The calculated areas under MS CO₂ curve and the corresponding proportions of different carbonate phases.

		Area under the MS CO ₂ curve			Total
		Carbonated Ca-Al AFm phases	Carbonated hydroxalcalite-like phase	Calcium carbonate	
Mildly carbonated	Sample A (Figure 5.6(a))	4.93*10 ⁻¹⁰	1.94*10 ⁻⁹	1.07*10 ⁻⁸	1.32* ⁻⁸
	Sample B (Figure 5.6(b))	2.04*10 ⁻¹⁰	1.29*10 ⁻⁹	3.38*10 ⁻⁹	4.87*10 ⁻⁹
	Sample C (Figure 5.6(c))	3.51*10 ⁻¹⁰	1.82*10 ⁻⁹	6.91*10 ⁻⁹	9.08*10 ⁻⁹
	S1 (Figure 5.8(f))	3.87*10 ⁻¹⁰	6.80*10 ⁻¹⁰	3.20*10 ⁻⁹	4.27*10 ⁻⁹
	S2 (Figure 5.11(d))	3.68*10 ⁻¹⁰	1.59*10 ⁻⁹	6.47*10 ⁻⁹	8.43*10 ⁻⁹
Fully carbonated	Sample D (Figure 5.3)	4.17*10 ⁻¹⁰	1.62*10 ⁻⁹	1.30*10 ⁻⁸	1.51*10 ⁻⁸
	S1 (Figure 5.10)	3.28*10 ⁻⁹	3.99*10 ⁻⁹	8.10*10 ⁻⁸	8.83*10 ⁻⁸
	S2 (Figure 5.11(c))	2.58*10 ⁻⁹	6.64*10 ⁻⁹	4.58*10 ⁻⁸	5.50*10 ⁻⁸
		CO ₂ binding share of each carbonate phase (%)			
		Carbonated Ca-Al AFm phases	Carbonated hydroxalcalite-like phase	Calcium carbonate	
Mildly carbonated	Sample A	3.75	14.77	81.48	
	Sample B	4.19	26.47	69.34	
	Sample C	3.87	20.04	76.09	
	S1	9.07	15.94	74.99	
	S2	4.37	18.87	76.76	
Fully carbonated	Sample D	2.76	10.73	86.51	
	S1	3.72	4.52	91.76	
	S2	4.69	12.07	83.24	

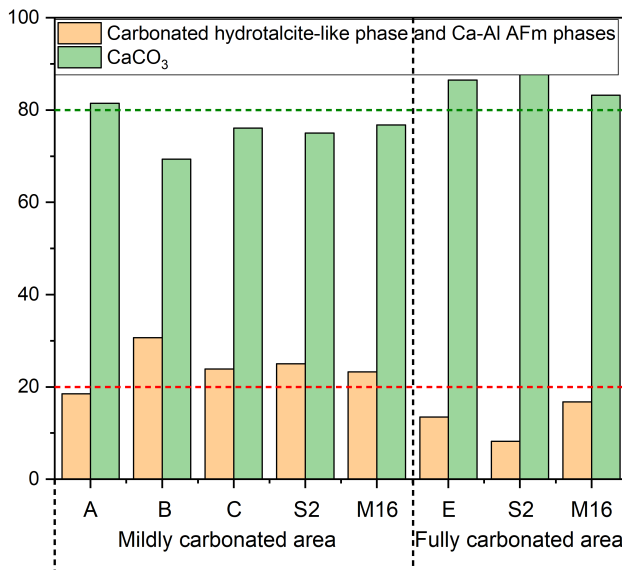


Figure 5.13: The ratio of CO₂ bound in CaCO₃ and carbonated hydroxalcalite-like plus Ca-Al AFm phases of investigated samples.

The thermogravimetric analysis showed that portlandite was able to persist longer than monosulfate (Figure 5.8(b)) although, the amount of portlandite produced at such a high slag replacement was close to monosulfate. The reaction between CO₂ and portlandite is kinetically rapid [25]; however, calcium carbonate mainly nucleates and grows on the surface of portlandite, slowing down its further reaction with CO₂ [41].

With the proceeding of carbonation when monosulfate and/or portlandite had already been consumed, hydrotalcite-like phase continued exchanging CO₂ with hydroxide and water molecules that were originally positioned in the interlayer space. Likely due to its capacity to absorb CO₂, the CO₂ share of hydrotalcite-like with respect to the entire bound CO₂ dropped to around 10% in the fully carbonated area. As confirmed earlier, hydrotalcite-like phase can maintain its network structure during carbonation and does not contribute to the pore structure coarsening. This is especially important for slag cement paste as pore structure/porosity plays a key factor to control the penetration of CO₂. Ultimately, the CO₂ entering the matrix can only be bound by calcium from C-S(A)-H gel phase. This process was not the topic of the thesis; the readers could refer to [4–7] if interested.

5.5. CONCLUSIONS

THIS chapter observed the carbonation products of slag-rich cement paste from three aspects, i.e., long term exposure in the field, natural indoor exposure, and accelerated carbonation testing, and laid emphasis on the carbonation of hydrotalcite-like phase and monosulfate, particularly. Overall, mineralogy of the carbonation products was found to be similar under different exposure environments. The main conclusions drawn were as follows:

- In the fully carbonated area, no monosulfate and calcium hydroxide was observed. The main CO₂-bearing phases in this area were calcium carbonate, carbonated hydrotalcite-like phase and Ca-Al AFm phases. In the mildly carbonated area, monosulfate and calcium hydroxide were detected again. Calcium carbonate was the main CO₂-bearing phase, and a small amount of CO₂ was absorbed into hydrotalcite-like phase.
- With the continuous supply of CO₂, monosulfate would be consumed at first. From this aspect, the nonexistence of calcium monosulfoaluminate can be treated as an indicator of potential carbonation-related damage. Furthermore, neither hemi- nor mono-carboaluminate was identified under the exposure conditions studied.
- Carbonated hydrotalcite-like phase was the *secondary* CO₂-bearing phase next to calcium carbonate. It was structurally resistant against carbonation. The Mg/Al atomic ratios of hydrotalcite-like phase in the carbonated and mildly carbonated areas did not vary significantly.
- In all the exposure conditions studied, carbonated Ca-Al AFm phases bound around 5% of the entire bound CO₂ in the matrix. Hydrotalcite-like phase fixed more than 15% CO₂ at the beginning. However, this value decreased to around

10% by full carbonation. Therefore, more than 20% CO₂ was fixed by hydrotalcite-like phase as well as Ca-Al AFm phases at first, and these reactions were harmless without any detrimental effect on cement matrix.

REFERENCES

- [1] Y. Zhang and O. Çopuroğlu, *The role of hydrotalcite-like phase and monosulfate in slag cement paste during atmospheric and accelerated carbonation*, *Cement and Concrete Composites* **132**, 104642 (2022).
- [2] R. B. Polder, T. Nijland, and M. de Rooij, *Blast furnace slag cement concrete with high slag content (CEM III/B)–experiences with the durability in the netherlands since the 1920's*, NPRA report SVV **270**, 72 (2014).
- [3] V. G. Papadakis, *Effect of supplementary cementing materials on concrete resistance against carbonation and chloride ingress*, *Cement and Concrete Research* **30**, 291 (2000).
- [4] J. J. Chen, J. J. Thomas, H. F. Taylor, and H. M. Jennings, *Solubility and structure of calcium silicate hydrate*, *Cement and Concrete Research* **34**, 1499 (2004).
- [5] A. E. Morandau and C. E. White, *In situ X-ray pair distribution function analysis of accelerated carbonation of a synthetic calcium–silicate–hydrate gel*, *Journal of Materials Chemistry A* **3**, 8597 (2015).
- [6] T. F. Sevelsted and J. Skibsted, *Carbonation of C–S–H and C–A–S–H samples studied by ¹³C, ²⁷Al and ²⁹Si MAS NMR spectroscopy*, *Cement and Concrete Research* **71**, 56 (2015).
- [7] B. Wu and G. Ye, *Study of carbonation rate of synthetic CSH by XRD, NMR and FTIR*, *Heron* **64**, 21 (2019).
- [8] M. Castellote, L. Fernandez, C. Andrade, and C. Alonso, *Chemical changes and phase analysis of OPC pastes carbonated at different CO₂ concentrations*, *Materials and Structures* **42**, 515 (2009).
- [9] N. Hyvert, A. Sellier, F. Duprat, P. Rougeau, and P. Francisco, *Dependency of C–S–H carbonation rate on CO₂ pressure to explain transition from accelerated tests to natural carbonation*, *Cement and Concrete Research* **40**, 1582 (2010).
- [10] S. A. Bernal, J. L. Provis, B. Walkley, R. San Nicolas, J. D. Gehman, D. G. Brice, A. R. Kilcullen, P. Duxson, and J. S. van Deventer, *Gel nanostructure in alkali-activated binders based on slag and fly ash, and effects of accelerated carbonation*, *Cement and Concrete Research* **53**, 127 (2013).
- [11] A. Leemann and F. Moro, *Carbonation of concrete: the role of CO₂ concentration, relative humidity and CO₂ buffer capacity*, *Materials and Structures* **50**, 1 (2017).
- [12] R. Taylor, I. Richardson, and R. Brydson, *Composition and microstructure of 20-year-old ordinary Portland cement–ground granulated blast-furnace slag blends containing 0 to 100% slag*, *Cement and Concrete Research* **40**, 971 (2010).

- [13] G. Villain, M. Thiery, and G. Platret, *Measurement methods of carbonation profiles in concrete: Thermogravimetry, chemical analysis and gammadensimetry*, Cement and Concrete Research **37**, 1182 (2007).
- [14] M. Thiery, G. Villain, P. Dangla, and G. Platret, *Investigation of the carbonation front shape on cementitious materials: Effects of the chemical kinetics*, Cement and Concrete Research **37**, 1047 (2007).
- [15] A. Morandeau, M. Thiery, and P. Dangla, *Investigation of the carbonation mechanism of CH and CSH in terms of kinetics, microstructure changes and moisture properties*, Cement and Concrete Research **56**, 153 (2014).
- [16] F. Georget, B. Lothenbach, W. Wilson, F. Zunino, and K. L. Scrivener, *Stability of hemicarboxylate under cement paste-like conditions*, Cement and Concrete Research **153**, 106692 (2022).
- [17] I. Richardson, *Tobermorite/jennite-and tobermorite/calcium hydroxide-based models for the structure of CSH: applicability to hardened pastes of tricalcium silicate, -dicalcium silicate, portland cement, and blends of portland cement with blast-furnace slag, metakaolin, or silica fume*, Cement and Concrete Research **34**, 1733 (2004).
- [18] J. I. Escalante-Garcia and J. H. Sharp, *The chemical composition and microstructure of hydration products in blended cements*, Cement and Concrete Composites **26**, 967 (2004).
- [19] D. Le Cornec, Q. Wang, L. Galois, G. Renaudin, L. Izoret, and G. Calas, *Greening effect in slag cement materials*, Cement and Concrete Composites **84**, 93 (2017).
- [20] A. Schwab, J. Hickey, J. Hunter, and M. K. Banks, *Characteristics of blast furnace slag leachate produced under reduced and oxidized conditions*, Journal of Environmental Science Health Part A **41**, 381 (2006).
- [21] Y. Zhang, E. Schlangen, and O. Çopuroğlu, *Effect of slags of different origins and the role of sulfur in slag on the hydration characteristics of cement-slag systems*, Construction and Building Materials **316**, 125266 (2022).
- [22] S. Walspurger, P. D. Cobden, O. V. Safonova, Y. Wu, and E. J. Anthony, *High CO₂ storage capacity in alkali-promoted hydrotalcite-based material: In situ detection of reversible formation of magnesium carbonate*, Chemistry—A European Journal **16**, 12694 (2010).
- [23] X. Ke, S. A. Bernal, and J. L. Provis, *Uptake of chloride and carbonate by Mg-Al and Ca-Al layered double hydroxides in simulated pore solutions of alkali-activated slag cement*, Cement and Concrete Research **100**, 1 (2017).
- [24] P. Sahoo, S. Ishihara, K. Yamada, K. Deguchi, S. Ohki, M. Tansho, T. Shimizu, N. Eisaku, R. Sasai, and J. Labuta, *Rapid exchange between atmospheric CO₂ and carbonate anion intercalated within magnesium rich layered double hydroxide*, ACS applied materials interfaces **6**, 18352 (2014).

- [25] G. W. Groves, A. Brough, I. G. Richardson, and C. M. Dobson, *Progressive changes in the structure of hardened C₃S cement pastes due to carbonation*, *Journal of the American Ceramic Society* **74**, 2891 (1991).
- [26] C. W. Hargis, B. Lothenbach, C. J. Müller, and F. Winnefeld, *Carbonation of calcium sulfoaluminate mortars*, *Cement and Concrete Composites* **80**, 123 (2017).
- [27] H. Justnes, J. Skocek, T. A. Østnor, C. J. Engelsen, and O. Skjølsvold, *Microstructural changes of hydrated cement blended with fly ash upon carbonation*, *Cement and Concrete Research* **137**, 106192 (2020).
- [28] K. De Weerd, G. Plusquellec, A. B. Revert, M. Geiker, and B. Lothenbach, *Effect of carbonation on the pore solution of mortar*, *Cement and Concrete Research* **118**, 38 (2019).
- [29] F. Georget, W. Soja, and K. L. Scrivener, *Characteristic lengths of the carbonation front in naturally carbonated cement pastes: Implications for reactive transport models*, *Cement and Concrete Research* **134**, 106080 (2020).
- [30] H. F. Taylor, *Cement chemistry*, Vol. 2 (Thomas Telford London, 1997).
- [31] T. Matschei, B. Lothenbach, and F. P. Glasser, *Thermodynamic properties of Portland cement hydrates in the system CaO–Al₂O₃–SiO₂–CaSO₄–CaCO₃–H₂O*, *Cement and Concrete Research* **37**, 1379 (2007).
- [32] Cizer, K. Van Balen, J. Elsen, and D. Van Gemert, *Real-time investigation of reaction rate and mineral phase modifications of lime carbonation*, *Construction and Building Materials* **35**, 741 (2012).
- [33] V. Shah, K. Scrivener, B. Bhattacharjee, and S. Bishnoi, *Changes in microstructure characteristics of cement paste on carbonation*, *Cement and Concrete Research* **109**, 184 (2018).
- [34] S. Miyata, *Physico-chemical properties of synthetic hydrotalcites in relation to composition*, *Clays and Clay minerals* **28**, 50 (1980).
- [35] S. Miyata, *Anion-exchange properties of hydrotalcite-like compounds*, *Clays and Clay minerals* **31**, 305 (1983).
- [36] W. T. Reichle, *Synthesis of anionic clay minerals (mixed metal hydroxides, hydrotalcite)*, *Solid State Ionics* **22**, 135 (1986).
- [37] M. Zajac, J. Skibsted, P. Durdzinski, F. Bullerjahn, J. Skocek, and M. B. Haha, *Kinetics of enforced carbonation of cement paste*, *Cement and Concrete Research* **131**, 106013 (2020).
- [38] J. T. Klopoggea, J. Kristófb, and R. L. Frosta, *Thermogravimetric analysis-mass spectrometry (TGA-MS) of hydrotalcites containing CO₃²⁻, NO₃⁻, Cl, SO₄²⁻ or ClO₄⁻*, *Clay Odyssey* **1**, 451 (2001).

- [39] E. Bernard, W. J. Zucha, B. Lothenbach, and U. Mäder, *Stability of hydrotalcite (Mg-Al layered double hydroxide) in presence of different anions*, *Cement and Concrete Research* **152**, 106674 (2022).
- [40] G. G. Litvan, *Variability of the nitrogen surface area of hydrated cement paste*, *Cement and Concrete Research* **6**, 139 (1976).
- [41] I. Galan, F. P. Glasser, D. Baza, and C. Andrade, *Assessment of the protective effect of carbonation on portlandite crystals*, *Cement and Concrete Research* **74**, 68 (2015).

6

THE EFFECT OF SLAG CHEMISTRY ON CO₂ BINDING CAPACITY OF C₃S-SLAG (-GYPSUM) SYSTEM

The objective of this chapter was to figure out the correlation between slag chemistry and CO₂ binding capacity of the blended system. To simplify the composition of mixture, model paste containing C₃S, synthetic slags covering the common composition range and gypsum was employed. To accelerate the carbonation process, the specimen was ground to powders after 3 months of sealed curing, which were then exposed to CO₂ directly. The carbonation mechanism was investigated through a complementary set of analytical methods, and TG-DTG-MS was employed to quantify the CO₂ binding capacity of each mixture. Finally, the effect of slag composition on absorbing CO₂ was discussed.

6.1. INTRODUCTION

IT is well accepted that the carbonation resistance of cementitious materials mainly depends on pore structure (CO₂ diffusion) and CO₂ binding capacity. The generally higher carbonation rate of slag cement paste is partially due to its lower amount of calcium hydroxide, which is consumed in the pozzolanic reaction with slag [1–5]. Although a lower permeability is obtained by proper curing for slag cement paste (lower CO₂ diffusion coefficient), the reduction in CO₂ binding capacity because of the reduced portlandite content and alkalinity of pore solution dominates over the pore refinement [6, 7].

Therefore, CO₂ binding capacity of slag cement paste is of high importance for predicting its carbonation potential. However, the effect of slag chemistry on CO₂ binding capacity has not been experimentally determined previously, and such information is still scarce both for industry and academia. Thus, the aim of this chapter was to figure out the correlation between slag chemistry and CO₂ binding capacity of the blended system. To simplify the composition of mixture, model paste containing C₃S, synthetic slags covering the common composition range and gypsum was employed. As the major constituent of cement, C₃S dominates the properties of the hardened paste. Understanding the carbonation behavior of this model paste helps generate a fundamental insight into the carbonation of real slag cement paste. According to the results in [8], calcite, aragonite, and vaterite were inhomogeneously formed in the CO₂-contaminated C₃S pastes. C-S-H gel phase of reduced Ca/Si ratio and increased silicate polymerization were also formed during the early stage of carbonation [9]. Additionally, it was concluded that the carbonation rate of C₃S paste was actually controlled by the solution environment [10].

To accelerate the carbonation process, the specimen was ground to powders after 3 months of sealed curing, which were then exposed to CO₂ directly. The carbonation mechanism was investigated through a complementary set of analytical methods, and TG-DTG-MS was employed to quantify the CO₂ binding capacity of each mixture. Meanwhile, the effect of slag composition on absorbing CO₂ was discussed.

6.2. MATERIALS AND METHODOLOGY

6.2.1. SAMPLE INFORMATION

ANALYTICAL reagent C₃S and gypsum were employed in this chapter to produce C₃S-slag (-gypsum) system. Eight synthetic slags (M0, M8, M16, CS1, CS2; A3, A12, A18) covering the common composition range were also used. For the detailed information of these synthetic slags, please refer to Section 4.2.1. In general, these slags presented a similar properties except for the difference in chemical composition. X-ray diffraction measurement of C₃S is illustrated in Figure 6.1, and it indicated that C₃S showed a triclinic polymorph.

6.2.2. EXPERIMENTAL METHODS

A summary of the specimens prepared for the investigation is listed in Table 6.1. To keep consistent, the substitution level of C₃S was 70 wt.%, and the water to binder ratio was 0.4. Group I consisted of slag M0, M8, M16, CS1, and CS2 mixtures. The main target

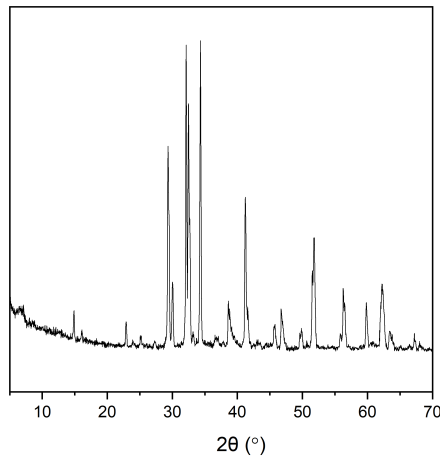


Figure 6.1: XRD scans of analytical reagent C₃S used in the research.

Table 6.1: Compositions (wt.%) of the mixtures.

Group	C ₃ S	Gypsum	Slag	SO ₃ /(C ₃ S+gypsum)	Slag/(C ₃ S+gypsum)
I	30	0	70	0	7/3
II	26.775	3.225	70	5%	7/3

of this group was to examine the effect of MgO content and CaO/SiO₂ ratio of slag on CO₂ binding capacity of the blended system. As for Group II, gypsum was incorporated by replacing C₃S, and it was comprised of slag A3, A12, and A18 mixtures. This group was designed to manifest the interaction between alumina of slag and gypsum, and its influence on CO₂ binding capacity. Paste was prepared and cast in the plastic bottle of 20 mL, which was sealed with thin para film on the seal to avoid any ingress of CO₂ and evaporation of vapor, and stored in the laboratory for further study.

After 3 months of curing, specimens were demoulded, and slices cut from the specimens were ground and meshed to powder below 63 μm, allowing full carbonation on a practical time scale [11]. Then, powders of each mixture were evenly distributed over a Petri dish and exposed in the CO₂ chamber directly. Accelerated carbonation test was performed in the carbonation chamber regulated by CO₂ concentration of 3%±0.2, at 20±3 °C and 65±5% of RH (using saturated NaNO₂ solution). The carbonation age was up to one month to ensure full carbonation.

XRD and TGA were performed to identify phase assemblage evolution before and after carbonation, and the process was performed as explained in Section 4.2.2 and 4.2.3, respectively. The emission of H₂O and CO₂ from sample after heating was also identified with mass spectrometer Netzsch QMS 430 C.

FTIR was carried out using Spectrum TM 100 Optical ATR-FTIR spectrometer over the wavelength range from 600 to 4000 cm⁻¹ to characterize the alteration of molecule structure of C-S-H gel phase due to CO₂ attack. The procedure was explained in Section 4.2.2.

Polished section was also prepared for microanalysis according to the procedure described in Section 3.2.2.

6.3. RESULTS

6.3.1. CARBONATION PRODUCTS

PURE C₃S SYSTEM

It is well recognized that the hydration of C₃S follows the following Equation 6.1 [12, 13], and its main precipitations are nanocrystalline/amorphous C-S-H gel phase jointly with the crystallization of portlandite, Ca(OH)₂. It is noted that x is the Ca/Si atomic ratio and y is the amount of water bound in C-S-H gel phase

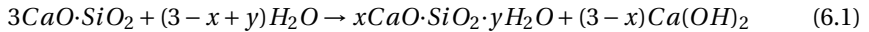


Figure 6.2(a) presents the TG and DTG curves of C₃S paste after 3 months of sealed curing. There were two distinct endothermic peaks on the DTG curve, corresponding to the water loss of C-S-H gel phase between 100 and 150 °C and the dehydroxylation of portlandite between 400 and 500 °C.

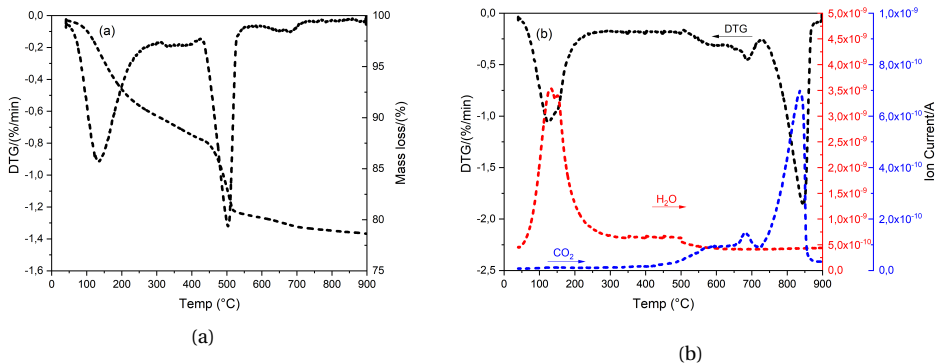


Figure 6.2: (a) TG and DTG results of C₃S paste after 3 months of curing; (b) DTG result, H₂O and CO₂ MS curves of hydrated C₃S powder after full carbonation.

Figure 6.2(b) illustrates the DTG result, H₂O and CO₂ MS curves of hydrated C₃S powders after accelerated carbonation test. The main CO₂-binding phase was calcium carbonate, the decomposition peak of which started from around 500 °C in the DTG graph. These peaks implied the presence of different morphologies of calcium carbonate, calcite in particular, which were commonly seen in the accelerated carbonation test of cementitious materials [14–16]. The peak at 100-150 °C suggested the persistence of C-S-H gel phase, although its Ca/Si ratio had decreased remarkably due to the removal of calcium atom from silicate chain [17–19].

XRD results (Figure 6.3) reveal the presence of portlandite and minor unhydrated C₃S particles in the pure C₃S system at 90 days. For C-S-H gel phase, the main peaks were located at around (2θ=) 30° (see PDF 034-0002 and 033-0306), which was very difficult to distinguish from that of C₃S. On the other hand, the peak for portlandite

vanished after accelerated carbonation test, meaning that all of it had been carbonated and transformed into calcium carbonate, in agreement with the results determined by TGA (Figure 6.2(b)). Additionally, the peak for unhydrated C_3S particle also disappeared, probably associated with its continuous hydration or carbonation [20].

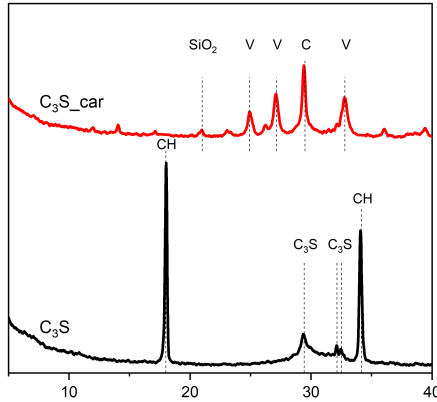
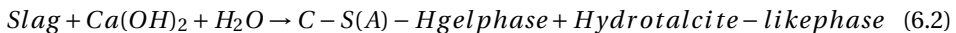


Figure 6.3: XRD analysis of C_3S paste after curing of 3 months and hydrated C_3S powder after carbonation. CH: portlandite; C: calcite; V: vaterite.

The small hump centered at around 21° was related to the formation of poorly ordered silica gel due to the carbonation of C-S-H gel phase [2]. Calcite and vaterite were identified as the main polymorphs of $CaCO_3$. No trace of aragonite was found by XRD. The intensified peak at $\sim 800^\circ C$ in the DTG curve in Figure 6.2(b) also indicated the mass precipitation of calcite. The results in [21] pointed out that compared with aragonite, vaterite was formed preferentially on the surface of portlandite due to their similar symmetries and positive surface charge. Also, the environment in the carbonation chamber (low temperature, i.e., $\sim 20^\circ C$) favored the coexistence of vaterite and calcite [22].

C_3S -SLAG SYSTEM

With the gradual addition of slag, portlandite, the main hydration product of C_3S , reacts with slag and contributes to the formation of C-S(A)-H gel phase and hydrotalcite-like phase, as the following Equation 6.2 demonstrates [23]. Five slags with different chemical compositions were employed to produce C_3S -slag system in this section, namely slag M0, M8, M16, CS1, and CS2 mixtures.



TG-DTG-MS

Compared with the hydration of pure C_3S , two evident differences occurred in the DTG curve of C_3S -slag system (Figure 6.4(a)). One was the reduction of portlandite content implied by the intensity of peak between 400 and $500^\circ C$. The other one was the precipitation of hydrotalcite-like phase with a tiny shoulder and a distinct peak located

at approximately 250 and 350 °C, respectively. As a Mg-Al LDHs, its amount was positively related to the MgO content of slag. Thus the most hydrotalcite-like phase was detected in slag M16 mixture while there was nearly no hydrotalcite-like phase formed in slag M0 mixture.

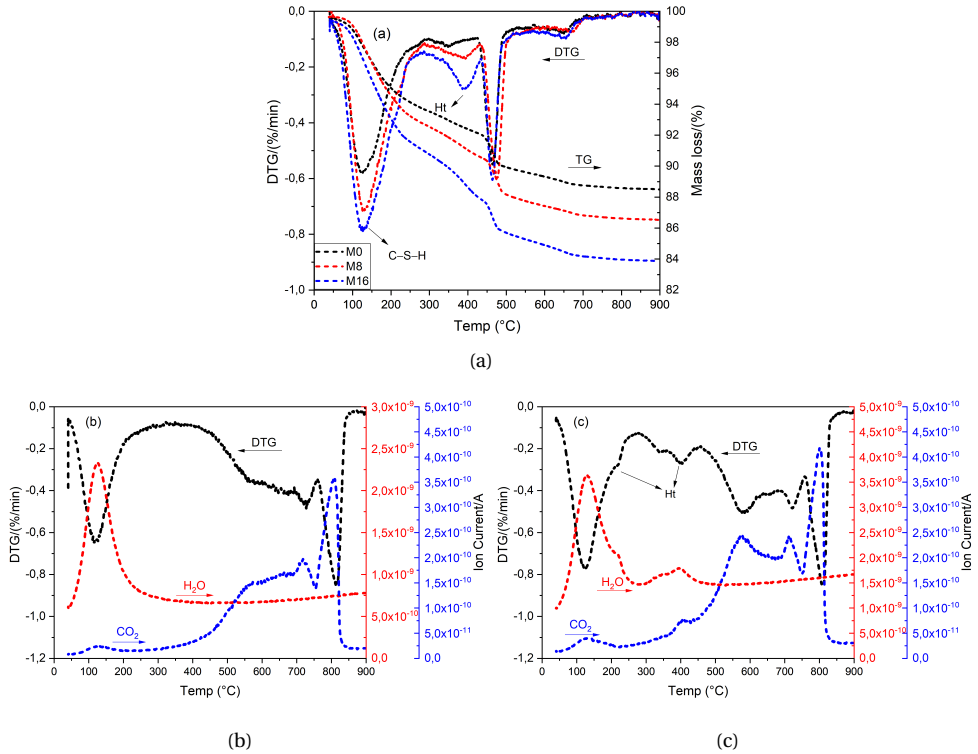


Figure 6.4: (a) Representative TG and DTG results of C₃S-slag pastes after 3 months of curing; DTG result, H₂O and CO₂ MS curves of hydrated (b) slag M0 and (c) slag M16 powders after carbonation.

Representative DTG results, H₂O and CO₂ MS curves of carbonated slag M0 and M16 powders are plotted in Figure 6.4(b) and 6.4(c), respectively. Similarly, the main CO₂-binding phase was calcium carbonate, and decomposition peaks after 500 °C in the DTG graph suggested the presence of various morphologies of CaCO₃. The peak located at 300-450 °C indicated the persistence of hydrotalcite-like phase after carbonation (Figure 6.4(c)). As displayed in the MS curves, both H₂O and CO₂ were liberated from this phase after heating, meaning that both H₂O and CO₂ were absorbed in the interlayer space due to its stacked layer structure [24–26]. Conversely, no hydrotalcite-like phase was formed in slag M0 mixture, thus there was no release of H₂O nor CO₂ at 300-450 °C in this mixture (Figure 6.4(b)). As for the small peak at ~150 °C in the MS CO₂ curve, it can be ascribed to the release of CO₂ from carbonated Ca-Al AFm phases owing to the carbonation of e.g., AFm-OH and AFm-SO₄ phases (see discussion in Section 5.4.1).

XRD

Representative XRD results (Figure 6.5(a)) reveal the presence of hydrotalcite-like

phase, portlandite, and unhydrated C_3S clinker in C_3S -slag system after hydration. The intensity of peak indicating portlandite became weaker with the gradual addition of MgO in slag, suggesting a higher reactivity of slag with more MgO incorporation, and thus more portlandite was consumed in the pozzolanic reaction with slag. Also, the peak for hydrotalcite-like phase was more visible in slag M16 blend, consistent with the results measured by TGA (Figure 6.4(a)).

After accelerated carbonation test, the peak for portlandite disappeared in all mixtures. Hydrotalcite-like phase was still observed after such a heavy CO_2 attack (Figure 6.5(b)), in agreement with the results examined by TGA (Figure 6.4(c)). Similar to the carbonation products of pure C_3S system, calcite and vaterite were identified as the main polymorphs of $CaCO_3$ in these pastes.

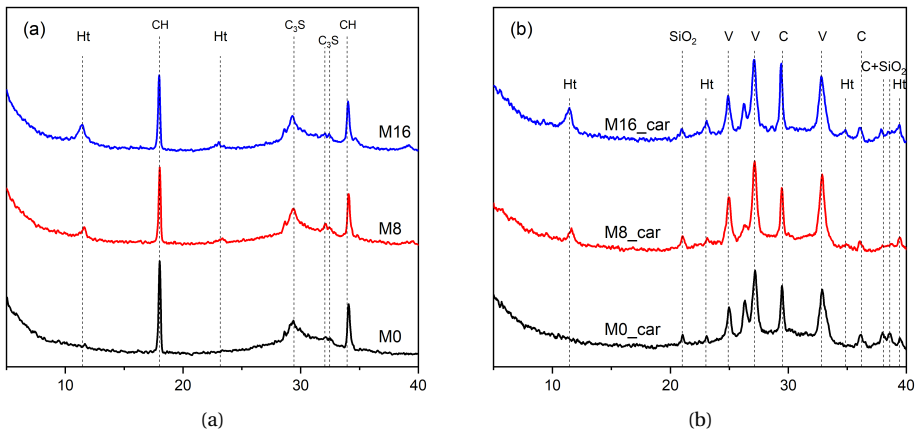


Figure 6.5: Representative XRD analysis of (a) C_3S -slag pastes after 3 months of curing and (b) hydrated powders after carbonation. Ht: hydrotalcite-like phase; CH: portlandite; C: calcite; V: vaterite.

FTIR

FTIR was used to examine the carbonation products of C_3S -slag system, especially the alteration of C-S(A)-H gel phase at molecular level. Figure 6.6 displays the FTIR spectra of representative mixtures before and after carbonation. Commonly, positions of silicate group in FTIR spectra suggest the presence of different molecular structures of C-S-H gel phase [27–30]. Regardless of slag chemistry, Q2 was the main unit of C-S(A)-H gel phase of all investigated pastes after hydration. After carbonation, the Si-O-T stretching band was characterized by signals appearing at ~ 1200 and ~ 1100 cm^{-1} , which was linked with the yield of Q4 and Q3 silicate units, respectively. No doubt, this shift was associated with the gradual polymerization of silicate units due to the carbonation-induced decalcification of C-S(A)-H gel phase [31–33].

The carbonation was also confirmed through three types of carbonate bands observed in the FTIR spectra, i.e., strong broad band at 1400 – 1500 cm^{-1} , representing the asymmetric stretching of carbonate, narrow band at 875 – 1000 cm^{-1} due to the bending of carbonate, and in-plane bending of carbonate at ~ 710 cm^{-1} [21].

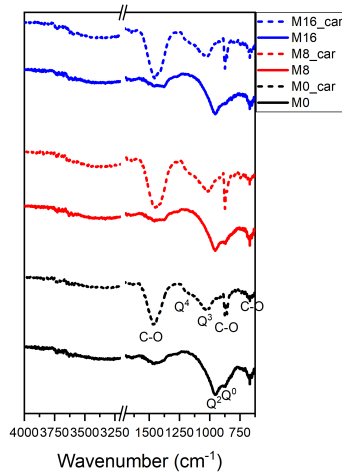


Figure 6.6: Representative FTIR spectra of C₃S-slag pastes after 3 months of curing and hydrated powders after carbonation (Normalized, %).

C₃S-SLAG-GYPSUM SYSTEM

With the addition of gypsum, aluminate dissolved from slag (in the form of AlO_2^-) reacts with SO_4^{2-} ions from gypsum and participates into ettringite as Equation 2.6 shows. Moreover, ettringite transforms into calcium monosulfoaluminate with the gradual supply of aluminate dissolved from slag (see Equation 2.7). To investigate their effects on capturing CO₂, three slags with different chemical compositions (different alumina contents) were employed to produce C₃S-slag-gypsum system (Group II shown in Table 6.1), namely slag A3, A12, and A18 mixtures.

TG-DTG-MS

Compared with the hydration of C₃S-slag mixture, another two differences occurred in the DTG curve of C₃S-slag-gypsum system (Figure 6.7(a)). One was the presence of ettringite. Although the decomposition peaks for C-S(A)-H gel phase and ettringite overlapped in 100-150 °C, this peak became much sharper and more intensified in gypsum-containing system due to the formation of ettringite. The other one was the precipitation of monosulfate with a tiny shoulder located at approximately 200 °C, as shown in the insert graph. Its occurrence was associated with the Al₂O₃ content of slag, and together with the results of XRD (Figure 6.8(a)), monosulfate was only detected in slag A12 and A18 mixtures. Furthermore, note that the peak for hydroxalcalite-like phase almost vanished in slag A18 mixture although it contained 7.98 wt.% MgO.

The DTG results, H₂O and CO₂ MS curves of carbonated slag A3 and A18 powders are plotted in Figure 6.7(b) and 6.7(c), respectively. Still, the main CO₂-binding phase was calcium carbonate. The peak located at 300-500 °C suggested the persistence of hydroxalcalite-like phase after carbonation in slag A3 blend.

XRD

Besides portlandite and unhydrated C₃S, XRD scans (Figure 6.8(a)) reveal the presence of ettringite and monosulfate in slag A12 and A18 blends owing to the addition of gypsum. It also can be seen that there was few ettringite and monosulfate detected

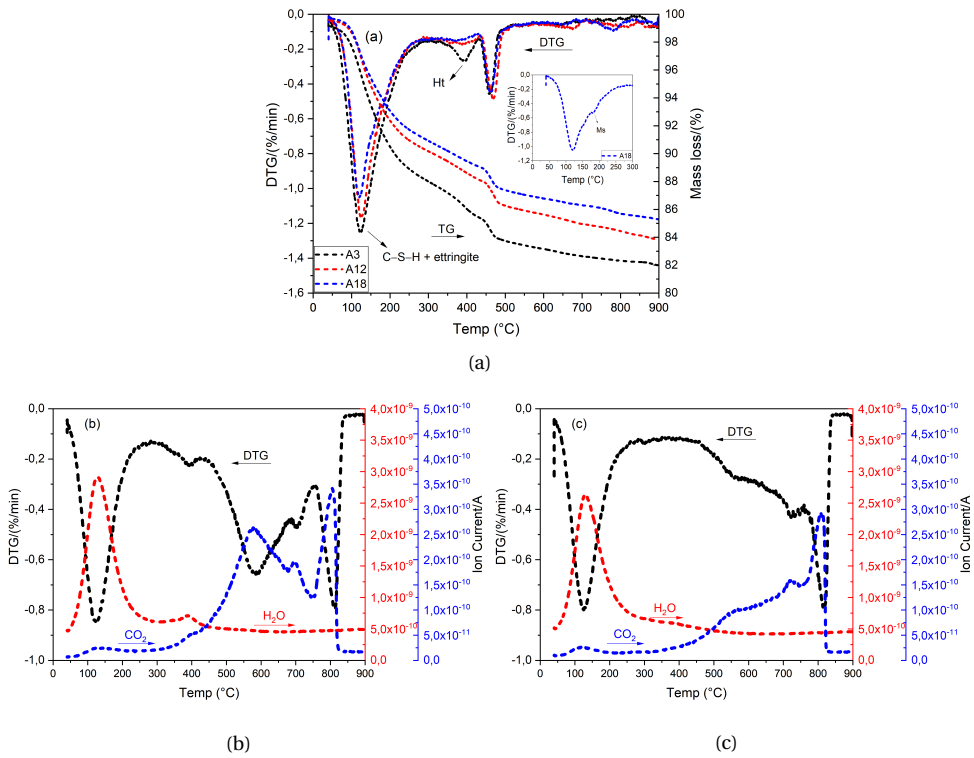


Figure 6.7: (a) TG and DTG results of C₃S-slag-gypsum pastes after 3 months of curing; DTG result, H₂O and CO₂ MS curves of hydrated (b) slag A3 and (c) slag A18 powders after carbonation. Ms: calcium monosulfoaluminate; Ht: hydrotalcite-like phase.

by XRD in slag A3 blend because of its low alumina content.

Meanwhile, the addition of gypsum seemed to exert no influence on the mineralogy of carbonation products, which was almost the same to that of C₃S-slag system (Figure 6.5(b)). The peak for ettringite and monosulfate disappeared totally after carbonation, and the possible intermediates, e.g., hemi- and/or mono-carboaluminate as the carbonation products of ettringite and calcium monosulfoaluminate [34], were not detected in these three mixtures in the present research.

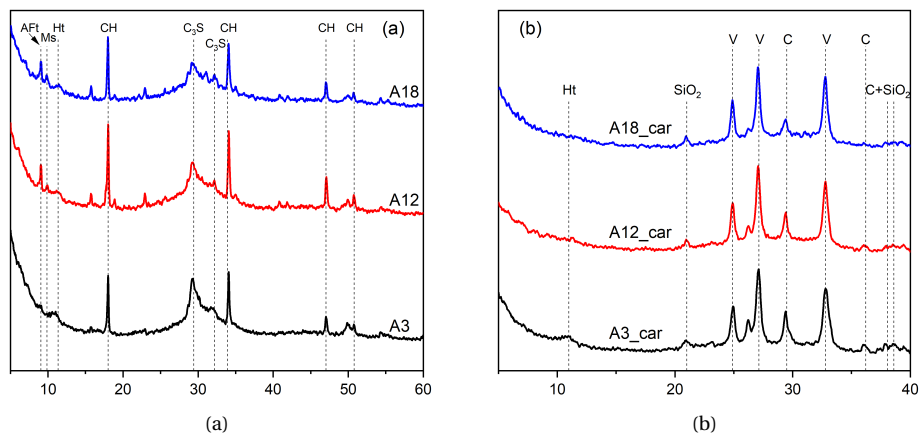


Figure 6.8: XRD analysis of (a) C₃S-slag-gypsum pastes after curing of 3 months and (b) hydrated powders after carbonation. AFt: ettringite; Ms: calcium monosulfoaluminate; Ht: hydrotalcite-like phase; CH: portlandite; C: calcite; V: vaterite.

FTIR

As Figure 6.9 displays, FTIR spectra of C₃S-slag-gypsum mixture presents a similar characteristic to that of mixtures without gypsum before and after carbonation. Q2 was the main unit of C-S(A)-H gel phase of the blended pastes after hydration. After carbonation, the Si-O-T stretching band shifted left to ~1200 and ~1100 cm⁻¹, indicating the formation of Q4 and Q3 silicate units, respectively.

6.3.2. THE AMOUNTS OF CO₂ BOUND IN DIFFERENT PHASES

Besides the work in Section 5.4.2, pure agent CaCO₃ (VWR Chemicals BDH) was employed as standard to calculate the CO₂ concentration of each carbonate phase after accelerated carbonation test under the same analytical condition. Figure 6.10(a) shows the DTG result, CO₂ MS curve of pure CaCO₃. The area under the MS CO₂ curve corresponding to 44.0 wt.% CO₂ releasing from CaCO₃ was determined using commercial software OriginPro 2019. Similarly, the CO₂ concentration of each carbonate phase can thus be estimated in the corresponding temperature range of decomposition as shown in Figure 6.10(b), using slag M16 as an example. Portlandite and C-S(A)-H gel phase were the main CO₂ binding phases, and their carbonation products were calcium carbonate of different forms. Hydrotalcite-like and Ca-Al AFm phases (including ettringite, AFm-OH, and AFm-SO₄ in the present research), due to their stacked layer structures, also absorbed a certain amount of CO₂, forming

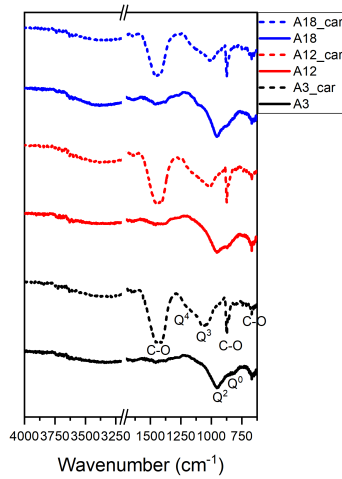


Figure 6.9: Representative FTIR spectra of C_3S -slag-gypsum pastes after 3 months of curing and hydrated powders after carbonation (Normalized, %).

carbonated hydrotalcite-like phase and Ca-Al AFm phases, respectively. The area A1, A2, and A3 depicted in Figure 6.10(b) corresponded to certain amounts of CO_2 releasing from carbonated Ca-Al AFm phases, carbonated hydrotalcite-like phase, and calcium carbonate, respectively.

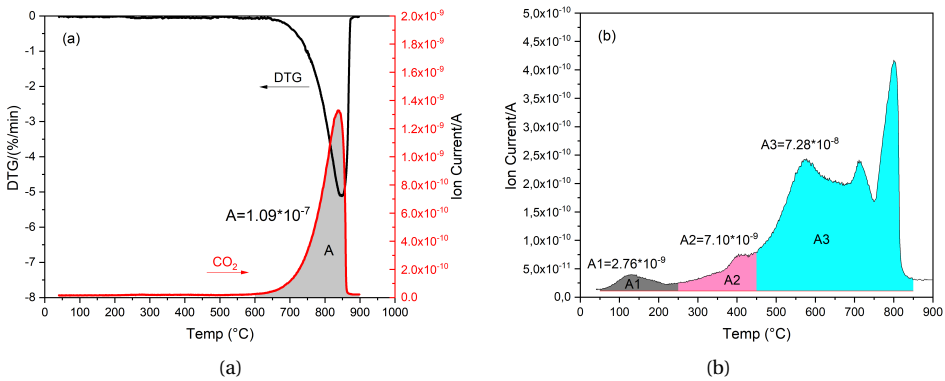


Figure 6.10: (a) The DTG result, CO_2 MS curve of pure $CaCO_3$; (b) The CO_2 MS curve of carbonated slag M16 powder.

As described in Section 6.3.1, there was no fundamental change of the CO_2 -binding phases in C_3S -slag (-gypsum) system after carbonation. The areas under MS CO_2 curve and the corresponding CO_2 proportions shared by different carbonate phases in all investigated samples are summarized and given in Table 6.2.

As can be seen in Table 6.2, the CO_2 bound in C_3S -slag (-gypsum) system was mainly present in calcium carbonate, originated from the carbonation of portlandite and C-S(A)-H gel phase (from the hydration of C_3S and slag both). It was noted that

Table 6.2: The areas under MS CO₂ curve and the corresponding CO₂ proportions of different carbonate phases.

		Area under the MS CO ₂ curve			Total
		Carbonated Ca-Al AFm phases	Carbonated hydrotalcite-like phase	Calcium carbonate (CaCO ₃)	
Pure CaCO ₃		-	-	1.09*10 ⁻⁷	1.09*10 ⁻⁷
Pure C ₃ S		-	-	7.00*10 ⁻⁸	7.00*10 ⁻⁸
Group I	M0	3.12*10 ⁻⁹	-	6.08*10 ⁻⁸	6.39*10 ⁻⁸
	M8	1.85*10 ⁻⁹	4.94*10 ⁻⁹	6.04*10 ⁻⁸	6.72*10 ⁻⁸
	M16	2.76*10 ⁻⁹	7.10*10 ⁻⁹	7.08*10 ⁻⁸	8.06*10 ⁻⁸
	CS1	2.13*10 ⁻⁹	4.80*10 ⁻⁹	6.99*10 ⁻⁸	7.69*10 ⁻⁸
	CS2	2.07*10 ⁻⁹	3.26*10 ⁻⁹	6.48*10 ⁻⁸	7.02*10 ⁻⁸
Group II	A3	2.31*10 ⁻⁹	5.54*10 ⁻⁹	6.50*10 ⁻⁸	7.28*10 ⁻⁸
	A12	1.85*10 ⁻⁹	3.56*10 ⁻⁹	5.29*10 ⁻⁸	5.83*10 ⁻⁸
	A18	2.63*10 ⁻⁹	1.38*10 ⁻⁹	4.36*10 ⁻⁸	4.76*10 ⁻⁸
		CO ₂ proportion shared by each carbonate phase (%)			CO ₂ in the carbonated powders (wt.%)
		Carbonated Ca-Al AFm phases	Carbonated hydrotalcite-like phase	Calcium carbonate (CaCO ₃)	
Pure CaCO ₃		-	-	100	44.0
Pure C ₃ S		-	-	100	28.26
Group I	M0	4.88	-	95.12	25.79
	M8	2.75	7.37	89.88	27.12
	M16	3.42	8.85	87.73	32.54
	CS1	2.77	6.25	90.98	31.04
	CS2	2.95	4.64	92.41	28.34
Group II	A3	3.17	7.61	89.22	29.38
	A12	3.17	6.11	90.72	23.53
	A18	5.53	2.90	91.57	19.21

Ca-Al AFm phases played a minor role in absorbing CO₂, sharing less than 5% of CO₂ among all carbonate phases. With sufficient Al₂O₃, they absorbed a little more than 5% of CO₂ in slag A18 mixture although the absolute amount (area) levelled off roughly. The role of hydrotalcite-like phase in binding CO₂ started to emerge with the gradual addition of MgO in slag, and the binding ability was positively related to its content after hydration. The most hydrotalcite-like phase was detected in slag M16 paste, and it was able to absorb up to ~9% CO₂ after full carbonation.

6.4. DISCUSSION

COMMONLY, it is recognized that CO₂ binding capacity of C₃S-slag (-gypsum) system should be positively related to the reactivity of slag. Although portlandite, one of the main CO₂-binding phase, would be consumed in the pozzolanic reaction with slag, secondary precipitations, e.g., hydrotalcite-like phase and C-S(A)-H gel phase, would also act as CO₂-binding phases. In Chapter 4, the correlation between slag chemistry and its reactivity was discussed. It was found that slag reactivity was favorably affected by increasing Al₂O₃ and MgO contents. In other words, slag M0 and A3 presented low reactivity, while slag M16 and A18 showed high reactivity. However, based on the results present in this chapter, the correlation between slag chemistry and CO₂ binding capacity of C₃S-slag (-gypsum) system differed.

As mentioned, Al₂O₃-rich slag shows high reactivity because the increased Al₂O₃ content is reported to enhance the reaction involving the formation of ettringite [35–37]. Also, the formation of calcium monosulfoaluminate became increasingly prominent with the gradual incorporation of Al₂O₃ in slag, as shown in Figure 6.7(a). Again, no hemi- and mono-carboaluminate was confirmed by XRD as the intermediates of ettringite and monosulfate carbonation in this chapter with model paste. They disappeared completely after carbonation. A possible explanation here was

that owing to the full carbonation of sample powders, intermediates, including hemi- and mono-carboaluminate, had carbonated further and led to the formation of calcium carbonate and gypsum [7]. On the other hand, gypsum was also not detected by XRD in the study. As for the small peak at ~ 150 °C in the MS CO₂ curve in all investigated samples, it was ascribed to the formation of carbonated Ca-Al AFm phases (see the discussion in chapter 5). These carbonate phases cannot be identified by XRD, probably they were amorphous or nano-crystalline. Fortunately, they only played a minor role in absorbing CO₂, sharing less than 5% of CO₂ among all carbonate phases as Table 6.2 and Figure 6.11 illustrate.

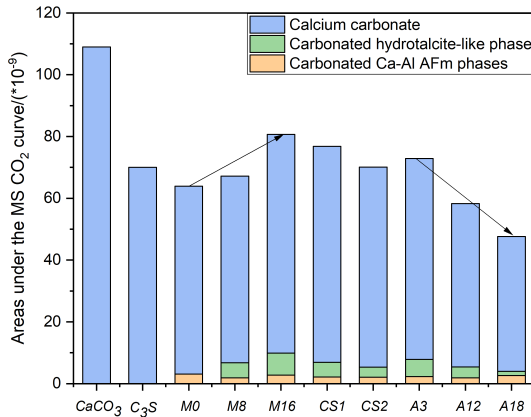


Figure 6.11: The areas under MS CO₂ curve corresponding to different carbonate phases.

Additionally, it was noticed that the total CO₂ binding capacity decreased significantly with the increasing Al₂O₃ content from slag A3 to A18 blend (Figure 6.11), in contrast to the reactivity of slag (see Chapter 4). This decline trend was exhibited in three aspects: (1) The CO₂ amount bound in carbonated Ca-Al AFm phases was stable, i.e., the enhanced ettringite and monosulfate formations with increasing alumina content of slag did not exert positive effect on CO₂ binding capacity. (2) The CO₂ content absorbed by hydrotalcite-like phase decreased. In fact, the high Al₂O₃ content of slag suppressed the formation of hydrotalcite-like phase as confirmed in Figure 6.7(a), in agreement of results reported in [38, 39]. (3) The remarkable decrease of CO₂ bound in calcium carbonate. Considering the low amount of portlandite remained at 90 days in these mixtures (Figure 6.7(a)), the decrease was more likely to be caused by the reduced carbonation degree of C-S(A)-H gel phase.

Figure 6.12(a) and 6.12(b) show representative BSE images of slag M16 and A18 mixtures at 90 days, respectively. Unhydrated C₃S grains as well as inner products surrounding the unreacted cores (circled in Figure 6.12(a)), and so-called Hadley grains, which hydrated completely to leave hollow hydration shell (circled in Figure 6.12(b)) were distributed everywhere, embedded into the matrix together with unhydrated slag particles. Slag particle hydrated slowly, and precipitates as the rims of unhydrated slag particles were formed as a whole with the surrounding matrix.

Figure 6.12(c) illustrates the representative atomic ratio of Al/Ca against Si/Ca of

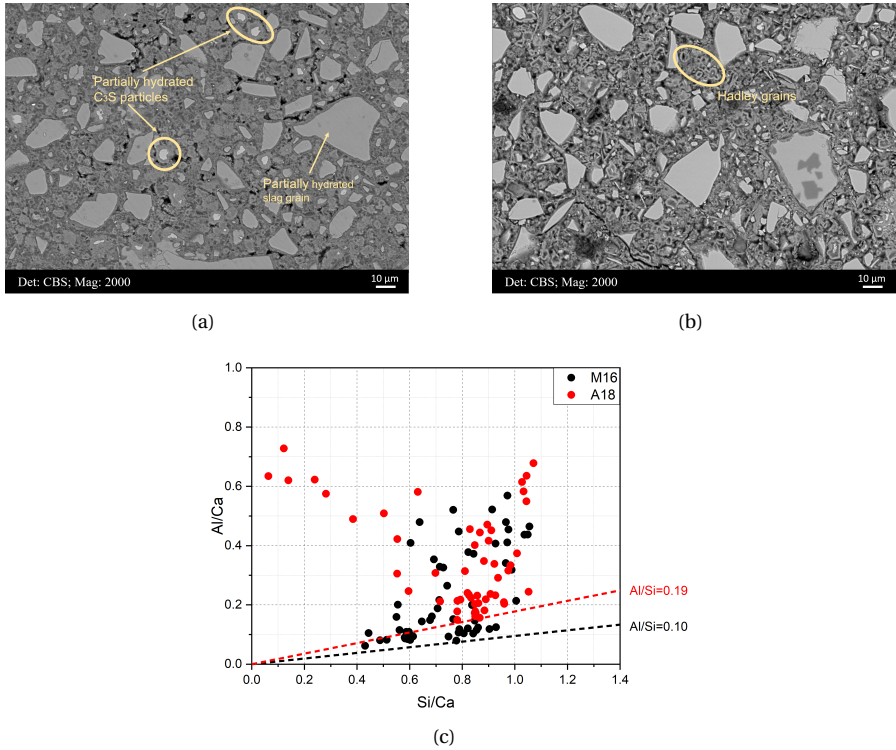


Figure 6.12: (a) and (b) Representative BSE images of slag M16 and A18 mixtures at 90 days, respectively; (c) Atomic ratio of Al/Ca against Si/Ca of slag M16 and A18 mixtures after 3 months of curing.

slag M16 and A18 mixtures at 90 days. In fact, The Ca/Si atomic ratio measured in all these samples fluctuated at 1.0~1.1 (except slag CS1 and CS2 mixtures because of their low CaO/SiO₂ ratios of raw slags). However, the values of Al/Si atomic ratio varied considerably among these mixtures. The highest Al/Si ratio was determined in slag A18 mixture, close to 0.20, double of that in slag M16 mixture. It explained the reduced carbonation degree of C-S(A)-H gel phase in slag A18 mixture. For one thing, aluminum uptake in C-S-H gel phase increased the content of bridging silicate tetrahedron [40], and a more polymerized unit commonly exhibited better carbonation resistance [41, 42]. For another, coupling a high aluminum content, aluminate of pentahedral and octahedral coordination were produced [17, 43]. The presence of those species correlated with a lower kinetic degradation for C-S(A)-H gel phase by the limited CO₂ access [43].

Based on the results of R3 test in Chapter 4, higher reactivity was observed with the increasing amount of MgO in slag. TGA (Figure 6.4) and XRD (Figure 6.5) results in this chapter suggested that the increasing MgO content in slag effectively favored the formation of hydrotalcite-like phase, consistent with the results in [44–46]. As discussed in Section 5.4.1, due to its stacked layer morphology, the space between layers presents a large specific surface area comparable to that of C-S-H gel phase [47], and is the natural site to fix CO₂ molecules [48, 49]. In all investigated samples, hydrotalcite-like phase was able to absorb up to ~10% CO₂ at most, and this value was positively associated with the Mg/Al atomic ratio of raw slag as Figure 6.13 displays. It thus explained the increasing CO₂ binding capacity with the rising of MgO content in slag. On the other hand, although containing 7.98 wt.% MgO, the high Al₂O₃ content in slag A18 suppressed the formation of hydrotalcite-like phase, and a small amount of CO₂ was bound in it as a result.

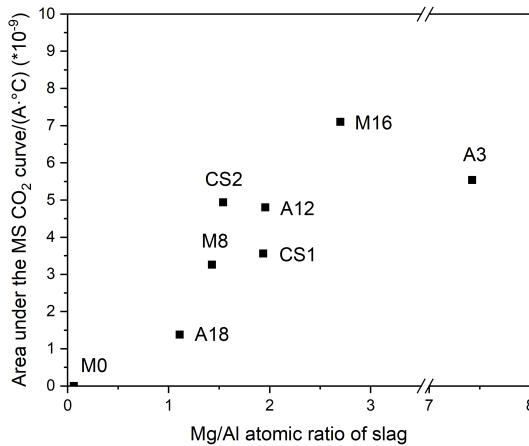


Figure 6.13: The area under MS CO₂ curve corresponding to hydrotalcite-like phase vs. Mg/Al atomic ratio of raw slag.

In general, portlandite and C-S-H gel phase (in particular) were the main CO₂-binding phases in cementitious materials, and their carbonation products were calcium carbonate of different forms. In this study, calcium carbonate took up more

than 85% CO₂ after full carbonation. An interesting phenomenon occurred here that the amount of CaCO₃ formed in slag CS1 and CS2 mixtures was unexpectedly high, compared to their low CaO contents in raw slags (Table 4.1) and relatively low reactivity (see Chapter 4).

Figure 6.14 illustrates the representative atomic ratio of Al/Ca against Si/Ca of slag M16 and CS1 mixtures at 90 days. A significant reduction of Ca/Si atomic ratio was measured in slag CS1 mixture, to approximately 0.85 (to around 0.79 in slag CS2 mixture). As confirmed in [17, 19], C-S-H gel phase with a lower Ca/Si ratio was decomposed faster than that with a higher Ca/Si ratio. Moreover, it was much easier for C-S-H gel phase with a lower Ca/Si ratio to decalcify and reach Ca/Si ratio of 0.67 [50]. Due to the low CaO/SiO₂ ratio of raw slag CS1 and CS2, C-S(A)-H gel phase with a much lower Ca/Si atomic ratio was formed in these two mixtures. It explained the high CaCO₃ content obtained in slag CS1 and CS2 mixtures after carbonation.

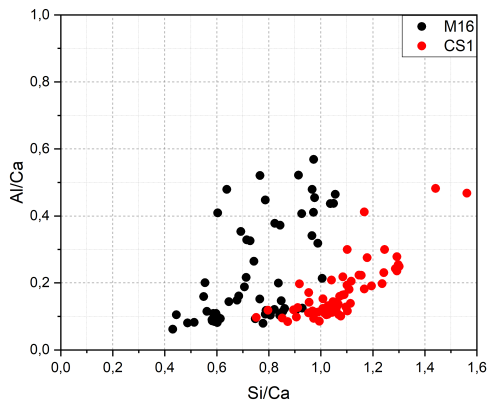


Figure 6.14: Atomic ratio of Al/Ca against Si/Ca of slag M16 and CS1 mixtures after 3 months of curing.

6.5. CONCLUSIONS

BASED on C₃S-slag (-gypsum) system, the chapter investigated the effect of slag chemistry on CO₂ binding capacity. Overall, the mineralogy of carbonation products did not change fundamentally with various slag compositions. The main conclusions drawn were as follows:

- C-S(A)-H gel phase, portlandite, and hydrotalcite-like phase were identified as the main hydrates of C₃S-slag system. With gypsum, ettringite occurred in the system, and monosulfate was also formed with the continuous supply of aluminate dissolved from slag.
- After accelerated carbonation test, three CO₂-bearing phases were formed: carbonated Ca-Al AFm phases (amorphous or nano-crystalline), carbonated hydrotalcite-like phase, and calcium carbonate (vaterite and calcite), irrespective of slag chemistry and the addition of gypsum.

- Carbonated Ca-Al AFm phases played a minor role in absorbing CO₂, sharing less than 5% of CO₂ among all carbonate phases. Hydrotalcite-like phase was able to absorb up to ~10% CO₂, and this value was positively associated with the Mg/Al atomic ratio of raw slag. CaCO₃, originated from the carbonation of portlandite and C-S(A)-H gel phase (in particular), took up more than 85% CO₂ after full carbonation.
- Generally, the CO₂ binding capacity of C₃S-slag (-gypsum) system was not directly related to the reactivity of slag. System with a Al₂O₃-rich slag presented a low CO₂ binding capacity, while a low CaO/SiO₂ ratio slag contributed to a high CO₂ amount captured in the system.

REFERENCES

- [1] P. Sulapha, S. Wong, T. Wee, and S. Swaddiwudhipong, *Carbonation of concrete containing mineral admixtures*, Journal of materials in civil engineering **15**, 134 (2003).
- [2] P. H. Borges, J. O. Costa, N. B. Milestone, C. J. Lynsdale, and R. E. Streatfield, *Carbonation of CH and C-S-H in composite cement pastes containing high amounts of BFS*, Cement and Concrete Research **40**, 284 (2010).
- [3] Y. Gao, L. Cheng, Z. Gao, and S. Guo, *Effects of different mineral admixtures on carbonation resistance of lightweight aggregate concrete*, Construction and Building Materials **43**, 506 (2013).
- [4] R. Bucher, P. Diederich, G. Escadeillas, and M. Cyr, *Service life of metakaolin-based concrete exposed to carbonation: Comparison with blended cement containing fly ash, blast furnace slag and limestone filler*, Cement and Concrete Research **99**, 18 (2017).
- [5] V. Shah and S. Bishnoi, *Carbonation resistance of cements containing supplementary cementitious materials and its relation to various parameters of concrete*, Construction and Building Materials **178**, 219 (2018).
- [6] B. Wu and G. Ye, *Development of porosity of cement paste blended with supplementary cementitious materials after carbonation*, Construction and Building Materials **145**, 52 (2017).
- [7] H. Justnes, J. Skocek, T. A. Østnor, C. J. Engelsen, and O. Skjølvold, *Microstructural changes of hydrated cement blended with fly ash upon carbonation*, Cement and Concrete Research **137**, 106192 (2020).
- [8] J. Ibáñez, L. Artús, R. Cuscó, López, E. Menéndez, and M. C. Andrade, *Hydration and carbonation of monoclinic C₂S and C₃S studied by Raman spectroscopy*, Journal of Raman Spectroscopy **38**, 61 (2007).
- [9] G. W. Groves, A. Brough, I. G. Richardson, and C. M. Dobson, *Progressive changes in the structure of hardened C₃S cement pastes due to carbonation*, Journal of the American Ceramic Society **74**, 2891 (1991).

- [10] D. Wang, C. Xiong, W. Li, and J. Chang, *Growth of calcium carbonate induced by accelerated carbonation of tricalcium silicate*, ACS Sustainable Chemistry Engineering **8**, 14718 (2020).
- [11] S. A. Bernal, R. M. De Gutierrez, J. L. Provis, and V. Rose, *Effect of silicate modulus and metakaolin incorporation on the carbonation of alkali silicate-activated slags*, Cement and Concrete Research **40**, 898 (2010).
- [12] F. Begarin, S. Garrault, A. Nonat, and L. Nicoleau, *Hydration of alite containing aluminium*, Advances in Applied Ceramics **110**, 127 (2011).
- [13] B. Mota, T. Matschei, and K. Scrivener, *The influence of sodium salts and gypsum on alite hydration*, Cement and Concrete Research **75**, 53 (2015).
- [14] G. Villain, M. Thiery, and G. Platret, *Measurement methods of carbonation profiles in concrete: Thermogravimetry, chemical analysis and gammadensimetry*, Cement and Concrete Research **37**, 1182 (2007).
- [15] M. Thiery, G. Villain, P. Dangla, and G. Platret, *Investigation of the carbonation front shape on cementitious materials: Effects of the chemical kinetics*, Cement and Concrete Research **37**, 1047 (2007).
- [16] A. Morandau, M. Thiery, and P. Dangla, *Investigation of the carbonation mechanism of CH and CSH in terms of kinetics, microstructure changes and moisture properties*, Cement and Concrete Research **56**, 153 (2014).
- [17] T. F. Sevelsted and J. Skibsted, *Carbonation of C–S–H and C–A–S–H samples studied by ^{13}C , ^{27}Al and ^{29}Si MAS NMR spectroscopy*, Cement and Concrete Research **71**, 56 (2015).
- [18] R. Hay, J. Li, and K. Celik, *Phase evolution, micromechanical properties, and morphology of calcium (alumino) silicate hydrates C-(A-)S-H under carbonation*, Cement and Concrete Research **152**, 106683 (2022).
- [19] B. Wu and G. Ye, *Study of carbonation rate of synthetic CSH by XRD, NMR and FTIR*, Heron **64**, 21 (2019).
- [20] M. Zajac, A. Lechevallier, P. Durdzinski, F. Bullerjahn, J. Skibsted, and M. B. Haha, *CO₂ mineralisation of portland cement: Towards understanding the mechanisms of enforced carbonation*, Journal of Co2 Utilization **38**, 398 (2020).
- [21] L. Black, C. Breen, J. Yarwood, K. Garbev, P. Stemmermann, and B. Gasharova, *Structural features of C–S–H (I) and its carbonation in air—a raman spectroscopic study. Part II: carbonated phases*, Journal of the American Ceramic Society **90**, 908 (2007).
- [22] E. T. Stepkowska, J. Pérez-Rodríguez, M. Sayagues, and J. Martínez-Blanes, *Calcite, vaterite and aragonite forming on cement hydration from liquid and gaseous phase*, Journal of thermal analysis calorimetry **73**, 247 (2003).

- [23] W. Chen and H. Brouwers, *The hydration of slag, part 2: reaction models for blended cement*, Journal of Materials Science **42**, 444 (2007).
- [24] S. Miyata, *Physico-chemical properties of synthetic hydrotalcites in relation to composition*, Clays and Clay minerals **28**, 50 (1980).
- [25] S. Miyata, *Anion-exchange properties of hydrotalcite-like compounds*, Clays and Clay minerals **31**, 305 (1983).
- [26] W. T. Reichle, *Synthesis of anionic clay minerals (mixed metal hydroxides, hydrotalcite)*, Solid State Ionics **22**, 135 (1986).
- [27] B. O. Mysen, F. J. Ryerson, and D. Virgo, *The influence of TiO₂ on the structure and derivative properties of silicate melts*, American Mineralogist **65**, 1150 (1980).
- [28] Y. Sun, Z. Zhang, L. Liu, and X. Wang, *FTIR, Raman and NMR investigation of CaO–SiO₂–P₂O₅ and CaO–SiO₂–TiO₂–P₂O₅ glasses*, Journal of Non-Crystalline Solids **420**, 26 (2015).
- [29] G. H. Kim and I. Sohn, *Effect of Al₂O₃ on the viscosity and structure of calcium silicate-based melts containing Na₂O and CaF₂*, Journal of Non-Crystalline Solids **358**, 1530 (2012).
- [30] S. M. Han, J. G. Park, and I. Sohn, *Surface kinetics of nitrogen dissolution and its correlation to the slag structure in the CaO–SiO₂, CaO–Al₂O₃, and CaO–SiO₂–Al₂O₃ slag system*, Journal of non-crystalline solids **357**, 2868 (2011).
- [31] Y. Okada, T. Masuda, M. Takada, L. Xu, and T. Mitsuda, *Relationship between NMR ²⁹Si chemical shifts and FT-IR wave numbers in calcium silicates*, in *Nuclear magnetic resonance spectroscopy of cement-based materials* (Springer, 1998) pp. 69–78.
- [32] W. Ashraf and J. Olek, *Carbonation behavior of hydraulic and non-hydraulic calcium silicates: potential of utilizing low-lime calcium silicates in cement-based materials*, Journal of materials science **51**, 6173 (2016).
- [33] M. Zajac, J. Skibsted, P. Durdzinski, F. Bullerjahn, J. Skocek, and M. B. Haha, *Kinetics of enforced carbonation of cement paste*, Cement and Concrete Research **131**, 106013 (2020).
- [34] C. W. Hargis, B. Lothenbach, C. J. Müller, and F. Winnefeld, *Carbonation of calcium sulfoaluminate mortars*, Cement and Concrete Composites **80**, 123 (2017).
- [35] S. Kucharczyk, M. Zajac, and J. Deja, *The influence of limestone and Al₂O₃ content in the slag on the performance of the composite cements*, Procedia Engineering **108**, 402 (2015).
- [36] S. Kucharczyk, M. Zajac, C. Stabler, R. M. Thomsen, M. Ben Haha, J. Skibsted, and J. Deja, *Structure and reactivity of synthetic CaO–Al₂O₃–SiO₂ glasses*, Cement and Concrete Research **120**, 77 (2019).

- [37] S. Blotevogel, A. Ehrenberg, L. Steger, L. Doussang, J. Kaknics, C. Patapy, and M. Cyr, *Ability of the R3 test to evaluate differences in early age reactivity of 16 industrial ground granulated blast furnace slags (GGBS)*, *Cement and Concrete Research* **130**, 105998 (2020).
- [38] M. Whittaker, M. Zajac, M. Ben Haha, F. Bullerjahn, and L. Black, *The role of the alumina content of slag, plus the presence of additional sulfate on the hydration and microstructure of Portland cement-slag blends*, *Cement and Concrete Research* **66**, 91 (2014).
- [39] M. B. Haha, B. Lothenbach, G. Le Saout, and F. Winnefeld, *Influence of slag chemistry on the hydration of alkali-activated blast-furnace slag — Part II: Effect of Al_2O_3* , *Cement and Concrete Research* **42**, 74 (2012).
- [40] I. Richardson, *Tobermorite/jennite-and tobermorite/calcium hydroxide-based models for the structure of CSH: applicability to hardened pastes of tricalcium silicate, -dicalcium silicate, portland cement, and blends of portland cement with blast-furnace slag, metakaolin, or silica fume*, *Cement and Concrete Research* **34**, 1733 (2004).
- [41] J. Li, Q. Yu, H. Huang, and S. Yin, *Effects of Ca/Si ratio, aluminum and magnesium on the carbonation behavior of calcium silicate hydrate*, *Materials* **12**, 1268 (2019).
- [42] L. Irbe, R. Beddoe, H. Hilbig, and D. Heinz, *The role of aluminium in CASH during chemical attack on concrete*, in *Second International Conference on the Chemistry of Construction Materials-ICCCM 2016*.
- [43] E. Kangni Foli, S. Poyet, P. Le Bescop, T. Charpentier, A. Dauzeres, and J.-B. D'espinoise de Lacaillerie, *Calcium alumino-silicates hydrates (CASH) carbonation kinetics*, in *ICCC 2019-15th International Congress on the Chemistry of Cement*.
- [44] M. B. Haha, B. Lothenbach, G. Le Saout, and F. Winnefeld, *Influence of slag chemistry on the hydration of alkali-activated blast-furnace slag — Part I: Effect of MgO*, *Cement and Concrete Research* **41**, 955 (2011).
- [45] S. A. Bernal, R. San Nicolas, R. J. Myers, R. M. de Gutiérrez, F. Puertas, J. S. van Deventer, and J. L. Provis, *MgO content of slag controls phase evolution and structural changes induced by accelerated carbonation in alkali-activated binders*, *Cement and Concrete Research* **57**, 33 (2014).
- [46] B. Walkley, R. San Nicolas, M.-A. Sani, S. A. Bernal, J. S. van Deventer, and J. L. Provis, *Structural evolution of synthetic alkali-activated $CaO-MgO-Na_2O-Al_2O_3-SiO_2$ materials is influenced by Mg content*, *Cement and Concrete Research* **99**, 155 (2017).
- [47] G. G. Litvan, *Variability of the nitrogen surface area of hydrated cement paste*, *Cement and Concrete Research* **6**, 139 (1976).

- [48] S. Walspurger, P. D. Cobden, O. V. Safonova, Y. Wu, and E. J. Anthony, *High CO₂ storage capacity in alkali-promoted hydrotalcite-based material: In situ detection of reversible formation of magnesium carbonate*, *Chemistry–A European Journal* **16**, 12694 (2010).
- [49] P. Sahoo, S. Ishihara, K. Yamada, K. Deguchi, S. Ohki, M. Tansho, T. Shimizu, N. Eisaku, R. Sasai, and J. Labuta, *Rapid exchange between atmospheric CO₂ and carbonate anion intercalated within magnesium rich layered double hydroxide*, *ACS applied materials interfaces* **6**, 18352 (2014).
- [50] X. Liu, P. Feng, Y. Cai, X. Yu, C. Yu, and Q. Ran, *Carbonation behavior of calcium silicate hydrate (CSH): Its potential for CO₂ capture*, *Chemical Engineering Journal* **431**, 134243 (2022).

7

EFFECT OF MgO CONTENT ON THE QUANTITATIVE ROLE OF HYDROTALCITE-LIKE PHASE IN A CEMENT-SLAG SYSTEM DURING CARBONATION

This chapter was designed to study the influence of MgO content of slag on the carbonation characteristics of cement-slag system where slag was used as a primary SCM (70 wt.% replacement to simulate CEM III/B). To avoid potential interferences from other factors, synthetic slags with different MgO contents manufactured in the laboratory were used to produce the cement-slag system. The phase assemblage, microstructure, and micro-mechanical properties of each mixture before and after accelerated carbonation testing were compared. Through quantitative analysis of hydrotalcite-like phase, the effect of MgO content in slag on carbonation characteristics was highlighted.

Parts of this chapter were published in Cement and Concrete Composites **134**, 104765 (2022) [1] and Materials **15**, 6347 (2022) [2].

7.1. INTRODUCTION

As discussed in Chapter 2, due to the heterogeneity of raw materials fed into the furnace, the production technology and standard formulation, the chemical composition and property of slag vary -as an end product- from location to location. Questions regarding the effect of slag components on the evolution of phase assemblages, microstructure development and *durability* of cement-slag systems are of great interest. A further insight into slag chemistry could help design slag-rich concrete structures with high durability-related performance.

Generally, the amount of MgO in European slag varies from approximately 0 to 17 wt.%, according to [3]. Based on [4, 5], it was in the range of 5~15 wt.% in North America. The MgO content of slag produced in Austria was a little lower, typically ≤ 10 wt.%. In fact, the MgO content of slag was directly related to the composition of flux agent (essentially limestone and dolomite) added into the furnace, which was matched to the melting rate of iron ore in order to achieve a lower melting point, thin-bodied and iron-free blast furnace slag [6]. To lower the liquidus temperature of molten phase for metallurgical reasons [7–9], increasing the amount of limestone over dolomitic rocks have been preferred, leading to the emerging trend that only lime-rich and magnesium-poor slag has been produced and used in cement production (see discussion in Chapter 3). According to the European standard EN 15167-1, it is required that $(\text{CaO}+\text{MgO})/\text{SiO}_2 > 1$, which means that the effect of MgO in slag is considered similar to that of CaO, and a deficiency in one component could be compensated by the other. From this perspective, the gradual change in slag composition mentioned earlier should not impose any adverse effect on its engineering properties.

In the past decade much more effort has been devoted to investigating the effect of MgO content of slag on the evolution of phase assemblages of alkali-activated slag (AAS) systems [10–13]. Some common conclusions identified were: gradual increase of MgO content in slag increases the amount of hydrotalcite-like phase formed and lowers the aluminum content uptake by C-S-H gel phase. However, to the best of authors' knowledge, few investigations went deep into the correlation between *slag chemistry* and *durability characteristics* of slag-containing cementitious systems. The works in [14, 15] confirmed that the formation of hydrotalcite-like phase could reduce the susceptibility to carbonation of AAS produced with higher MgO content, as it appeared to act as an internal CO₂ sorbent. Results in [16] revealed that a higher MgO content slag precursor for AAS had shown higher resistance to accelerated carbonation-induced degradation due to the improvement in the resistance to gel decalcification and capillary pore formation during carbonation. Questions, such as whether the observations on the AAS systems could be extended to slag-rich cement systems directly remain to be addressed. Additionally, researchers recognized the beneficial effect of hydrotalcite-like phase during carbonation; however, most analysis was qualitative. Therefore, understanding the effect of hydrotalcite-like phase quantitatively during carbonation is vital towards achieving the full potential of slag performance in concrete.

Thus, this chapter was designed to study the influence of MgO content of slag on the carbonation characteristics of cement-slag system where slag was used as a primary SCM (70 wt.% replacement to simulate CEM III/B). To avoid potential interferences

from other factors, synthetic slags with different MgO contents manufactured in the laboratory were used to produce the cement-slag system. The phase assemblage, microstructure, and micro-mechanical properties of each mixture before and after accelerated carbonation testing were compared. Through quantitative analysis of hydrotalcite-like phase, the effect of MgO content in slag on carbonation characteristics was highlighted.

7.2. MATERIALS AND METHODOLOGY

7.2.1. MATERIALS

SYNTHETIC slags with different MgO contents (M0, M8, and M16) and CEM I 42,5 N were used to produce cement-slag system.

The properties of CEM I 42,5 N was introduced in Chapter 5. For chemical composition and particle size distribution of synthetic slags, please refer to Chapter 4. Their CaO/SiO₂ ratios were kept at around 1 and the amounts of Al₂O₃ fluctuated at about 14 wt.%, while MgO content varied from 0.33 (for M0) to 16.07 wt.% (for M16). Quartz with a similar PSD was also introduced to cast an cement-quartz sample, acting as a reference.

7.2.2. METHODOLOGY

Similarly, cement was partially replaced by slag and quartz at a constant substitution level of 70 wt.%. The paste mixtures were prepared using a water to binder ratio of 0.40 and cast in cylindrical plastic containers of 20 mL, which were sealed with thin para film to prevent further ingress of CO₂ and evaporation of mixing water. All specimens were stored at 20±3 °C until further use.

After 3 months of curing, specimens of each mixture were taken out of the plastic bottles, the top surface (~5 mm in thickness) of which were removed after demoulding. Before transferring them to the carbonation chamber, the specimens were conditioned for one month in a RH-controlled climate chamber at 65% and 20 °C for pretreatment. Only the freshly cut surfaces were exposed to CO₂ and the other surfaces were sealed to ensure one dimensional gas penetration. Accelerated carbonation testing was performed in a carbonation chamber with regulated CO₂ concentration of 3%±0.2, at 20±3 °C and 65±5% of RH (using saturated NaNO₂ solution). The total duration of carbonation was up to 6 months.

After the designated hydration and carbonation periods, small discs were sawn from the specimens, crushed and immersed in isopropanol solution to exchange the available pore solution. For the detailed information about XRD and TGA-MS measurements, please refer to Chapter 5. As for FTIR analysis, the same procedure was employed according to the description in Chapter 6.

Mercury intrusion porosimetry (MIP) analysis was carried out on small paste samples. The relationship between pore diameter (D) and pore pressure (P) is given in Washburn equation as the following Equation 7.1 shows,

$$P = \frac{-4\gamma\cos(\theta)}{D} \quad (7.1)$$

of which the surface tension of mercury (γ) is 0.485 N/m at 25 °C and the contact angle between mercury and specimen (θ) is 140°. Three steps were involved in each measurement process, i.e., mercury intrusion at low pressure from 0 to 0.170 MPa; at high pressure from 0.170 to 210 MPa; and mercury extrusion. According to the equation, the maximum pressure achieved by the equipment corresponded to a minimal pore diameter of about 7 nm, based on a cylindrical pore model. Therefore, pores below this size cannot be detected.

SEM-EDS investigation was performed on selected samples prepared following the descriptions in Chapter 3.

The basic principle of nanoindentation is to press a tip with known properties into a material at a small scale. To obtain the micro-mechanical properties, i.e., modulus of elasticity and hardness, of slag cement paste before and after the accelerated carbonation testing, nanoindentation performed with Agilent Nano Indenter G200 (Keysight, Santa Rosa, CA, USA) equipped with a berkovich tip was used. The Continuous Stiffness Method (CSM) developed by Oliver and Pharr [17] was adopted to evaluate the indentation modulus E of different phases. This method superimposes a small oscillation on the primary loading signal and analyzes the response through a frequency-specific amplifier. It allows for the continuous measurement of contact stiffness throughout the indentation depth, which was set to 2000 nm in the study.

Thermodynamic modelling was also carried out using the Gibbs free energy minimization software GEMS [18, 19] with the thermodynamic data from PSI-GEMS database [20, 21] supplemented by cement specific data [22, 23]. The calcium-alkali aluminosilicate hydrate ideal solid solution model (CNASHss) proposed by Myers et al. [24] was employed to describe the C-S(A)-H gel phase in the system. MgAl-OH-LDHss containing three end-members with Mg/Al atomic ratios of 2, 3, and 4 reformulated into an ideal solid solution was employed to simulate the formation of hydrotalcite-like phase before carbonation [25]. For their corresponding carbonate forms, the database provided by [26] was incorporated in the model as candidate phases. The thermodynamic properties of these carbonate forms were calculated based on the ion-exchange constant provided by [27].

7.3. RESULTS

7.3.1. PHENOLPHTHALEIN SPRAY

THE typical cross-sectional surfaces of the specimens after phenolphthalein spray are shown in Figure 7.1. As can be seen, the carbonation depth decreased significantly with the increasing MgO content in slag, from more than 20 mm for slag M0 paste reduced to approximately 5 mm for slag M16 paste.

7.3.2. CARBONATION PRODUCTS

In this section, the authors characterized the carbonation products of slag cement paste by means of a series of analytical techniques. Powders used for tests were extracted within the 3 mm depth from the surface of the specimens exposed in the carbonation chamber to ensure (nearly) full carbonation as much as possible.

TG-DTG-MS

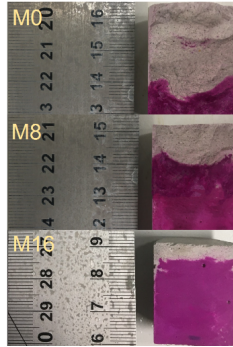


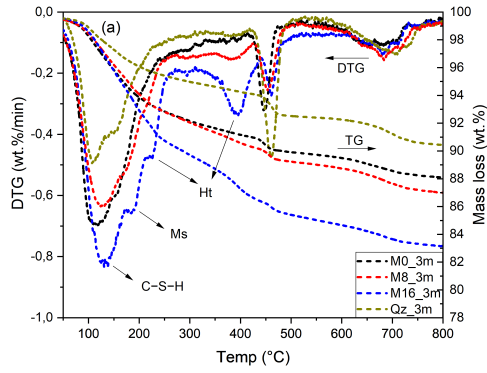
Figure 7.1: Typical sawn surfaces of the specimens after spraying with phenolphthalein solution.

TG-DTG results of cement-slag and -quartz mixtures after 3 months of curing are shown in Figure 7.2(a). The highest hydrotalcite-like phase content was detected in slag M16 mixture with a shoulder and a distinct peak located at approximately 250 and 350 °C, respectively. Conversely, there was no hydrotalcite-like phase observed in slag M0 mixture as negligible MgO was available in slag M0. The broad peak at 100-150 °C suggested the presence of C-S(A)-H gel phase. The shoulder at ~200 °C indicated the formation of monosulfate, sourced from the transformation of ettringite with time.

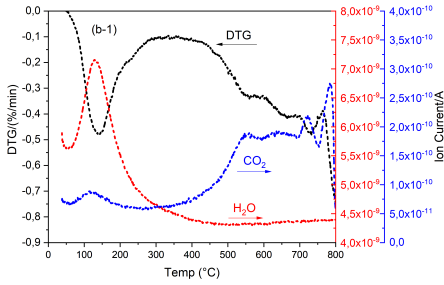
The DTG results, H₂O and CO₂ MS curves of fully carbonated cement-slag M0, M8, M16, and Qz pastes are plotted in Figure 7.2(b)-7.2(e), respectively. The main CO₂-bearing phase in Qz paste after carbonation was calcium carbonate, and three decomposition peaks starting from 500 °C in the DTG graph implied the presence of CaCO₃ of different polymorphs, all of which were commonly seen in the accelerated carbonation test [28–30]. No monosulfate was left, suggesting that it had been carbonated completely. Additionally, there were two new CO₂-bearing phases occurred upon carbonation of cement-slag paste. One was a carbonated hydrotalcite-like phase. The peak located at 350-450 °C indicated the persistence of hydrotalcite-like phase in slag M8 and M16 blends after carbonation. As displayed in the MS curves, both H₂O and CO₂ were liberated from this phase after heating, meaning that CO₂ was absorbed in the interlayer space to form its carbonate version, i.e., carbonated hydrotalcite-like phase. The small peak at ~150 °C in the MS CO₂ curve can be ascribed to the formation of carbonated Ca-Al AFm phases, due to the carbonation of AFm-OH and/or AFm-SO₄ phases (It was discussed in detail in Section 5.4.1). This peak was negligible in Qz mixture, partially because of its reduced monosulfate formation compared to cement-slag pastes.

XRD

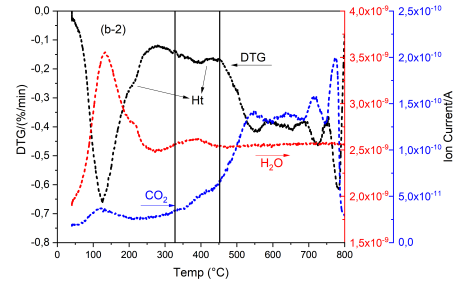
XRD results reveal the presence of hydrotalcite-like phase, monosulfate, portlandite, and unhydrated cement clinker (C₃S and β-C₂S in particular) in cement-slag system after hydration (Figure 7.3(a) and 7.3(c)). Intensity of the peak indicating portlandite became weaker with the gradual addition of MgO in slag, suggesting a higher reactivity of slag with more MgO incorporation, which led to a higher portlandite consumption during the pozzolanic reaction (see Chapter 4). Also, the peak for hydrotalcite-like



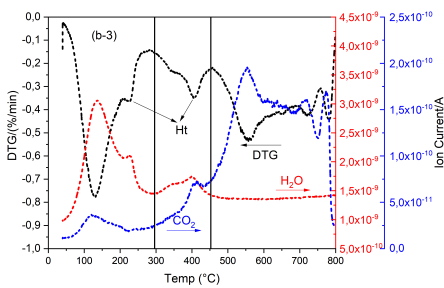
(a)



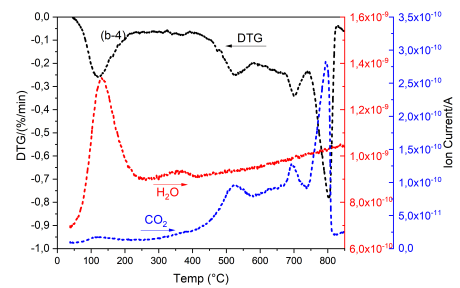
(b)



(c)



(d)



(e)

Figure 7.2: (a) TG and DTG results of cement-slag and quartz mixtures after 3 months of curing; (b)-(e) DTG results, H₂O and CO₂ MS curves of fully carbonated cement-slag M0, M8, M16, and Qz pastes, respectively.

phase was much more visible in slag M16 blend, consistent with the results measured by TGA in Figure 7.2(a).

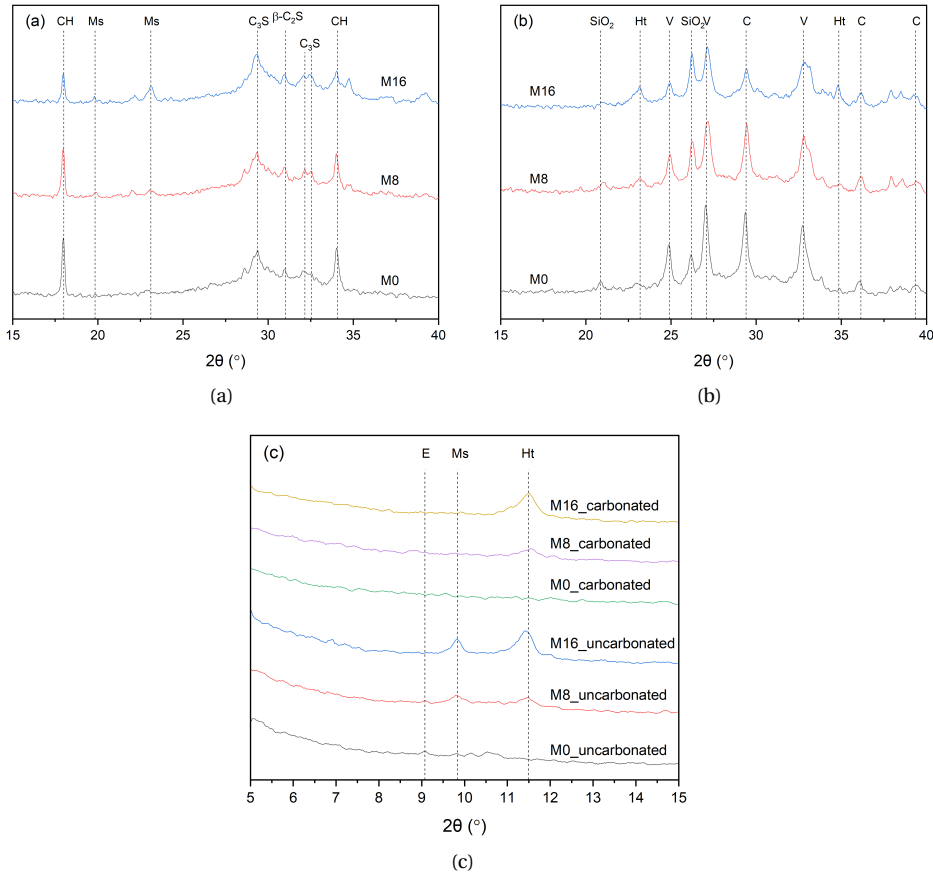


Figure 7.3: XRD analysis of cement-slag blends (a) after curing of 3 months; (b) after carbonation; and (c) 5 to 15° (2θ) of cement-slag blends before and after carbonation. CH: portlandite; E: ettringite; Ht: hydrotalcite-like phase. V: vaterite; C: calcite. The peak centered at around $2\theta = 21$ and 26° appeared to be associated with the formation of silica gel (labelled as SiO₂) [31] due to the carbonation of C-S(A)-H gel phase.

After the accelerated carbonation exposure (Figure 7.3(b) and 7.3(c)), the peak for portlandite disappeared in all mixtures, meaning that all calcium hydroxide had been carbonated, in agreement with the results measured by TGA (Figure 7.2(b) to 7.2(d)). Furthermore, the peak for unhydrated cement clinker also vanished, probably related to its continuous hydration or carbonation [32].

Hydrotalcite-like phase was still observed after such a heavy CO₂ attack while monosulfate was decomposed, as the peak of which disappeared after carbonation (Figure 7.3(c)). These results matched well with the findings revealed by TGA. Calcite and Vaterite were identified as the main polymorphs of CaCO₃ in all carbonated pastes. No trace of aragonite was found by XRD in these samples.

FTIR

FTIR was also used to investigate the carbonation products of cement-slag mixtures, especially for the alteration of C-S(A)-H gel phase at molecular level. Figure 7.4 illustrates the FTIR spectra of cement-slag mixtures before and after carbonation. The absorption bands between $3700\text{--}2500\text{ cm}^{-1}$ and at 1640 cm^{-1} indicated the presence of O-H bonds, associated with the stretching and bending vibration modes of H_2O [33], respectively. Because of drying, the intensity of water-related bonds decreased.

Regardless of the MgO content in slag, Q2 was the main unit of C-S(A)-H gel phase of all investigated cement-slag pastes before carbonation. After full carbonation, the Si-O-T stretching band was characterized by observing signals appearing at ~ 1200 and $\sim 1100\text{ cm}^{-1}$, which were linked with the yield of Q4 and Q3 silicate units, respectively. This shift was associated with the gradual polymerization of silicate units, due to the carbonation-induced decalcification of C-S(A)-H gel phase [34–36].

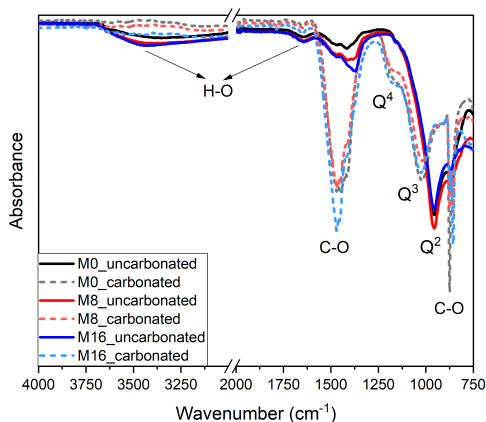


Figure 7.4: The FTIR spectra of cement-slag mixtures before and after carbonation, (Normalized, %).

The carbonate bonds were also recorded through three types of carbonate bands observed in the FTIR spectra, i.e., strong broad band at $1400\text{--}1500\text{ cm}^{-1}$, representing the asymmetric stretching of carbonate, narrow band at $875\text{--}1000\text{ cm}^{-1}$ due to the bending of carbonate, and in-plane bending of carbonate at $\sim 710\text{ cm}^{-1}$ (not shown in the graph) [37]. It was found that carbonate band was more pronounced in cement-slag M16 paste, confirmed by the increased band intensity at $1400\text{--}1500\text{ cm}^{-1}$.

7.3.3. DEGREE OF CO_2 UPTAKE OF DIFFERENT CARBONATE PHASES

To calculate the CO_2 concentration in each carbonate phase at different depths, besides that taken from 0–3 mm depth from the surface corresponding to (nearly) full carbonation (labelled as 1), powders were also extracted from carbonation front corresponding roughly to transitional/dissolution area (labelled as 2) [38], and mildly/non-carbonated area (labelled as 3), respectively as Figure 7.5 shows.

To keep consistent with the work in Section 6.3.2, pure CaCO_3 was employed as a standard to calibrate the CO_2 concentration in different CO_2 -bearing phases under the same analytical condition. Figure 7.6(a)–7.6(c) present the CO_2 uptake profile of slag

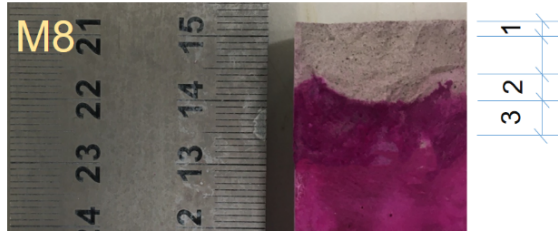


Figure 7.5: The positions where powders were extracted, using slag M8 paste as an example. 1: fully carbonated area; 2: transitional area; 3: mildly carbonated area.

Table 7.1: The calculated areas under the MS CO₂ curve of different carbonate phases.

		Area under the MS CO ₂ curve			Total
		Carbonated Ca-Al AFm phases	Carbonated hydrotalcite-like phase	Calcium carbonate	
Mildly carbonated	M0	$4.79 \cdot 10^{-10}$	-	$9.37 \cdot 10^{-9}$	$9.85 \cdot 10^{-9}$
	M8	$3.23 \cdot 10^{-10}$	$1.18 \cdot 10^{-9}$	$7.67 \cdot 10^{-9}$	$9.17 \cdot 10^{-9}$
	M16	$3.68 \cdot 10^{-10}$	$1.59 \cdot 10^{-9}$	$6.47 \cdot 10^{-9}$	$8.43 \cdot 10^{-9}$
Transitional	M0	$6.55 \cdot 10^{-10}$	-	$2.59 \cdot 10^{-8}$	$2.65 \cdot 10^{-8}$
	M8	$4.58 \cdot 10^{-10}$	$2.92 \cdot 10^{-9}$	$1.79 \cdot 10^{-8}$	$2.12 \cdot 10^{-8}$
	M16	$7.24 \cdot 10^{-10}$	$3.06 \cdot 10^{-9}$	$1.31 \cdot 10^{-8}$	$1.69 \cdot 10^{-8}$
Fully carbonated	M0	$2.91 \cdot 10^{-9}$	-	$3.92 \cdot 10^{-8}$	$4.21 \cdot 10^{-8}$
	M8	$2.05 \cdot 10^{-9}$	$4.00 \cdot 10^{-9}$	$3.99 \cdot 10^{-8}$	$4.60 \cdot 10^{-8}$
	M16	$2.58 \cdot 10^{-9}$	$6.64 \cdot 10^{-9}$	$4.58 \cdot 10^{-8}$	$5.50 \cdot 10^{-8}$
	Qz	$1.50 \cdot 10^{-9}$	-	$3.81 \cdot 10^{-8}$	$3.96 \cdot 10^{-8}$
Pure CaCO ₃		-	-	$1.09 \cdot 10^{-7}$	$1.09 \cdot 10^{-7}$

M16 paste at the specific sampling depths. The area A1, A2, and A3 corresponded to the amount of CO₂ released from carbonated Ca-Al AFm phases, carbonated hydrotalcite-like phase, and calcium carbonate, respectively.

The calculated areas under the MS CO₂ curves, as well as the CO₂ concentrations of the paste samples and calibration reagent are shown in Table 7.1 and 7.2, respectively. It was noticed that monosulfate and its carbonated form, i.e., carbonated Ca-Al AFm phases, played a minor role in absorbing CO₂, while the CO₂ binding capacity (data adapted from the full carbonation area) of each mixture was mainly dependent on the available CaO in portlandite and C-S(A)-H gel phase. The role of hydrotalcite-like phase in absorbing CO₂ started to emerge with the gradual addition of MgO in slag, and its binding ability was positively related to its content after hydration. It should be noted that the most hydrotalcite-like phase was detected in slag M16 paste (Figure 7.2(a) and 7.3(a)), where it was able to absorb up to ~2.68 g/100 g paste CO₂ in the interlayer space.

Moreover, it was interesting to find that the highest amount of CO₂ was bound in slag M16 paste in the fully carbonated area. On the other hand, the same paste absorbed the least amount of CO₂ in the mildly carbonated and transitional areas, compared to the other mixtures.

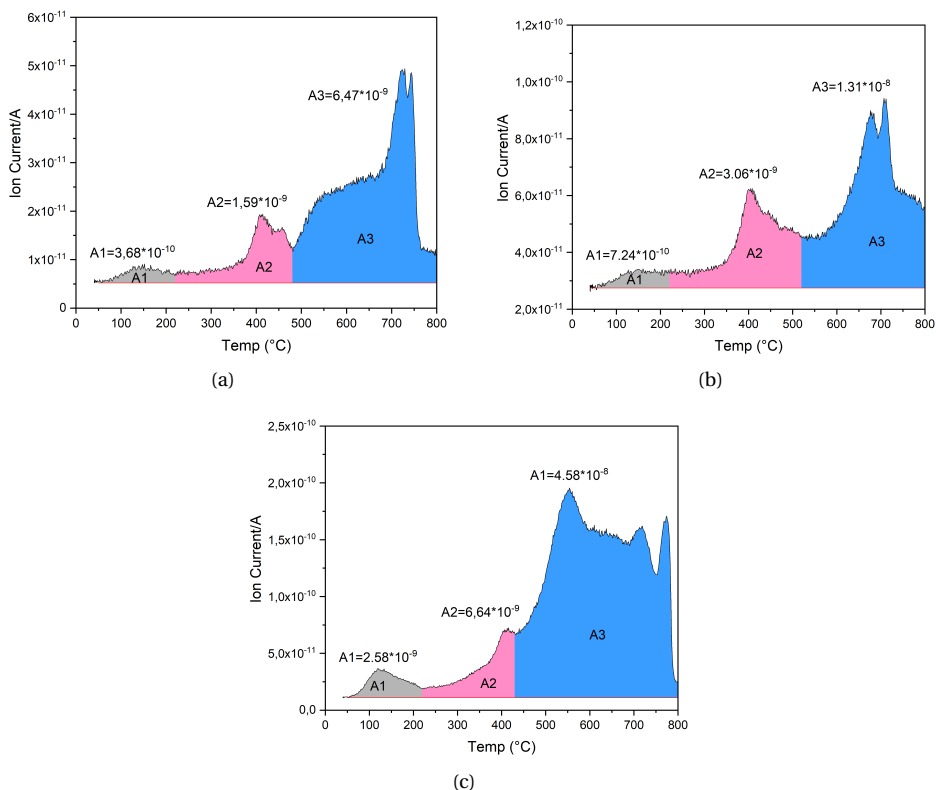


Figure 7.6: (a)-(c) The CO₂ MS curve of carbonated slag M16 paste at mildly carbonated, transitional, and fully carbonated areas, respectively.

Table 7.2: CO₂ concentrations of different carbonate phases calibrated with pure CaCO₃ (/100 g).

		CO ₂ concentration of each carbonate phase			Total
		Carbonated Ca-AlAFm phases	Carbonated hydrotalcite-like phase	Calcium carbonate	
Mildly carbonated	M0	0.19	-	3.79	3.98
	M8	0.13	0.48	3.09	3.70
	M16	0.15	0.64	2.61	3.40
Transitional	M0	0.25	-	10.45	10.70
	M8	0.17	1.17	7.22	8.56
	M16	0.30	1.23	5.29	6.82
Fully carbonated	M0	1.17	-	15.82	16.99
	M8	0.85	1.61	16.11	18.57
	M16	1.03	2.68	18.49	22.20
	Qz	0.51	-	15.38	15.99
Pure CaCO ₃		-	-	44.0	44.0

7.3.4. MICROSTRUCTURE

In this section and Section 7.3.5, the author attempted to analyze the impact of carbonation on microstructure development, elemental composition of the phase assemblages and micro-mechanical evolution. Samples used for measurements were selected from the carbonated area (colorless appearance after phenolphthalein spray) for each mixture.

MIP

Relative to the cement-quartz system, hydrates formed from the reaction between portlandite and slag helped refine the pore structure, which is shown clearly in Figure 7.7(a).

Generally, the critical pore diameter of cement-slag blends was less than $0.01\ \mu\text{m}$, corresponding to medium capillary pores based on the classification put forward in [39]. The value decreased significantly with increasing MgO content in slag. Moreover, it was noted that cement-slag M0 and quartz mixtures presented a bimodal pore structure while slag M8 and M16 pastes appeared to be a unimodal one. One should keep in mind that the maximum pressure that the equipment can apply was 210 MPa, and thus pore diameter smaller than $\sim 7\ \text{nm}$ (gel pore) cannot be detected here. Therefore, it was foreseeable that the critical pore diameter of cement-slag M16 blend would be smaller than 7 nm according to the trend of curve shown in Figure 7.7(a).

After accelerated carbonation test, the critical pore diameter all shifted right to the range of $0.1\text{--}100\ \mu\text{m}$, depending on the amount of magnesia in slag. It indicated a coarser pore structure was created after carbonation, because of the carbonation of C-S(A)-H gel phase. Similar results were also reported in [31, 40–42]. The carbonation of C-S(A)-H gel phase would produce a poorly organized silica gel of a low molar volume and a certain amount of free water initially bound within the gel phase, which certainly contributed to an increase in porosity.

Besides, pores in the range of $10\text{--}100\ \mu\text{m}$ appeared in slag M0 and M8 pastes after carbonation. It was possibly ascribed to the formation of micro-cracks. Especially for the carbonation of low Ca/Si ratio C-S(A)-H gel phase originated from the pozzolanic reaction, it can produce relatively large shrinkage [43], leading to a higher potential for the formation of micro-cracks. It was also reflected by the cumulative intrusion curve shown in Figure 7.7(d). The more magnesia in slag, the lower porosity after carbonation.

SEM-BSE

Figure 7.8(a) and 7.8(b) display the typical BSE images of a well-polished slag M8 sample exposed in the carbonation chamber for one month. Apparently, the polished sample surface experienced severe CO_2 attack. Micro-cracks induced by carbonation shrinkage were visible everywhere in the matrix and connected with each other, similar to the scene commonly seen in the cracked dryland.

Calcium carbonate was also observed as the main carbonation product, and it precipitated as agglomerates or clusters (Figure 7.8(a)). When looking closely, the intergrowth carbonates manifested round-like faces and edges (Figure 7.8(b)), probably related to the formation of metastable calcium carbonate, i.e., vaterite, which was also identified by XRD scans in Figure 7.3(b). The agglomerate of small particles in the

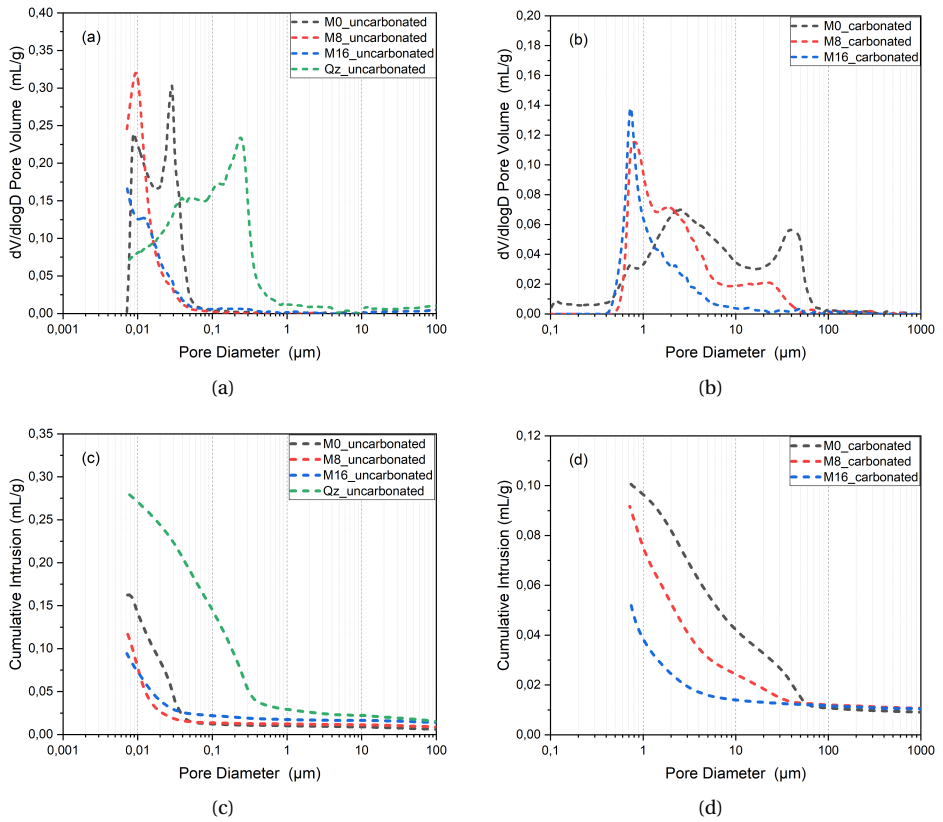


Figure 7.7: Differential pore size distribution of cement-slag and quartz systems measured (a) before and (b) after accelerated carbonation test; Cumulative intrusion of cement-slag and quartz systems measured (c) before and (d) after accelerated carbonation test.

left-bottom region of Figure 7.8(b) may be associated with the formation of amorphous calcium carbonate.

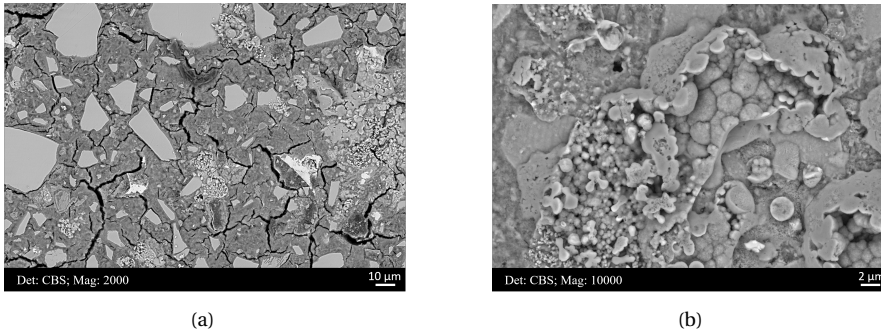


Figure 7.8: Typical BSE micrographs of a well-polished slag M8 sample surface exposed in the carbonation chamber for one month.

Figure 7.9 illustrates the typical microstructures of cement-slag pastes before and after accelerated carbonation testing (from the carbonated area). A small amount of unhydrated cement grains (circled and labelled as #1 in Figure 7.9(a)) were distributed in the matrix together with mass of unhydrated slag particles after 3 months of curing. Monosulfate existed as fine and compact crystals intermixed with C-S(A)-H gel phase (circled and labelled as #2 in Figure 7.9(a)). Slag hydrated slowly, and the hydrates precipitated at the rim of the unreacted slag particle (especially for slag M16 paste in Figure 7.9(e)), forming a dense transition with the surrounding matrix. Visually, the matrices of slag M8 and M16 pastes were more homogeneous and denser than that of slag M0.

The difference manifested in the microstructure of matrix among these slag cement pastes was even more evident after accelerated carbonation testing (Figure 7.9(b), 7.9(d), and 7.9(f)). Overall, they appeared more porous with a large quantity of black spots, indicating the formation of pores filled with epoxy resin. Moreover, slag M0 paste had developed network of wide cracks as shown in Figure 7.9(b) (To display the morphology of crack, the magnification of this BSE image was set at 1000 ×.). It verified the critical pore diameter in the range of 10-100 μm appearing in slag M0 paste after carbonation by MIP test. The most striking result was observed from the microstructure of carbonated slag M16 paste as shown in Figure 7.9(f), as the majority of microstructure was not affected by the carbonation process. Unreacted slag grains hydrated continuously under CO₂ attack, and the rim of slag after accelerated carbonation testing was significantly thicker than that before the carbonation. According to the results in [44], a demand for calcium ions was created in the pore solution during carbonation, leading to the migration of highly mobile calcium ions dissolved from unhydrated slag grains outwards, thus promoting the thickening of slag rims. One should keep in mind that the continuous hydration of slag was concluded from the thicker slag rims by observation roughly. To further verify this idea, determining the hydration degree of slag through e.g., BSE image analysis before and

after carbonation was recommended.

CHEMICAL COMPOSITION

C-S(A)-H gel phase

The elemental composition of cement matrix and rim around unhydrated slag grain were characterized before and after carbonation by SEM-EDS microanalysis with internal standards (standardless microanalysis). Typical plots of Al/Ca against Si/Ca in atomic ratio are presented in Figure 7.10. In general, the measured Ca/Si atomic ratios of C-S(A)-H gel phase after 3 months of curing fluctuated at around 1.10, irrespective of the amount of MgO incorporated into slag. It was in good agreement with the values determined in [45–47]. However, substantial decalcification occurred in the blended systems, and two different types of C-S(A)-H gel phase existed in the matrix after the accelerated carbonation exposure [48]. Especially for slag M0 paste (Figure 7.10(a)), the Ca/Si ratio reduced more significantly compared with that of slag M16 paste (Figure 7.10(b)). Besides, it was also found that the Al/Si atomic ratio of the decalcified C-S(A)-H gel phase was considerably higher than that of unaffected gel phase, further confirming the occurrence of amorphous alumina gel along with carbonation [48].

Hydrotalcite-like phase

As for hydrotalcite-like phase, it seemed to be unaffected by CO₂ attack. The Mg/Al atomic ratio derived from the regression analysis of Mg/Si vs. Al/Si scatter plot (Figure 7.11) remained nearly the same before and after carbonation. It also indicated that this phase kept intact during carbonation. In other words, the CO₂ uptake in the interlayer space would not decompose the network structure of hydrotalcite-like phase. The occurrence of scatter points with significantly higher Mg/Si and Al/Si values (circled in Figure 7.11(b)) demonstrated that slag grains in the carbonated area of M16 paste hydrated continuously during carbonation, consistent with the thicker rims illustrated by BSE image in Figure 7.9(f).

7.3.5. MICRO-MECHANICAL PROPERTIES

To obtain the micro-mechanical properties of cement matrices, especially for C-S(A)-H gel phase before and after the accelerated carbonation testing, two or three randomly chosen areas (in the carbonated area) were selected and around 800 nanoindents were made on each sample. The distance between individual indents was 40 μm. For the detailed statistical deconvolution process of the nanoindentation results, please refer to [49].

The relative frequency of indentation modulus obtained from the samples after 3 months of curing are shown in Figure 7.12(a), 7.12(c), and 7.12(e). The highest peak in the frequency histogram was quite narrow with a low variance, which was supposed to be C-S(A)-H gel phase. It was determined as 17.74±5.27 GPa for this phase in slag M0 blend. On the other hand, two C-S(A)-H gel phases were separated in the other two blends, i.e., 17.66±2.99 GPa together with 20.83±7.63 GPa in slag M8 mixture, and 21.28±2.17 GPa as well as 23.72±7.10 GPa in slag M16 mixture, corresponding to low density and high density C-S(A)-H gel phase, respectively. Meanwhile, it was noted that the peak regarding high density C-S(A)-H gel phase was a little broader, probably overlapped with neighboring phases, including low density C-S(A)-H gel phase [50–52]

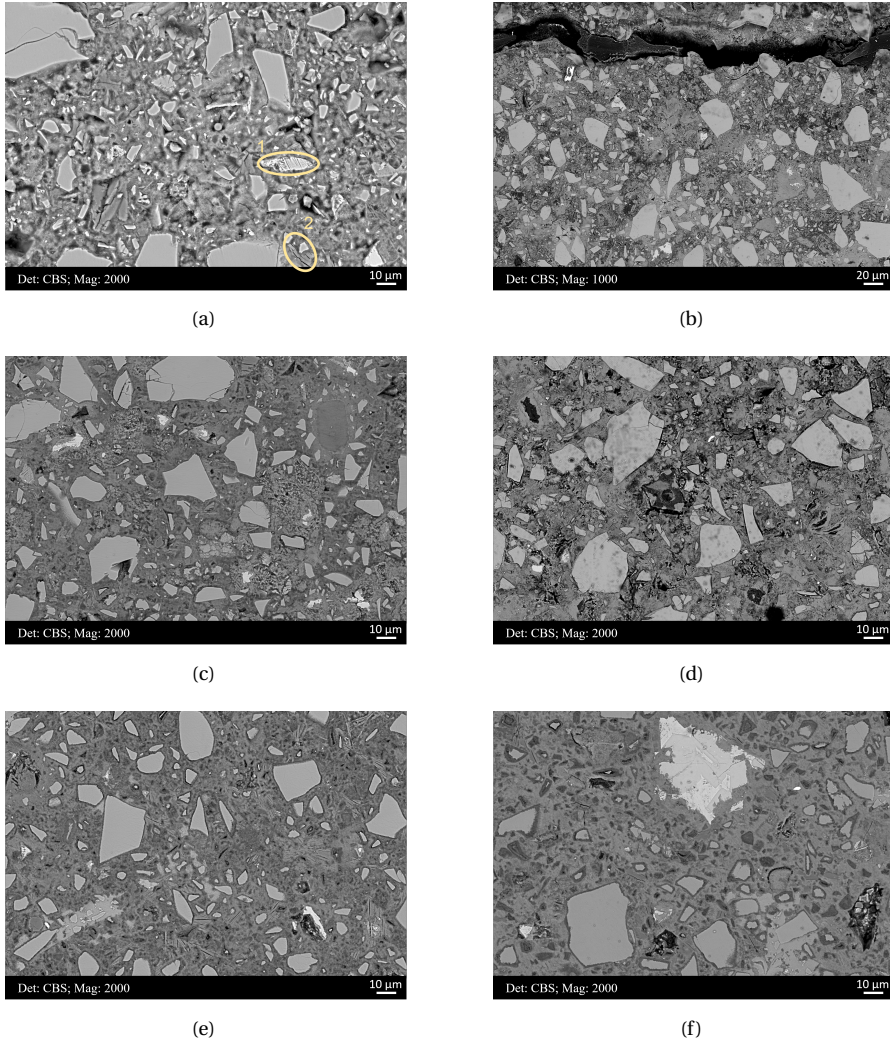


Figure 7.9: (a), (c), and (e): Microstructures of cement-slag M0, M8, and M16 mixtures after 3 months of curing, respectively; and (b), (d), and (f): Carbonated areas of cement-slag M0, M8, and M16 mixtures, respectively.

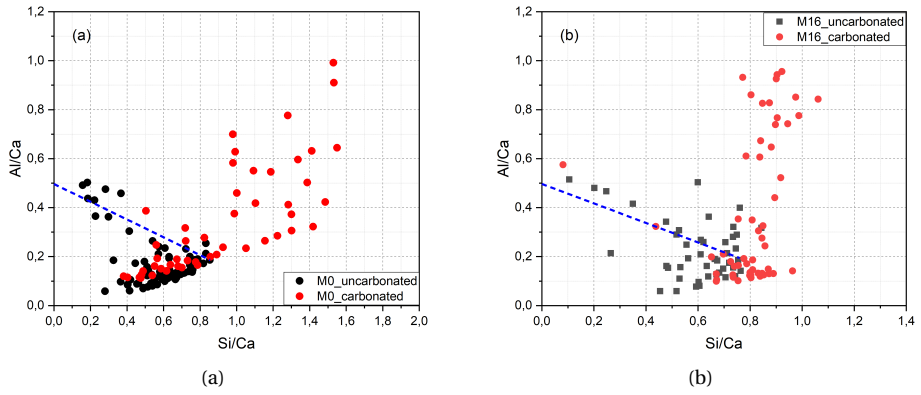


Figure 7.10: Typical plots of Al/Ca against Si/Ca in atomic ratio of slag (a) M0 and (b) M16 pastes before and after carbonation.

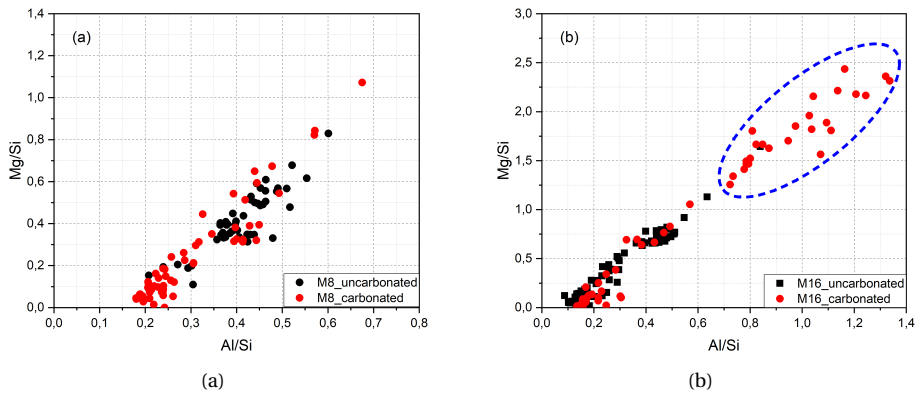


Figure 7.11: Typical plots of Mg/Si against Al/Si in atomic ratio of slag (a) M8 and (b) M16 pastes before and after carbonation.

and calcium hydroxide [53]. Moreover, the Gaussian peak below 4 GPa in slag M0 system was believed to be linked to the pores in the testing area. This peak vanished in the other two blends, implying a denser and less porous matrix was obtained. This result agreed well with the MIP measurement reported in Figure 7.7(a) and 7.7(c) and BSE micrographs illustrated in Figure 7.9(a), 7.9(c), and 7.9(e), where with the increasing MgO content of slag, the porosity of cement-slag system decreased.

The hump centered at 31.09 ± 8.95 GPa in slag M0 blend was associated with the wide presence of portlandite because of its relatively low reactivity (see Chapter 4). This small peak shifted right to 44.18 ± 14.27 GPa and 39.06 ± 14.02 GPa in slag M8 and M16 mixtures, respectively. This can be explained in two ways: (1) more portlandite was consumed by pozzolanic reaction in these two mixtures and thus more hydrotalcite-like phase was precipitated. The work in [2] found that the indentation modulus of hydrotalcite-like phase was larger than 40 GPa roughly. (2) values from unreacted slag grains (> 50 GPa commonly) were also incorporated in this broad peak.

Compared with the uncarbonated samples, the major difference occurring in the carbonated pastes was the reduction of modulus value of C-S(A)-H gel phase, due to its degradation or decalcification after CO₂ attack (Figure 7.12(b), 7.12(d), and 7.12(f)). In slag M0 and M8 blends, the frequency distribution of C-S(A)-H gel phase indentation modulus was found to exhibit a bimodal distribution, centered at 8.71 ± 3.34 GPa together with 18.07 ± 5.18 GPa for slag M0 mixture, and 11.44 ± 2.78 GPa as well as 20.08 ± 3.40 GPa for slag M8 mixture, corresponding to the degraded and unaffected C-S(A)-H gel phase, respectively. Furthermore, the frequency density of degraded C-S(A)-H gel phase even exceeded that of unaffected one in slag M0 paste after carbonation.

However, in slag M16 mixture, there was no obvious decrease observed for the indentation modulus of C-S(A)-H gel phase in the carbonated area. The corresponding values before and after carbonation were nearly the same. The result agreed with the BSE micrographs shown in Figure 7.9(f), where large areas were unaffected by carbonation.

Here in the carbonated pastes, the peak centered at around 30 GPa should include the contribution from carbonates [54, 55]. These carbonates, existing in different forms, had been found to accumulate in the pores and interact with C-S-H gel phase as well as portlandite by a strong ionic-covalent bond [56].

7.4. DISCUSSION

7.4.1. DISTRIBUTION OF MG AFTER CARBONATION

IT is well known that magnesium dissolved from slag cannot move into cement matrix during hydration owing to its low diffusion ability. Figure 7.13 reveals a typical BSE micrograph of carbonated slag M8 paste, and the Mg and Al mappings correspondingly. Compared with aluminum, magnesium appeared to be distributed within the original slag grain regions, and cannot diffuse into the matrix although C-S(A)-H gel phase surrounding slag particles was degraded remarkably. The matrix became porous after carbonation, e.g., the top left and bottom right regions of the micrograph. The results found in TGA (Figure 7.2(c) and 7.2(d)) and XRD (Figure 7.3(c)) also identified its

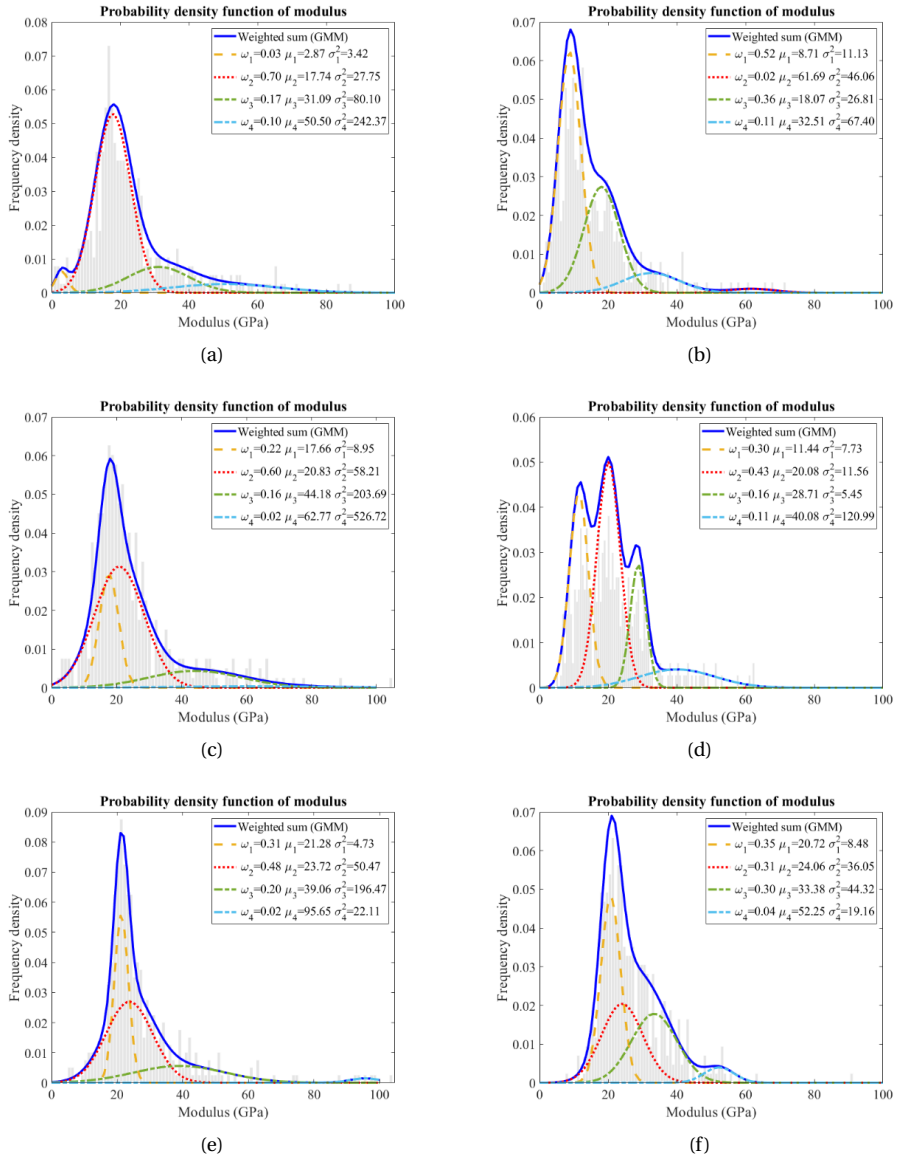


Figure 7.12: Elastic modulus of (a), (c), and (e): cement-slag M0, M8, and M16 mixtures after 3 months of curing, respectively; (b), (d), and (f): cement-slag M0, M8, and M16 mixtures after carbonation, respectively.

persistence even in the fully carbonated area. In addition, the Mg/Al atomic ratio derived from the regression analysis of Mg/Si vs. Al/Si scatter plot (Figure 7.11) remained nearly the same before and after carbonation. These findings were consistent with the results from [32], which also concluded that hydrotalcite-like phase seemed to be stable towards carbonation. Thus, it was concluded that hydrotalcite-like phase formed in slag rim was able to remain intact during carbonation.

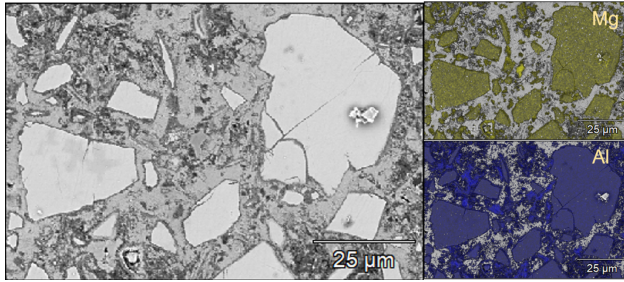


Figure 7.13: Left: a typical BSE micrograph of carbonated slag M8 paste, and right top and bottom: the Mg and Al mappings correspondingly.

It was commonly recognized that the carbonation rate of cement blended with slag was generally higher than that of pure cement due to its lower calcium hydroxide and higher C-S(A)-H gel phase content with lower Ca/Si atomic ratio [31, 57–60]. The carbonation between portlandite and CO₂ was a volume expansion reaction, and the main reaction product, i.e., different forms of calcium carbonate could help refine the pore structure, preventing the further ingress of CO₂. However, the carbonation of C-S-H gel phase was a volume shrinkage process, coarsening the pore structure and increasing the porosity [31, 42, 61]. Different from reactions mentioned above, hydrotalcite-like phase binds CO₂ in the interlayer space and maintains its network structure during carbonation, thus few volumetric changes are observed during this process [62]. From this point of view, increasing the amount of hydrotalcite-like phase produced in the system, or increasing MgO content of slag, is definitely beneficial for improving the carbonation resistance of cement-slag system.

7.4.2. CO₂ BINDING OF HYDROTALCITE-LIKE PHASE AT DIFFERENT DEPTHS

Generally, the carbonation resistance of cement-based systems is dependent on two factors: the alkali content (phase composition and particularly portlandite content) and the pore structure. Portlandite and C-S(A)-H gel phase are considered as the main CO₂ binding phases in the blended cement [63]. However, the role of hydrotalcite-like phase in absorbing CO₂ has been largely neglected, especially when the substitution level of slag is high, e.g., as in CEM III/B.

As shown in Table 7.1 and 7.2, when shifting from mildly carbonated area to fully carbonated area, the absolute amount of CO₂ absorbed in each carbonate phase increased correspondingly. However, the proportion distributed among different carbonate phases was different. The proportion of CO₂ absorbed into carbonated Ca-Al AFm phases was minor, fluctuating at less than 5%. The proportion in carbonated

hydratocite-like phase went down while the calcium carbonate share went up. It was clearly illustrated by the ratio of CO₂ amount absorbed by carbonated hydratocite-like phase to calcium carbonate (Figure 7.14). Regardless of the MgO content of slag, this ratio decreased significantly when entering into the totally carbonated area.

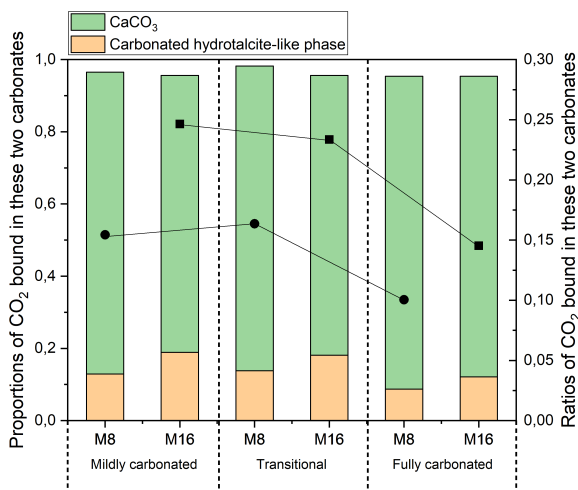


Figure 7.14: The proportion of CO₂ bound in CaCO₃ and carbonated hydratocite-like phase, and the ratio between these two phases from mildly to fully carbonated area.

It illustrates us a different routine about the carbonation sequence of hydration products in cement-slag system. Initially, hydratocite-like phase, portlandite, and C-S(A)-H gel phase absorb CO₂ synchronously. Especially for hydratocite-like phase, due to its stacked layer morphology, the space between layers presents a specific surface area comparable to that of C-S-H gel phase [64], and provides the natural site to fix free CO₂ molecules [65, 66]. It shares more than 15% CO₂ in the mildly carbonated and transitional areas, and this value is positively associated with the magnesia content of slag. Probably due to the complete carbonation of hydratocite-like phase, the proportion of CO₂ bound by hydratocite-like phase decreases in the fully carbonated area, and more CO₂ is fixed into calcium carbonate at this depth.

7.4.3. THERMODYNAMIC MODELLING

Figure 7.15(a) and 7.15(b) illustrate the evolution of phase assemblages during step-wise carbonation, using slag M0 and M16 pastes as examples. The reaction degree of clinker phases of cement at 90 days was estimated using the empirical kinetic approach proposed by Parrot [67], and the parameters were reported by Lothenbach et al. in [68]. It was also assumed that 30% slag dissolved during this period. For simplicity, it was postulated that each component of slag dissolved congruently.

At zero CO₂ addition into the system, C-S(A)-H gel phase was modelled as the main hydration product with a certain amount of hydratocite-like phase. A minor quantity of monosulfate, hydrogarnet, and strätlingite formation was also predicted. These phases agreed with the findings commonly obtained for slag cement pastes [47, 69, 70].

With the gradual addition of CO_2 into the system, the change in phase assemblage configurations started to occur. For the decalcification of C-S(A)-H gel phase, readers could refer to [26, 71]. Calcite was predicted to be the only calcium carbonate formation, although different forms of CaCO_3 were detected in the experiments. As for the carbonation of monosulfate, hemi- and mono-carbonate were predicted as the intermediates. Carbonated ettringite was estimated as the main sulfate-bearing phase, which was further carbonated to produce gypsum. However, none of them was observed either by TGA or XRD in the present research.

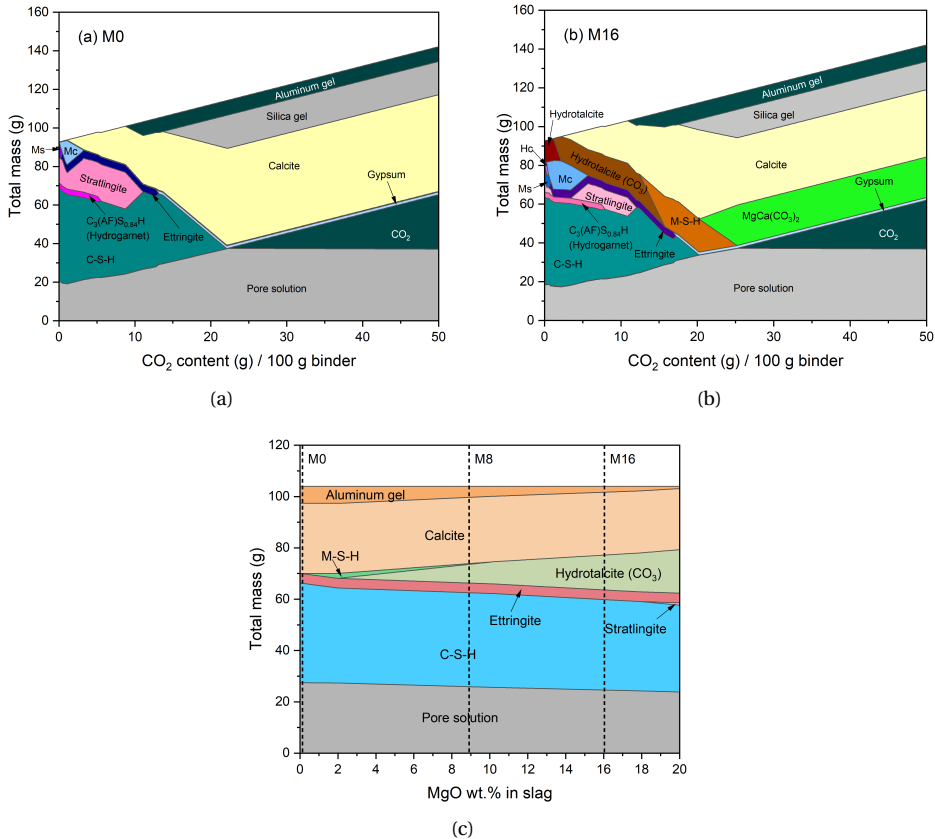


Figure 7.15: Thermodynamic modelling of the phase assemblages in slag (a) M0 and (b) M16 pastes during the step-wise carbonation; (c) Phase assemblages of cement-slag system with the gradual addition of MgO at a certain amount of CO_2 uptake (10 g CO_2 /100 g binder).

Figure 7.15(c) presents the evolution of phase assemblages at 10 g CO_2 / 100 g binder as a function of MgO content of slag. The main CO_2 -binding phase in slag M0 mixture was CaCO_3 , while more CO_2 was absorbed in hydrotalcite-like phase and less in CaCO_3 as a result in slag M16 mixture. In the initial stage, hydrotalcite-like phase was unaffected by CO_2 attack, then it transformed into the carbonate form, namely hydrotalcite-like phase (CO_3) in the graph. This phase was able to keep intact for a continuous CO_2 supply

and converted to magnesium silicate hydrate (M-S-H) gel in the later stage, and dolomite ($\text{MgCa}(\text{CO}_3)_2$) was assumed to be the final Mg-bearing phase. However, based on the experimental results in the present research, hydrotalcite-like phase would absorb CO_2 upon carbonation. Meanwhile, carbonated hydrotalcite-like phase was not observed to decompose in the study. These disagreements identified between experimental and modelling results need more research in the future.

When concentrating on carbonated hydrotalcite-like phase and calcium carbonate, thermodynamic modelling also illustrates a decreasing trend regarding the ratio of CO_2 amount bound in these two phases (C_{Ht}/C_{cc}) (Figure 7.16). This trend was consistent with the experimental results shown in Figure 7.14. Roughly, the graph can be divided into three zones where the progress of CO_2 uptake in slag cement systems can be explained. According to the experimental and modelling findings, initially, hydrotalcite-like phase starts to absorb the carbonate ions earlier due to the low solubility product of its carbonate forms [26], thus, a relatively high (C_{Ht}/C_{cc}) ratio is observed in the mildly carbonated area. With the continuous supply of CO_2 , the (C_{Ht}/C_{cc}) ratio decreases in the transitional area as the CO_2 -binding ability of these two phases are remarkably different (44/100 (wt/wt) for CaCO_3 and 44/484 (wt/wt) for $\text{Mg}_4\text{Al}_2(\text{OH})_{12}(\text{CO}_3)\cdot 4(\text{H}_2\text{O})$) although some CO_2 molecules were physically bound in the interlayer space, which cannot be captured by the modelling. Finally in the fully carbonated zone, hydrotalcite-like phase cannot absorb CO_2 anymore, which facilitates formation of CaCO_3 upon new CO_2 ingress, decreasing the (C_{Ht}/C_{cc}) ratio further.

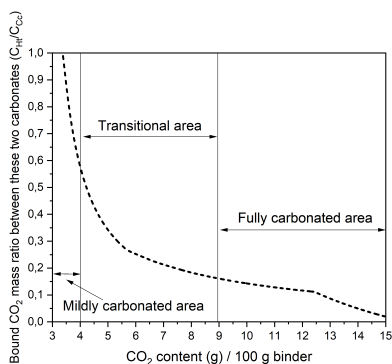


Figure 7.16: The ratio of CO_2 bound in carbonated hydrotalcite-like phase to CaCO_3 with the gradual ingress of CO_2 through modelling.

7.5. CONCLUSIONS

IN this chapter the author investigated the effect of MgO content of slag on the carbonation characteristics of specific cement-slag systems through accelerated carbonation testing and focused on the quantitative role of hydrotalcite-like phase, in particular. The main conclusions drawn were as follows:

- The gradual increase of MgO in slag composition did not change the mineralogy of carbonation products fundamentally. While calcium carbonate was the main CO_2 -

bearing phase, hydrotalcite-like phase and Ca-Al AFm phases did absorb almost 20 wt.% of the entire bound CO₂, as well. Calcite and vaterite were identified as the main polymorphs of CaCO₃ in all pastes.

- After the accelerated carbonation testing, the critical pore diameter in slag cement paste increased to the range of 0.1-100 μm, depending on the amount of magnesia in slag. The critical pore diameter in the range of 10-100 μm appeared in slag M0 and M8 pastes after carbonation was possibly ascribed to the formation of micro-cracks caused by carbonation shrinkage.
- There were large areas unaffected by the carbonation process in slag M16 paste in the carbonated zone. Unreacted slag grains hydrated continuously during carbonation, and the slag rims were significantly thicker after carbonation. As it was also reflected by nanoindentation testing, there was no obvious decrease observed on the indentation modulus of C-S(A)-H gel phase in slag M16 paste, while it reduced significantly for slag M0 and M8 pastes.
- Hydrotalcite-like phase can maintain its network structure and remain intact during carbonation (i.e., binding CO₂ in its interlayer space). Thus, magnesium was still contained within the original slag grain region, and the Mg/Al atomic ratio remained nearly the same before and after carbonation.
- Hydrotalcite-like phase shared more than 15% CO₂ in the mildly carbonated and transitional zones, and this value was positively correlated with the magnesia content of slag. The proportion decreased in the fully carbonated area, and more CO₂ was fixed into calcium carbonate. It was consistent with the thermodynamic modelling that the ratio of CO₂ bound in carbonated hydrotalcite-like phase to CaCO₃ decreased continuously with the gradual ingress of CO₂.

REFERENCES

- [1] Y. Zhang, M. Liang, Y. Gan, and O. Çopuroğlu, *Effect of MgO content on the quantitative role of hydrotalcite-like phase in a cement-slag system during carbonation*, *Cement and Concrete Composites* **134**, 104765 (2022).
- [2] Y. Zhang, M. Liang, Y. Gan, and O. Çopuroğlu, *Micro-Mechanical Properties of Slag Rim Formed in Cement-Slag System Evaluated by Nanoindentation Combined with SEM*, *Materials* **15**, 6347 (2022).
- [3] A. Ehrenberg and D. Algermissen, *Alternative Nutzungsmöglichkeiten von Elektroofenschlacke zur Klinker- und Hüttensands substitution*, in *Berliner Konferenz Mineralische Nebenprodukte und Abfälle 4* (2017).
- [4] ACI, *Slag cement in concrete and mortar*, Report (American Concrete Institute, 2003).
- [5] E. Özbay, M. Erdemir, and H. İ. Durmuş, *Utilization and efficiency of ground granulated blast furnace slag on concrete properties—A review*, *Construction and Building Materials* **105**, 423 (2016).

- [6] Y. Yang, K. Raipala, and L. Holappa, *Ironmaking*, in *Treatise on process metallurgy* (Elsevier, 2014) pp. 2–88.
- [7] G. Mußnug, *Beitrag zur Frage der Mahlbarkeit von Hochofenschlacken (Zementschlacken) und klinkern*, *Zement* **31**, 183 (1942).
- [8] T. Jiang, S. Wang, Y. Guo, F. Chen, and F. Zheng, *Effects of basicity and MgO in slag on the behaviors of smelting vanadium titanomagnetite in the direct reduction-electric furnace process*, *Metals* **6**, 107 (2016).
- [9] F. Shen, X. Hu, H. Zheng, X. Jiang, Q. Gao, H. Han, and F. Long, *Proper MgO/Al₂O₃ ratio in blast-furnace slag: Analysis of proper MgO/Al₂O₃ ratio based on observed data*, *Metals* **10**, 784 (2020).
- [10] E. Douglas, A. Bilodeau, and V. Malhotra, *Properties and durability of alkali-activated slag concrete*, *Materials Journal* **89**, 509 (1992).
- [11] K. Gong and C. E. White, *Impact of chemical variability of ground granulated blast-furnace slag on the phase formation in alkali-activated slag pastes*, *Cement and Concrete Research* **89**, 310 (2016).
- [12] M. B. Haha, B. Lothenbach, G. Le Saout, and F. Winnefeld, *Influence of slag chemistry on the hydration of alkali-activated blast-furnace slag — Part I: Effect of MgO*, *Cement and Concrete Research* **41**, 955 (2011).
- [13] B. Walkley, R. San Nicolas, M.-A. Sani, S. A. Bernal, J. S. van Deventer, and J. L. Provis, *Structural evolution of synthetic alkali-activated CaO-MgO-Na₂O-Al₂O₃-SiO₂ materials is influenced by Mg content*, *Cement and Concrete Research* **99**, 155 (2017).
- [14] S. A. Bernal, R. San Nicolas, R. J. Myers, R. M. de Gutiérrez, F. Puertas, J. S. van Deventer, and J. L. Provis, *MgO content of slag controls phase evolution and structural changes induced by accelerated carbonation in alkali-activated binders*, *Cement and Concrete Research* **57**, 33 (2014).
- [15] S. M. Park, J. Jang, and H. K. Lee, *Unlocking the role of MgO in the carbonation of alkali-activated slag cement*, *Inorganic Chemistry Frontiers* **5**, 1661 (2018).
- [16] S. Y. Wang, E. McCaslin, and C. E. White, *Effects of magnesium content and carbonation on the multiscale pore structure of alkali-activated slags*, *Cement and Concrete Research* **130**, 105979 (2020).
- [17] W. C. Oliver and G. M. Pharr, *An improved technique for determining hardness and elastic modulus using load and displacement sensing indentation experiments*, *Journal of materials research* **7**, 1564 (1992).
- [18] T. Wagner, D. A. Kulik, F. F. Hingerl, and S. V. Dmytrieva, *GEM-Selektor geochemical modeling package: TSolMod library and data interface for multicomponent phase models*, *The Canadian Mineralogist* **50**, 1173 (2012).

- [19] D. A. Kulik, T. Wagner, S. V. Dmytrieva, G. Kosakowski, F. F. Hingerl, K. V. Chudnenko, and U. R. Berner, *GEM-Selektor geochemical modeling package: revised algorithm and GEMS3K numerical kernel for coupled simulation codes*, *Computational Geosciences* **17**, 1 (2013).
- [20] W. Hummel, U. Berner, E. Curti, F. Pearson, and T. Thoenen, *Nagra Technical Report NTB 02-16*, Wettingen, Switzerland (2002).
- [21] W. Hummel, U. Berner, E. Curti, F. Pearson, and T. Thoenen, *Nagra/PSI chemical thermodynamic data base 01/01*, *Radiochimica Acta* **90**, 805 (2002).
- [22] T. Matschei, B. Lothenbach, and F. P. Glasser, *Thermodynamic properties of Portland cement hydrates in the system $\text{CaO}-\text{Al}_2\text{O}_3-\text{SiO}_2-\text{CaSO}_4-\text{CaCO}_3-\text{H}_2\text{O}$* , *Cement and Concrete Research* **37**, 1379 (2007).
- [23] B. Lothenbach, T. Matschei, G. Möschner, and F. P. Glasser, *Thermodynamic modelling of the effect of temperature on the hydration and porosity of Portland cement*, *Cement and Concrete Research* **38**, 1 (2008).
- [24] R. J. Myers, S. A. Bernal, and J. L. Provis, *A thermodynamic model for C-(N-)ASH gel: CNASH_ss. Derivation and validation*, *Cement and Concrete Research* **66**, 27 (2014).
- [25] R. J. Myers, B. Lothenbach, S. A. Bernal, and J. L. Provis, *Thermodynamic modelling of alkali-activated slag cements*, *Applied Geochemistry* **61**, 233 (2015).
- [26] X. Ke, S. A. Bernal, J. L. Provis, and B. Lothenbach, *Thermodynamic modelling of phase evolution in alkali-activated slag cements exposed to carbon dioxide*, *Cement and Concrete Research* **136**, 106158 (2020).
- [27] S. Miyata, *Anion-exchange properties of hydrotalcite-like compounds*, *Clays and Clay minerals* **31**, 305 (1983).
- [28] G. Villain, M. Thiery, and G. Platret, *Measurement methods of carbonation profiles in concrete: Thermogravimetry, chemical analysis and gammadensimetry*, *Cement and Concrete Research* **37**, 1182 (2007).
- [29] M. Thiery, G. Villain, P. Dangla, and G. Platret, *Investigation of the carbonation front shape on cementitious materials: Effects of the chemical kinetics*, *Cement and Concrete Research* **37**, 1047 (2007).
- [30] A. Morandau, M. Thiery, and P. Dangla, *Investigation of the carbonation mechanism of CH and CSH in terms of kinetics, microstructure changes and moisture properties*, *Cement and Concrete Research* **56**, 153 (2014).
- [31] P. H. Borges, J. O. Costa, N. B. Milestone, C. J. Lynsdale, and R. E. Streatfield, *Carbonation of CH and C-S-H in composite cement pastes containing high amounts of BFS*, *Cement and Concrete Research* **40**, 284 (2010).

- [32] M. Zajac, A. Lechevallier, P. Durdzinski, F. Bullerjahn, J. Skibsted, and M. B. Haha, *CO₂ mineralisation of portland cement: Towards understanding the mechanisms of enforced carbonation*, *Journal of Co2 Utilization* **38**, 398 (2020).
- [33] P. Yu, R. J. Kirkpatrick, B. Poe, P. F. McMillan, and X. Cong, *Structure of calcium silicate hydrate (C-S-H): Near-, Mid-, and Far-infrared spectroscopy*, *Journal of the American Ceramic Society* **82**, 742 (1999).
- [34] Y. Okada, T. Masuda, M. Takada, L. Xu, and T. Mitsuda, *Relationship between NMR ²⁹Si chemical shifts and FT-IR wave numbers in calcium silicates*, in *Nuclear magnetic resonance spectroscopy of cement-based materials* (Springer, 1998) pp. 69–78.
- [35] W. Ashraf and J. Olek, *Carbonation behavior of hydraulic and non-hydraulic calcium silicates: potential of utilizing low-lime calcium silicates in cement-based materials*, *Journal of materials science* **51**, 6173 (2016).
- [36] M. Zajac, J. Skibsted, P. Durdzinski, F. Bullerjahn, J. Skocek, and M. B. Haha, *Kinetics of enforced carbonation of cement paste*, *Cement and Concrete Research* **131**, 106013 (2020).
- [37] L. Black, C. Breen, J. Yarwood, K. Garbev, P. Stemmermann, and B. Gasharova, *Structural features of C–S–H (I) and its carbonation in air—a raman spectroscopic study. Part II: carbonated phases*, *Journal of the American Ceramic Society* **90**, 908 (2007).
- [38] G. Rimmelé, V. Barlet-Gouédard, O. Porcherie, B. Goffé, and F. Brunet, *Heterogeneous porosity distribution in Portland cement exposed to CO₂-rich fluids*, *Cement and Concrete Research* **38**, 1038 (2008).
- [39] S. Mindess, J. F. Young, and D. Darwin, *Concrete Prentice-Hall*, **481** (1981).
- [40] V. Ngala and C. Page, *Effects of carbonation on pore structure and diffusional properties of hydrated cement pastes*, *Cement and Concrete Research* **27**, 995 (1997).
- [41] M. Frías and S. Goñi, *Accelerated carbonation effect on behaviour of ternary Portland cements*, *Composites Part B: Engineering* **48**, 122 (2013).
- [42] B. Wu and G. Ye, *Development of porosity of cement paste blended with supplementary cementitious materials after carbonation*, *Construction and Building Materials* **145**, 52 (2017).
- [43] J. J. Chen, J. J. Thomas, H. F. Taylor, and H. M. Jennings, *Solubility and structure of calcium silicate hydrate*, *Cement and Concrete Research* **34**, 1499 (2004).
- [44] V. Shah, K. Scrivener, B. Bhattacharjee, and S. Bishnoi, *Changes in microstructure characteristics of cement paste on carbonation*, *Cement and Concrete Research* **109**, 184 (2018).

- [45] I. Richardson, *Tobermorite/jennite-and tobermorite/calcium hydroxide-based models for the structure of CSH: applicability to hardened pastes of tricalcium silicate, -dicalcium silicate, portland cement, and blends of portland cement with blast-furnace slag, metakaolin, or silica fume*, Cement and Concrete Research **34**, 1733 (2004).
- [46] J. I. Escalante-Garcia and J. H. Sharp, *The chemical composition and microstructure of hydration products in blended cements*, Cement and Concrete Composites **26**, 967 (2004).
- [47] R. Taylor, I. Richardson, and R. Brydson, *Composition and microstructure of 20-year-old ordinary Portland cement-ground granulated blast-furnace slag blends containing 0 to 100% slag*, Cement and Concrete Research **40**, 971 (2010).
- [48] T. F. Sevelsted and J. Skibsted, *Carbonation of C-S-H and C-A-S-H samples studied by ^{13}C , ^{27}Al and ^{29}Si MAS NMR spectroscopy*, Cement and Concrete Research **71**, 56 (2015).
- [49] C. M. Bishop, *Pattern recognition and Machine Learning*, Springer **128** (2006).
- [50] G. Constantinides, F.-J. Ulm, and K. Van Vliet, *On the use of nanoindentation for cementitious materials*, Materials and structures **36**, 191 (2003).
- [51] G. Constantinides and F.-J. Ulm, *The effect of two types of CSH on the elasticity of cement-based materials: Results from nanoindentation and micromechanical modeling*, Cement and Concrete Research **34**, 67 (2004).
- [52] G. Constantinides and F.-J. Ulm, *The nanogranular nature of C-S-H*, Journal of the Mechanics Physics of Solids **55**, 64 (2007).
- [53] D. Davydov, M. Jirasek, and L. Kopecký, *Critical aspects of nano-indentation technique in application to hardened cement paste*, Cement and Concrete Research **41**, 20 (2011).
- [54] B. J. Zhan, D. X. Xuan, C. S. Poon, and K. L. Scrivener, *Multi-scale investigation on mechanical behavior and microstructural alteration of CSH in carbonated Alite paste*, Cement and Concrete Research **144**, 106448 (2021).
- [55] L. Mo, F. Zhang, and M. Deng, *Mechanical performance and microstructure of the calcium carbonate binders produced by carbonating steel slag paste under CO_2 curing*, Cement and Concrete Research **88**, 217 (2016).
- [56] X. Ouyang, D. Koleva, G. Ye, and K. Van Breugel, *Understanding the adhesion mechanisms between CSH and fillers*, Cement and Concrete Research **100**, 275 (2017).
- [57] P. Sulapha, S. Wong, T. Wee, and S. Swaddiwudhipong, *Carbonation of concrete containing mineral admixtures*, Journal of materials in civil engineering **15**, 134 (2003).

- [58] Y. Gao, L. Cheng, Z. Gao, and S. Guo, *Effects of different mineral admixtures on carbonation resistance of lightweight aggregate concrete*, *Construction and Building Materials* **43**, 506 (2013).
- [59] R. Bucher, P. Diederich, G. Escadeillas, and M. Cyr, *Service life of metakaolin-based concrete exposed to carbonation: Comparison with blended cement containing fly ash, blast furnace slag and limestone filler*, *Cement and Concrete Research* **99**, 18 (2017).
- [60] V. Shah and S. Bishnoi, *Carbonation resistance of cements containing supplementary cementitious materials and its relation to various parameters of concrete*, *Construction and Building Materials* **178**, 219 (2018).
- [61] O. Copuroglu, A. Fraaij, and J. Bijen, *Microstructural change of blast furnace slag cement paste due to carbonation*, in *Application of Codes, Design and Regulations: Proceedings of the International Conference held at the University of Dundee, Scotland, UK on 5–7 July 2005* (Thomas Telford Publishing) pp. 229–234.
- [62] E. Bernard, W. J. Zucha, B. Lothenbach, and U. Mäder, *Stability of hydrotalcite (Mg-Al layered double hydroxide) in presence of different anions*, *Cement and Concrete Research* **152**, 106674 (2022).
- [63] S. von Greve-Dierfeld, B. Lothenbach, A. Vollpracht, B. Wu, B. Huet, C. Andrade, C. Medina, C. Thiel, E. Gruyaert, H. Vanoutrive, *et al.*, *Understanding the carbonation of concrete with supplementary cementitious materials: a critical review by RILEM TC 281-CCC*, *Materials and structures* **53**, 1 (2020).
- [64] G. G. Litvan, *Variability of the nitrogen surface area of hydrated cement paste*, *Cement and Concrete Research* **6**, 139 (1976).
- [65] S. Walspurger, P. D. Cobden, O. V. Safonova, Y. Wu, and E. J. Anthony, *High CO₂ storage capacity in alkali-promoted hydrotalcite-based material: In situ detection of reversible formation of magnesium carbonate*, *Chemistry—A European Journal* **16**, 12694 (2010).
- [66] P. Sahoo, S. Ishihara, K. Yamada, K. Deguchi, S. Ohki, M. Tansho, T. Shimizu, N. Eisaku, R. Sasai, and J. Labuta, *Rapid exchange between atmospheric CO₂ and carbonate anion intercalated within magnesium rich layered double hydroxide*, *ACS applied materials interfaces* **6**, 18352 (2014).
- [67] L. Parrot, *Prediction of cement hydration*, in *Proceedings of the British Ceramic Society*, Vol. 35, pp. 41–53.
- [68] B. Lothenbach, G. Le Saout, E. Gallucci, and K. Scrivener, *Influence of limestone on the hydration of Portland cements*, *Cement and Concrete Research* **38**, 848 (2008).
- [69] H. F. Taylor, *Cement chemistry*, Vol. 2 (Thomas Telford London, 1997).

- [70] K. Luke and E. Lachowski, *Internal composition of 20-year-old fly ash and slag-blended ordinary Portland cement pastes*, *Journal of the American Ceramic Society* **91**, 4084 (2008).
- [71] Z. Shi, B. Lothenbach, M. R. Geiker, J. Kaufmann, A. Leemann, S. Ferreiro, and J. Skibsted, *Experimental studies and thermodynamic modeling of the carbonation of Portland cement, metakaolin and limestone mortars*, *Cement and Concrete Research* **88**, 60 (2016).

8

EFFECT OF Al_2O_3 CONTENT IN SLAG ON THE RELATIONSHIP BETWEEN SLAG REACTIVITY AND CARBONATION RESISTANCE

Synthetic slags with different Al_2O_3 contents were used in this chapter. Phase assemblage, microstructure, and CO_2 binding capacity of each mixture before and after accelerated carbonation test were compared. Combining the data from Chapter 7, the author attempted to complement the existing results available in the literature about the effect of slag chemistry on the carbonation characteristics of cement-slag system at high replacement level. Meanwhile, the author tried to build the connection among slag chemistry, slag reactivity, and carbonation resistance of cement-slag system to formulating improved blast furnace slag composition for better carbonation resistance performance.

8.1. INTRODUCTION

IN Chapter 7, the author examined the influence of MgO content in slag on the carbonation characteristics of slag-rich cement system, where it was found that carbonation resistance significantly improved as the MgO content increased in slag, in which hydrotalcite-like phase played a key role. In this chapter, another main oxide, i.e., Al_2O_3 , was investigated with respect to its role during carbonation of hydrated slag cement systems.

In general, the amount of Al_2O_3 in slag produced in Europe varies from approximately 5 to 18 wt.% according to [1]. Based on [2, 3], it is in the range of 7~18 wt.% in North America. The value fluctuates at 12~15 wt.% for slag produced in Austria. According to European standard EN 15167-1, no specific requirement is put forward regarding the Al_2O_3 content of slag. Although most Al_2O_3 acts as network former in the network structure of slag, it is noted that Al_2O_3 -rich slag cement paste shows good performance at early age. Increased Al_2O_3 content of slag is reported to enhance reaction heat release and early age strength development [4, 5]. Due to the higher molar volume of Al-containing phases, e.g., ettringite and monosulfate, they can fill up pores, thus are beneficial for the compressive strength development [6]. In Chapter 4, the author also confirmed the positive correlation between Al_2O_3 content of slag and reactivity.

However, to the best of author's knowledge, few researches go deep into the correlation between the carbonation resistance of a slag-containing system (where slag was used as a main component, e.g., alkali-activated slag and CEM III/B) and slag chemistry. In Chapter 6, it was found that system with a Al_2O_3 -rich slag presented a low CO_2 binding capacity. Questions such as whether Al_2O_3 -rich slag contributes to an improvement of carbonation resistance and whether slag reactivity indicated by rapid test (e.g., R3 test) can be extended to characterize carbonation resistance of slag-containing systems etc. remain to be answered. Therefore, this chapter aimed to fill up the gap by investigating the effect of Al_2O_3 content of slag on the carbonation characteristics of cement-slag system where slag was used as a primary SCM (i.e., 70 wt.% replacement to simulate CEM III/B).

To avoid potential interferences from other factors, synthetic slags with different Al_2O_3 contents (A3, A12, A18, CS1, and CS2) were used in the study. Phase assemblage, microstructure, and CO_2 binding capacity of each mixture before and after accelerated carbonation test were compared. Combining the data from Chapter 7, the author attempted to complement the existing results available in the literature about the effect of slag chemistry on the carbonation characteristics of cement-slag system at high replacement level. Meanwhile, the author tried to build the connection among slag chemistry, slag reactivity, and carbonation resistance of cement-slag system to formulating improved blast furnace slag composition for better carbonation resistance performance.

8.2. MATERIALS AND METHODOLOGY

8.2.1. MATERIALS

SYNTHETIC slags with different Al_2O_3 contents, named as A3, A12, A18, CS1, and CS2, and CEM I 42,5 N were used in the study to cast cement-slag paste.

For various properties of these synthetic slags, please refer to Chapter 4. For synthetic slag A3, A12 and A18, CaO/SiO_2 ratio was maintained at around 1.0 and the amount of MgO was stabilized at about 9 wt.%, while Al_2O_3 content increased from 3.69 (A3) to 18.19 wt.% (A18). As for synthetic slag CS1 and CS2, their Al_2O_3 contents were maintained at a high level, i.e., 14.51 and 17.12 wt.%, respectively while the CaO/SiO_2 ratios were reduced to less than 1.0. Similarly, Qz with a similar PSD was also introduced to cast cement-quartz paste, acting as a reference.

8.2.2. METHODOLOGY

In the blended cement paste, cement was partially replaced by slag (70 wt.%). Paste specimens were prepared in each mixture using distilled water with a water/binder (cement+slag) ratio of 0.40. All the materials were in weight percentage with respect to total binder content. The binders were mixed and then transferred immediately to the moulds (40×40×40 mm). After one day, specimens were demoulded and sealed curing was performed at 20 ± 2 °C for further investigation.

After 3 months of curing, specimens were transferred to a RH-controlled climate chamber at 65% and 20 °C for pretreatment for one month. Accelerated carbonation test was performed in the carbonation chamber sequentially regulated by CO_2 concentration of $3\%\pm 0.2$, at 20 ± 3 °C and $65\pm 5\%$ of RH (using saturated NaNO_2 solution). Only one side was exposed to CO_2 and the rest sides were sealed to ensure one dimensional diffusion. The carbonation age was up to 6 months.

At the end of the predesignated hydration and carbonation periods, small discs were sawn from the specimens, crushed and immersed in isopropanol solution to exchange water. For the detailed information of XRD and TGA-MS measurements, please refer to Chapter 5. As for FTIR analysis, the same procedure was employed according to the description in Chapter 6. MIP analysis was carried out following the steps introduced in Chapter 7, and SEM-EDS investigation was performed on selected samples prepared following the instructions in Chapter 3.

8.3. RESULTS

8.3.1. PHENOLPHTHALEIN SPRAY

THE typical cross-sectional surfaces of the specimens after phenolphthalein spray are shown in Figure 8.1. It was noted that slag A3, A12, A18, and CS1 pastes exhibited similar carbonation depths in the range of 10-15 mm. On the other hand, the carbonation depth of slag CS2 paste was approximately 20 mm, significantly higher than the others.

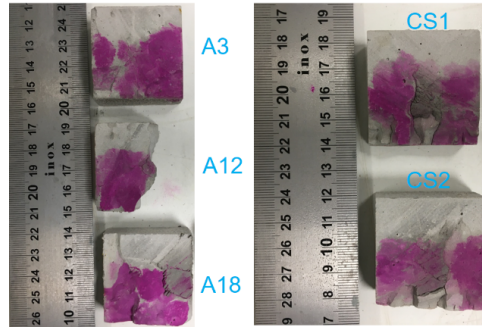


Figure 8.1: Typical sawn surfaces of the specimens after spraying with phenolphthalein solution.

8.3.2. CARBONATION PRODUCTS

In this section, the authors characterized carbonation products by means of a series of techniques. To better understand the effect of CO_2 attack on the evolution of phase assemblage, powders were taken from the top layer of specimens (within 3 mm depth from the surface) exposed in the carbonation chamber to ensure (nearly) full carbonation as much as possible.

TG-DTG-MS

Figure 8.2(a) reveals the representative TG-DTG results of cement-slag and quartz mixtures at 90 days of curing. The peak at 400-500 °C indicated the formation of portlandite. Expectedly, the most portlandite was identified in cement-quartz blend while the least amount of portlandite was found in slag A18 mixture due to its relatively high reactivity (see Chapter 4). Hydrotalcite-like phase was detected in slag-containing mixtures with a distinct peak located at approximately 350 °C. Additionally, the shoulder at ~200 °C implied the formation of monosulfate, originated from the transformation of ettringite with time. Note that its amount was positively associated with the amount of alumina content in slag, i.e., nearly no monosulfate was found in slag A3 blend while slag A18 mixture presented the most distinct shoulder at ~200 °C. Meanwhile, the peak at 100-150 °C suggested the presence of C-S(A)-H gel phase.

Figure 8.2 8.2(b)-8.2(e) show the DTG results, H_2O and CO_2 MS curves of fully carbonated cement-slag A3, CS1, A18, and Qz pastes, respectively. No doubt that the main CO_2 -bearing phase in all pastes was calcium carbonate, and three decomposition peaks starting from ~450 °C in the DTG graph implied the presence of calcium carbonate of different polymorphs, all of which were commonly seen in the accelerated carbonation test of cementitious materials [7–9]. Monosulfate and portlandite had been carbonated and decomposed completely, as neither of them was observed in the fully carbonated area.

The peak located at 300-450 °C indicated the persistence of hydrotalcite-like phase after carbonation in slag-containing blends. As displayed in the MS curves, both H_2O and CO_2 were released at this temperature range. Moreover, a small peak at ~150 °C occurred in the MS CO_2 curve, irrespective of the addition of slag or Al_2O_3 content of slag. It can be ascribed to the release of CO_2 from carbonated Ca-Al AFm phases (amorphous or nano-crystalline), sourced from the carbonation of AFm-OH and/or AFm- SO_4 phases

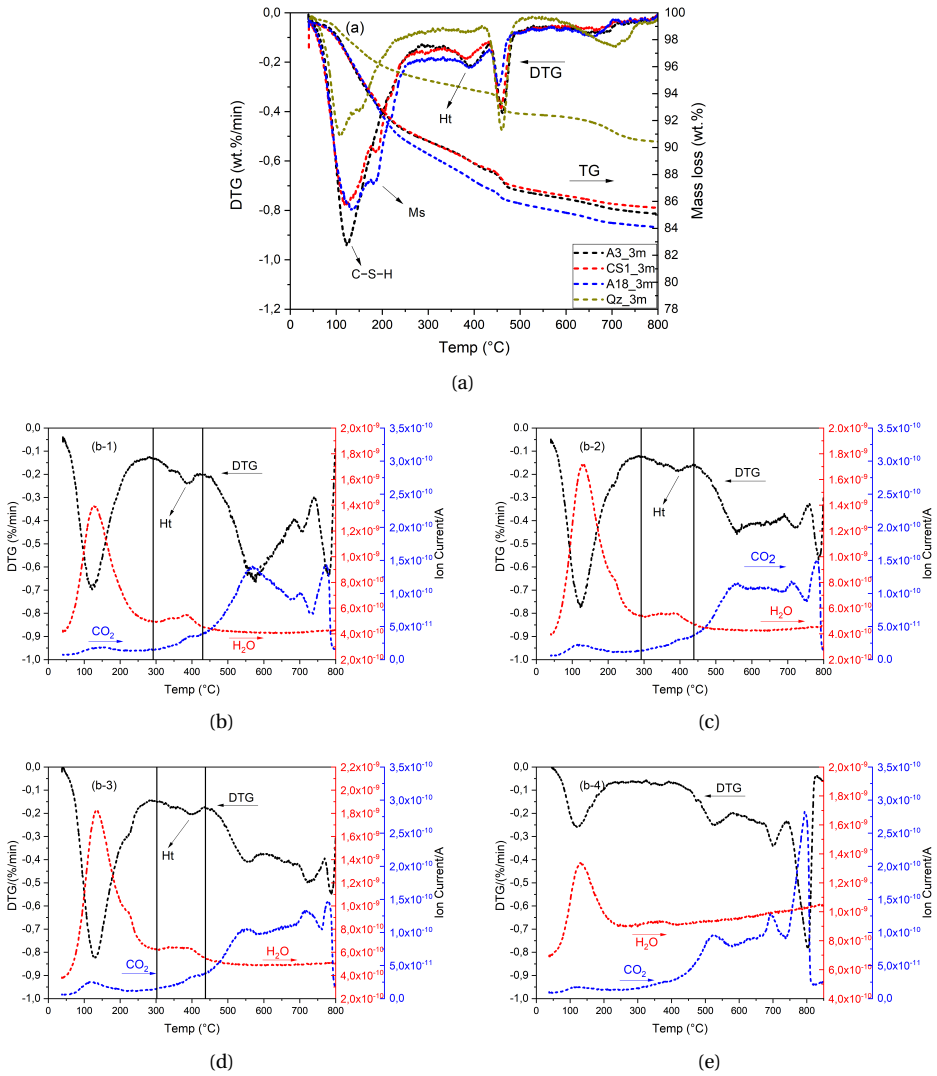


Figure 8.2: (a) TG and DTG results of representative cement-slag and quartz mixtures after 3 months of curing; (b-1)-(b-4) DTG results, H₂O and CO₂ MS curves of fully carbonated cement-slag A3, CS1, A18, and Qz pastes, respectively. Ht: hydrocalcite-like phase; Ms: calcium monosulfoaluminate.

(see discussion in Section 5.4.1). This peak was negligible in slag A3 and Qz mixtures, probably owing to their reduced monosulfate formation after hydration when compared with other pastes.

XRD

XRD results (Figure 8.3(a)) confirm the presence of monosulfate, hydrotalcite-like phase, portlandite, and unhydrated cement clinker (C_3S and $\beta-C_2S$ in particular) in slag cement paste after hydration. The peak intensity of portlandite reduced with the gradual addition of Al_2O_3 in slag. Monosulfate was detected in slag A12 and A18 mixtures. On the other hand, the peak for monosulfate and portlandite disappeared in all mixtures after carbonation (Figure 8.3(b)). These results were consistent with the TGA findings (Figure 8.2). Moreover, it was noted that the peak for unhydrated cement clinkers (C_3S and $\beta-C_2S$) also disappeared in the fully carbonated area, likely due to the continuation of hydration or carbonation [10].

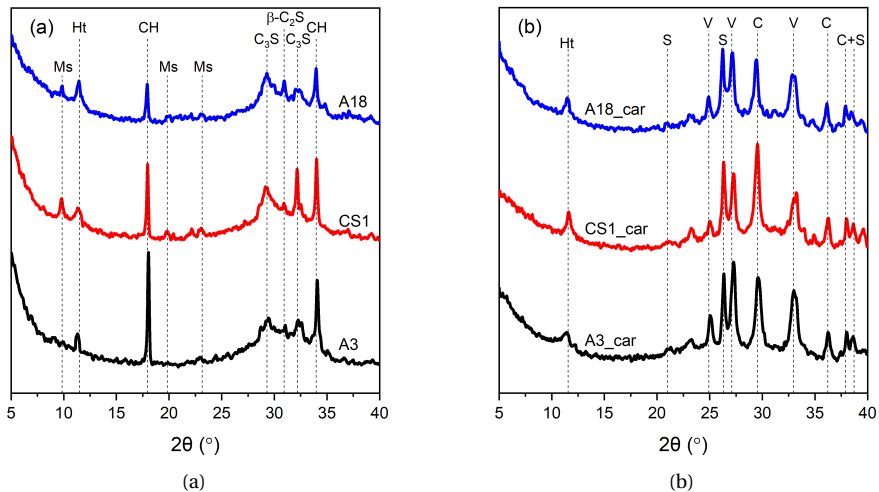


Figure 8.3: XRD analysis of representative cement-slag blends (a) at 90 days after curing; (b) after full carbonation. Ms: calcium monosulfoaluminate; Ht: hydrotalcite-like phase; CH: portlandite; C: calcite; V: vaterite. The peak centered at around $2\theta = 21$ and 26° appeared to be associated with the formation of silica gel (labelled as S) due to the carbonation of C-S-H gel phase [11].

Hydrotalcite-like phase was detected after such a heavy CO_2 attack, i.e., the peak of which was located at $\sim 11^\circ$ (2θ) both before and after carbonation. Calcite and vaterite were identified as the main polymorphs of calcium carbonate. It is worth mentioning here that amorphous calcium carbonate could not be detected by XRD and no trace of aragonite was confirmed in these carbonated samples.

FTIR

As Figure 8.4 shows, FTIR spectra of slag cement pastes presented similar characteristics after 3 months of curing, and Q2 ($\sim 950\text{ cm}^{-1}$) was the main unit of C-S(A)-H gel phase of all investigated mixtures before carbonation. Moreover, the silicate group in these samples also showed a similar feature after carbonation, i.e., the Si-O-T stretching band shifted left to ~ 1200 and $\sim 1100\text{ cm}^{-1}$, indicating the formation

of Q4 and Q3 silicate units, respectively. This shift was associated with the gradual polymerization of silicate units, namely the carbonation-induced decalcification of C-S(A)-H gel phase [12–14].

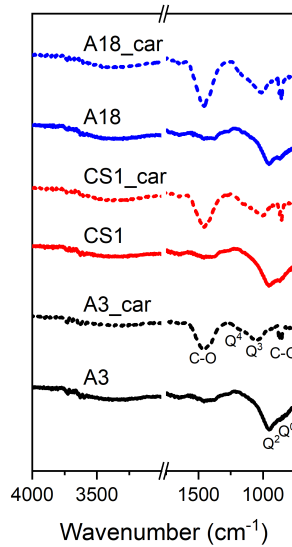


Figure 8.4: The FTIR spectra of slag cement pastes after 3 months of curing and accelerated carbonation test, (Normalized, %).

The strong broad band at 1400–1500 cm^{-1} and narrow band at 875–1000 cm^{-1} , representing the asymmetric stretching and bending of carbonate, respectively further confirmed the reaction with CO_2 and production of CO_3 band [15].

Collectively, the variation of slag chemistry did not change the type of carbonation products of slag cement fundamentally, and three CO_2 binding phases were identified, i.e., calcium carbonate (including amorphous calcium carbonate, vaterite, and calcite), carbonated hydrotalcite-like phase, and carbonated Ca–Al AFm phases which cannot be detected by XRD. The formation of silica gel after carbonation was identified by both XRD and FTIR.

8.3.3. DEGREE OF CO_2 UPTAKE OF DIFFERENT CARBONATE PHASES

To calculate the CO_2 concentration in each carbonate phase at different depths, powders were extracted from the regions with different degrees of carbonation (consistent with the work in Section 7.3.3). These regions were designated as: (nearly) fully carbonated zone (label 1), transitional/dissolution zone (label 2) [16], and mildly/non-carbonated area (label 3), respectively as Figure 8.5 shows.

Figure 8.6(a) and 8.6(b) display the DTG results, H_2O and CO_2 MS curves of the powders taken from mildly carbonated and transitional areas of slag A18 paste, respectively (For fully carbonated area, it was shown in Figure 8.2(d)). The carbonation degree in these two areas was lower than that in full carbonation area, indicated by the reduced CO_2 ion current. Nonetheless, the same carbonate phases can be identified in these three areas, i.e., carbonated Ca–Al AFm phases, carbonated hydrotalcite-like



Figure 8.5: The positions where powders were extracted, using slag A18 paste as an example. 1: fully carbonated area; 2: transitional area; 3: mildly carbonated area.

phase as well as calcium carbonate. Additionally, portlandite was observed in the transitional area while both portlandite and monosulfate were detected in the mildly carbonated area.

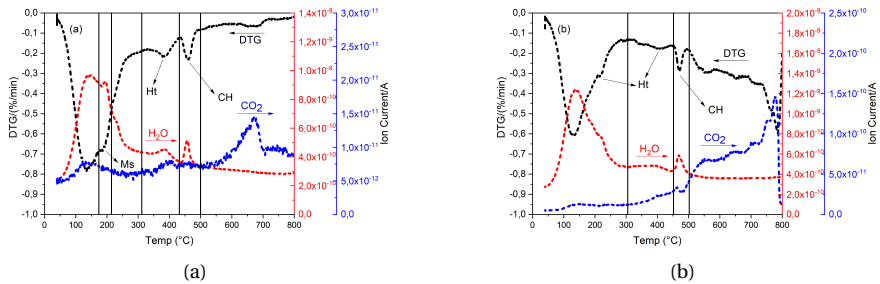


Figure 8.6: DTG results, H_2O and CO_2 MS curves of (a) mildly carbonated and (b) transitional areas of slag A18 paste, respectively. Ms: calcium monosulfaluminate; Ht: hydrotalcite-like phase; CH: portlandite.

Similar to the work in Chapter 6 and 7, pure $CaCO_3$ reagent was employed as a reference to calibrate the CO_2 concentration of each carbonate phase at different depths, using slag A18 paste as an example shown in Figure 8.7(a)-8.7(c). The area A1, A2 and A3 were related to certain amounts of CO_2 liberated from carbonated Ca-Al AFm phases, carbonated hydrotalcite-like phase, and calcium carbonate, respectively.

The calculated areas under the MS CO_2 curve and CO_2 concentrations calibrated with pure $CaCO_3$ (/100 g carbonated paste) of different carbonate phases in each mixture are given in Table 8.1 and 8.2, respectively. No doubt that the absolute amount of CO_2 bound in different carbonate phases increased significantly from mildly to fully carbonated area. Also, it was found that various forms of calcium carbonate bound the majority of CO_2 diffused into the paste, through the reactions with portlandite and C-S(A)-H gel phase. Meanwhile, it can be seen that the CO_2 binding capacity (data adapted from full carbonation area) of each mixture was similar, and it fluctuated at 15-20 wt.%, irrespective of alumina content in slag.

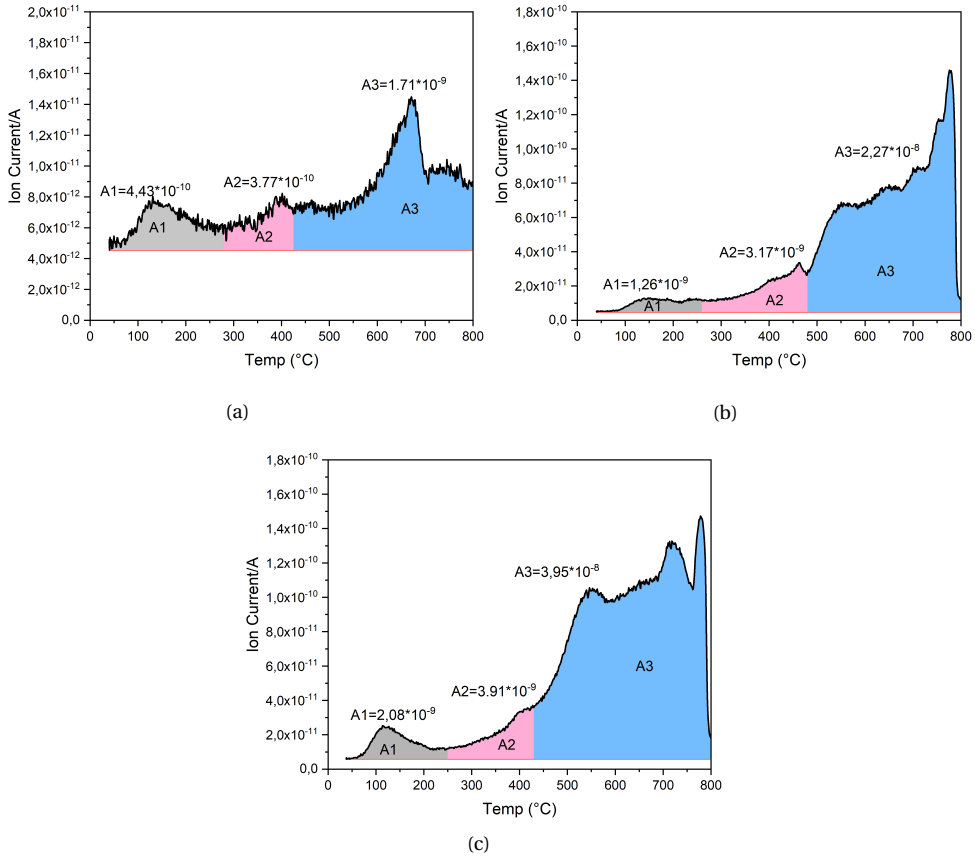


Figure 8.7: (a)-(c) The CO₂ MS curve of carbonated slag A18 paste in mildly carbonated, transitional, and fully carbonated areas, respectively.

Table 8.1: The calculated areas under the MS CO₂ curve of different carbonate phases.

		Area under the MS CO ₂ curve			Total
		Carbonated Ca-Al AFm phases	Carbonated hydroxalcalite-like phase	Calcium carbonate	
Mildly carbonated	A3	$7.39 \cdot 10^{-10}$	$1.02 \cdot 10^{-9}$	$2.97 \cdot 10^{-9}$	$4.73 \cdot 10^{-9}$
	A12	$6.50 \cdot 10^{-10}$	$9.68 \cdot 10^{-10}$	$2.81 \cdot 10^{-9}$	$4.43 \cdot 10^{-9}$
	A18	$4.43 \cdot 10^{-10}$	$3.77 \cdot 10^{-10}$	$1.71 \cdot 10^{-9}$	$2.53 \cdot 10^{-9}$
	CS1	$4.12 \cdot 10^{-10}$	$8.63 \cdot 10^{-10}$	$2.68 \cdot 10^{-9}$	$3.96 \cdot 10^{-9}$
	CS2	$5.39 \cdot 10^{-10}$	$9.35 \cdot 10^{-10}$	$2.84 \cdot 10^{-9}$	$4.13 \cdot 10^{-9}$
Transitional	A3	$1.23 \cdot 10^{-9}$	$3.17 \cdot 10^{-9}$	$2.05 \cdot 10^{-8}$	$2.49 \cdot 10^{-8}$
	A12	$1.71 \cdot 10^{-9}$	$3.89 \cdot 10^{-9}$	$2.56 \cdot 10^{-8}$	$3.12 \cdot 10^{-8}$
	A18	$1.26 \cdot 10^{-9}$	$3.17 \cdot 10^{-9}$	$2.27 \cdot 10^{-8}$	$2.71 \cdot 10^{-8}$
	CS1	$1.43 \cdot 10^{-9}$	$3.35 \cdot 10^{-9}$	$2.31 \cdot 10^{-8}$	$2.79 \cdot 10^{-8}$
	CS2	$1.52 \cdot 10^{-9}$	$3.46 \cdot 10^{-9}$	$2.38 \cdot 10^{-8}$	$2.88 \cdot 10^{-8}$
Fully carbonated	A3	$1.56 \cdot 10^{-9}$	$2.84 \cdot 10^{-9}$	$3.94 \cdot 10^{-8}$	$4.38 \cdot 10^{-8}$
	A12	$1.94 \cdot 10^{-9}$	$5.11 \cdot 10^{-9}$	$3.73 \cdot 10^{-8}$	$4.43 \cdot 10^{-8}$
	A18	$2.08 \cdot 10^{-9}$	$3.91 \cdot 10^{-9}$	$3.95 \cdot 10^{-8}$	$4.55 \cdot 10^{-8}$
	CS1	$1.74 \cdot 10^{-9}$	$4.25 \cdot 10^{-9}$	$3.72 \cdot 10^{-8}$	$4.32 \cdot 10^{-8}$
	CS2	$1.83 \cdot 10^{-9}$	$4.87 \cdot 10^{-9}$	$3.85 \cdot 10^{-8}$	$4.52 \cdot 10^{-8}$
	Qz a	$1.50 \cdot 10^{-9}$	-	$3.81 \cdot 10^{-8}$	$3.96 \cdot 10^{-8}$
	Pure CaCO ₃	-	-	$1.09 \cdot 10^{-7}$	$1.09 \cdot 10^{-7}$

Table 8.2: CO_2 concentrations of different carbonate phases calibrated with pure $CaCO_3$ (/100 g).

		CO ₂ concentration of each carbonate phase			Total
		Carbonated Ca-Al AFm phases	Carbonated hydrotoalcite-like phase	Calcium carbonate	
Mildly carbonated	A3	0.30	0.41	1.20	1.91
	A12	0.26	0.40	1.13	1.79
	A18	0.18	0.15	0.69	1.02
	CS1	0.17	0.35	1.08	1.60
	CS2	0.23	0.39	1.15	1.67
Transitional	A3	0.50	1.28	8.27	10.05
	A12	0.69	1.57	10.33	12.59
	A18	0.50	1.28	9.16	10.94
	CS1	0.58	1.35	9.33	11.26
	CS2	0.62	1.40	9.61	11.63
Fully carbonated	A3	0.63	1.15	15.90	17.68
	A12	0.78	2.06	15.04	17.88
	A18	0.84	1.58	15.95	18.37
	CS1	0.70	1.72	15.02	17.44
	CS2	0.74	1.97	15.54	18.25
	Qz	0.51	-	15.38	15.99
	Pure $CaCO_3$	-	-	44.0	44.0

8.3.4. MICROSTRUCTURE

In this section, the author aimed to analyze the impact of carbonation on the microstructure development and the evolution of phase assemblages in the cement-slag systems. Samples used for measurements were selected from the carbonated area (colorless appearance after phenolphthalein spray) for each mixture.

MIP

As Figure 8.8(a) illustrates, the critical pore diameter of cement-slag system fluctuated at around $0.01 \mu m$, and it exhibited a decreasing trend with the increasing Al_2O_3 content of slag. Slag CS1 and CS2 pastes exhibited a relatively larger critical pore diameter between 0.01 and $0.02 \mu m$ due to the decreased CaO/SiO₂ ratio. Compared with cement-quartz mixture which displayed a bimodal pore structure (in the range of 0.01 - $1 \mu m$), secondary precipitations from the pozzolanic reaction between portlandite and slag helped refine and densify the pore structure of paste considerably.

After accelerated carbonation test, the critical pore diameter of each mixture all shifted right to the range of 0.1 - $10 \mu m$ (Figure 8.8(b)). Due to the carbonation of C-S(A)-H gel phase, a much coarser pore structure was produced after carbonation. The decalcification of C-S-H gel phase produced a poorly organized silica gel of a lower molar volume. At the same time, free water initially bound within the C-S-H gel phase was released during carbonation and evaporated with drying, which also contributed to an enhanced porosity [11, 17–19]. As can be seen, slag A12 and A18 pastes showed a similar critical pore diameter (8.8(b)) and porosity (8.8(c)) after carbonation, and slag CS1 and CS2 blends illustrated the most porous microstructure during CO₂ attack.

SEM-BSE

Figure 8.9 illustrates the representative microstructure of specimens before and after accelerated carbonation test. Unhydrated cement grains (e.g., circled and labelled #1 in Figure 8.9(a)) were found in all pastes and distributed in the matrix with unhydrated slag particles after 3 months of curing. Portlandite was clearly identified as large

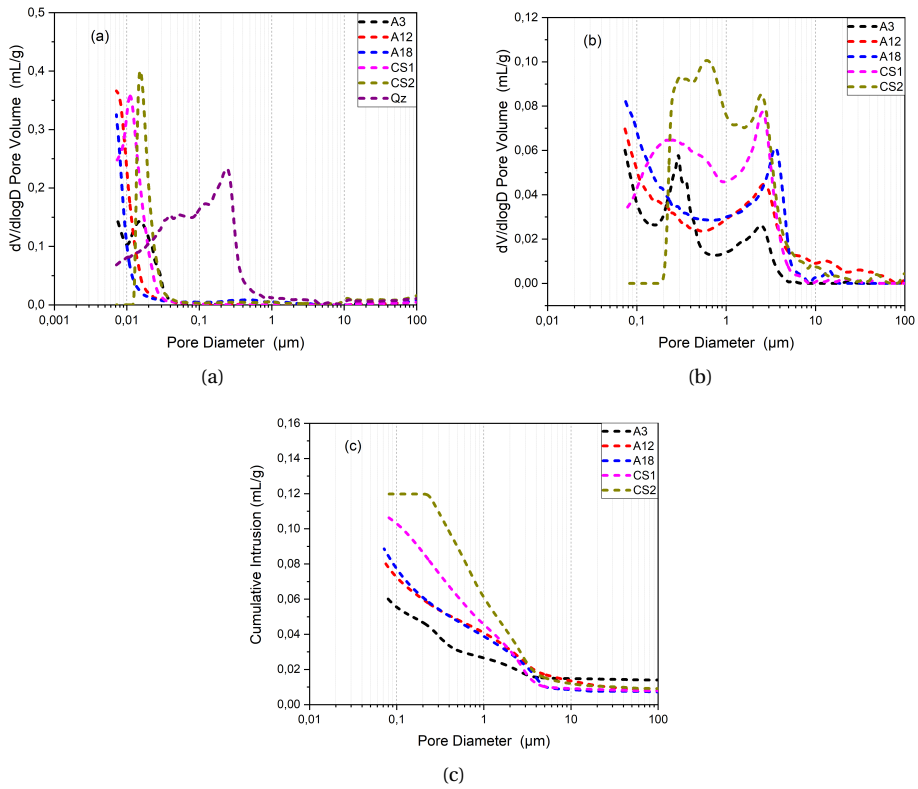


Figure 8.8: Differential pore size distribution of cement-slag and quartz mixtures measured (a) before and (b) after accelerated carbonation test; (c) cumulative intrusion measured after accelerated carbonation test.

clusters (e.g., circled and labelled #2 in Figure 8.9(a)). Because of the rich alumina content in slag A18, monosulfate existed as fine and compact crystal intermixed with C-S(A)-H gel phase across the matrix (circled and labelled #3 in Figure 8.9(e)).

After carbonation, specimens appeared much more porous with a large quantity of black spots, indicating the formation of pores filled with epoxy resin (Figure 8.9(b), 8.9(d), and 8.9(f)). It further verified the change of critical pore radii upon carbonation in the range of 0.1-10 μm measured by MIP.

CHEMICAL COMPOSITION

C-S(A)-H gel phase

Scatter plots of Al/Ca against Si/Ca in atomic ratio are shown in Figure 8.10. In general, the measured Ca/Si atomic ratio of C-S(A)-H gel phase after 3 months of curing fluctuated at around 1.0. This value was in line with the earlier reports [20–22]. On the other hand, substantial decalcification occurred in the blended system after accelerated carbonation testing which led to a reduction of Ca/Si atomic ratio of C-S(A)-H gel phase. Part of the gel remained unaffected during the CO_2 attack as several Ca/Si ratio readings were similar to the readings on the uncarbonated matrix. The other part was decalcified, especially for that circled in Figure 8.10(b) presenting a higher Si/Ca atomic ratio. Moreover, scatter points indicating the existence of monosulfate in slag A18 mixture disappeared after carbonation, confirming the decomposition of this phase after carbonation.

Hydrotoalcite-like phase

Consistent with the previous results, hydrotoalcite-like phase seemed to be unaffected by CO_2 attack. The Mg/Al atomic ratios derived from the regression analysis of Mg/Si against Al/Si scatter plots (Figure 8.11) remained nearly unchanged before and after carbonation. In other words, hydrotoalcite-like phase remained intact during carbonation, and the CO_2 uptake in its interlayer space would not decompose its network structure.

8.4. DISCUSSION

8.4.1. SLAG CHEMISTRY VS. CO_2 BINDING ABILITY

IT is well recognized that the carbonation resistance of cementitious materials depends on two main factors: one is CO_2 binding capacity and the other one is pore structure. In cement-based systems, portlandite and C-S(A)-H gel phase (especially for blended cements where most portlandite has been consumed in pozzolanic reaction) are regarded as the main phases to be carbonated. However, the role of minor hydrates, e.g., hydrotoalcite-like phase and monosulfate in taking up CO_2 has been largely neglected. These minor phases are essential particularly when the slag substitution level is high, e.g., CEM III/B, or 70 wt.% in the present research, and alkali-activated slag system. Therefore, the author believe that influence of slag chemistry on the CO_2 binding capacity of slag cement paste deserves a deeper discussion, in which the CO_2 binding ability of different phases should be emphasized.

In Chapter 6, the author employed model paste to discuss the correlation between CO_2 binding capacity and slag chemistry, and here the author turned to real slag cement paste. It was defined that the results measured from fully carbonated area as

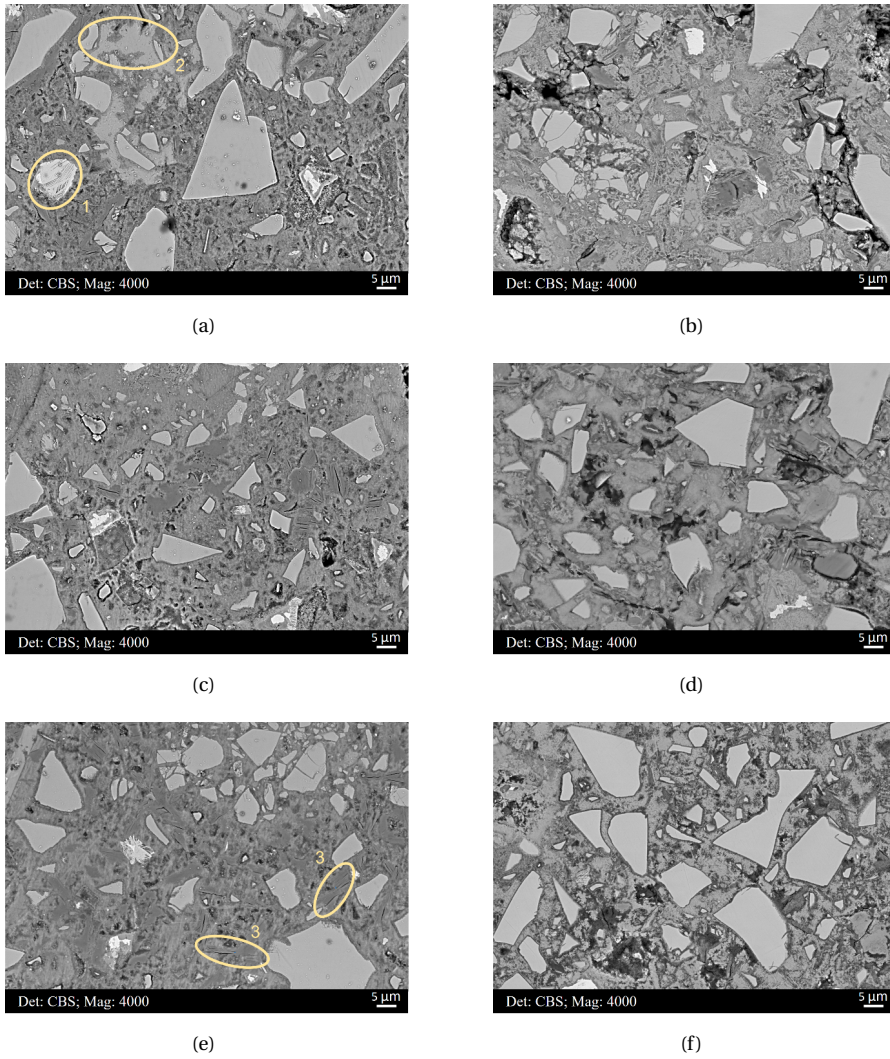


Figure 8.9: (a), (c), and (e): Microstructure of cement-slag A3, CS1, and A18 mixtures after curing of 3 months, respectively; and (b), (d), and (f): carbonated area of cement-slag A3, CS1, and A18 mixtures, respectively.

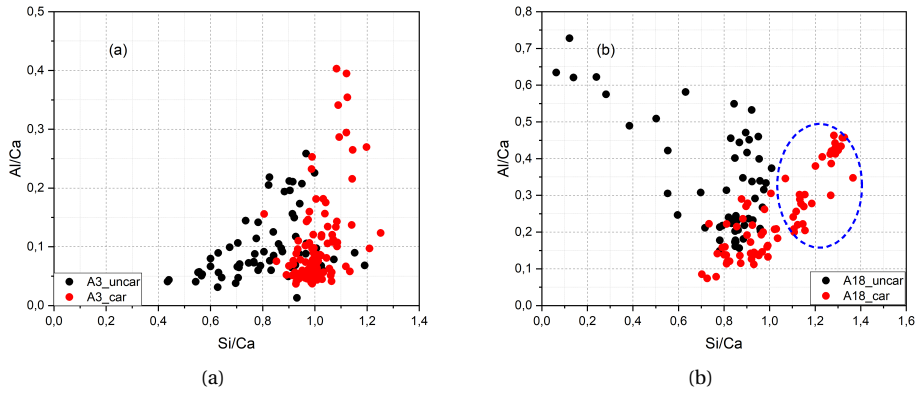


Figure 8.10: Representative plots of Al/Ca against Si/Ca in atomic ratio of slag (a) A3 and (b) A18 pastes before and after carbonation.

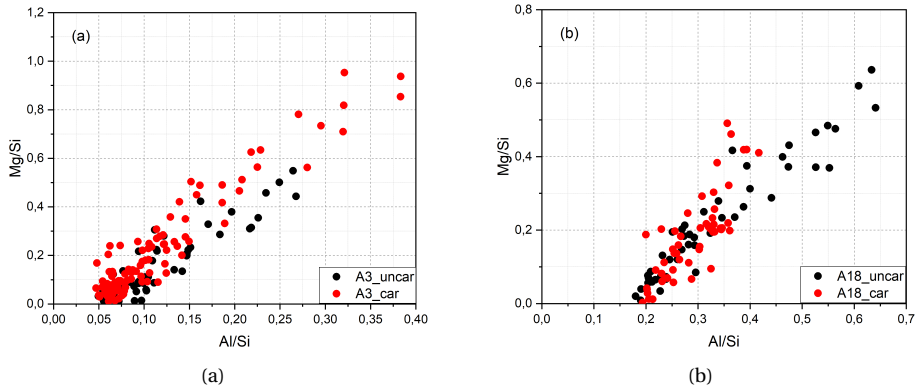


Figure 8.11: Representative plots of Mg/Si against Al/Si in atomic ratio of slag (a) A3 and (b) A18 pastes before and after carbonation.

CO₂ binding capacity of real cement-slag system. One should keep in mind that it is difficult for C-S-H gel phase produced in the real cementitious materials to decalcify to a Ca/Si ratio of 0.67. Six months of accelerated carbonation test was performed in the study and the author considered that the surface area had (nearly) been carbonated completely. Data from this Chapter and Chapter 7 would be analyzed together to cover the common range of slag chemistry.

Figure 8.12 demonstrates that the areas under MS CO₂ curves, or CO₂ binding capacity of the specimens increased significantly with the increasing MgO content from slag M0 to M16 blend; however, Al₂O₃ seemed to have negligible effect on CO₂ binding capacity. In other words, the enhanced ettringite and monosulfate formations with increasing alumina content in slag did not influence the CO₂ binding capacity positively. It was reasonable as the CO₂ concentration bound in carbonated Ca-Al AFm phases was stable, less than 1 wt.% (Table 8.2).

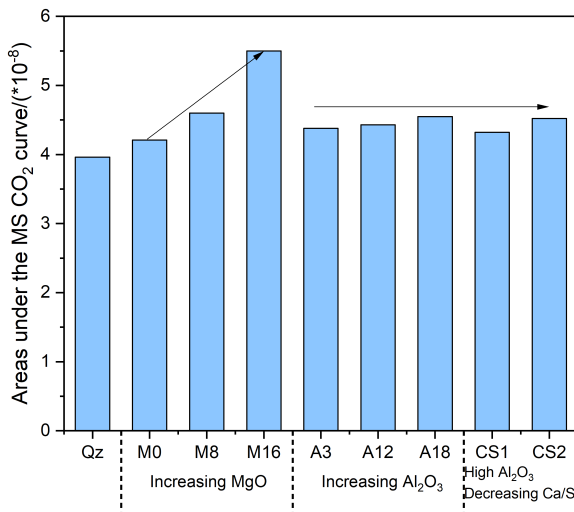


Figure 8.12: The areas under MS CO₂ curves or CO₂ binding capacity against slag chemistry.

As shown in Table 8.1 and 8.2, the absolute amount of CO₂ absorbed in each buffer phase increased when shifting from mildly carbonated to fully carbonated area. Similar to the results shown in Figure 7.14, the proportions distributed among these buffer phases confirmed that the proportion of CO₂ absorbed into carbonated Ca-Al AFm phases plus hydrotalcite-like phase decreased while that from calcium carbonate increased (Figure 8.13). Initially, monosulfate, hydrotalcite-like phase, portlandite, and C-S(A)-H gel phase acted as the CO₂ binding phases together. Especially for monosulfate and hydrotalcite-like phase, they shared around 30% CO₂ in total in the mildly carbonated area because of their stacked layer morphology, and this value decreased to ~20% in the transitional area and less than 20% in the fully carbonated area. It can be suggested that there is a limit for the stacked layer structure to absorb CO₂, when the space between layers is occupied by CO₂ completely, CO₂ can only be fixed into calcium carbonate. Therefore, the proportion of CO₂ bound in calcium

carbonate went up under continuous CO_2 attack. Note that contrary to the reaction between CO_2 and C-S-H gel phase which is a volume decrease reaction, the stacked layer structure can maintain its structure and would not lead to a pore structure coarsening during carbonation.

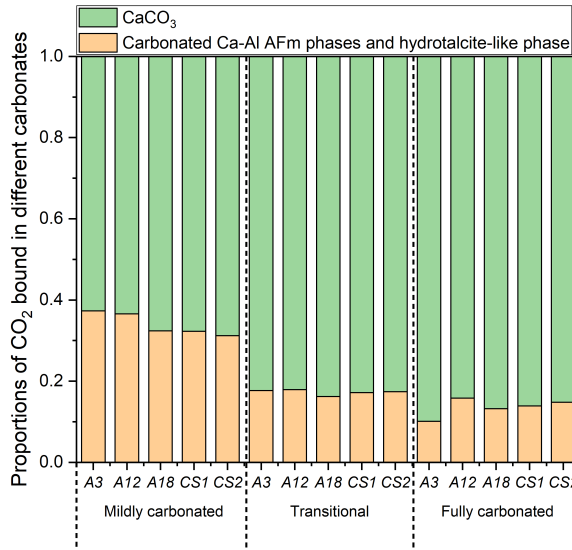


Figure 8.13: The proportions of CO_2 bound in $CaCO_3$ and carbonated Ca-Al AFm phases plus hydrotalcite-like phase from mildly to fully carbonated area of each mixture.

8.4.2. SLAG REACTIVITY VS. CARBONATION RESISTANCE OF CEMENT-SLAG SYSTEM

Al_2O_3 -rich slag cement paste shows good performance at the early age of hydration [4, 5]. Based on R3 and dissolution tests, the results in Chapter 4 also verified that slag reactivity positively affected by its alumina content. Besides, three levels of reactivity were classified, i.e., low reactivity (slag M0 and A3), medium reactivity (slag M8, A12, CS1, and CS2), and high reactivity (slag M16 and A18). However, when estimating the carbonation resistance of these cement-slag mixtures according to two important parameters, i.e., pore structure and CO_2 binding capacity [23], the classification employed for reactivity was not applicable anymore.

Yet, cement-slag M16 mixture exhibited the best carbonation resistance. It showed the least carbonation depth based on phenolphthalein spray (5-10 mm) (For the results regarding slag M0, M8, and M16, please refer to Chapter 7.), the highest CO_2 binding capacity (Figure 8.12), and the smallest critical pore diameter after carbonation. As for slag M0, CS1, and CS2, they presented the worst carbonation resistance when blended with cement. Their carbonation depths were much greater (close to 20 mm), and they displayed a bimodal pore structure with larger pore volume after carbonation. For slag M8, A3, A12, and A18, they showed a medium carbonation resistance in the slag rich cement pastes with similar CO_2 binding capacity.

Although high alumina content slag cement pastes (CS1 (14.51 wt.%), CS2 (17.12 wt.%), and A18 (18.19 wt.%)) show good early age performance owing to the enhanced formation of ettringite and monosulfate, they do not perform equally good against CO₂ attack. The specimens with slag CS1 and CS2 formed a relatively larger critical pore diameter after 3 months of curing (10-20 nm as shown in Figure 8.8(a)), which was the main reason for their lower carbonation resistance compared to other specimens. In other words, the adverse effect of CaO/SiO₂ ratio reduction on the hydration can be compensated by higher amount of Al₂O₃ but the same argument cannot be extended to the carbonation resistance. For instance, the slag A18 paste showed a mediocre carbonation resistance. This behavior can be explained by taking the following two aspects into consideration. Firstly, enhanced ettringite and monosulfate formations (due to high alumina content) do not influence the CO₂ binding capacity positively. Secondly, aluminum uptake in C-S-H gel phase increases the amount of bridging silicate tetrahedra [20], and a greater number of polymerized units commonly exhibit a better carbonation resistance by the limited CO₂ access [24, 25]. Thus, the CO₂ binding capacity seemed to be unaffected by the Al₂O₃ content in slag (Figure 8.12).

8.4.3. THERMODYNAMIC MODELLING

Figure 8.14 illustrates the thermodynamic modelling results of phase assemblage evolution during the step-wise carbonation, using cement-slag A18 paste as an example. The reaction degree of clinker phases of cement at 90 days was estimated using the empirical kinetic approach of Parrot [26], and the parameters were reported by Lothenbach et al. in [27]. The hydration degree of slag A18 was estimated to be 30% after 3 months of curing. For simplicity, it was assumed that slag dissolved congruently.

Here the author attempted to discuss the phase transition of Al-bearing and SO₄-bearing phases after CO₂ addition.

After the decomposition of monosulfate, ettringite was modelled to be the main sulfate-bearing phase (intermediate), which was further carbonated to yield gypsum. In fact, the migration of element sulfur from carbonated to uncarbonated area was also verified by pore solution analysis [28] and EDS mapping [29]. However, no gypsum was detected in the present study and other blended cement systems [11, 30]. Probably this secondary gypsum was amorphous [30], or the amount of sulfate in the system was too low as it was formed in the carbonated supersulfated cement paste [31]. Besides, sulfate ions can also be absorbed by amorphous silica gel formed after carbonation. This factor should be taken into account in the further research. As for the transformation routine of Al-bearing phases, monosulfate and strätlingite started to decompose upon CO₂ contact. Hemi- and mono-carbonates were predicted as intermediates. Monocarbonate was decomposed into calcite and subsequently to strätlingite as the carbonation proceeded. Hydrogarnet persisted initially and also transformed into strätlingite with the continuous CO₂ attack. Al-gel was predicted as the final Al-bearing phase. Apparently, several disagreements existed between GEMS modelling and experimental results. It should be noted that the formation of hemi- and mono-carbonates was not observed by XRD or TGA in this study at any carbonation depth. The authors considered that monosulfate (including other Ca-Al AFm phases) would not decompose during carbonation, and absorb CO₂ into interlayer space

because of its layered microstructure. It was consistent with the results in [32], which also concluded that monosulfate can incorporate some carbonates, forming carbonate/sulfate-AFm solid solution.

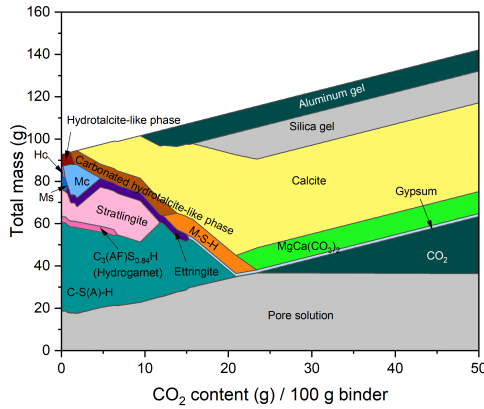


Figure 8.14: Thermodynamic modelling of the phase assemblages in A18 paste during the step-wise carbonation. Hc: calcium hemicarbonate; Mc: calcium monocarbonate; Ms: calcium monosulfoaluminate.

8.5. CONCLUSIONS

THIS chapter investigated the carbonation characteristics of predefined cement-slag systems through accelerated carbonation test, and attempted to build a connection among slag chemistry, slag reactivity, and carbonation resistance of the system. The main conclusions drawn were as follows:

- After accelerated carbonation testing, three CO_2 binding phases were identified irrespective of the gradual addition of alumina content in slag, i.e., carbonated Ca-Al AFm phases (amorphous or nano-crystalline), carbonated hydratalcite-like phase, and calcium carbonate (vaterite and calcite).
- The critical pore diameter of slag cement pastes increased to the range of 0.1-10 μm after carbonation. A bimodal pore structure and significantly larger pore volume appeared in the carbonated CS1 and CS2 slag pastes.
- Carbonated Ca-Al AFm phases and hydratalcite-like phase bound around 30% of the total CO_2 that diffused into the mildly carbonated area. This value decreased to about 20% in the transitional area and less than 20% in the fully carbonated area.
- The CO_2 binding capacity of each mixture was similar, fluctuating at 15-20 wt.% in the completely carbonated area. In other words, the enhanced ettringite and calcium monosulfoaluminate formation with the increasing alumina content did not exert a positive influence on CO_2 binding capacity.

- The slag reactivity classification proposed in Chapter 4 cannot be extended to predict carbonation resistance of a cement-slag system directly. The main challenge occurred for slags with high alumina content. The experiments showed that Al_2O_3 -rich slag was reactive as a blended cement component but it did not contribute to carbonation resistance.

REFERENCES

- [1] A. Ehrenberg and D. Algermissen, *Alternative Nutzungsmöglichkeiten von Elektroofenschlacke zur Klinker- und Hüttensandsubstitution*, in *Berliner Konferenz Mineralische Nebenprodukte und Abfälle 4* (2017).
- [2] ACI, *Slag cement in concrete and mortar*, Report (American Concrete Institute, 2003).
- [3] E. Özbay, M. Erdemir, and H. İ. Durmuş, *Utilization and efficiency of ground granulated blast furnace slag on concrete properties—A review*, *Construction and Building Materials* **105**, 423 (2016).
- [4] M. Whittaker, M. Zajac, M. Ben Haha, F. Bullerjahn, and L. Black, *The role of the alumina content of slag, plus the presence of additional sulfate on the hydration and microstructure of Portland cement-slag blends*, *Cement and Concrete Research* **66**, 91 (2014).
- [5] S. Blotevogel, A. Ehrenberg, L. Steger, L. Doussang, J. Kaknics, C. Patapy, and M. Cyr, *Ability of the R3 test to evaluate differences in early age reactivity of 16 industrial ground granulated blast furnace slags (GGBS)*, *Cement and Concrete Research* **130**, 105998 (2020).
- [6] R. Snellings, X. Li, F. Avet, and K. Scrivener, *Rapid, Robust, and Relevant (R3) Reactivity Test for Supplementary Cementitious Materials*, *ACI MATERIALS JOURNAL* **116** (2019).
- [7] G. Villain, M. Thiery, and G. Platret, *Measurement methods of carbonation profiles in concrete: Thermogravimetry, chemical analysis and gammadensimetry*, *Cement and Concrete Research* **37**, 1182 (2007).
- [8] M. Thiery, G. Villain, P. Dangla, and G. Platret, *Investigation of the carbonation front shape on cementitious materials: Effects of the chemical kinetics*, *Cement and Concrete Research* **37**, 1047 (2007).
- [9] A. Morandeau, M. Thiery, and P. Dangla, *Investigation of the carbonation mechanism of CH and CSH in terms of kinetics, microstructure changes and moisture properties*, *Cement and Concrete Research* **56**, 153 (2014).
- [10] M. Zajac, A. Lechevallier, P. Durdzinski, F. Bullerjahn, J. Skibsted, and M. B. Haha, *CO₂ mineralisation of portland cement: Towards understanding the mechanisms of enforced carbonation*, *Journal of Co2 Utilization* **38**, 398 (2020).

- [11] P. H. Borges, J. O. Costa, N. B. Milestone, C. J. Lynsdale, and R. E. Streatfield, *Carbonation of CH and C–S–H in composite cement pastes containing high amounts of BFS*, *Cement and Concrete Research* **40**, 284 (2010).
- [12] Y. Okada, T. Masuda, M. Takada, L. Xu, and T. Mitsuda, *Relationship between NMR ^{29}Si chemical shifts and FT-IR wave numbers in calcium silicates*, in *Nuclear magnetic resonance spectroscopy of cement-based materials* (Springer, 1998) pp. 69–78.
- [13] W. Ashraf and J. Olek, *Carbonation behavior of hydraulic and non-hydraulic calcium silicates: potential of utilizing low-lime calcium silicates in cement-based materials*, *Journal of materials science* **51**, 6173 (2016).
- [14] M. Zajac, J. Skibsted, P. Durdzinski, F. Bullerjahn, J. Skocek, and M. B. Haha, *Kinetics of enforced carbonation of cement paste*, *Cement and Concrete Research* **131**, 106013 (2020).
- [15] L. Black, C. Breen, J. Yarwood, K. Garbev, P. Stemmermann, and B. Gasharova, *Structural features of C–S–H (I) and its carbonation in air—a raman spectroscopic study. Part II: carbonated phases*, *Journal of the American Ceramic Society* **90**, 908 (2007).
- [16] G. Rimmelé, V. Barlet-Gouédard, O. Porcherie, B. Goffé, and F. Brunet, *Heterogeneous porosity distribution in Portland cement exposed to CO₂-rich fluids*, *Cement and Concrete Research* **38**, 1038 (2008).
- [17] B. Wu and G. Ye, *Development of porosity of cement paste blended with supplementary cementitious materials after carbonation*, *Construction and Building Materials* **145**, 52 (2017).
- [18] V. Ngala and C. Page, *Effects of carbonation on pore structure and diffusional properties of hydrated cement pastes*, *Cement and Concrete Research* **27**, 995 (1997).
- [19] M. Frías and S. Goñi, *Accelerated carbonation effect on behaviour of ternary Portland cements*, *Composites Part B: Engineering* **48**, 122 (2013).
- [20] I. Richardson, *Tobermorite/jennite-and tobermorite/calcium hydroxide-based models for the structure of CSH: applicability to hardened pastes of tricalcium silicate, -dicalcium silicate, portland cement, and blends of portland cement with blast-furnace slag, metakaolin, or silica fume*, *Cement and Concrete Research* **34**, 1733 (2004).
- [21] J. I. Escalante-Garcia and J. H. Sharp, *The chemical composition and microstructure of hydration products in blended cements*, *Cement and Concrete Composites* **26**, 967 (2004).
- [22] R. Taylor, I. Richardson, and R. Brydson, *Composition and microstructure of 20-year-old ordinary Portland cement–ground granulated blast-furnace slag blends containing 0 to 100% slag*, *Cement and Concrete Research* **40**, 971 (2010).

- [23] S. von Greve-Dierfeld, B. Lothenbach, A. Vollpracht, B. Wu, B. Huet, C. Andrade, C. Medina, C. Thiel, E. Gruyaert, H. Vanoutrive, *et al.*, *Understanding the carbonation of concrete with supplementary cementitious materials: a critical review by RILEM TC 281-CCC*, *Materials and structures* **53**, 1 (2020).
- [24] J. Li, Q. Yu, H. Huang, and S. Yin, *Effects of Ca/Si ratio, aluminum and magnesium on the carbonation behavior of calcium silicate hydrate*, *Materials* **12**, 1268 (2019).
- [25] L. Irbe, R. Beddoe, H. Hilbig, and D. Heinz, *The role of aluminium in CASH during chemical attack on concrete*, in *Second International Conference on the Chemistry of Construction Materials-ICCCM 2016*.
- [26] L. Parrot, *Prediction of cement hydration*, in *Proceedings of the British Ceramic Society*, Vol. 35, pp. 41–53.
- [27] B. Lothenbach, G. Le Saout, E. Gallucci, and K. Scrivener, *Influence of limestone on the hydration of Portland cements*, *Cement and Concrete Research* **38**, 848 (2008).
- [28] K. De Weerd, G. Plusquellec, A. B. Revert, M. Geiker, and B. Lothenbach, *Effect of carbonation on the pore solution of mortar*, *Cement and Concrete Research* **118**, 38 (2019).
- [29] F. Georget, W. Soja, and K. L. Scrivener, *Characteristic lengths of the carbonation front in naturally carbonated cement pastes: Implications for reactive transport models*, *Cement and Concrete Research* **134**, 106080 (2020).
- [30] H. Justnes, J. Skocek, T. A. Østnor, C. J. Engelsen, and O. Skjølsvold, *Microstructural changes of hydrated cement blended with fly ash upon carbonation*, *Cement and Concrete Research* **137**, 106192 (2020).
- [31] Y. Xie, T. Sun, Z. Shui, C. Ding, and W. Li, *The impact of carbonation at different CO₂ concentrations on the microstructure of phosphogypsum-based supersulfated cement paste*, *Construction and Building Materials* **340**, 127823 (2022).
- [32] F. Georget, B. Lothenbach, W. Wilson, F. Zunino, and K. L. Scrivener, *Stability of hemihydrate under cement paste-like conditions*, *Cement and Concrete Research* **153**, 106692 (2022).

III

CONCLUSIONS

9

CONCLUSIONS AND RECOMMENDATIONS

In this chapter, retrospection and conclusions of this Ph.D. thesis were summarized and discussed. Additionally, recommendations were given for possible further work.

9.1. RETROSPECTION

IN order to design cement-slag system that is more resistant to carbonation, the main aim of this thesis was to understand the connection among slag chemistry, reactivity, and carbonation resistance of slag-rich cement pastes. For this purpose, the variation of slag composition was firstly identified through (1) literature review and (2) unhydrated slag grains existing in old slag concrete structures with different service life. Then, synthetic slags covering the identified composition range were produced in the laboratory, to eliminate potential interferences and focus on slag chemistry only. Subsequently, the effect of slag composition on slag reactivity and carbonation resistance of slag-rich cement paste were investigated systematically. When evaluating reactivity, two methods, i.e., R3 and dissolution tests were employed. Several indices, including cumulative heat release, bound water content, Si^{4+} concentration, and dissolution rate etc. were used as criterion to evaluate slag reactivity. Moreover, carbonation depth, CO_2 binding capacity, and critical pore diameter were selected as the main parameters to evaluate the carbonation resistance of the system. Through all these measurements, the correlation among slag chemistry-reactivity-carbonation resistance was built. In the thesis, the following attempts were made to achieve the research objects.

Chapter 3 investigated the feasibility of using EDS microanalysis as a tool for quantitative measurement of the chemical compositions of unhydrated slags in existing field concretes. In the experimental study, seven concrete samples representing various service life durations were collected in the Netherlands. A favorable microanalysis protocols for acceptable elemental quantification accuracy was proposed, including sample preparation, instrumental parameters, electron-slag interaction volume, and microanalysis standards. The results revealed the variation trend of slag composition with time in the Netherlands.

In **Chapter 4**, nine synthetic slags based on $\text{CaO-SiO}_2\text{-Al}_2\text{O}_3\text{-MgO}$ system and one commercial slag were considered to determine the correlation between slag chemistry and reactivity. The idea behind the design of synthetic slags was to cover the variation of slag composition reviewed in **Chapter 2** and identified in **Chapter 3**. These raw slags were characterized by XRD, ESEM, as well as FTIR to ensure that the only variable was slag chemistry. In order to study reactivity, two methods were employed in the study. The first one was hydraulicity/R3 test on a model blended system composed of slag, calcium hydroxide, limestone and potassium-hydroxide and -sulfate solutions. The other one was the dissolution test of slag powders in strong NaOH solution. Additionally, the author attempted to estimate the reactivity of slag using a novel graphical method based on a cartesian coordinate system of $(\text{CaO/SiO}_2)\text{-}(\text{Al}_2\text{O}_3\text{+MgO})$ in weight percentage.

Chapter 5 observed the carbonation products in the slag-rich cementitious systems (mainly CEM III/B) upon three different exposure conditions, namely, long term exposure in the field, indoor natural exposure, and accelerated carbonation testing. The phase assemblage was identified through TGA, XRD, and SEM-EDS. TG-DTG-MS was employed to calculate the CO_2 concentration in different hydrates. Especially, emphasis was laid on the carbonation of minor hydrates, i.e., monosulfate and hydrotalcite-like phase. The results obtained in this chapter can be served as a basis for

the following chapters.

Chapter 6 examined the correlation between slag chemistry and CO₂ binding capacity. To simplify the composition of mixture, model paste containing C₃S, synthetic slags and gypsum was employed. To accelerate the carbonation process, the specimen was ground to powders after 3 months of sealed curing, which were exposed to CO₂ directly. The carbonation mechanism was investigated through a complementary set of analytical methods including TGA, XRD, and FTIR. Similarly, TG-DTG-MS was employed to quantify the CO₂ binding capacity of each mixture, and the influence of slag composition on CO₂ binding capacity was discussed.

In **Chapter 7** and **8**, the effect of MgO and Al₂O₃ contents of slag on the carbonation characteristics of cement-slag system was explored, respectively. Accelerated carbonation testing was performed on slag cement paste. The evolution of phase assemblage (TGA, XRD, FTIR, and SEM-EDS), microstructure (MIP and SEM) and micro-mechanical properties (Nanoindentation) development of each mixture before and after carbonation testing were evaluated. Finally, the correlation among slag chemistry, reactivity, and carbonation resistance was discussed comprehensively combining the data of **Chapter 6, 7, and 8**.

9.2. CONCLUSIONS

MAIN concluding remarks of the thesis were drawn and highlighted as follows:

- *Quantitative EDS microanalysis provides reliable quantification regarding the four main metal oxides contents (CaO, SiO₂, Al₂O₃, and MgO) of slag. Also, standard-based EDS microanalysis is a favorable tool to characterize unhydrated slag grains in existing field concretes, which is important for predicting long-term performance as well as for clarifying cement type for recycling purposes.*

An evident increasing in CaO and SiO₂ contents was found in slag used in recent years, opposite to that of Al₂O₃ and MgO. Especially for MgO, it showed a gradual decreasing tendency over the past years. For sulfur and titanium, a large relative deviation was found among different characterization methods when determining their concentrations, which was related to the heterogeneity of slag particle and oxidation state of sulfur.

- *It was found that higher Al₂O₃ and MgO contents of slag led to a higher reactivity, and the adverse effect of decreasing CaO/SiO₂ ratio on reactivity could also be compensated by introducing higher Al₂O₃ and/or MgO contents. These results highlighted the importance of minor components of slag composition for reactivity. Besides, it also confirmed that the reactivity of slag used in the Netherlands decreased gradually due to the reduced MgO content with years.*

The reactivity determined from calorimetric measurement, bound water content quantification of the model pastes, as well as Si⁴⁺ concentration and its dissolution rate from dissolution test followed similar tendency. The graphic method put forward in Chapter 4 explained the interaction among different metal oxides and can be used as a simple evaluation tool for industry.

- *The main CO₂-bearing phases in slag cement paste were carbonated Ca-Al AFm*

phases (amorphous or nano-crystalline), carbonated hydrotalcite-like phase, and calcium carbonate (vaterite and calcite), irrespective of slag chemistry.

With the continuous supply of CO₂, monosulfate would be consumed at first. From this aspect, the nonexistence of calcium monosulfoaluminate can be treated as an indicator of potential carbonation-related damage. Carbonated hydrotalcite-like phase was the secondary CO₂-bearing phase next to calcium carbonate. It was structurally resistant against carbonation. The Mg/Al atomic ratios of hydrotalcite-like phase did not vary significantly during carbonation.

- *More than 20% CO₂ was fixed by carbonated hydrotalcite-like phase as well as the Ca-Al AFm phases at first, and these reactions were harmless without any detrimental effect on cement matrix. The evidence indicated that these two phases can be the key components towards formulating blast furnace slag systems resistant to carbonation.*

In all the exposure conditions, carbonated Ca-Al AFm phases bound around 5% of the entire bound CO₂ in the matrix. Hydrotalcite-like phase fixed more than 15% CO₂ at the beginning, and this value was positively associated with the magnesia content of slag. However, this value decreased to around 10% by the full carbonation, and more CO₂ was fixed into calcium carbonate. Thus, increasing the amount of MgO in slag, more hydrotalcite-like phase can be produced in the matrix, and it was believed to formulate cement-slag system with improved carbonation resistance.

- *Generally, the CO₂ binding capacity of the blended system was not directly related to the reactivity of slag.*

Mixture with a Al₂O₃-rich slag presented a low CO₂ binding capacity, while a low CaO/SiO₂ ratio slag contributed to a high CO₂ amount captured in the system. In other words, the enhanced ettringite and monosulfate formation with the increasing alumina content in slag did not exert a positive influence on CO₂ binding capacity. Thus, Al₂O₃-rich slag should not be considered when carbonation resistance is of high priority.

- *The classification employed for slag reactivity cannot be extended to characterize carbonation resistance of cement-slag system directly.*

The main challenge occurred for slags with high alumina content. The experiments showed that Al₂O₃-rich slag was reactive as a blended cement component but it did not contribute to carbonation resistance. Therefore, considering the effect of slag chemistry on reactivity and carbonation resistance together, CaO/SiO₂ ≈ 1, high MgO (> 10 wt.%) and moderate Al₂O₃ (10-15 wt.%) contents slag was recommended to design slag rich concrete structure with improved hydration performance and carbonation resistance.

9.3. RECOMMENDATIONS FOR FURTHER STUDY

WITH respect to the scope of this thesis, several extensions of the presented study can be taken into account in further research regarding:

- As found in Chapter 3, a large relative deviation was found among different characterization methods when determining the concentrations of trace elements in slag. Therefore, a higher resolution technique such as WDS should be considered when these elements are of concern. A suitable protocols based on WDS microanalysis should be explored in the future.
- It was noted that there was a trend for consistent production of lime-rich slag in steelmaking manufacturing. However, for synthetic and commercial slags employed in the thesis, the CaO/SiO_2 ratio was kept at around 1 (Chapter 4). It deserves further research that whether this continuous increase in CaO content of slag (i.e., $\text{CaO}/\text{SiO}_2 \gg 1$) can enhance slag performance in cement paste, including reactivity, hydration, and durability etc.
- In the thesis, emphasis was laid on the carbonation behavior of monosulfate and hydrotalcite-like phase. To further explore this idea, carbonation test should also be performed on the synthesized pure hydration products. Also, thermodynamic properties of these pure phases before and after carbonation can be measured, providing the essential database for thermodynamic modelling (e.g., GEMS).
- The thesis built a connection among slag chemistry, reactivity, and carbonation resistance of slag-rich cement paste. Similarly, a further work can be extended to other durability-related performance, e.g., freezing and thawing, chloride and sulfate attack, etc. Under this circumstance, a whole picture among slag chemistry, reactivity, and durability of slag-rich cement paste can be depicted.
- Considering the influence of slag chemistry on reactivity and carbonation resistance together, $\text{CaO}/\text{SiO}_2 \approx 1$, high MgO and moderate Al_2O_3 contents slag was recommended to design slag rich concrete structure with improved hydration performance and carbonation resistance. To reduce CO_2 emission in cement industry further, even higher replacement level with such kind of slag can be used, e.g., CEM III/C, to achieve a similar performance with CEM III/B using normal slag.
- Considering the positive effect of hydrotalcite-like phase during CO_2 attack and other potential durability-related issues, adding dolomite as filler should be better than adding limestone to cement-slag system. Thus, cement-slag-dolomite system is recommended for investigation in the future.

ACKNOWLEDGMENTS

At the end of my Ph.D. journey, I would like to express my so many appreciations to the people and institutions who have helped and supported me over the past 4 years.

The research work presented in the thesis was sponsored by China Scholarship Council (CSC) and BAM Infraconsult B.V. Their financial support ensures the accomplishment of the work done at the Microlab, Section Materials and Environment, Faculty of Civil Engineering and Geosciences, Delft University of Technology, Delft, The Netherlands.

First of all, I would like to thank my promotor Dr. Oğuzhan Çopuroğlu, for giving me the opportunity to study in TU Delft. The first time we met each other was a cold spring morning with rains three years ago in Delft. I am very grateful for his frank during the meeting. One month later, I came to Delft again, be a member of Microlab officially. He is an extraordinary expert in our field, and discussions with him always bring me new understandings on my work. For my manuscripts, he is patient and careful to give constructive comments. His guidance, support, and comments helped me a lot both in research and life. I would keep these memories in my mind, Teşekkür ederim!

I would also like to give sincere gratitude to my another promotor Prof. Erik Schlangen, who gave me 100% support and a lot of inspirations during the Ph.D. It is always pleasant to talk with him. In life, he is kind, patient and friendly, and his sense of humor never lets you feel nervous and stressed. He creates a wonderful environment and atmosphere for the Microlab, Dank u!

Appreciation goes to the chairperson Prof. K. van Breugel and all committee members, Prof. Qingfang Lyu, Prof. S.R. van der Laan, Prof.dr. H.M. Jonkers, Dr. Ö. Cizer, Dr. G. Ye, and Prof. M.A.N. Hendriks for taking time to read the preliminary version of this thesis, propose comments and attend my Ph.D. defense.

Special gratitude extends to Branko Šavija and Guang Ye. From their courses, "Concrete Sciences and Technology" as well as "Micromechanics and Computational Modelling of Building Materials", I obtained valuable advice and ideas for my research topic, which helped me to finish the Ph.D study. Appreciation also goes to Dessi Koleva and Mladena Luković. They attended my Go No Go meeting 2 years ago, and provided many unique suggestions for my investigation. Also, I would like to express my great gratitude to my officemates, Emanuele Rossi and Fernando França de Mendonça Filh. It is really a great pleasure to share my life with you. Additionally, I want to give many thanks to Patrick Holthuisen, who helped me translate the summary from English to Dutch.

As a experiment-based project, I want to take a special moment to express my gratitude to those who helped me with the experiments. Arjan Thijssen helped me in ESEM, MIP, XRD, and PSD measurements. Especially for ESEM, he provided me many suggestions from sample preparation to data analysis, which is very important for my research. John van den Berg gave me many trainings in High temperature oven,

TGA-MS, BET, and carried out numbers of ICP-OES tests. Without his unselfish support, I cannot finish these experiments on time. Maiko van Leeuwen also helped me in many experiments, including cutting, polishing and grinding, compressive strength test and accelerated carbonation test. It is always fun to work with him. Most importantly, Go Oranje Go for the World Cup! Ton Blom taught me how to use the cutting machine and compressive machine in the Stevin-II lab, and I am very grateful to him. Moreover, Karthikeyan Saravanakumar (MSc) helped me prepare many samples, Paul Vermeulen installed the equipment for carbonation test, Ruud Hendriks (3ME) helped me in XRF measurement, Anna Alberda van Ekenstein and Bart Hendrix shared me samples collected from field. I would like to thank all of them. Besides, Jeanette van den Bos and René Albers (Ecocem Benelux B.V.) are gratefully acknowledged for the technical discussions and providing me different commercial slags. Furthermore, our secretaries Iris Batterham, Jacqueline van Unen-Berghenhenegouwen, Jaap Meijer, and Sandra Schuchmann are also highly appreciated for their kind help on various daily issues.

Besides, I want to express my gratitude to Hua Dong, Zhenming Li, Shi Xu, Shizhe Zhang, Boyu Chen, Yading Xu, Yu Chen, Lu Cheng, Ze Chang, Xuhui Liang, Yun Chen, Zhiyuan Xu, Zhi Wan, Yitao Huang, Shan He, Chen Liu, Minfei Liang, Yu Zeng, Hu Shi, and Jinbao Xie. Thank you for helping and supporting me over these years. My gratitude also goes to Anne Linde van Overmeir, Ameya Kamat, Claudia Romero Rodríguez, Farnaz Aghabeyk, Guilherme da Silva Munhoz, Luiz Miranda de Lima Junior, and Marija Nedeljković. Thanks for all the great time we have spent together.

Appreciation goes to all the other colleagues of Microlab: Zhiwei Qian, Xuliang Hou, Jiayi Chen, Bei Wu, Hao Huang, Albina Kostuchenko, Ali Ghaderiaram, Clarissa Justino de Lima, Damian Palin, Kuba Pawlowicz, Mohammad Fotouhi, Irving Alfredo Flores Beltran, and Stefan Chaves Figueiredo. Also, I want to thank the help and friendship from all former colleagues: Zhipei Chen, Hongzhi Zhang, Wenjuan Lyu, Yibin Zuo, Yidong Gan, Xingliang Yao, Dawei Gu, and Yask Kulshreshtha.

Finally, I want to express my deepest gratitude to my family. Although it has been 3 years since we met last time, their support always surrounds me. Special thanks to my mother, and I know this period was difficult for her. Thank you for the love and understanding!

Yu Zhang
Delft, Nov 2022